Stony Brook University

Lithosphere Deformation Methods and Models Constrained by Surface Fault Data on Mars

A Dissertation Presented

by

Lada L. Dimitrova

to

The Graduate School

in Partial Fulfillment of the

Requirements

for the Degree of

Doctor of Philosophy

in

Geosciences

Stony Brook University

August 2009

Stony Brook University

The Graduate School

Lada L. Dimitrova

We, the dissertation committee for the above candidate for the
Doctor of Philosophy degree, hereby recommend
acceptance of this dissertation.

William Holt - Dissertation Advisor

Professor, Department of Geosciences

Daniel Davis - Chairperson of Defense

Professor, Department of Geosciences

Hanna Nekvasil

Professor, Department of Geosciences

Scott McLennan

Professor, Department of Geosciences

Gregory Neumann

Geophysicist, Planetary Geodynamics Group, NASA GSFC

This dissertation is accepted by the Graduate School

Lawrence Martin
Dean of the Graduate School

Abstract of the Dissertation

Lithosphere Deformation Methods and Models Constrained by Surface Fault Data on Mars

by

Lada L. Dimitrova

Doctor of Philosophy

in

Geosciences

Stony Brook University

2009

Models of lithospheric deformation tie observed field measurements of gravity and topography with surface observations of tectonic features. An understanding of the sources of stress, and the expected style, orientation, and magnitudes of stress and associated elastic strain is important for understanding the evolution of faulting on Mars and its relationship to loading. At the same time, theoretical models of deformation mechanisms and forces, when tied to tectonic observations, can be interpreted in terms of major tectonic events and allow insights into the planet's history and evolution as well as its internal structure and processes. This is particularly important for understanding solid planetary bodies other than Earth where the seismic data is either sparse, e.g. the Moon, or non-existent, e.g. Mars. This kind of research has implications for, and benefits from, an understanding of the petrology and surface processes.

In this work, I use MGS MOLA and Radio Science data products (topography and gravity) to systematically test new geodynamic models and evaluate lithosphere dynamics on Mars as a function of time, while satisfying geologic surface observations (surface features) that have been and are being catalogued and studied from Viking, MOLA, MOC, and THEMIS IR images. I investigate (1) the role of internal loads (internal body force effects), (2) loading from the surface and base of lithosphere, and the effects of this loading on membrane and flexural strains and stresses, and (3) the role of global contraction, all viewed in the context of how the surface elastic layer has changed as the planet has evolved. I show that deviatoric stresses associated with gravitational potential differences do a good job at matching the normal faults; however, fitting all the surface-breaking faults is more difficult. I argue that global planetary contraction is an unlikely source of significant deformation.

Instead, the simplest inverse models show that small lateral variations $(1-6\%)$ in crust and mantle density in conjunction with small vertical displacement, $O(100m)$, provide sufficient additional GPE and membrane stress to fit the majority of the data. These inverse models are consistent with lithosphere modification by erosion from running water.

Contents

List of Figures

List of Tables

Acknowledgements

This thesis is an endeavour that would not have been possible without the support, encouragement, and help from many people.

Firstly, I would like to thank my advisor, Dr. William E. Holt. This thesis was inspired by his suggestion for a first semester project. In the subsequent years, he has given me the freedom to explore this and many other topics in the face of what have seemed to be insurmountable hurdles – from lack of fault data to funding issues. For this, as well as his inspiration, encouragement, and guidance I am grateful.

Special thanks are due Dr. A. John Haines from the University of Cambridge, UK. His mathematical skill has made it possible to dream up more problems than have made it into this thesis, but that have shaped my understanding of this subject. It will take me many years into the future to explore all that he has taught me.

Dr. Richard A. Schultz, from the University of Nevada at Reno, gave me my first data. His continued support and encouragement have been invaluable.

Dr. Gregory Neumann has stepped in on numerous occasions – from discussing my first AGU poster to reading this document on a short notice.

I had the privilege my first semester to be a teaching assistant for Dr. Daniel M. Davis; his teaching and advice as well as friendly conversations in the years that followed have made this experience easier. Dr. Hanna Nekvasil has opened her door and advice-book for me more often than I would like to count.

Navigating a university bureaucracy is never trivial; however, Iris Roth, Andrea Illausky, Owen Evans, Elizabeth Barnum, Loretta Budd, and Diane Isigro have made it easier.

Drs. Lucy Flesch and Saad Haaq were kind and generous to open their home to me twice, for collaboration on the COMSOL project. Back at home, Lauren Beavon and Brian Hahn were some of the nicest officemates.

Intellectual discussions with fellow students Matthew Wander, Daniel Hernandez, and Elliot Klein have been very helpful.

I was lucky enough to work with several undergraduates. Mark Haines, from Robinson College, contributed numerous scripts including the majority of the MARTIAN website.

Most importantly I would like to thank my parents for their love, support and help. Without them this thesis would have never happened. Friends, most notably Matthew Wander, KarenAnn Jurecki, Stacey Cochiara and Matt Whitaker, have each lent their ears to my troubles and triumphs, and encouraged me to not give up. Last, but not least, I must thank Philip Lenharth for his love and support.

Chapter 1

Introduction

Introduction

Tectonic features, observed on the surface of planetary bodies, present important clues to the history and evolution of the solar system. These geologic features reflect the structure and the dynamic processes which have shaped each planet. Together with topography and gravity, maps of surface features are also one of the easiest and most commonly collected spatial data.

Models of lithospheric deformation tie observed field measurements of gravity and topography with surface observations of tectonic features. An understanding of the sources of stress, and the expected style, orientation, and magnitudes of stress and associated elastic strain is important for understanding the evolution of faulting on Mars and its relationship to loading. At the same time, theoretical models of deformation mechanisms and forces, when tied to tectonic observations, can be interpreted in terms of major tectonic events and allow insights into the planet's history and evolution as well as its internal structure and processes. This is particularly important for understanding solid planetary bodies other than Earth where the seismic data is either sparse, e.g. the Moon, or non-existent, e.g. Mars. This kind of research has implications for, and benefits from, an understanding of the petrology and surface processes.

Since the late 1960s, it was recognized that plate tectonics explains many and diverse features on Earth. Consequently, even though there is much debate on the driving forces behind plate tectonics, it has been accepted by geoscientists in all disciplines. In contrast, the remaining rocky planetary bodies show little to no evidence of active plate tectonics. In the case of smaller bodies, such as Mercury and the Moon, this is due to their relatively small size. Earth-sized and larger, including superearth, bodies are expected to have plate tectonics (*Valencia et al.*, 2007) although they may not if, for example, they have lost their water, e.g. Venus. Consequently, processes other than plate tectonics play a significant role in these planets' evolution; yet such processes are difficult to study on Earth due to the overwhelming dominance of plate tectonics.

Level of tectonic activity also differentiates the rocky planets in our solar system. On one hand, Earth and Venus have experienced sufficient activity that most of their early

histories have been destroyed; on the other hand, Mercury and the Moon seem to have experienced little to no activity after the first two to three billion years. In contrast, Mars appears to have just the right conditions such as to maintain geologic and tectonic activity throughout its life and to have preserved this record in features exposed at the surface. Tectonic features on Mars are abundant. Brittle-frictional deformation is indicated by a variety of structural features – tensional (simple and complex grabens, rifts, tension cracks, troughs) (*Wise et al.*, 1979; *Tanaka and Golombek*, 1989; *Frey*, 1979), compressional (wrinkle ridges, lobate scarps) (*Watters and Maxwell*, 1986; *Chicarro et al.*, 1985), and to a much smaller extent strike-slip (*Schultz*, 1989; *Mangold et al.*, 2000; *Okubo and Schultz*, 2006). Although some have argued for the presence of plate tectonics in early Mars history (*Sleep*, 1994; *Connerney et al.*, 1999, e.g.), the evidence is scant and not commonly accepted. Thus, insights into the composition, structure, and history of Mars are fundamental to understanding the solar system as a whole, and also provide additional insight into the evolutionary history of Earth.

The unprecedented volume, quality, and coverage of data that has become available over the last decade make it now possible to apply mature theoretical dynamic models (previously applied to Earth) that may help resolve longstanding scientific issues such as the formation and timing of extensive graben sets radial to Tharsis (*Banerdt et al.*, 1992; *Anderson et al.*, 2001), origin and distribution of wrinkle ridges (*Watters*, 1991, 2003; *Head et al.*, 2002; *Schultz*, 2000b,a, 2003), the relative contribution of surface and intra lithosphere loading (*Banerdt and Golombek*, 2000; *Phillips et al.*, 2001; *Dimitrova et al.*, 2006) and internal loading due to chemical or convection buoyancies (*Sleep and Phillips*, 1985; *Harder and Christensen*, 1996; *Harder*, 2000; *Zhong*, 2002; *Lowry and Zhong*, 2003).

In this work, I use MGS MOLA and Radio Science data products (topography and gravity) to systematically test new geodynamic models and evaluate lithosphere dynamics on Mars as a function of time, while satisfying geologic surface observations (surface features) that have been and are being catalogued and studied from Viking, MOLA, MOC, and THEMIS IR images (*Anderson et al.*, 2001; *Schultz*, 2000b, 2003; *Neuffer and Schultz*, 2006; *Artita and Schultz*, 2005; *Knapmeyer et al.*, 2006, e.g.). I investigate (1) the role of internal loads (internal body force effects), (2) loading from the surface and base of litho-

sphere, and the effects of this loading on membrane and flexural strains and stresses, and (3) the role of global contraction, all viewed in the context of how the surface elastic layer has changed as the planet has evolved.

The sources of stress, elastic strain, and permanent deformation include (1) body forces associated with gravitational potential energy (GPE) differences (*Molnar and Lyon-Caen*, 1998; *Fleitout*, 1991; *Jones et al.*, 1996; *Flesch et al.*, 2001) within the lithosphere (inferred from topography and crustal thickness estimates on Mars (*Zuber et al.*, 2000; *Neumann et al.*, 2004), (2) membrane and flexural elastic response to surface loads as well as loads applied from below *Turcotte et al.* (1981); *Willemann and Turcotte* (1982); *Banerdt* (1986); *Phillips et al.* (2001), and (3) contractional (compressional) stresses. Although radial and tangential basal tractions associated with mantle convection (inferred from observationally constrained large-scale mantle circulation models) (*Kiefer et al.*, 1996; *Zhong and Zuber*, 2001; *Zhong*, 2002; *Roberts and Zhong*, 2004) may impact the lithospheric stresses, they are not included in this study. Instead, I investigate when and where the GPE, flexural and membrane, and global contraction stresses are insufficient to explain the faulting and consequently require an additional source of stress such as mantle circulation.

The load distribution responsible for lithospheric stresses and strains is directly constrained by crustal thickness estimates (*Zuber et al.*, 2000; *Neumann et al.*, 2004) inferred from MOLA topography (*Zuber et al.*, 2000; *http://pds.nasa.gov*, accessed 2003) and MGS gravity models (*Tyler et al.*, 2001; *Lemoine et al.*, 2001; *http://pds.nasa.gov*, accessed 2003). I begin by assuming that, to first order, the boundary between crust and underlying mantle at the time of faulting was the same as today (*Nimmo and Tanaka*, 2005). I then consider additional sources of stress - either due to global contraction, or membrane and GPE stresses. The latter is separated into effects due to the assumptions of uniform crust and mantle densities and dynamic processes that may have modified the lithosphere since the time of faulting.

The dissertation is organized as follows. It consists of an Introduction and Conclusion chapters: Chapter 1 and 6 respectively. Chapter 2 focuses on the Tharsis province, which due to its large scale and complex deformation, has long been the focus of studies on the Martian geologic evolution. It presents the deviatoric stress field associated with horizontal

gradients in gravitational potential energy (GPE) and briefly discusses the importance of using the correct reference level for GPE calculations. It compares the expected fault style and orientation associated with the GPE stress field and the normal faulting in Tharsis, as mapped by *Anderson et al.* (2001), using an inner product measure. The excellent fit of the model to the data suggests that at the time of faulting elastic thicknesses and membrane stresses were small, a combination of brittle and ductile lithospheric deformation was likely to be widespread, GPE stresses dominated, and the topography was supported by buoyancy forces. Chapter 2 is published in *Geophysical Research Letters* (*Dimitrova et al.*, 2006). Currently there are two datasets of normal faults – the dataset of Anderson et al. [2001] and the dataset of Knapmeyer et al. [2006]. We compare these data in the appendix of Chapter 2. In the appendix of chapter 2, I compare the normal fault data in the western hemisphere of Mars from the studies of *Anderson et al.* (2001) and *Knapmeyer et al.* (2006). I also compare two end-member flexure models – the model of Banerdt and Golombek [2000] and a new model based on pressure differences at the bottom of the lithosphere – with the normal fault data in Tharsis. I point out the inability of these models to match the fault data. Subsequent chapters use the global reverse and normal fault data of *Knapmeyer et al.* (2006). Chapter 3, submitted to the *Journal of Geophysical Research-Planets*, returns to the GPE associated stress field and includes the full 3-D spherical methodology as well as a comparison with the global fault data. In addition, I investigate if global contraction, in the presence of the GPE stress field, can explain the reverse faults. Chapter 4 examines the assumptions in the GPE associated model that (1) present-day topography is the paleotopography, (2) present-day crustal thickness is the paleo-crustal thickness, (3) the crustal and mantle densities are uniform, $2900 kg/m^3$ and $3500 kg/m^3$ respectively, consistent with values assumed by *Neumann et al.* (2004) for the crustal thickness model. I invert for the minimum additional stress filed, associated with perturbations in gravitational potential energy differences and vertical displacements, and argue that small lateral variations in density as well as possible material removal and/or subsidence associated with crater excavation and erosion since the time of faulting are sufficient to explain the faulting. This work is in preparation to be submitted to the *Journal of Geophysical Research-Planets*. The thin-sheet and flexure approximations taken in present-day lithospheric stress models as-

sume zero vertical gradients in horizontal or vertical velocity or displacement respectively. In Chapter 5 I discuss a new methodology, which not only avoids these assumptions, but also addresses many of the numerical challenges in modeling of lithospheric deformation, e.g., large horizontal to vertical aspect ratio of the area geometry, discontinuous material properties, and layers that pinch out. This chapter is a part of a paper in preparation for *Geophysical Journal International*.

Bibliography

Anderson, R. C., J. M. Dohm, M. P. Golombek, A. F. C. Haldemann, B. J. Franklin, K. L. Tanaka, J. Lias, and B. Peer, Primary centers and secondary concentrations of tectonic activity through time in the western hemisphere of Mars, *Journal of Geophysical Research*, *106*, 20563–20586, 2001, DOI: 10.1029/2000JE001278.

Artita, K. S., and R. A. Schultz, Significance of deformation band-like strike-slip faults on Mars, in *36th Annual Lunar and Planetary Science Conference*, vol. 36, p. 2225, 2005.

Banerdt, W. B., Support of long-wavelength loads on Venus and implications for internal structure, 1986, DOI: 10.1029/JB091iB01p00403.

Banerdt, W. B., and M. P. Golombek, Tectonics of the Tharsis region of Mars: Insights from MGS topography and gravity, in *Lunar and Planetary Institute Conference Abstracts*, vol. 31, p. 2038, 2000.

Banerdt, W. B., M. P. Golombek, and K. L. Tanaka, Stress and tectonics on Mars, in *Mars*, pp. 249–297, 1992, n/a 1, 1992.

Chicarro, A. F., P. H. Schultz, and P. Masson, Global and regional ridge patterns on Mars, *Icarus*, *63*, 153–174, 1985, DOI: 10.1016/0019-1035(85)90025-9.

Connerney, J. E. P., et al., Magnetic lineations in the ancient crust of Mars, *Science*, *284*, 794, 1999, DOI: 10.1126/science.284.5415.794.

Dimitrova, L. L., W. E. Holt, A. J. Haines, and R. A. Schultz, Toward understanding the history and mechanisms of martian faulting: The contribution of gravitational potential energy, *Geophysical Research Letters*, *33*, 08202, 2006, DOI: 10.1029/2005GL025307.

Fleitout, L., The sources of lithospheric tectonic stresses, *Philosophical Transactions of the Royal Society of London Series a-Mathematical Physical and Engineering Sciences*, *337*(1645), 73–81, 1991.

Flesch, L. M., A. J. Haines, and W. E. Holt, Dynamics of the India-Eurasia collision zone, *Journal of Geophysical Research*, *106*, 16435–16460, 2001, DOI: 10.1029/2001JB000208.

Frey, H., Martian canyons and African rifts - structural comparisons and implications, *Icarus*, *37*, 142–155, 1979, A&AA ID. AAA025.097.008 DOI: 10.1016/0019-1035(79)90122-2.

Harder, H., Mantle convection and the dynamic geoid of Mars, *Geophysical Research Letters*, *27*, 301, 2000, DOI: 10.1029/1999GL008418.

Harder, H., and U. R. Christensen, A one-plume model of martian mantle convection, *Nature*, *380*, 507–509, 1996, DOI: 10.1038/380507a0.

Head, J. W., M. A. Kreslavsky, and S. Pratt, Northern lowlands of Mars: Evidence for widespread volcanic flooding and tectonic deformation in the Hesperian period, *Journal of Geophysical Research (Planets)*, *107*, 5003, 2002, DOI: 10.1029/2000JE001445.

http://pds.nasa.gov, NASA planetary data system

Jones, C. H., J. R. Unruh, and L. J. Sonder, The role of gravitational potential energy in active deformation in the southwestern united states, *Nature*, *381*(6577), 37–41, 1996.

Kiefer, W. S., B. G. Bills, and R. S. Nerem, An inversion of gravity and topography for mantle and crustal structure on Mars, *Journal of Geophysical Research*, *101*, 9239–9252, 1996, DOI: 10.1029/95JE03699.

Knapmeyer, M., J. Oberst, E. Hauber, M. Whlisch, C. Deuchler, and R. Wagner, Working models for spatial distribution and level of Mars' seismicity, *Journal of Geophysical Research (Planets)*, *111*, 11006, 2006, DOI: 10.1029/2006JE002708.

Lemoine, F. G., D. E. Smith, D. D. Rowlands, M. T. Zuber, G. A. Neumann, D. S. Chinn, and D. E. Pavlis, An improved solution of the gravity field of Mars (gmm-2b) from Mars Global Surveyor, *Journal of Geophysical Research*, *106*, 23359–23376, 2001, DOI: 10.1029/2000JE001426.

Lowry, A. R., and S. Zhong, Surface versus internal loading of the Tharsis rise, Mars, *Journal of Geophysical Research (Planets)*, *108*, 5099, 2003, DOI: 10.1029/2003JE002111.

Mangold, N., P. Allemand, P. G. Thomas, and G. Vidal, Chronology of compressional deformation on Mars: evidence for a single and global origin, *Planetary and Space Science*, *48*, 1201–1211, 2000.

Molnar, P., and H. Lyon-Caen, Some simple physical aspects of the support, structure, and evolution of mountain belts, *Processes in Continental Lithospheric Deformation, Geol. Soc. Amer. Spec. Pap*, *218*, 6203–6227, 1998.

Neuffer, D. P., and R. A. Schultz, Mechanisms of slope failure in Valles Marineris, Mars, *Quarterly Journal of Engineering Geology and Hydrogeology*, *39*, 227–240, 2006, Neuffer, D. P. Schultz, R. A. Part 3.

Neumann, G. A., M. T. Zuber, M. A. Wieczorek, P. J. McGovern, F. G. Lemoine, and D. E. Smith, Crustal structure of Mars from gravity and topography, *Journal of Geophysical Research (Planets)*, *109*, 08002, 2004, DOI: 10.1029/2004JE002262.

Nimmo, F., and K. Tanaka, Early crustal evolution of Mars, *Annual Review of Earth and Planetary Sciences*, *33*, 133–161, 2005, DOI: 10.1146/annurev.earth.33.092203.122637.

Okubo, C. H., and R. A. Schultz, Variability in Early Amazonian Tharsis stress state based on wrinkle ridges and strike-slip faulting, *Journal of Structural Geology*, *28*, 2169–2181, 2006, DOI: 10.1016/j.jsg.2005.11.008.

Phillips, R. J., et al., Ancient geodynamics and global-scale hydrology on Mars, *Science*, *291*, 2587–2591, 2001, DOI: 10.1126/science.1058701.

Roberts, J. H., and S. Zhong, Plume-induced topography and geoid anomalies and their implications for the Tharsis rise on Mars, *Journal of Geophysical Research (Planets)*, *109*, 03009, 2004, DOI: 10.1029/2003JE002226.

Schultz, R., Fault-population statistics at the Valles Marineris extensional province, Mars: implications for segment linkage, crustal strains, and its geodynamical development, *Tectonophysics*, *316*, 169–193, 2000a, DOI: 10.1016/S0040-1951(99)00228-0.

Schultz, R. A., Strike-slip faulting of ridged plains near Valles Marineris, Mars, *Nature*, *341*, 424–426, 1989, DOI: 10.1038/341424a0.

Schultz, R. A., Localization of bedding plane slip and backthrust faults above blind thrust faults: Keys to wrinkle ridge structure, *Journal of Geophysical Research*, *105*, 12035–12052, 2000b, DOI: 10.1029/1999JE001212.

Schultz, R. A., Seismotectonics of the Amenthes Rupes thrust fault population, Mars, *Geophysical Research Letters*, *30*, 36–1, 2003, DOI: 10.1029/2002GL016475.

Sleep, N. H., Martian plate tectonics, *Journal of Geophysical Research*, *99*, 5639, 1994, DOI: 10.1029/94JE00216.

Sleep, N. H., and R. J. Phillips, Gravity and lithospheric stress on the terrestrial planets with reference to the Tharsis region of Mars, *Journal of Geophysical Research*, *90*, 4469–4489, 1985, DOI: 10.1029/JB090iB06p04469.

Tanaka, K. L., and M. P. Golombek, Martian tension fractures and the formation of grabens and collapse features at Valles Marineris, in *Lunar and Planetary Science Conference*, vol. 19, pp. 383–396, 1989.

Turcotte, D. L., R. J. Willemann, W. F. Haxby, and J. Norberry, Role of membrane stresses in the support of planetary topography, *Journal of Geophysical Research*, *86*, 3951–3959, 1981, DOI: 10.1029/JB086iB05p03951.

Tyler, G. L., G. Balmino, D. P. Hinson, W. L. Sjogren, D. E. Smith, R. A. Simpson, S. W. Asmar, P. Priest, and J. D. Twicken, Radio science observations with Mars global sur-

veyor: Orbit insertion through one Mars year in mapping orbit, *Journal of Geophysical Research*, *106*, 23327–23348, 2001, DOI: 10.1029/2000JE001348.

Valencia, D., R. J. O'Connell, and D. D. Sasselov, Inevitability of plate tectonics on super-earths, *Astrophysical Journal*, *670*, L45–L48, 2007, DOI: 10.1086/524012; eprintid: arXiv:0710.0699.

Watters, T. R., Origin of periodically spaced wrinkle ridges on the Tharsis plateau of Mars, *Journal of Geophysical Research*, *96*, 15599, 1991, DOI: 10.1029/91JE01402.

Watters, T. R., Thrust faults along the dichotomy boundary in the eastern hemisphere of Mars, *Journal of Geophysical Research (Planets)*, *108*, 5054, 2003, DOI: 10.1029/2002JE001934.

Watters, T. R., and T. A. Maxwell, Orientation, relative age, and extent of the Tharsis plateau ridge system, *Journal of Geophysical Research*, *91*, 8113–8125, 1986, DOI: 10.1029/JB091iB08p08113.

Willemann, R. J., and D. L. Turcotte, The role of lithospheric stress in the support of the Tharsis rise, *Journal of Geophysical Research*, *87*(NB12), 9793–9801, 1982.

Wise, D. U., M. P. Golombek, and G. E. McGill, Tharsis province of Mars - geologic sequence, geometry, and a deformation mechanism, *Icarus*, *38*, 456–472, 1979, A&AA ID. AAA025.097.039 DOI: 10.1016/0019-1035(79)90200-8.

Zhong, S., Effects of lithosphere on the long-wavelength gravity anomalies and their implications for the formation of the Tharsis rise on Mars, *Journal of Geophysical Research (Planets)*, *107*, 5054, 2002, DOI: 10.1029/2001JE001589.

Zhong, S., and M. T. Zuber, Degree-1 mantle convection and the crustal dichotomy on Mars, *Earth and Planetary Science Letters*, *189*, 75–84, 2001, DOI: 10.1016/S0012-821X(01)00345-4.

Zuber, M. T., et al., Internal structure and early thermal evolution of Mars from Mars Global

Surveyor topography and gravity, *Science*, *287*, 1788–1793, 2000, DOI: 10.1126/science.287.5459.1788.

Chapter 2

Towards Understanding the History and Mechanisms of Martian Faulting: The Contribution of Gravitational Potential Energy

Towards Understanding the History and Mechanisms of Martian Faulting: The Contribution of Gravitational Potential Energy

Lada L. Dimitrova, William E. Holt, A. John Haines, and R. A. Schultz

(Published in *Geophysical Research Letters*, 33, L08202, 2006)

Abstract

Current stress solutions for Mars match the long wavelength signal of present day topography and gravity but fail to match many surface faults, including the normal faults in northern Claritas Fossae north to Tantalus and Alba Fossae. A deviatoric stress field associated with horizontal gradients of gravitational potential energy (GPE) provides an excellent fit, as measured by objective functions, to many of the normal faults in the western Martian hemisphere as well as wrinkle ridges circumferential to Tharsis; $\sim 70\%$ of the faults have a misfit ≤ 0.1. The fit of faults to the GPE-derived stress field reflects the thermal state of the planet at the times of faulting, and suggests that at such times elastic thicknesses and membrane stresses were small, and topography was supported by buoyancy forces.

2.1 Introduction

The quantification of lithospheric dynamics on Mars is of fundamental importance to the understanding of Martian geologic history and surface morphology. An understanding of the sources of stress, and the expected style, orientation, and magnitudes of stress and associated strain is important for understanding the evolution of faulting on Mars and its relationship to loading. The unprecedented volume, quality, and coverage of the data make it now possible to apply mature theoretical dynamic models (previously applied to Earth) that may help resolve long-standing scientific issues such as the formation and timing of extensive graben sets radial to Tharsis and the distribution of wrinkle ridges (*Banerdt et al.*, 1992; *Banerdt and Golombek*, 2000; *Anderson et al.*, 2001; *Watters*, 1993; *Head et al.*, 2002; *Schultz*, 2000, 2003).

The Tharsis province, due to its large scale and complex deformation, has long been the focus of studies on the Martian geologic evolution, and has been intensely studied with Viking, Mariner, and Mars Global Surveyor (MGS) data. Early models seemed to require more than one mechanism – a combination of lithospheric uplift, isostasy, and flexure – to explain the region's evolution (*Banerdt et al.*, 1992, and references therein). More recently, *Banerdt and Golombek* (2000) proposed that the seeming need of multiple mechanisms was due to the quality of data available prior to MGS, and *Phillips et al.* (2001) furthermore argued that the faulting is explained by membrane flexure alone.

Banerdt and Golombek (2000) calculated the deflection of the lithosphere due to the Tharsis load alone while satisfying the long wavelength signal of present day topography and gravity. The resulting stress field has radial compressive stresses throughout Tharsis. *Banerdt and Golombek* (2000) show only the extensional component of the strains, which is consistent with normal faulting on pre-existing faults radial to Tharsis and away from the load, e.g. Memnonia, Sirenum, Thaumasia, southern Claritas, and Tempe Fossae. However, the faulting extending from northern Claritas Fossae north to Tantalus and Alba Fossae is not well explained by the membrane model, which predicts zero extension in these areas (*Banerdt and Golombek*, 2000), where the density of normal faults is high (*Anderson et al.*, 2001).

Therefore, as pointed out by *Banerdt and Golombek* (2000), these faults may have formed under different conditions (topography and gravity) than we see today. In particular, while the bulk of the crust formed 4.5 Ga and later additions were volumetrically minor (*Nimmo and Tanaka*, 2005), gravity and elastic thicknesses are unlikely to have remained unchanged for the last 4.5 Gy. For example, it is conceivable that mantle circulation rather than flexure played a significant role in the early support of Tharsis, producing a different gravity field during that time (*Lowry and Zhong*, 2003, and references therein).

In this paper we consider a different source of stress – stress associated with internal buoyancy forces, i.e., gravitational potential energy (GPE), constrained by topography and crustal thickness models of *Zuber et al.* (2000); *Neumann et al.* (2004). We test the validity of the stress model by comparing it with the strain geometry of the surface faults.

2.2 Methodology

We solve the 3-D force-balance equations for the vertically integrated deviatoric stress field associated with topography and crustal thickness variations using the thin-sheet method discussed in *Flesch et al.* (2001), which is appropriate when the horizontal scale of the features is much larger than the layer thickness and horizontal gradients in basal tractions are small. The deviatoric stress solution is the unique solution that balances the body force distribution, in this case GPE differences, while providing a global minimum of the second invariant of stress. This finite element thin-sheet approach does not require detailed descriptions of the lithosphere rheology, but only a decision of whether we choose to treat the lithosphere as generally viscous or elastic. The solution is computed over a global grid of $2.5^\circ \times 2.5^\circ$ resolution, which is based on the ability of current gravity models to resolve crustal thickness differences down to wavelengths of $300km$. The integrated vertical stress, whose gradients need to be balanced by the gradients of the integrated horizontal deviatoric stresses, has units of potential energy per unit area. We assume $\rho_{crust} = 2900kg/m^3$, $\rho_{mantle} = 3500kg/m^3$, and $g = 3.7m/s^2$, consistent with the values used by *Neumann et al.* (2004) in estimating the crustal thickness model.

GPE is calculated by integrating to a depth, L, as the base of the thin shell (*Molnar and Lyon-Caen*, 1988), which corresponds to the highest point within the lithosphere where decoupling occurs below the elastic layer. For example, if there is decoupling between the brittle upper crust and ductile lower crust, this depth is the brittle-ductile transition. On the other hand, if there is coupling between the brittle and ductile lithosphere, this depth is the contact between the mantle lithosphere and the convecting mantle. Assuming no brittle-ductile lithospheric decoupling, the shallowest choice for such uniform depth is the deepest extent of the crust on the planet ($L \sim 92.84$ km below zero topography level at Arsia Mons). Although estimates of elastic thickness have shown variability (*Banerdt et al.*, 1992; *Nimmo and Tanaka*, 2005, and references therein), such effects are likely to be of second order as long as L encompasses the elastic layer in all regions.

2.3 Results

The Martian deviatoric stress field associated with horizontal GPE gradients shows, to first order, deviatoric extension over topographically high areas transitioning to deviatoric compression at topographically low areas (Fig. 1) due to the large degree 1 signal of the topographic and crustal dichotomy. A notable exception to this pattern is areas with low topography but thin crust, which exhibit propensity for deviatoric extension, e.g., Isidis Plantitia and to a smaller extent Utopia, Argyre, and Acidalia Planitae. This effect is amplified if we consider greater depths L, i.e., thicker coupled layers (see Fig. S4).

We calculate the expected fault styles associated with the dynamic model. *Anderson* (1951) showed how styles of faulting in the upper crust relate to principal stress magnitudes and orientations, connecting the three major fault types to tectonic regimes. Since the Martian surface is a free surface and the vertical stress is a principal stress, we can define a normalized parameter

$$A_0 = (\tau_1 + \tau_2)/\sqrt{\tau_1^2 + \tau_2^2} \tag{1}$$

to discriminate among the three major geologic fault styles associated with the styles of the deviatoric stress field from the dynamic solution. Here τ_1 and τ_2 are the principal horizontal deviatoric stresses, and the vertical deviatoric stress is $-(\tau_1 + \tau_2)$. Apart from the exceptions already noted in connection with low topography and thin crust, normal faulting is predicted as the dominant fault style for topographically high areas, thrust faulting for topographically low areas, and strike-slip faulting potentially in between (Fig. 2).

We develop objective measures for the fit of stresses and associated strains with surface fault data (fault strike θ, rake λ, dip δ, and slip magnitude u). For each area k, we perform a *Kostrov* (1974) moment tensor summation to estimate the total strain tensor, ε_{ij}^k, in which it is assumed that the unit moment tensor $m_{ij}^k(\theta, \lambda, \delta)$ and the slip magnitude u_k do not vary with depth within the faulted layer (*Schultz*, 2003).

We define objective functions that measure the correlation and misfit between the dynamically predicted stress field and the strain from fault observations as

$$C_{full} = (\varepsilon \cdot \tau) \,/\, (ET), \quad M_{full} = 0.5\,(1 - C_{full}), \tag{2}$$

where the metrics E and T and the inner product $\varepsilon \cdot \tau$ are defined as

$$E = \sqrt{\varepsilon_{ij}\varepsilon_{ij}}, \quad T = \sqrt{\tau_{ij}\tau_{ij}}, \quad \varepsilon \cdot \tau = \varepsilon_{ij}\tau_{ij}. \tag{3}$$

Here ε_{ij} is the 3-D strain from the *Kostrov* (1974) summation of fault data, and τ_{ij} is the vertically integrated 3-D deviatoric stress (or strain) tensor obtained from the solution to the force-balance equations. This objective function is minimized when the tensor solution of stress or strain from the dynamic calculations is consistant with the formation of faults with the same strike and style as the fault data; thus, it accounts for fault strike and fault style, defined by the relative magnitudes of the principal axis of the stress tensor. The misfit function has values from 0 to 1, with 0 misfit indicating a perfect fit.

Fig. 3B shows the misfit of 19,897 normal fault segments as identified in *Anderson et al.* (2001) with the GPE model from Fig. 1. We have assumed a uniform amount of slip for each fault as a first approximation. Although fault displacements scale primarily with length, mechanical length depends on fault segmentation, spacing and linkage, which are not recognized in the data set at the scale of the study. Thus, our ε_{ij} reflects the simplest and least biased approach to incorporating fault-related strain to compare with the stress model. Furthermore, the strain tensor is linearly proportional to the slip, and the misfit function M_{full} is insensitive to scalar multiples of either the strain or stress tensor, and thus it is insensitive to the actual value of u_k. The GPE model fits a large fraction of the normal faults (69% of the faults have $M_{full} \leq 0.1$). The exceptions are areas in Margaritifer Terra, Olympus Mons and north of Alba Patera. Since the misfit measure in Eqn. 2 reflects both misfit to the fault strike and the fault style, we need a second measure to explain the cause of the misfit.

A second measure of misfit between the fault data and stress data can be obtained if we consider whether the stress field is consistent with the strike and style of pre-existing faults. That is, we rotate the horizontal coordinates for fault strain and model stress such that the x' direction is aligned with the fault, and the metric and inner products are defined as

$$E = \sqrt{\varepsilon'_{iy}\varepsilon'_{iy}}, \quad T = \sqrt{\tau'_{iy}\tau'_{iy}}, \quad \varepsilon \cdot \tau = \varepsilon'_{iy}\tau'_{iy}. \tag{4}$$

Using these in Eqn. 2, we define a misfit $M_{pre-existing}$ of the model stress to the pre-existing faults, which measures whether the model stress field is aligned with the prescribed fault strike such as to produce the style of faulting, in our case normal faulting, and ignores any along strike stresses. This new misfit is plotted in Fig. 3C, and overall a slight improvement to the fit is observed (Fig. 3.D, 71% of the faults have $M_{pre-existing} \leq 0.1$). A few areas show a marked improvement (much lower $M_{pre-existing}$ than M_{full}), e.g., the east-west fault at $170-157.5^{o}W, -15^{o}S$, indicating that there we largely misfit the relative magnitudes of the along-strike stress as compared to the fault-normal stress. Otherwise, in areas of misfit to the normal faults, the misfit is to the stress orientation and the fault-normal stress style.

We calculate vertically integrated deviatoric stresses, and thus it is possible that the misfitted faults were created in response of near-surface stress that is not representative of the entire column, as may happen for example for shallow faults in the presence of a detachment layer.

We have also performed a preliminary investigation of the shortening directions for several sets of wrinkle ridges as identified by *Watters* (1993); *Head et al.* (2002); *Withers and Neumann* (2001). While the fit to the north-trending wrinkle ridges in Solis and southern Lunae Planae is poor (Fig. 4A), our GPE deviatoric stresses fit a large portion of the wrinkle ridges in the northern plains (Fig. 4B).

2.4 Conclusions

Previous stress solutions for Mars match the long wavelength signal of present day topography and gravity but fail to match many of the surface faults, including northern Claritas Fossae north to Tantalus and Alba Fossae. Here, we have shown that a deviatoric stress field associated with horizontal gradients of gravitational potential energy provides an excellent fit to most of the normal faults in Tharsis as well as many wrinkle ridges circumferential to Tharsis. This result suggests that many of the faults were created at times when elastic thicknesses and membrane and flexural stresses were small, a combination of brittle and ductile deformation was likely to be widespread, and GPE stresses dominated.

Normal faults and wrinkle ridges are not synchronous, according to the inferred strati-

graphic ages (*Anderson et al.*, 2001). Our model considers the time-averaged effect of internal buoyancy forces on the deviatoric lithospheric stresses. These buoyancy forces, together with radial basal tractions, supported the topography during the times of faulting. Perhaps the timing of faulting, as well as the misfit of existing models with the faulting in some regions, could be explained by systematic modeling of time-dependent sources of stress. Such sources include sub- and intra- lithospheric volcanic loads (*McGovern et al.*, 2001), as well as localized reduction in elastic strength (and membrane and flexural stresses) due to heating associated with volcanism, against a background of progressive cooling and thickening of the lithosphere resulting in increase of membrane and flexural stresses. For example, it is possible that the GPE associated stresses, during times of low elastic strength, may be responsible for most of the normal faults in the Tharsis province and the wrinkle ridges in the northern plains, while a time-dependent combination of stress sources may explain the normal faults in Tantalus and Tempe Fossae and the wrinkle ridge structures in Lunae and Solis Planae.

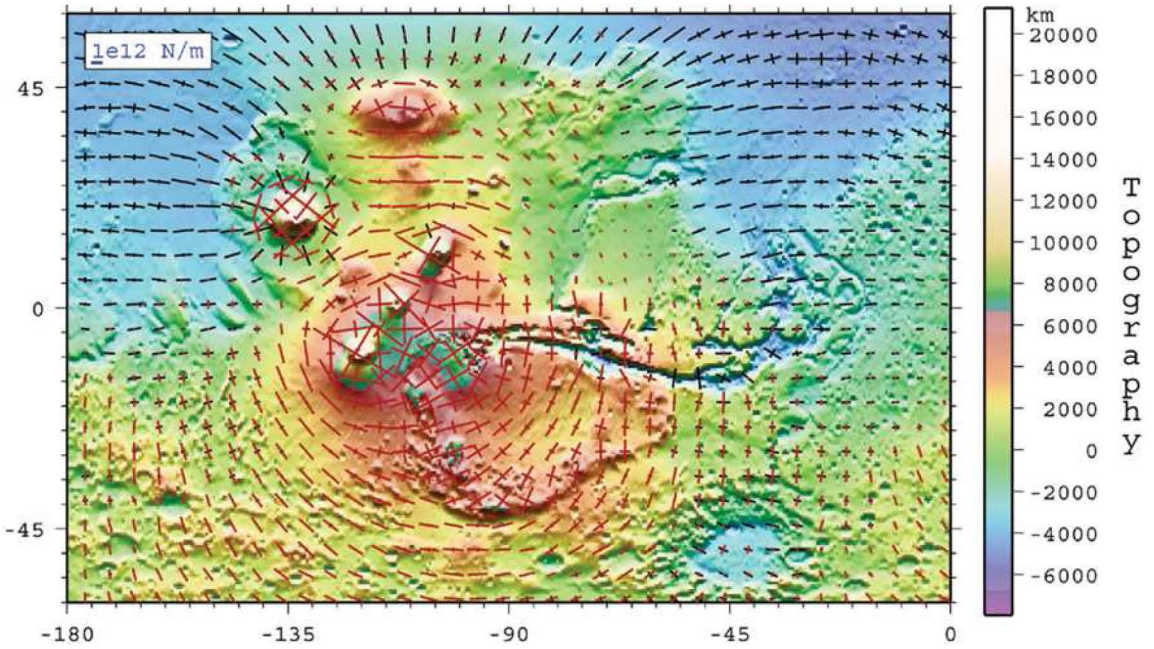

Figure 1: Vertically integrated ($L = 92.8km$) deviatoric lithospheric stresses associated with GPE variations calculated from MOLA topography and inferred crustal thickness (*Neumann et al.*, 2004), and assuming Poisson's ratio of 0.5. Red arrows represent deviatoric extension, while black arrows represent deviatoric compression. Global map is given in Fig. S3.

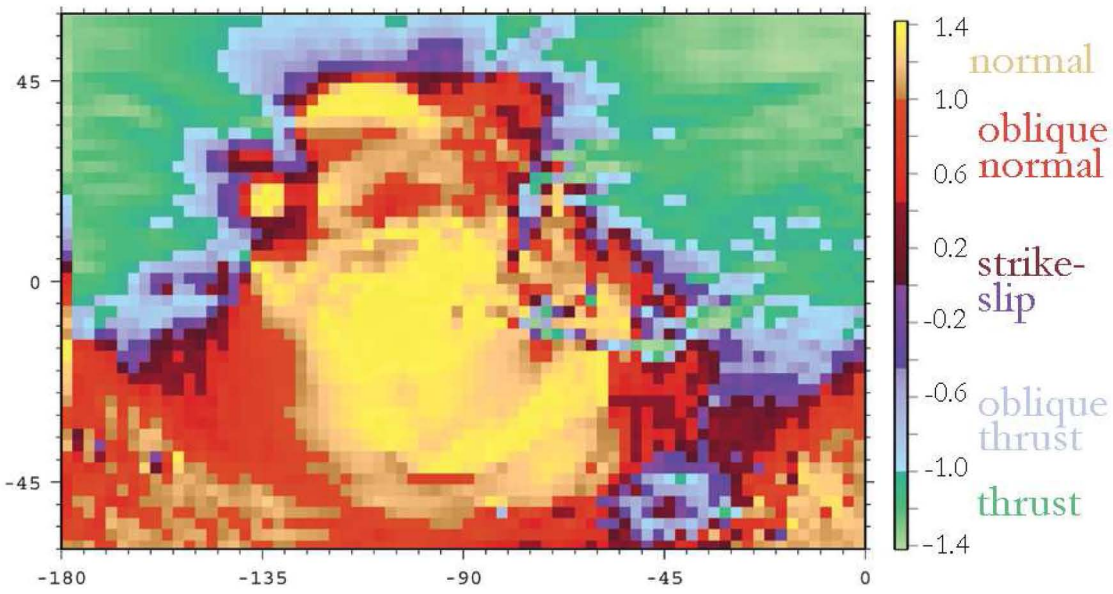

Figure 2: Predicted fault style, as defined in Eqn. 1 from the deviatoric stress field in Fig. 1. Global map is given in Fig. S5.

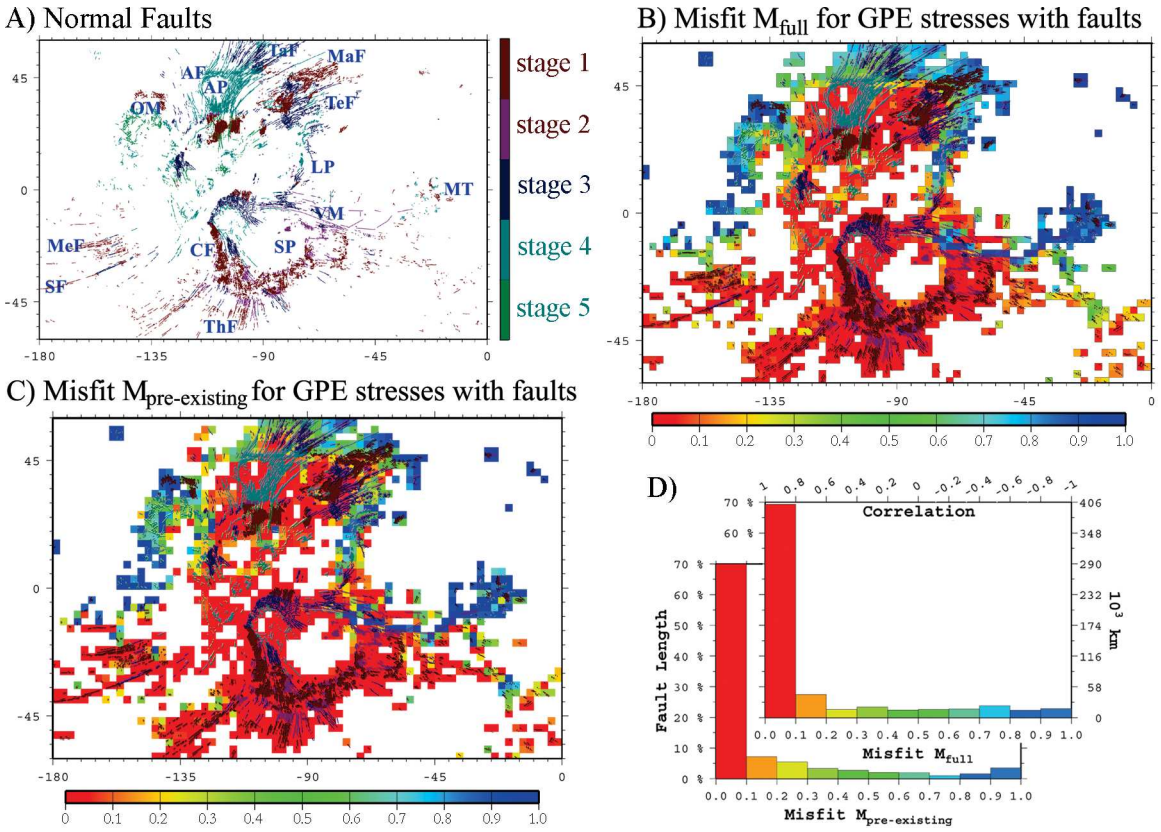

Figure 3: A) Normal faults as identified by *Anderson et al.* (2001) (stage 1 – Noachian, stage 2 – Late Noachian-Early Hesperian, stage 3 – Early Hesperian, stage 4 – Late Hesperian-Early Amazonian, stage 5 – Middle-Late Amazonian). Areas discussed in the text include Alba Fossae (AF), Alba Patera (AP), Claritas Fossae (CF), Lunae Planum (LP), Mareotis Fossae (MaF), Memnonia Fossae (MeF), Margaritifer Terra (MT), Olympus Mons (OM), Sirenum Fossae (SF), Solis Planum (SP), Tantalus Fossae (TaF), Tempe Fossae (TeF), Thaumasia Fossae (ThF), and Valles Marineris (VM). B) The misfit M_{full} as defined in 2 between the faults in A) and the full deviatoric stress field from Fig. 1. C) The misfit $M_{pre-existing}$ as defined in the text between the faults in A) and the deviatoric stress field from Fig. 1 while ignoring along fault-strike components of stress. D) Histograms of the percent and length of faults fitted for various values of the misfits in B and C.

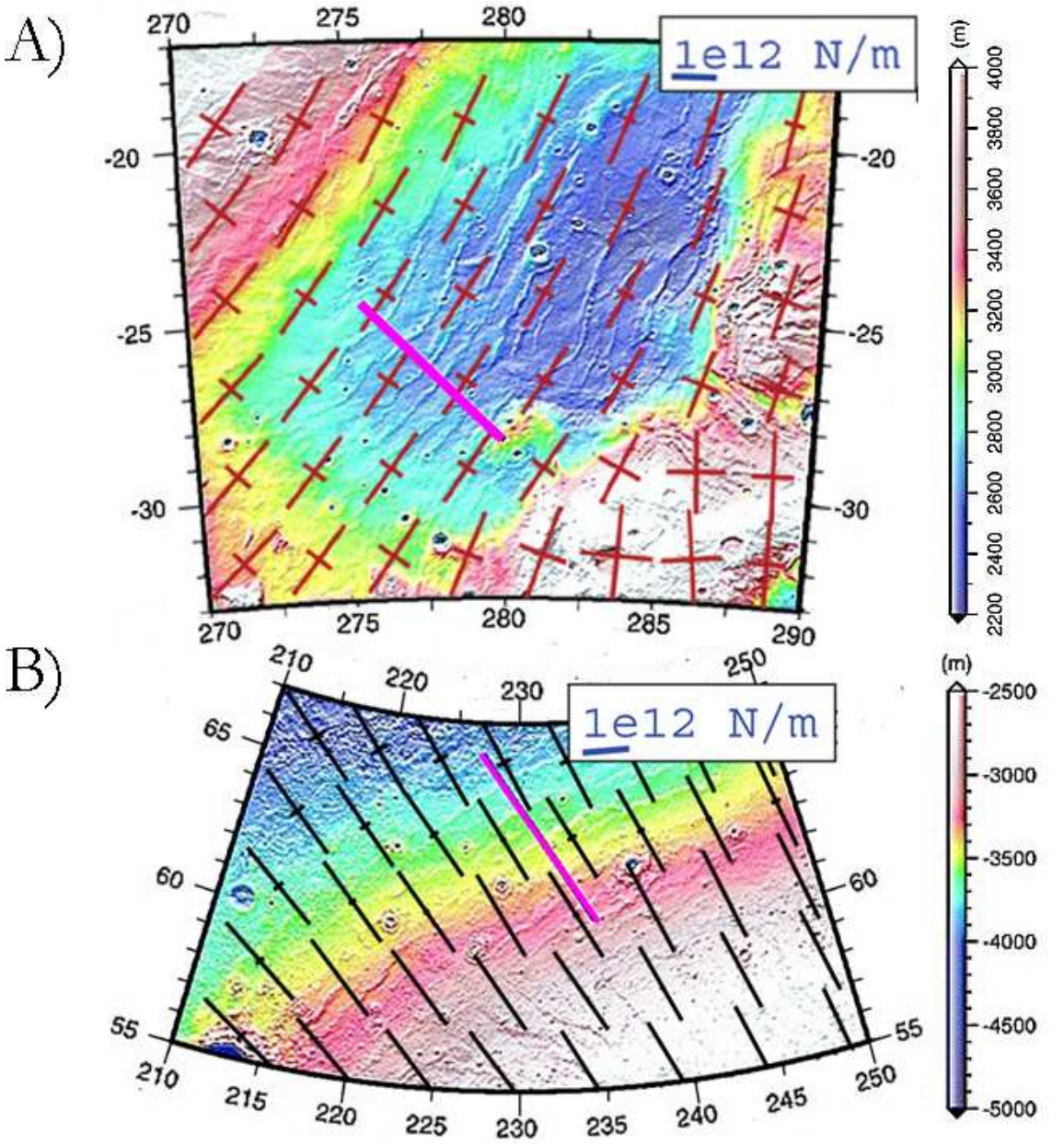

Figure 4: Wrinkle ridge structures with transects roughly perpendicular to the ridges in A) Solis Planum and B) northern flank of Alba Patera (*Montesi and Zuber*, 2003, and references therein) overlain by the GPE deviatoric stress field from Fig. 1. Additional maps are given in Figs. S7, S8.

Bibliography

Anderson, E. M. (1951), *The dynamics of faulting and dike formation with application to Britain*, 2 ed., 206 pp., Oliver and Boyd, Edinburgh.

Anderson, R. C., J. M. Dohm, M. P. Golombek, A. F. C. Haldemann, B. J. Franklin, K. L. Tanaka, J. Lias, and B. Peer (2001), Primary centers and secondary concentrations of tectonic activity through time in the western hemisphere of Mars, *J. Geophys. Res.*, *106*, 20,563–20,585, doi:10.1029/2000JE001278.

Banerdt, W., and M. Golombek (2000), Tectonics of the Tharsis region of Mars: Insights from MGS topography and gravity, *Lunar Planet Sci. 31st*, abstract 2038.

Banerdt, W. B., M. P. Golombek, and K. L. Tanaka (1992), Stress and tectonics on Mars, in *MARS*, edited by H. H. Kieffer, B. M. Jakosky, C. W. Snyder, and M. S. Matthews, pp. 249–297, Univ. of Arizona Press, Tuscon.

Flesch, L. M., A. J. Haines, and W. E. Holt (2001), Dynamics of the India-Eurasia collision zone, *J. Geophys. Res.*, *106*, 16,435–16,460, doi:10.1029/2001JE000228.

Head, J., M. Kreslavsky, and S. Pratt (2002), Northern lowlands of Mars: evidence for widespread volcanic flooding and tectonic deformation in the Hesperian period, *J. Geophys. Res.*, *107*, E15004, doi:10.1029/2000JE001445.

Kostrov, B. (1974), Seismic moment and energy of earthquakes, and seismic flow of rock, *Izv. Acad. Sci. USSR Phys. Solid Earth*, *1*, 23–40.

Lowry, A. R., and S. J. Zhong (2003), Surface versus internal loading of the Tharsis rise, Mars, *J. Geophys. Res.*, *108*, 5099, doi:10.1029/2003JE002111.

McGovern, P., et al. (2001), Surface versus internal loading of the Tharsis rise, Mars, *J. Geophys. Res.*, *107*, 23,769, doi:10.1029/2000JE001314.

Molnar, P., and H. Lyon-Caen (1988), Some simple physical aspects of the support, structure, and evolution of mountain belts, in *Special Paper - Geol. Soc. Am.*, vol. 218, edited by J. Clark, Sydney P., B. C. Burchfiel, and J. Suppe, pp. 179–207.

Montesi, L. G. J., and M. T. Zuber (2003), Clues to the lithospheric structure of Mars from wrinkle ridge sets and localization instability, *J. Geophys. Res.*, *108*, 5048, doi: 10.1029/2002JE001974.

Neumann, G., M. Zuber, M. Wieczorek, P. McGovern, F. Lemoine, and D. Smith (2004), The crustal structure of Mars from gravity and topography, *J. Geophys. Res.*, *108*, E08002, doi:10.1029/2004JE002262.

Nimmo, F., and K. Tanaka (2005), Early crustal evolution of Mars, *Annu. Rev. Earth Planet. Sci.*, *33*, 133–161, doi:10.1146/annurev.earth.33.092203.122637.

Phillips, P. J., et al. (2001), Ancient geodynamics and global-scale hydrology on Mars, *Science*, *291*, 2587–2591, doi:10.1126/science.1058701.

Schultz, R. A. (2000), Fault-population statistics at the Valles Marineris extensional province, Mars: Implications for segment linkage, crustal strains, and its geodynamical development, *Tectonophysics*, *316*(1-2), 169–193.

Schultz, R. A. (2003), Seismotectonics of the Amenthes Rupes thrust fault population, Mars, *Geophys. Res. Lett.*, *30*, 1303, doi:10.1029/2002GL016475.

Watters, T. R. (1993), The mechanical and thermal structure of Mercury's early lithosphere, *J. Geophys. Res.*, *98*(9), 17,049–17,060.

Withers, P., and G. A. Neumann (2001), Enigmatic northern plains of Mars: A network of ridges in this region opens a new tectonic window onto this planet, *Nature*, *410*, 651–651, doi:10.1038/35070640.

Zuber, M. T., et al. (2000), Internal structure and early thermal evolution of Mars from Mars Global Surveyor topography and gravity, *Science*, *287*(5459), 1788–1793.

Chapter 3

Evaluating Gravitational Potential Energy Stress Models and Global Contraction Hypothesis from a Global DataSet of Surface Faults

Evaluating Gravitational Potential Energy Stress Models and Global Contraction Hypothesis from a Global Dataset of Surface Faults

Lada L. Dimitrova and William E. Holt

(Submitted to *Journal of Geophysical Reseach – Planets*)

Abstract

It has long been known that the cooling of a planet gives rise to global deviatorically compressive thermal stresses. These thermal stresses have been considered as a possible explanation for reverse faulting on Mercury and Mars. I have evaluated the contribution of global contraction as recorded by the global fault data set in the presence of a lithospheric stress field associated with horizontal GPE gradients.

Fitting only the reverse faults, while disregarding other tectonic features, can be achieved trivially with global contraction stresses. The associated strains, radius decrease, and required temperature changes, are very small and are consistent with forward thermodynamical models of global contraction. However, global contraction cannot fit both normal and reverse faults. Consequently, the normal faults may have formed before the southern hemisphere reverse faulting. Alternatively, either the global contraction stresses dissipated after the formation of the southern reverse faults, but before the formation of the radial grabens in the Tharsis province, or an additional source of stress is needed, and this stress must be large and deviatorically extensional in the center of Tharsis and deviatorically compressional in the periphery. Both scenarios are problematic, suggesting that global contraction may not be a significant contributing factor for the formation of the reverse faults on Mars.

3.1 Introduction

A planet's evolution is recorded, in part, in the surficial expression of the tectonic features observed today. Theoretical models of deformation mechanisms and forces, when tied to these tectonic observations, can be interpreted in terms of major tectonic events and

allow some insights into the planet's internal structure and processes (*Carr*, 1974, 1981; *Wise et al.*, 1979; *Banerdt et al.*, 1992). This is particularly important for understanding solid planetary bodies other than Earth, where the seismic data is either sparse, e.g. the Moon, or non-existent, e.g. Mars.

In the past few decades a series of missions – flybys, orbiting spacecrafts, stationary and roving landers on the Martian surface – have produced a wealth of images and data on the surficial and global scale properties of Mars. Overall studies of the tectonic and geologic history of Mars as well as small scale detailed tectonic and geologic features have been produced from Mariner and Viking images (*Plescia and Saunders*, 1982; *Scott and Tanaka*, 1986; *Tanaka and Scott*, 1987; *Greeley and Guest*, 1987; *Tanaka et al.*, 1992; *Banerdt et al.*, 1992).

Several studies have focused on the classification, distribution and formation of compressional features (*Chicarro et al.*, 1985; *Golombek et al.*, 1991; *Watters*, 1991; *Watters*, 1993). The most abundant compressional tectonic features are wrinkle ridges followed by lobate scarps and high relief ridges, and can be found on both the eastern and western hemisphere on Mars. Both regional and global origin for these features has been proposed. Regional explanations have included a detached thicker cap underneath Tharsis (*Banerdt and Golombek*, 1990), cooling and subsidence of volcanic plains or removal of overburden by erosion in a laterally confined region (*Watters*, 1993, and references therein). On a global scale, it was also recognized that horizontally isotropic stress due to global contraction may have played a significant role in the formation of the compressional tectonic features (*Sleep and Phillips*, 1985; *Tanaka et al.*, 1991). Such global contraction is predicted by thermal history models *Schubert et al.* (1992).

In a cooling planet, the cold lithosphere alone can support deviatoric stresses and adjusts to decreasing volume of the interior. The resultant stresses are horizontally isotropic surface stresses, whose magnitude increases with time, while the vertical stress remains constant, equal to the depth integral of density and gravity with depth. In such a stress field, the associated contractional features are expected to be random, which is generally not the case on Mars. Therefore, the stresses from global contraction must be superposed on non-hydrostatic horizontal stresses.

Recently, two different models of the lithospheric stress have been employed to explain the majority of the faulting in and around Tharsis. The model of *Banerdt and Golombek* (2000) is dominated by the deflection of the lithosphere due to the Tharsis load, while the model of *Dimitrova et al.* (2006) is a solution to the depth integrated three dimensional force-balance equations for depth-integrated deviatoric stresses. In the model of *Dimitrova et al.* (2006) the forces are related to horizontal variations in the depth integrals of vertical stress, or gravity potential energy per unit area (hereafter referred to as GPE). The GPE values are constrained by existing crustal structure (*Zuber et al.*, 2000; *Neumann et al.*, 2004), which is generally uncompensated. The surface deviatoric stresses of *Banerdt and Golombek* (2000) and the depth integrated deviatoric stresses of *Dimitrova et al.* (2006) differ in magnitudes and, in many areas, have opposite patterns. Neither of these models incorporates the possible role of global contraction. The response of global contraction is added to the background deviatoric stress tensor field and this total stress tensor response can be compared with observations, such as strain patterns (faulting). The choice of a background deviatoric horizontal stress tensor field can therefore have a profound effect on the calculation of global contraction.

To date, the question of what, if any, is the role of global contraction in the tectonic history of Mars remains open. *Mangold et al.* (2000) have argued that compressional deformation is not due directly to the filling and cooling of volcanic plains based on the chronology of both tectonic features and the plains. They further argue that thermal compressive stress, initiated after the crust is formed, can produce a global contractional phase consistent with the timing of the peak of compressional tectonism in Late Hesperian. *Hauck et al.* (2003) note that strains from global contraction due to either long-term cooling of the interior or cooling of the mantle associated with an episode of high volcanic flux are generally too small, and only (among the thermally driven hypotheses) global climate change can produce the contractional strains with large temperature excursion on the order of a hundred years (or small ones over longer time period). *Searls and Phillips* (2007) concluded that differential compaction within Utopia and gravitational slumping of material towards the basin center does not affect the predicted faulting, and invoked global contraction as a possible explanation for the faulting.

These studies have elucidated the major problems that need to be addressed in order to explain the compressional tectonics on Mars: (1) What is the precise timing of reverse faulting and the emplacement of volcanic plains? (2) What was the non-hydrostatic background stress before contraction? and (3) What are the effects/constraints imposed by multiphase deformation associated with normal faulting?

In this study we examine the depth integrated deviatoric stress field solution of *Dimitrova et al.* (2006) and compare it with the normal and reverse fault data from *Knapmeyer et al.* (2006). We then solve for the additional, horizontally hydrostatic, stress needed to fit subsets of the fault data. We show that it is possible to fit the reverse fault data alone with small stresses and associated radius change. However, when we consider the timing of the normal and reverse faults together, global contraction becomes a problematic solution to the problem of the tectonic history on Mars.

3.2 Lithospheric Stress Model Associated with Gravitational Potential Energy Differences

3.2.1 Thin Sheet Methodology

We solve the depth-integrated three-dimensional force-balance equations for the depth integrated deviatoric stress field in the lithosphere (*Flesch et al.*, 2001). These solutions do not require detailed descriptions of the lithosphere rheology, but only a decision of whether we choose to treat the lithosphere as generally viscous or elastic. We will outline the major equations in Cartesian form below. In actuality, we use the corresponding equations for a spherical planet, which have the same structure but a more complicated form (see Appendix).

The 3-D Stoke's equations for steady motion with no rate of change of momentum are given by:

$$\frac{\partial \sigma_{ij}}{\partial x_j} + \rho g \hat{z} = 0, \tag{1}$$

where σ_{ij} is the total stress, ρ is the density, g is the gravitational acceleration, $\hat{z}$ is the

unit vector in the vertical direction, and a 3-D summation notation is implied (i.e., j takes values x, y, and z).

Following *England and McKenzie* (1982) and *Flesch et al.* (2001), we adopt a thin shell approximation. In this approach both $\frac{\partial \sigma_{xz}}{\partial x}$ and $\frac{\partial \sigma_{yz}}{\partial y}$ are much less than ρg, and hence vanish. This approximation enables us to use the third equation in (1), where $i = 3$, to define

$$\sigma_{zz}(z) = -\int_{-h}^{z} \rho(z') g dz', \tag{2}$$

We define the deviatoric stress tensor as

$$\tau_{ij} = \sigma_{ij} - \frac{1}{3}\sigma_{kk}\delta_{ij} = \sigma_{ij} - (\sigma_{zz} - \tau_{zz})\,\delta_{ij}, \tag{3}$$

with a 3-D summation notation implied. Using equation (3) to substitue for total stress, σ_{ij}, in the force-balance equations in (1), and then depth integrating these equations through a lithospheric thickness L we obtain:

$$\frac{\partial}{\partial x_\beta}\left(\overline{\tau}_{\alpha\beta} + \overline{\tau}_{\gamma\gamma}\delta_{ij}\right) = -F_\alpha, \tag{4}$$

where $\overline{\tau}_{\alpha\beta}$ is the vertically integrated horizontal deviatoric stress tensor, F_α are the applied horizontal body forces, and a 2-D summation notation with $\overline{\tau}_{\gamma\gamma} = \overline{\tau}_{xx} + \overline{\tau}_{yy} = -\overline{\tau}_{zz}$ is implied (i.e., α, β, γ take values x and y). For example, $F_\alpha = \frac{\partial \overline{\sigma}_{zz}}{x_\alpha}$ for GPE differences, $F_\alpha = -\tau_{\alpha z}(L)$ for tractions $\tau_{xz}(L)$ and $\tau_{yz}(L)$ at the base of the lithosphere, L, from mantle convection (not included in this model), and $F(L) \propto \frac{\partial \overline{U}_r/r}{\partial x_\alpha}$ for elastic membrane strains and stresses, where

$$\overline{\sigma}_{zz} = -\int_{-h}^{L}\left[\int_{-h}^{z} \rho(z') g dz'\right] dz, \tag{5}$$

is the vertically integrated vertical stress of a column of lithosphere and has units of potential energy per unit area on the planet surface (GPE), $\overline{U}_r(\phi,\theta) = \int_{-h}^{L} U_r(r,\phi,\theta)dr$ is the radial displacement due to loading, h is the topography, and L is the depth to the bottom of the deforming lithosphere. If the depth L varies from a constant depth, then the associated sliding tractions need to be accounted for. However, *Ghosh et al.* (2008) have shown that

in practice the effect from the variable depth cancel out with the effect of the associated sliding tractions, i.e., it is sufficient to integrate down to a constant depth below a mean elevation. The system of differential equations is linear in stress, allowing for separate solutions to the stress field from the various sources, F_α, to be summed to produce the total lithospheric deviatoric solution. In this model we focus on the GPE terms.

Using a finite-element approach we solve the force balance differential equations using the method of *Flesch et al.* (2001). In this methodology the global integral of the second invariant of deviatoric stress is minimized in the process of satisfying the Stoke's equation i.e. we minimize a functional:

$$I = \int_S \frac{1}{\mu}\left[\bar{\tau}_{\alpha\beta}\bar{\tau}_{\alpha\beta} + \bar{\tau}_{\gamma\gamma}^2\right] dS + \int_S 2\lambda_\alpha \left[\frac{\partial}{\partial x_\beta}(\bar{\tau}_{\alpha\beta} + \bar{\tau}_{\gamma\gamma}\delta_{\alpha\beta}) + F_\alpha\right] dS, \tag{6}$$

where λ_α are the Lagrange multipliers for the Stoke's equation and S is the planet surface. Using the variational principle we obtain:

$$\bar{\tau}_{\alpha\beta} = \frac{1}{2}\left[\frac{\partial\lambda_\alpha}{\partial x_\beta} + \frac{\partial\lambda_\beta}{\partial x_\alpha}\right]. \tag{7}$$

Note that $\bar{\tau}_{\alpha\beta}$ has the same functional dependence on the Lagrange multipliers λ_α as the strain/strain rate has on displacement/velocity.

Substituting the expression for $\bar{\tau}_{\alpha\beta}$ from equation (7) into equation (4) yields the force balance equations and the minimization of the functional I becomes equivalent to minimizing a functional:

$$J = \int_S \left\{ \left[\begin{pmatrix} \bar{\tau}_{xx} \\ \bar{\tau}_{yy} \\ \bar{\tau}_{xy} \end{pmatrix} - \begin{pmatrix} \Phi_{xx}^{obs} \\ \Phi_{yy}^{obs} \\ \Phi_{xy}^{obs} \end{pmatrix} \right]^T V^{-1} \left[\begin{pmatrix} \bar{\tau}_{xx} \\ \bar{\tau}_{yy} \\ \bar{\tau}_{xy} \end{pmatrix} - \begin{pmatrix} \Phi_{xx}^{obs} \\ \Phi_{yy}^{obs} \\ \Phi_{xy}^{obs} \end{pmatrix} \right] \right\} dS \tag{8}$$

where the covariance matrix V^{-1} relates to the Poisson's ratio ν and the potentials vector

Φ^{obs} relates to the body forces by

$$V^{-1} = \begin{pmatrix} \frac{1}{1-\nu} & \frac{\nu}{1-\nu} & 0 \\ \frac{\nu}{1-\nu} & \frac{1}{1-\nu} & 0 \\ 0 & 0 & 2 \end{pmatrix}, \tag{9}$$

and

$$\begin{pmatrix} \Phi_{xx}^{obs} \\ \Phi_{yy}^{obs} \\ \Phi_{xy}^{obs} \end{pmatrix} = \begin{pmatrix} -\overline{\sigma}_{zz}/3 \\ -\overline{\sigma}_{zz}/3 \\ 0 \end{pmatrix} \tag{10}$$

In other words, the minimization of the functional J leads to a solution of the force balance equations for the minimum vertically integrated deviatoric stress field associated with GPE differences (*Flesch et al.*, 2001).

The methodology of using optimization of equation (8) to solve the force balance equations for depth-integrated deviatoric stresses has been benchmarked (*Ghosh et al.*, 2008) with independent deviatoric stress output from a long wavelength (degree 12) full three-dimensional mantle circulation model. *Ghosh et al.* (2008) showed that the absolute viscosity of the lid (lithosphere) does not need to be known, only the input body force equivalent terms (spatial variations in depth-integrated vertical stresses (GPE), and applied basal tractions $\tau_{xz}(L)$ and $\tau_{yz}(L)$ associated with mantle convection). The combined contribution from these two sources yielded a total deviatoric stress field in the thin shell calculation that matched nearly exactly the deviatoric stress output for the lithospheric lid in the full 3-D calculation (*Ghosh et al.*, 2008). The benchmarking exercises of *Ghosh et al.* (2008) demonstrate the suitability of choice of functionals I and J for solving the depth-integrated force-balance equations for cases of constant lid viscosity. In the case of Mars we assume that $\tau_{xz}(L)$ and $\tau_{yz}(L)$ from mantle convection are negligible. However, the crustal structure for Mars has been estimated (*Zuber et al.*, 2000; *Neumann et al.*, 2004) and elevations are known. Thus, the depth integrals of vertical stress, from the surface of variable elevation down to a common-depth reference level, L, can be computed precisely. In the methodology that we employ, the topography need not be compensated. That is, $\sigma_{zz}(L)$ can be variable, which is the case for Mars. For example, in the benchmarking exercise there was

significant dynamic topography, and the thin shell method recovered the stresses precisely. In summary, if the crustal structure were accurate and basal tractions negligible, our thin shell methodology would accurately recover the depth integrated deviatoric stresses within the lithosphere of Mars.

For the thin shell calculations, it is important to define a reference level, L, as the base of the thin shell. This reference level corresponds to the highest point within the lithosphere where decoupling occurs below the elastic layer, and can be spatially variable. For example, in the case where there is complete decoupling between brittle upper crust and lower crust, this reference level consists of the brittle-ductile transition. In the case where there is coupling between brittle lithosphere and ductile lithosphere, then the reference level consists of the contact between convecting and non-convecting mantle/crust (base of lithosphere). The simplest reason for considering different reference levels is the case where elastic thickness will increase as the planet cools. Since we do not have good constraint for the variable bottom of the lithsophere, we choose a constant reference level, equal to the depth of the deepest crust ($L \approx 92.84$) km. In choosing this reference level, we assume that there is no mantle convection acting on the variable base of lithosphere, and no dynamic topography.

3.2.2 Model

Figures 1 and 2 show the horizontal deviatoric lithospheric stress fields associated with horizontal gradients in GPE derived from the topography of Zuber et al. [2000] and the crustal thickness model of Neumann et al. [2004]. We assume $\rho_{crust} = 2900 kg.m^{-3}$, $\rho_{mantle} = 3500 kg.m^{-3}$, $g = 3.7 m.s^{-2}$, consistent with the crustal thickness inversion parameters. In the absence of indicators for a brittle-ductile transition we have chosen the reference level $L = 92.84 km$, corresponding to the deepest extent of the crust below the areoid. Larger choices of L do not lead to significant differences in stress orientations; however, they do lead to somewhat larger stress magnitudes (supplementary figure 1). Finally, we use a Poisson's ratio $\nu = 0.5$, which corresponds to either a viscous or incompressible elastic rheology.

To first order the GPE solution shows deviatoric extension over topographically high areas transitioning to deviatoric compression at topographically low areas. A notable exception to this pattern are areas with low topography but thin crust, which exhibit propensity for extensional faulting, e.g. Isidis Plantia and to a smaller extent Utopia, Argyre, and Acidalia Plantiae. This effect is amplified if we consider elastic layers extending below the nominal reference level.

3.2.3 Comparison with Global Fault Datasets

To date there are two datasets of global fault features on Mars. Anderson et al. [2001] examined Viking images of the western hemisphere and compiled a database of reverse and normal faults in the western hemisphere of Mars. Recently the study was extended to cover the eastern hemisphere as well (*Anderson et al.*, 2006, 2008). An alternative dataset was produced by *Knapmeyer et al.* (2006) based on the MOLA maps. Both studies focus on normal and reverse faulting, since only a few strike-slip faults have been identified (*Schultz*, 1989; *Mangold et al.*, 2000; *Tanaka et al.*, 2003; *Okubo and Schultz*, 2006). Both studies dated each fault based on the unit containing the fault and absolute ages were reassigned afterwards, based on crater chronology models of *Hartmann and Neukum* (2001)]. For this study we have used the most recent MOLA-based dataset of *Knapmeyer et al.* (2006), which consist of 7000 reverse and normal faults (Figure 3). Note that the normal faults are located predominantly in the western hemisphere. In addition, almost all normal faults are located in high topography areas, with the exception of faults along the dichotomy boundary in the eastern hemisphere and north/northeast of Alba Patera. The reverse faults have a more global distribution, although there are only a few areas where normal and reverse faults overlap.

We first perform a *Kostrov* (1974) moment tensor summation to estimate the total strain tensor, ε_{ij}, for a given volume, V, for that period:

$$\varepsilon_{ij} = \frac{1}{2\mu V} \sum M_0 m_{ij}(\theta, \lambda, \delta), \tag{11}$$

where μ is the shear modulus, M_0 is the moment of slip on the fault and m_{ij} is the unit

moment tensor, which is a function of the fault strike, θ, rake, λ, and dip, δ . The moment of slip is defined as:

$$M_0 = \mu LDu, \tag{12}$$

where L is the fault length, D is the depth of faulting, and u is the magnitude of slip. Substituting into equation (A1) above we have the average strain tensor associated with the fault-related deformation within the volume l:

$$\varepsilon_{ij}^{l} = \frac{1}{2}\sum_{k=1}^{n}\frac{L_k u_k}{A} m_{ij}^{k}(\theta,\lambda,\delta), \tag{13}$$

where A is the area containing n fault segments, each having length L_k (*Holt and Haines*, 1995; *Schultz*, 2003). Therefore, the assumed thickness and shear modulus do not enter into the final estimate of the strain tensor for the area, since it is implicitly assumed in this formula that $m_{ij}(\theta,\lambda,\delta)$ and u do not vary with depth within the faulted or elastic layer.

Although fault displacements scale primarily with length, mechanical length depends on fault segmentation, spacing, and linkage, which are often not recognized in the global datasets. Hence, we assume uniform slip on each fault segment. The resulting ε_{ij} reflects the simplest and least-biased approach to incorporating fault-related strain to compare with the stress model. As would be seen later, the objective function that we plan to use to measure the fit between the faults and the stress models is insensitive to scalar multiples of either the strain or stress tensor, and thus it is insensitive to the actual value of u.

The strain from the *Kostrov* (1974) calculation for the normal and reverse faults of *Knapmeyer et al.* (2006) assuming unit slip, is shown in Figures 4,5,6 and 7. The majority of the deviatorically extensional strain is either circumferential to Tharsis and Elysium, since it arises from systems of radial grabens, or to a smaller extent, parallel to the topographic gradient near the dichotomy boundary, since it arises from a few normal faults parallel to the boundary. The deviatorically compressional strain on the other hand is radial to Tharsis, Hellas and Utopia, since it arises from circumferential compressional features. Note that we have assumed a uniform amount of slip for each fault as a first approximation. Consequently, the magnitude of the calculated strain does not reflect the real absolute strain and we will be comparing only the relative magnitudes and orientations of the princi-

pal strains with the relative magnitudes and orientations of the modeled principal deviatoric stresses.

We introduce a quantitative method to compare the model stress field associated with GPE gradients and the strain derived from Kostrov summation of the faults, where we seek to correlate the model stress with the fault strike and style. Thus we seek a correlation between the directions and relative magnitudes of the principal stresses, but not their absolute magnitudes. Following *Flesch et al.* (2007) and *Dimitrova et al.* (2006), we define objective functions that measure the correlation C between the strain derived from the fault data and the dynamically predicted stress field, as well as the misfit M between these as

$$C = \frac{\varepsilon \cdot \tau}{ET} \text{ and } M = \frac{1}{2}(1 - C), \tag{14}$$

where the metrics E and T and the inner product are defined as:

$$E = \sqrt{\varepsilon_{ij}\varepsilon_{ij}}, T = \sqrt{\tau_{ij}\tau_{ij}}, \varepsilon \cdot \tau = \varepsilon_{ij} \cdot \tau_{ij} \tag{15}$$

This objective function is minimized when the tensor solution of stress or strain from the dynamic calculations is consistent with the formation of faults with the same strike and style as the fault data; thus, it accounts for fault strike and fault style, defined by the relative magnitudes of the principal axis of the stress tensor. The misfit function has values from 0 to 1, with 0 misfit indicating a perfect fit. A value of 0.5 indicates decorrelation between the model stress and fault strain fields, e.g. a predicted strike-slip fault rotated by 45° from the actual normal or reverse fault. In addition, the correlation and misfit functions are insensitive to the stress or strain magnitudes due to the normalization of the $\varepsilon \cdot \tau$ term by both E and T.

The misfit of the GPE stress field to the fault data is shown in Figures 8 and 9. Almost all normal faults are located in high topography areas, with the exception of very few faults at low elevation along the eastern part of the dichotomy boundary and north/northeast of Alba Patera. Since the GPE associated stresses tend to be deviatorically extensional in areas of high topography, the fit to the normal faults is generally of high quality (figure 8).

Conversely, the abundance of reverse faults in the high topography areas of the southern hemisphere leads to a much poorer fit of the GPE associated stresses to the reverse faults (figure 9). Note that the northern hemisphere reverse faults are already fitted by the GPE model, and hence, they provide no constraint on the estimates for global contraction.

3.3 Inversions for a Global Contractional Stresses

3.3.1 Methodology

As discussed in *Sleep and Phillips* (1985); *Watters* (1993), and many others, planetary cooling can produce deviatoric stress due to the presence of an already cooled lithosphere, which alone can support deviatoric stresses. As the lithosphere cools, the interior volume decreases, and the horizontal stresses increase in magnitude, while the vertical stress remains constant, equal to the depth integral of density and gravity with depth. Such a stress field, when added to a non-horizontally hydrostatic stress field, changes the balance between the principal stress directions, pushing regions originally in deviatoric tension to deviatoric compression. Thus, we would like to solve for the horizontally homogeneous stress field, which when added to the GPE associated stress, minimizes the misfit to the fault data as defined in equations (14,8). Numerical stability, however, requires us to minimize a non-normalized version of the misfit, M/E. It is important to note that we are solving for the minimum global contractional stress that could fit the surface tectonic record; larger global contraction may have occurred, especially on sufficiently long time scales such that the resulting strains are small and can be accommodated in non brittle-frictional deformation.

3.3.2 Inversion Results

We show in Figures 10 and 11 the vertically integrated global stress field (GPE + global contraction stresses) obtained from the inversion of only the reverse faults. Figure 12 shows the misfit to the reverse faults overlaid on the reverse faults. Stresses associated with global contraction, when added to the stresses associated with GPE differences, can fit most of the reverse faults globally, although small misfits remain in Solis Planum, and north-northeast

of Olympus Mons. Thus, global contraction, together with GPE, seems a possible mechanism for predicting the reverse faults alone globally. If global contraction stresses, in addition to the GPE associated ones, are responsible for the reverse faulting in southern, or all of, Mars, then the radius change resulting in the calculated global contraction stress is given by

$$\delta R = R\left[1 - \sqrt{\frac{1}{1+\varepsilon}}\right] \text{ with } \varepsilon = \frac{\sigma}{2\mu h} \tag{16}$$

where R is the planet's radius, ε is the horizontal strain, σ is the lithospheric thickness, σ is the vertically integrated stress from global contraction, and μ is the shear modulus [Watters, 1993]. For the reverse faults, the vertically integrated global contraction stress required, $-0.7 \cdot 10^{12} N \cdot m^{-1}$, for values of μ ranging between $4 \cdot 10^{10} Pa$ and $8 \cdot 10^{10} Pa$ translates to a very small radius decrease of $0.08 km$ to $0.16 km$, consistent with those inferred by Nahm and Schultz [2007]. The associated temperature change is given by

$$\delta T = \frac{3\varepsilon}{\alpha_v} \tag{17}$$

where α_v is the volumetric coefficient of thermal expansion [e.g., Hauck et al., 2003]. For reasonable values of α_v on the order of $3 \cdot 10^{-5} K^{-1}$, this translates into temperature change on the order of $5 - 10^{\circ} K$, i.e., a very small temperature change.

However, the resultant stress field (Figure 10), produces radial compressional stresses on Tharsis that dominate over the circumferential extensional stress, thus degrading the fit to the normal faults, i.e., the combiend GPE and global contraction stresses from the fit to the reverse faults misfit the majority of the normal faults on Tharsis. In fact, it is impossible to find a contractional isotropic horizontal stress, which when added to the GPE associated stresses, that can fit both the normal and reverse faults. Figures 13 and 14 show the vertically integrated global stress field (GPE + global contraction stresses) obtained from the inversion of the entire fault population of reverse and normal faults. Comparing the misfit of this model (Figure 15) with the misfit from the inversion to the reverse faults alone stresses (Figure 12), this combined stress field has a degraded fit to the reverse faults in the southern hemisphere. Relative to the solution associated with GPE alone (Figures 8

and 9), the inversion of both normal and reverse faults yields an improved fit only in Sabaea Terra and Lunae Planum. In other words, in trying to fit the normal faults, the model fails to improve the misfit to the majority of the reverse faults in the southern hemisphere.

Consequently, either the normal faults formed before the southern hemisphere reverse faulting; or the stress regime needs to have changed back to one that that produces deviatoric extension in Tharsis. Regional studies indicate that it is unlikely that the normal faults formed before the southern hemisphere reverse faults (see also Fig 16). The stress results suggest that in areas where the GPE stresses alone are deviatorically extensional, and the combined GPE and global contraction stresses are deviatorically compressional (Figures 12 and 13), both normal and reverse faults would occur orthogonal to each other. In the western hemisphere, this is observed in Sirenum Terra and to a lesser extent in Aonia Terra. Areas around Olympus Mons and Alba Patera, however, have predominantly normal faults with very few reverse faults. In the eastern hemisphere, the highlands north-northwest of Hellas Plantia exhibit both normal and reverse faulting, but the remaining highlands do not. The majority of the normal faulting extending south-southeast from Utopia Plantia is not explained by either model.

If, however, the normal faults formed after the reverse faults, either global contractional stresses must have dissipated after the formation of the reverse faults in the southern hemisphere, but before the formation of the radial grabens in the Tharsis province; or a new, larger, source of stress is needed. The former case requires more than 60% of the contractional stress to be accomodated by frictional sliding or ductile deformation, so that the GPE associated stress field dominates again in the center of Tharsis. The latter case requires an additional stress field that is extensional in the center of Tharsis, and compressional in the periphery of Tharsis, i.e., opposite of that predicted by downward flexure-dominated models (*Banerdt and Golombek*, 2000; *Phillips et al.*, 2001; *Searls and Phillips*, 2007). Upward flexure, due to a large mantle plume beneath Tharsis, can produce such a stress field [Banerdt et al, 1992]; however, that would imply active mantle convection through the Late Hesperian.

The crustal and mantle lithosphere have different rheological parameters (Poisson's ratio), so we performed a series of inversions, modifying the global contractional stress

to reflect that difference. We considered contractional stresses, everywhere horizontally isotropic, whose magnitude is proportional to the sum of crustal thickness and the mantle thickness times the ratio of the Poisson's parameter for the crust and the mantle lithosphere. The latter was allowed to vary from 1 (illustrating the effect of variable lithospheric thickness alone) to 5 in increments of 0.5. The resulting surface integrals of the misfit to the reverse alone and both reverse and normal faults are shown in Table 1, where the base model is the GPE and laterally unform global contraction model from figure 10, 11. The biggest differences are due to the variable thicknesses, while the effect of the difference in the Poisson's ratios is small (also supplementary figure 2); however, all differences are minor.

Watters (1993), based on the cumulative length of contractional features as a function of age of the deformed units, noted that if the Early Hesperian is excluded, there is a gradual decrease in compressional deformation, as expected by thermal models (*Schubert et al.*, 1992), and concluded that if global contraction was important for the formation of tectonic features, its influence was most significant in the Early Hesperian. If we consider the cumulative length of the contractional features in this study as a function of age (Figure 16), we see a peak of compressional deformation in Late Noachian, followed by a peak throughout the Hesperian. In fact, very few contractional features have been mapped in the Amazonian. There is also no clear gradual decrease in compressional tectonic deformation.

Such age analysis is applicable only "if the tectonic features are roughly the same age as the units in which they occur" (*Watters*, 1993). A subsequent study by *Mangold et al.* (2000) shows that if chronological relationships between craters and structures are used in dating the faults, the age progression may change significantly. Constraining the timing of the normal and reverse faults, therefore, remains crucial to establish if global contraction is a possible source of compressional tectonic deformation.

3.4 Summary

Theoretical models of deformation mechanisms can be compared to the surficial expression of the tectonic features observed today and interpreted in terms of major tectonic

events, thus allowing us insights into the internal structure and processes on Mars. Previous workers hypothesized a period of global contraction during the Hesperian. In this study we evaluate the contribution of global contraction as recorded by a global fault data set in the presence of a lithospheric stress field associated with horizontal GPE gradients, and estimate the associated radius decrease.

The GPE associated stresses fit the majority of the normal faults as well as the northern hemisphere reverse faults. Stresses associated with global contraction and GPE differences can fit most of the reverse faults alone. The associated radius decrease and temperature difference are small, $0.08 - 0.16$ km and $5 - 10^{\circ}$ K respectively.

However, global contraction stresses, in conjunction with GPE associated stresses, cannot fit both the normal and reverse faults. Consequently, the normal faults may have formed before the southern hemisphere reverse faulting. Alternatively, either the global contractional stresses dissipated after the formation of the southern reverse faults, but before the formation of the radial grabens in the Tharsis province, or an additional source of stress is needed and this stress must be large and deviatorically extensional in the center of Tharsis and deviatorically compressional in the periphery. Both scenarios are problematic, suggesting that global contraction may not be a significant contributing factor for the formation of the reverse faults on Mars.

If we consider the cumulative length of the contractional features in this study as a function of age, we see a peak of compressional deformation in Late Noachian, followed by a peak throughout the Hesperian. In fact, very few contractional features have been mapped in the Amazonian. There is also no clear gradual decrease in compressional tectonic deformation as would be expected from thermal cooling models. These results, however, are biased due to the inherent assumption in the fault-age data that the tectonic features are roughly the same age as the units in which they occur, and indicate that detailed studies of the spatial and temporal distribution of faulting on Mars are needed.

		Ratio of Poisson's parameters for the crust and mantle lithosphere					
	base	1	1.5	2	2.5	3	3.5
reverse	437.0	344.6	343.7	343.3	343.0	342.9	342.8
normal and reverse	1070	903.2	901.1	900.1	899.5	899.1	898.9
	Ratio of Poisson's parameters for the crust and mantle lithosphere						
	4	4.5	5				
reverse	342.7	342.6	342.5				
normal and reverse	898.7	898.5	898.4				

Table 1: The surface integrals of the non-normalized misfit M/E (see text) to the reverse alone and both reverse and normal faults for the inversions of GPE and laterally varying in magnitude, but at each point horizontally isotropic, global contractional stress. The base model consists of GPE stresses and no lateral variation in the global contraction stress magnitude. For the remaining models, the magnitude of the contractional stress at each grid area was allowed to vary proportionally to the sum of crustal thickness, and the mantle thickness times the ratio of the Poisson's parameter for the crust and the mantle lithosphere. The latter was allowed to vary from 1 (illustrating the effect of variable lithospheric thickness alone) to 5 in increments of 0.5.

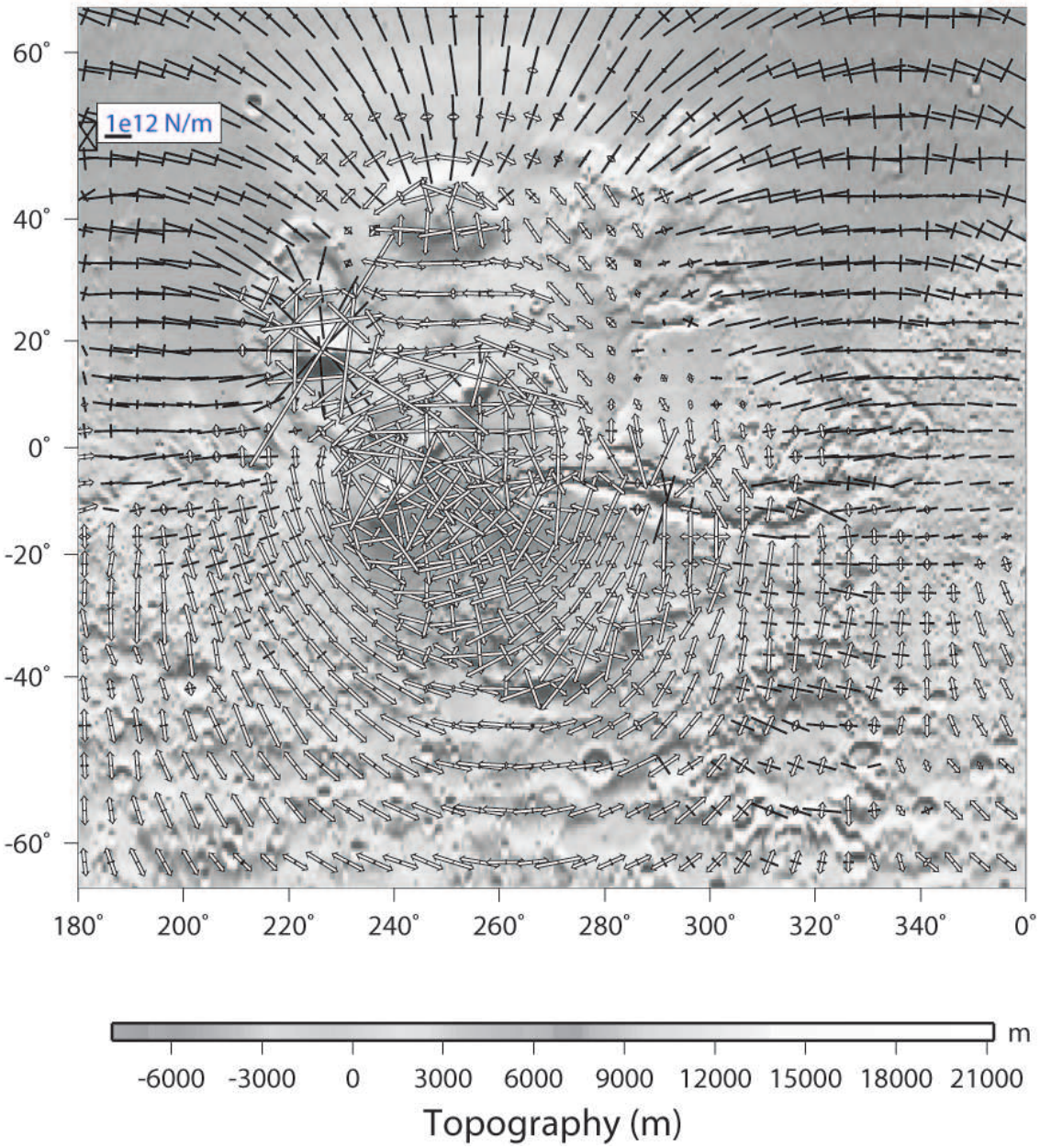

Figure 1: Vertically integrated ($L = 92.84km$) deviatoric lithospheric stresses associated with GPE variations calculated from MOLA topography (*Zuber et al.*, 2000) and inferred crustal thickness (*Neumann et al.*, 2004), and assuming Poisson's ratio of 0.5 in the western hemisphere of Mars. White arrows represent deviatoric extension, while black arrows represent deviatoric compression.

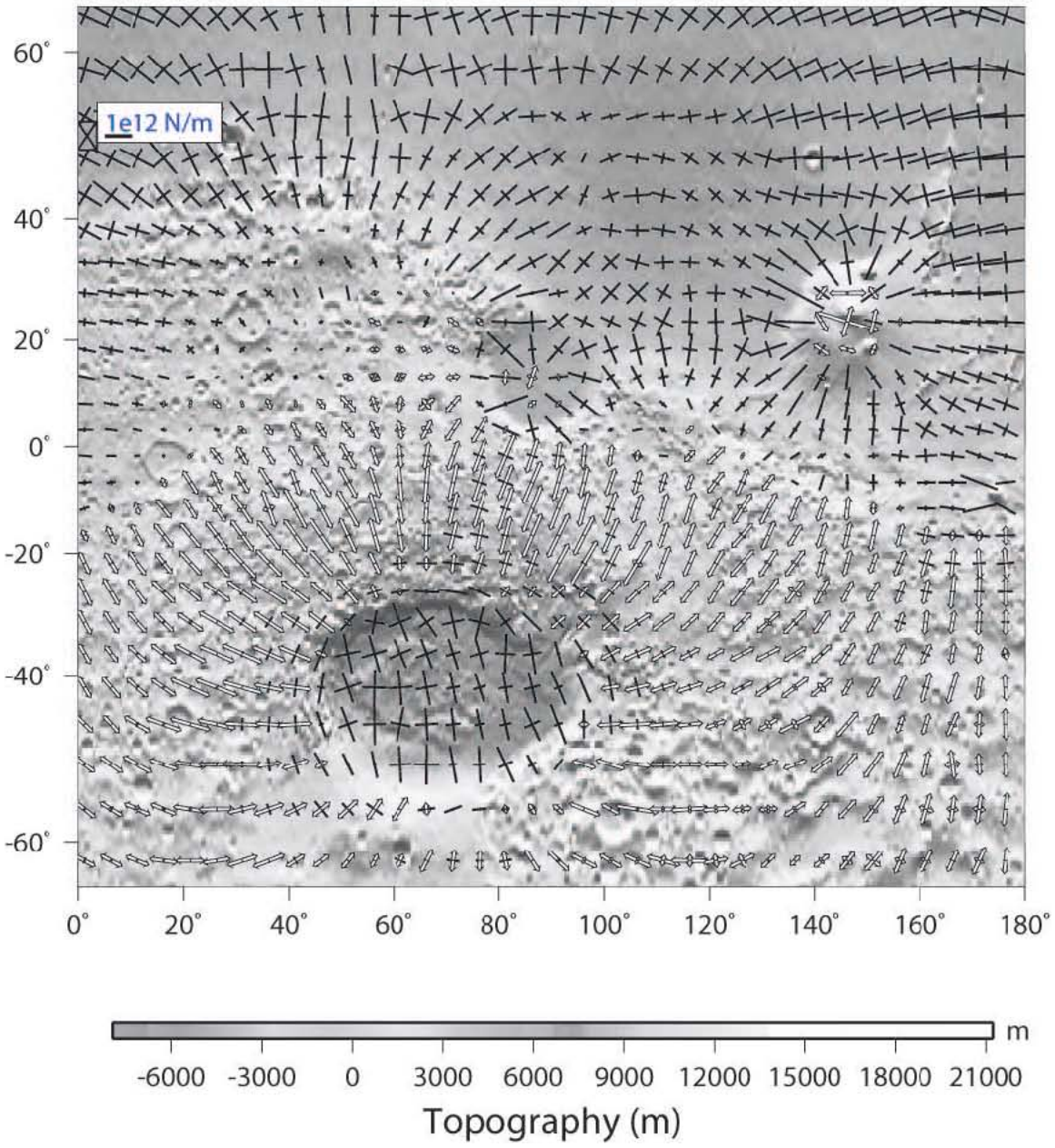

Figure 2: Vertically integrated ($L = 92.84km$) deviatoric lithospheric stresses associated with GPE variations calculated from MOLA topography (*Zuber et al.*, 2000) and inferred crustal thickness (*Neumann et al.*, 2004), and assuming Poisson's ratio of 0.5 in the eastern hemisphere of Mars. White arrows represent deviatoric extension, while black arrows represent deviatoric compression.

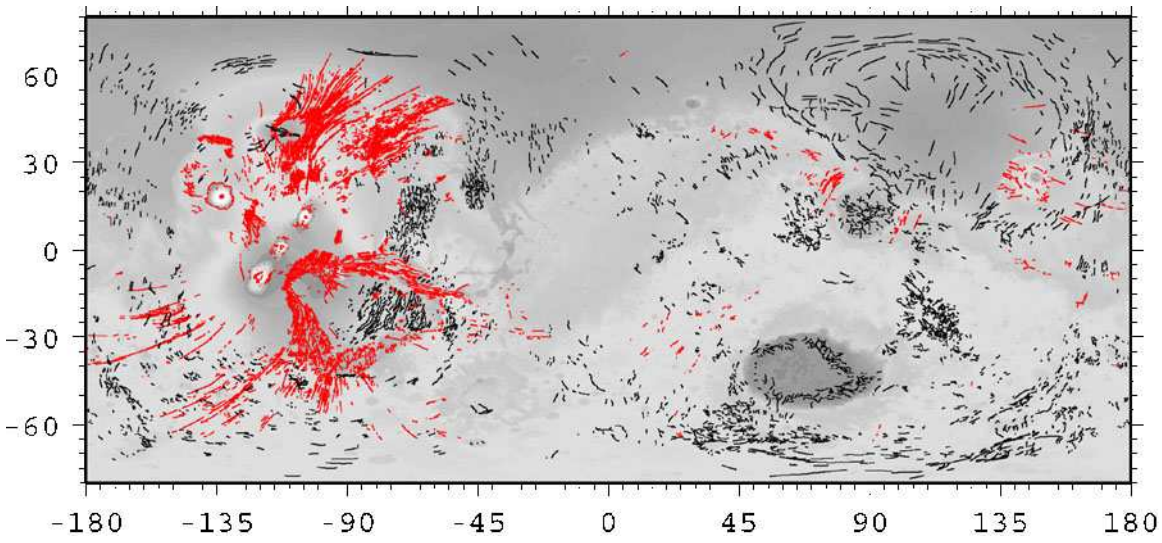

Figure 3: Normal (in red) and reverse (in black) faults from *Knapmeyer et al.* (2006).

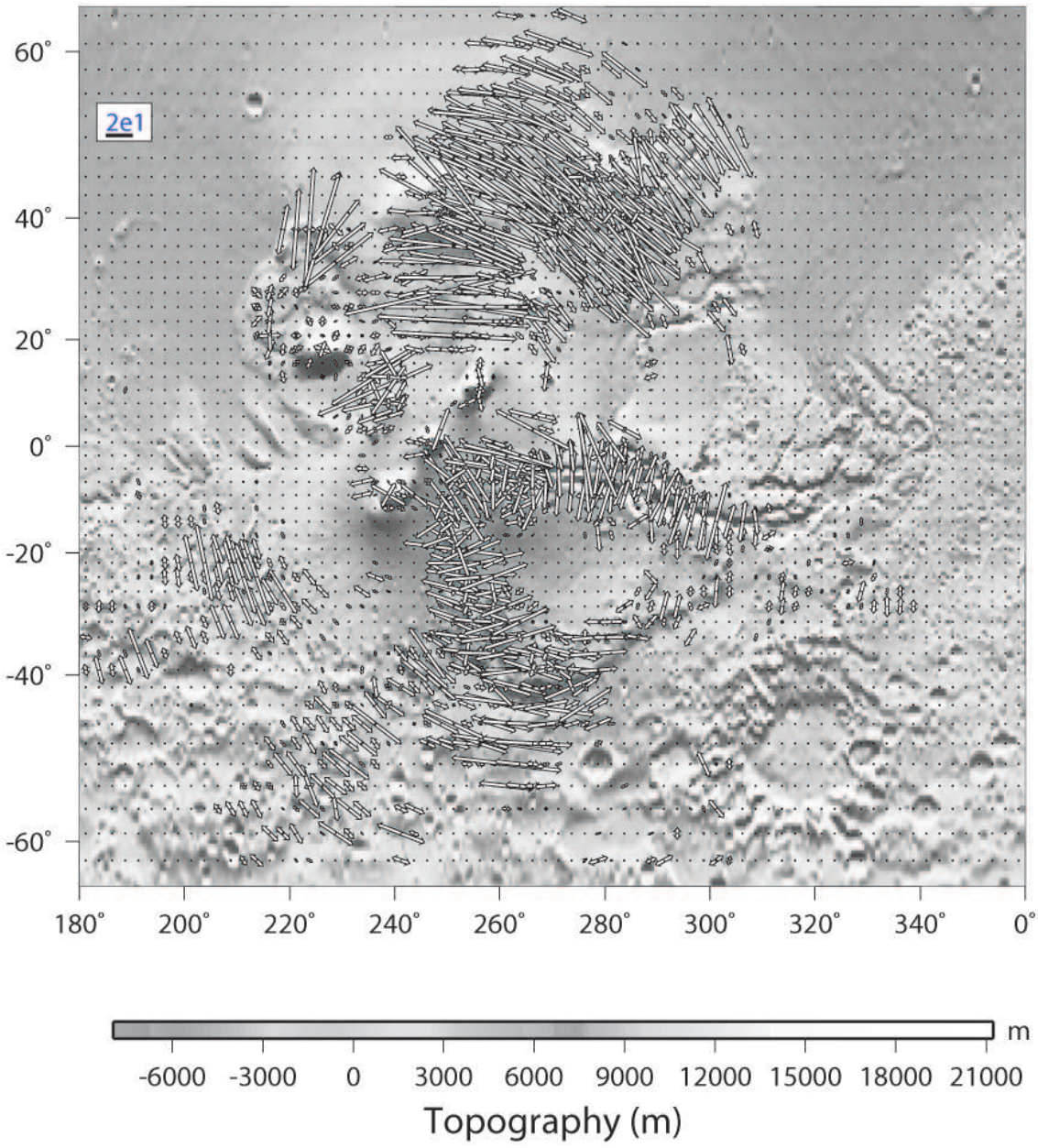

Figure 4: Deviatoric strain from Kostrov summation associated with the normal faults of *Knapmeyer et al.* (2006) in the western hemisphere of Mars. White arrows represent deviatoric extension. Note that we have assumed a uniform amount of slip for each fault as a first approximation. Consequently, the magnitude of the calculated strain does not reflect the real absolute strain, but only the orientation and relative magnitude of the tensor strain field.

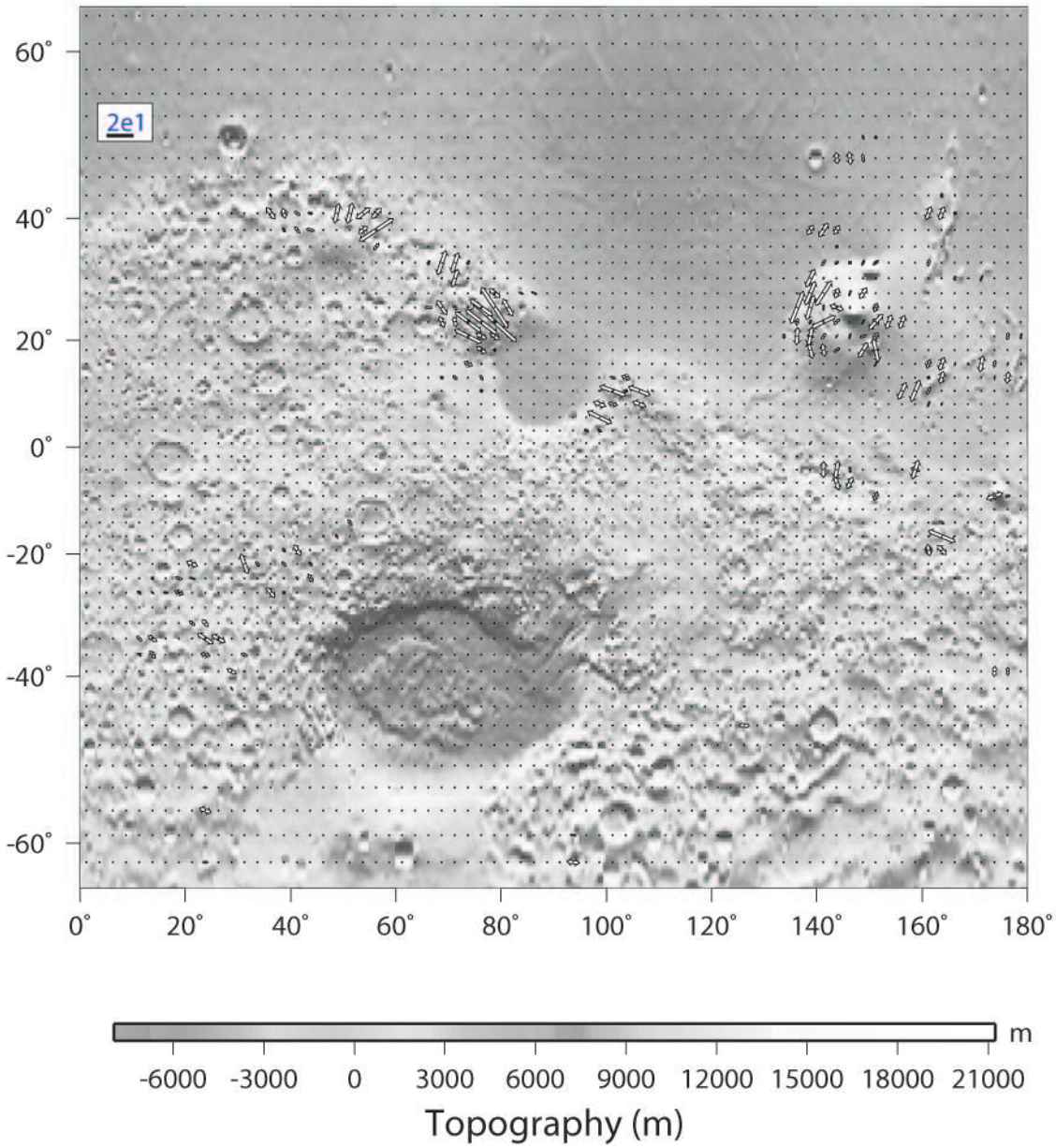

Figure 5: Deviatoric strain from Kostrov summation associated with the normal faults of *Knapmeyer et al.* (2006) in the eastern hemisphere of Mars. White arrows represent deviatoric extension. Note that we have assumed a uniform amount of slip for each fault as a first approximation. Consequently, the magnitude of the calculated strain does not reflect the real absolute strain, but only the orientation and relative magnitude of the tensor strain field.

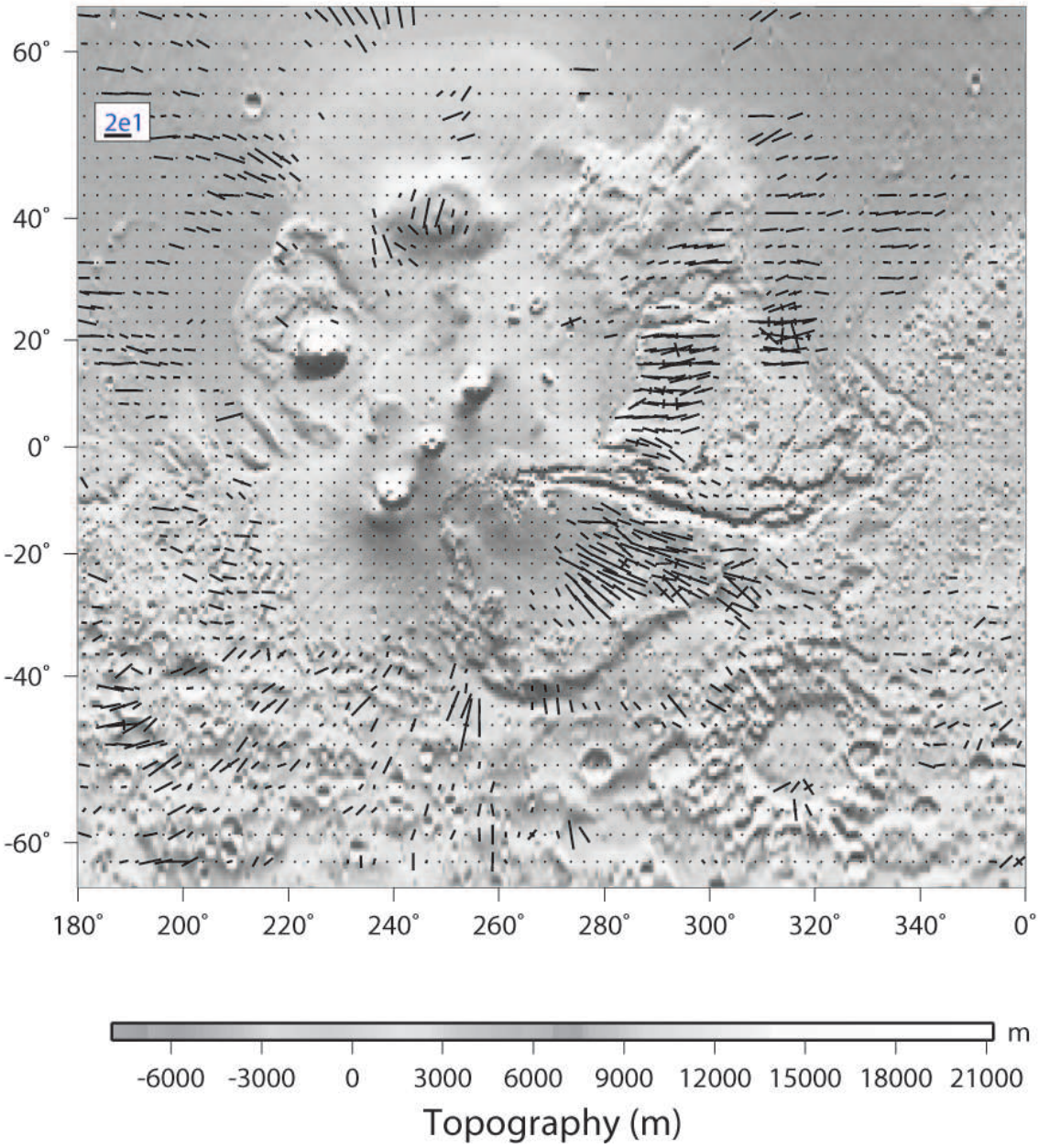

Figure 6: Deviatoric strain from Kostrov summation associated with the reverse faults of *Knapmeyer et al.* (2006) in the western hemisphere of Mars. Black filled-in arrows represent deviatoric compression. Note that we have assumed a uniform amount of slip for each fault as a first approximation. Consequently, the magnitude of the calculated strain does not reflect the real absolute strain, but only the orientation and relative magnitude of the tensor strain field.

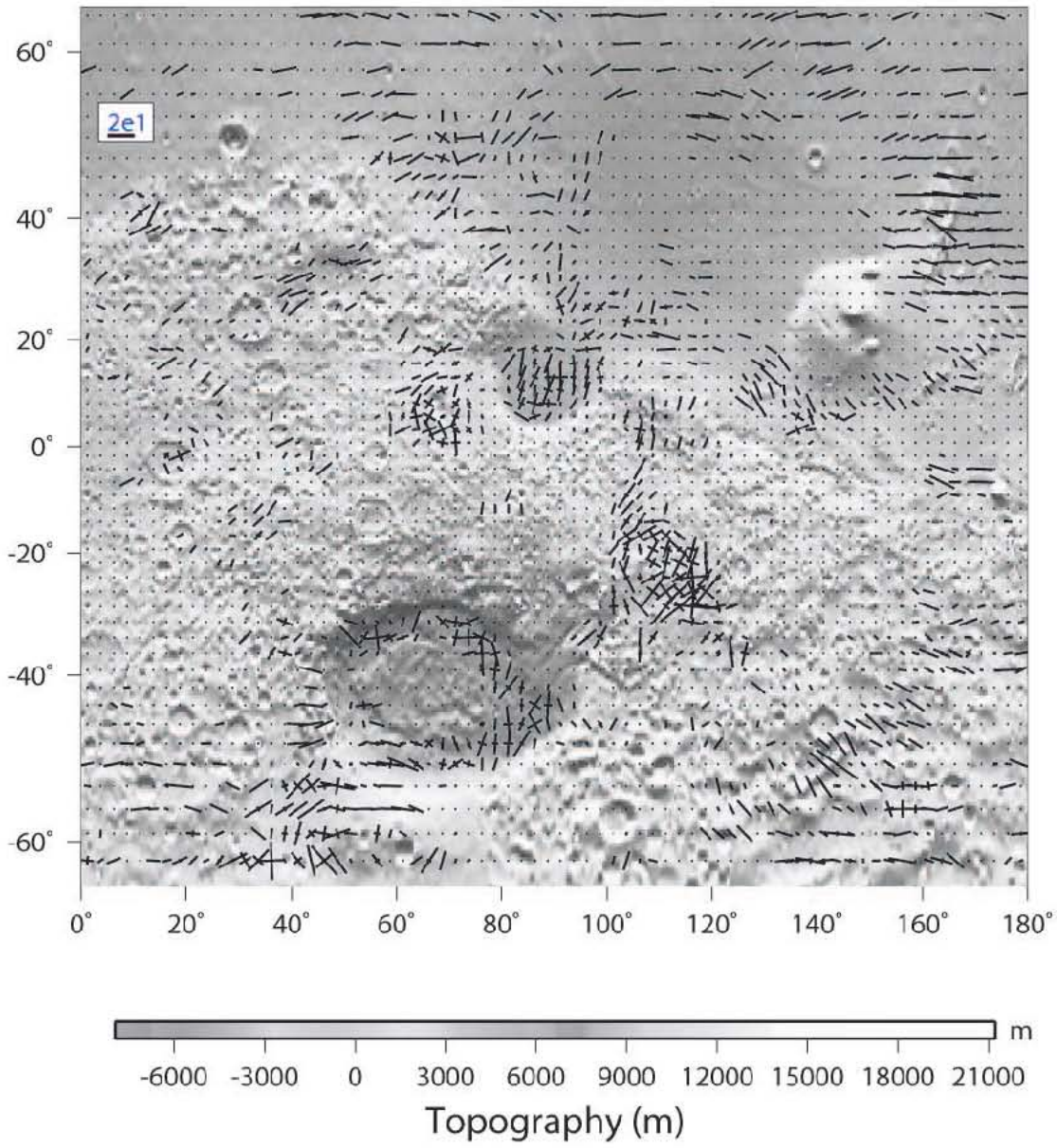

Figure 7: Deviatoric strain from Kostrov summation associated with the reverse faults of *Knapmeyer et al.* (2006) in the eastern hemisphere of Mars. Black filled-in arrows represent deviatoric compression. Note that we have assumed a uniform amount of slip for each fault as a first approximation. Consequently, the magnitude of the calculated strain does not reflect the real absolute strain, but only the orientation and relative magnitude of the tensor strain field.

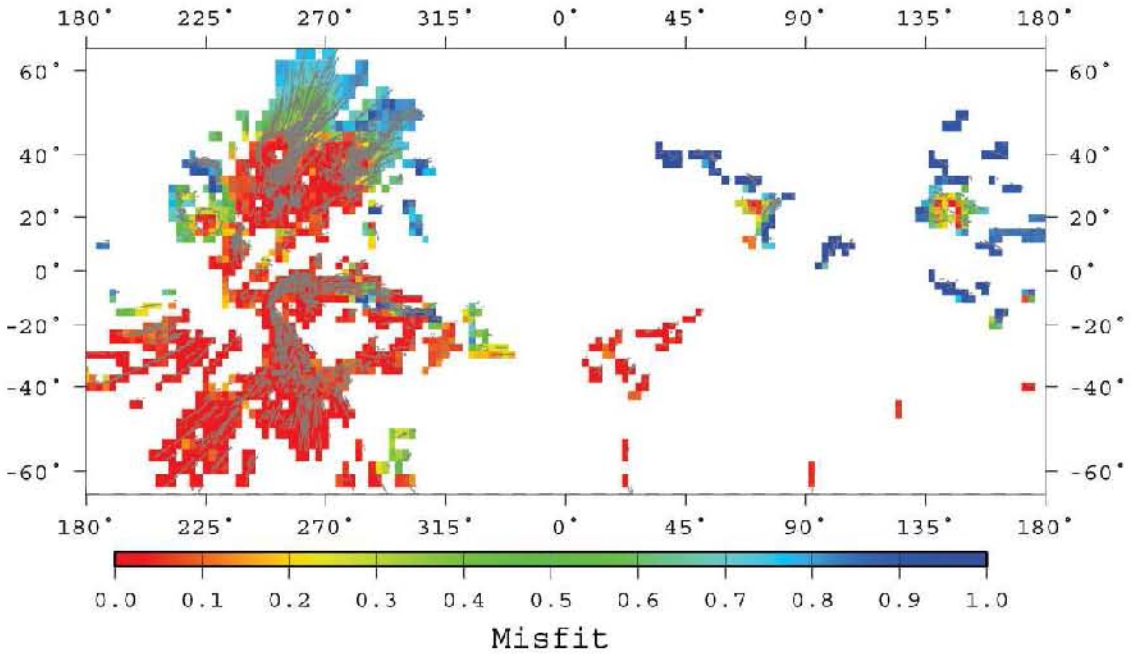

Figure 8: The misfit between the strain associated with the normal faults and the GPE associated stresses. Red means a very good fit, while green and blue mean poor fit.

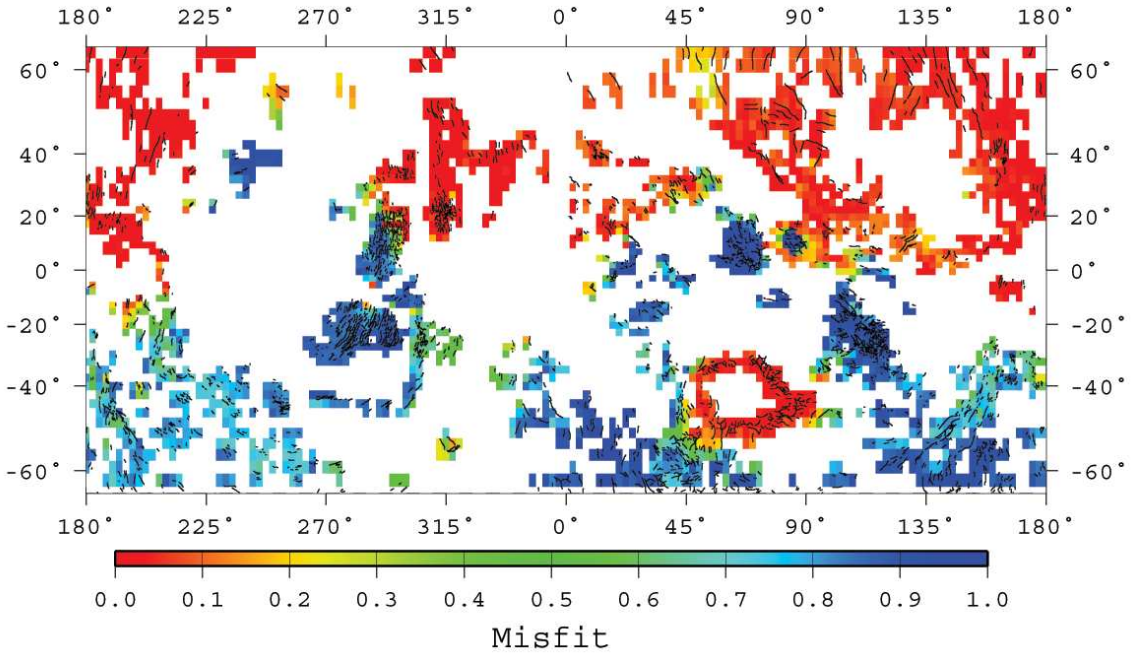

Figure 9: The misfit between the strain associated with the reverse faults and the GPE associated stresses. Red means a very good fit, while green and blue mean poor fit.

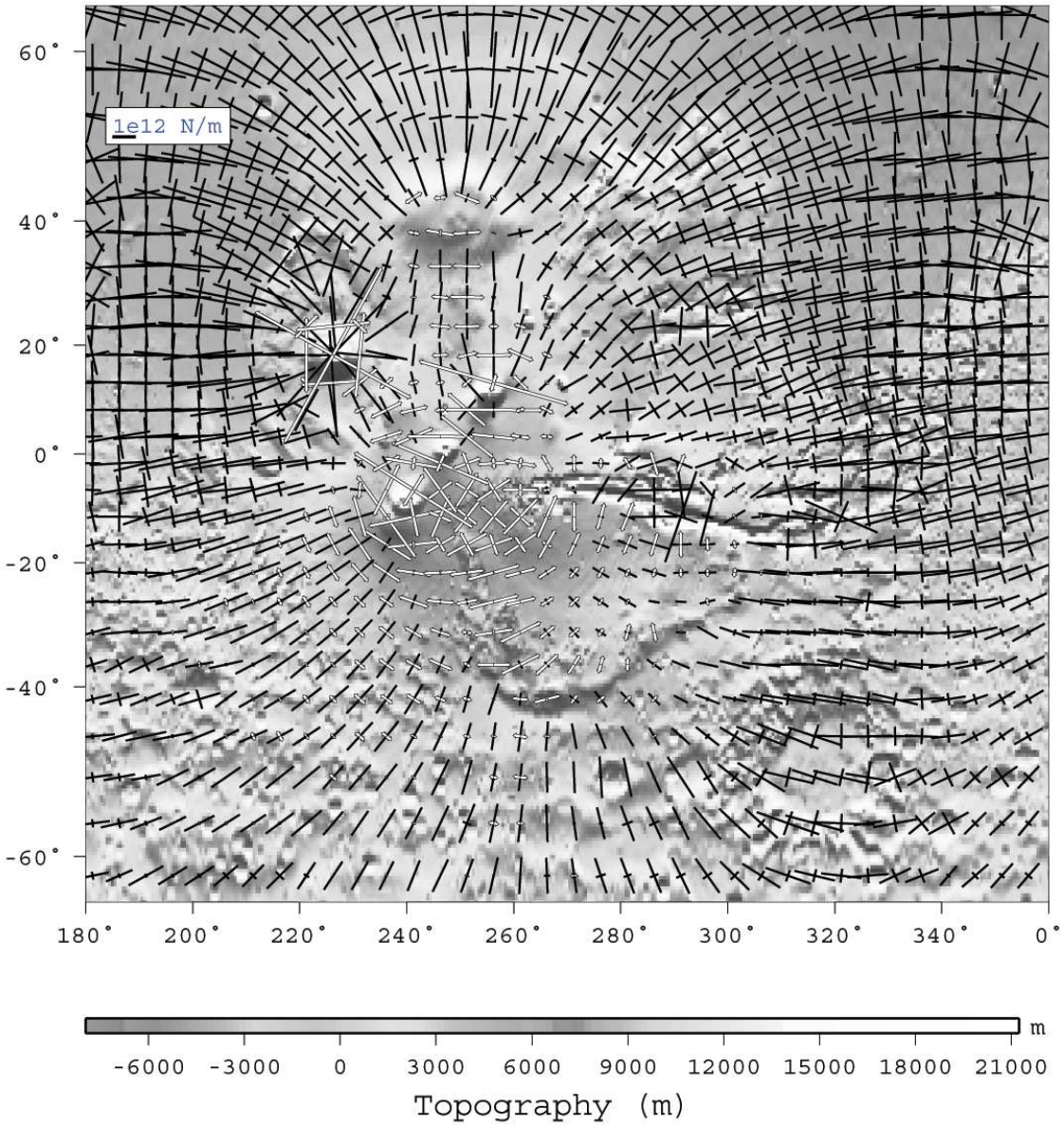

Figure 10: The combined vertically integrated GPE and uniform global contraction stresses for the inversion to the reverse faults in the western hemisphere of Mars. White arrows represent deviatoric extension, while black filled-in arrows represent deviatoric compression.

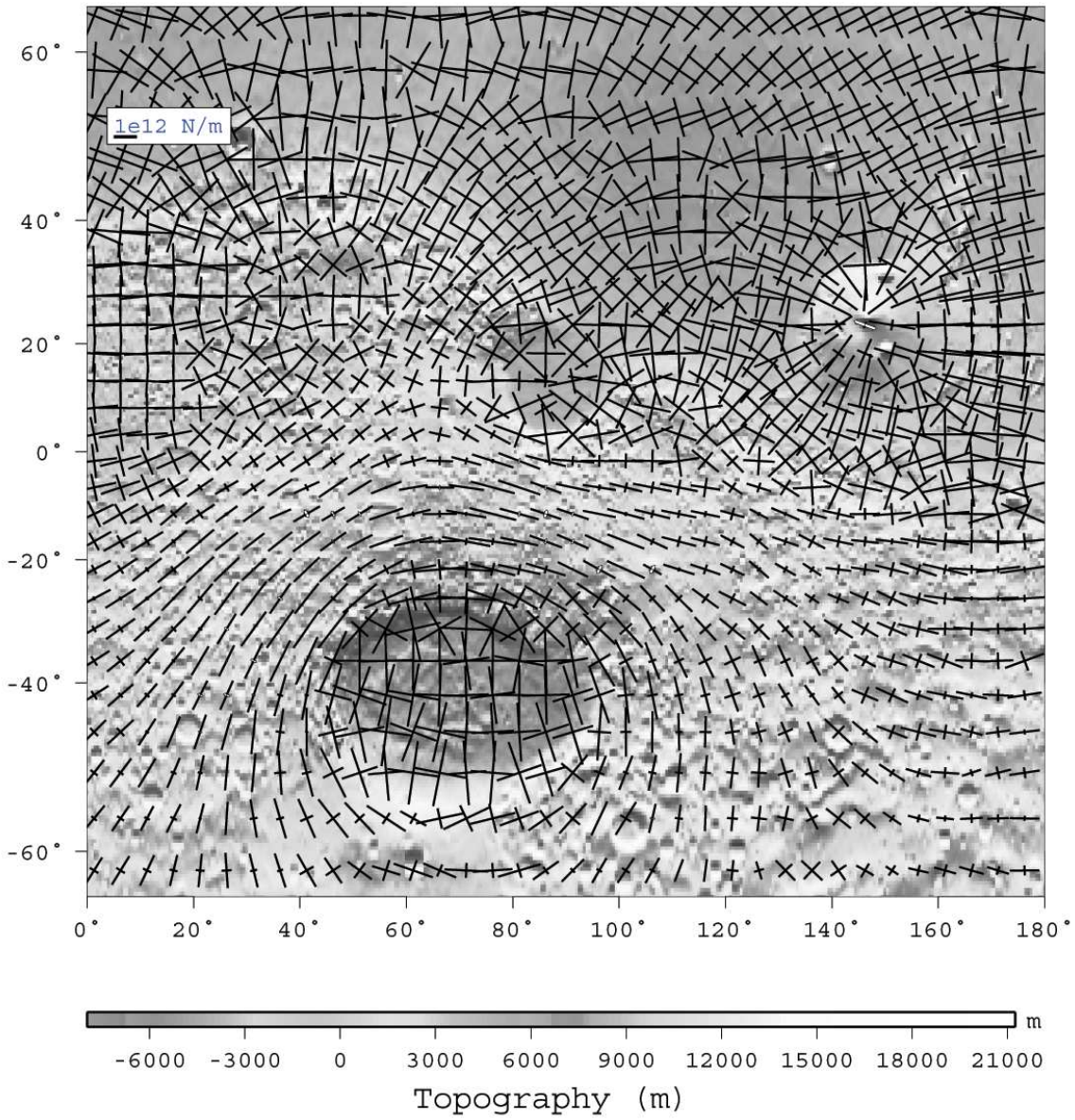

Figure 11: The combined vertically integrated GPE and uniform global contraction stresses for the inversion to the reverse faults in the eastern hemisphere of Mars. White arrows represent deviatoric extension, while black filled-in arrows represent deviatoric compression.

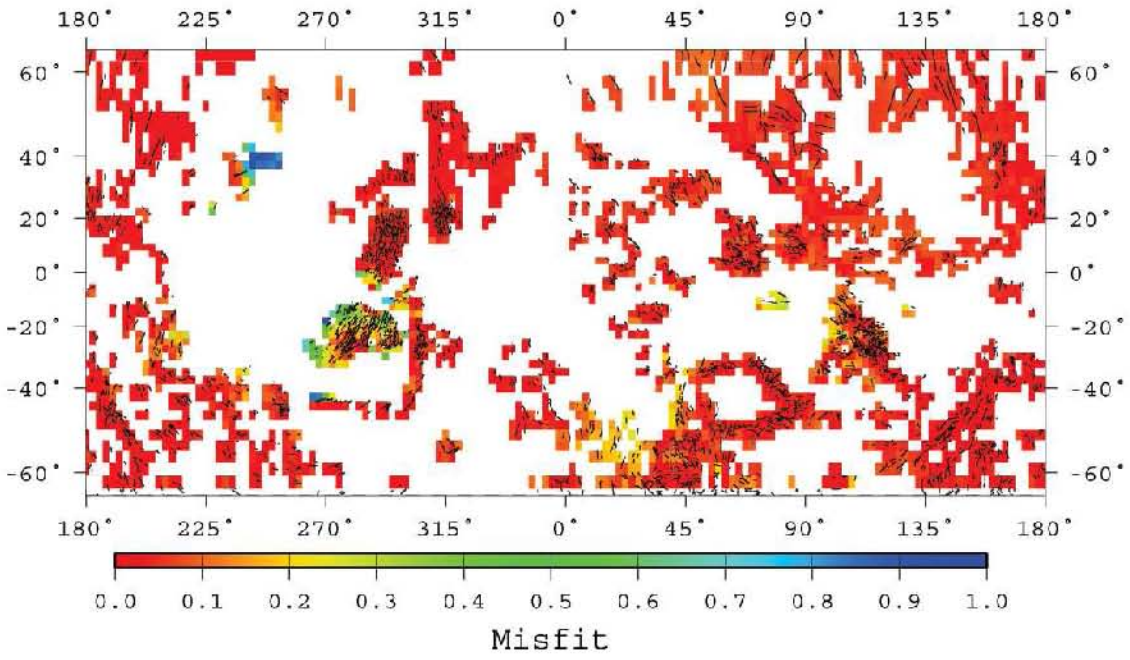

Figure 12: The misfit of the stress field from Figures 10 and 11 to the reverse faults. The reverse faults are shown in black.

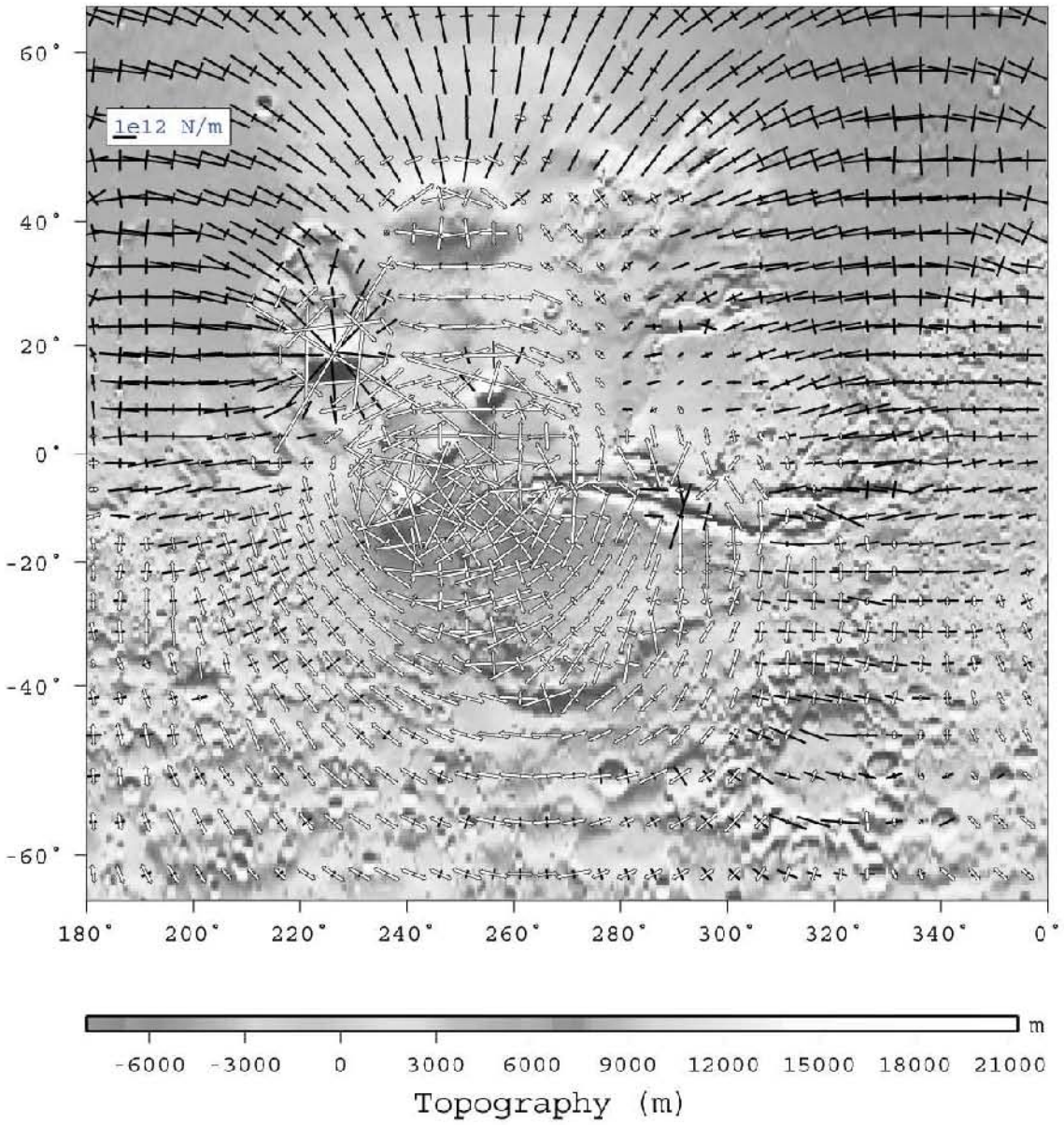

Figure 13: The combined vertically integrated GPE and uniform global contraction stresses for the inversion to both the normal and reverse faults in the western hemisphere of Mars. White arrows represent deviatoric extension, while black filled-in arrows represent deviatoric compression.

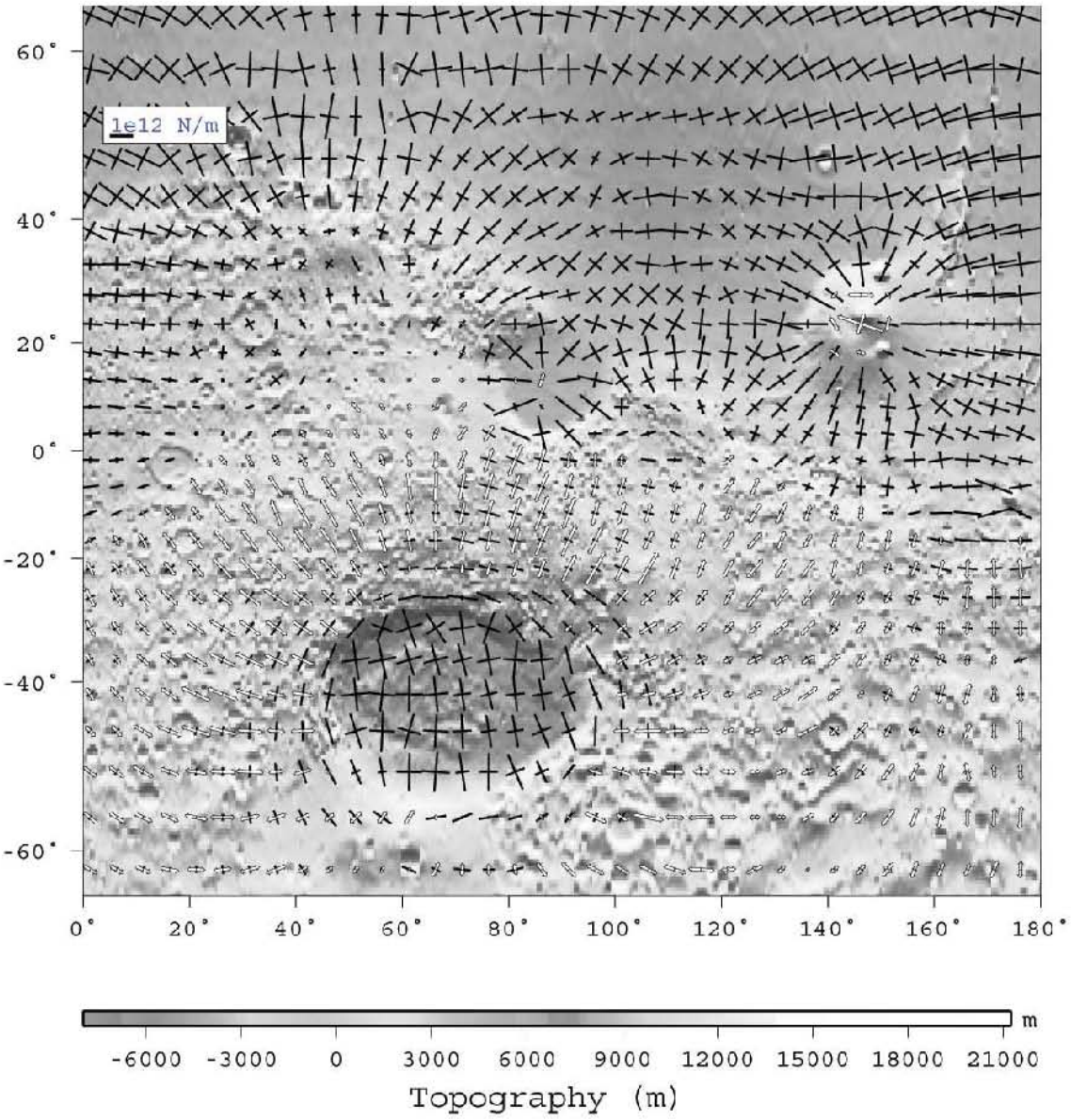

Figure 14: The combined vertically integrated GPE and uniform global contraction stresses for the inversion to both the normal and reverse faults in the eastern hemisphere of Mars. White arrows represent deviatoric extension, while black filled-in arrows represent deviatoric compression.

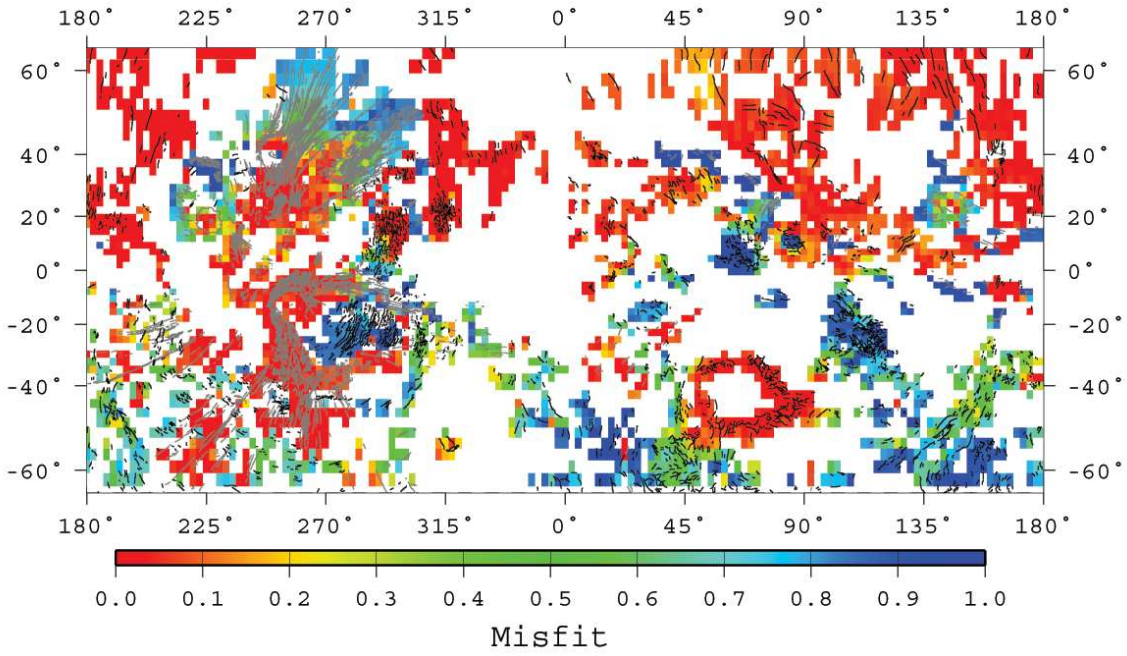

Figure 15: The misfit of the stress field from Figures 13 and 14 to both the normal and reverse faults. The reverse faults are shown in black, while the normal faults are shown in gray.

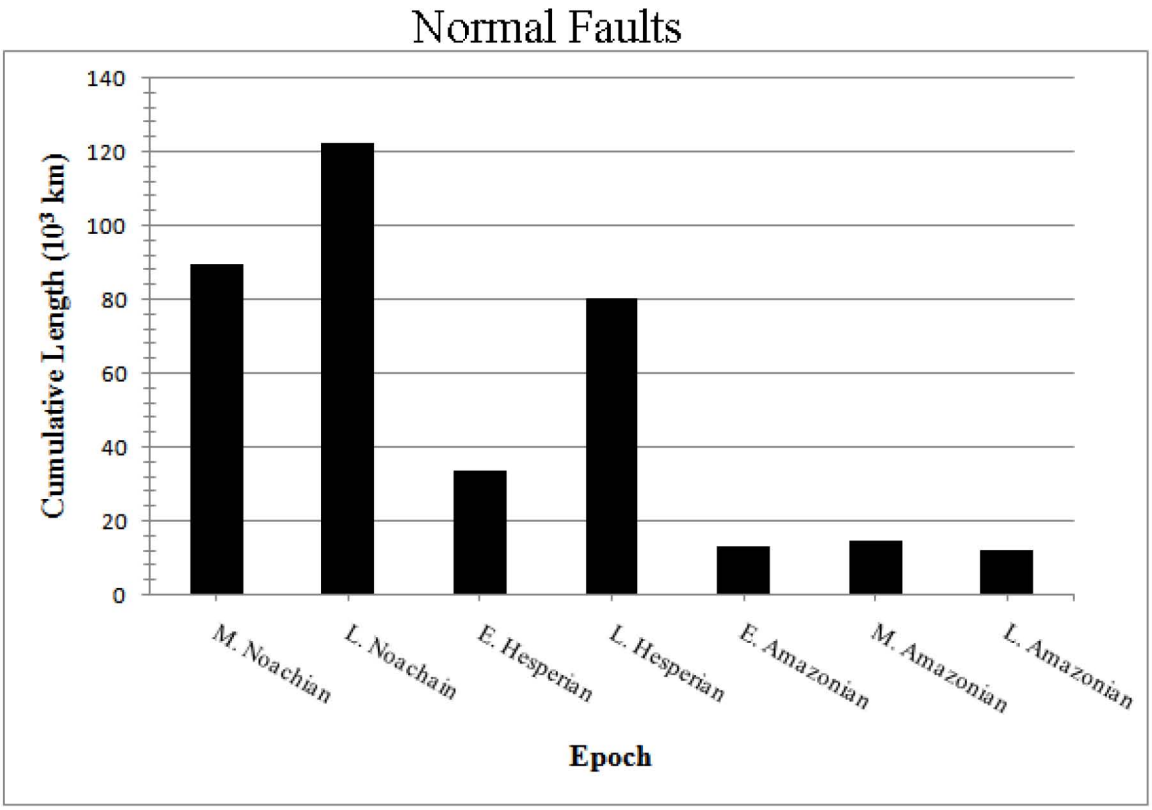

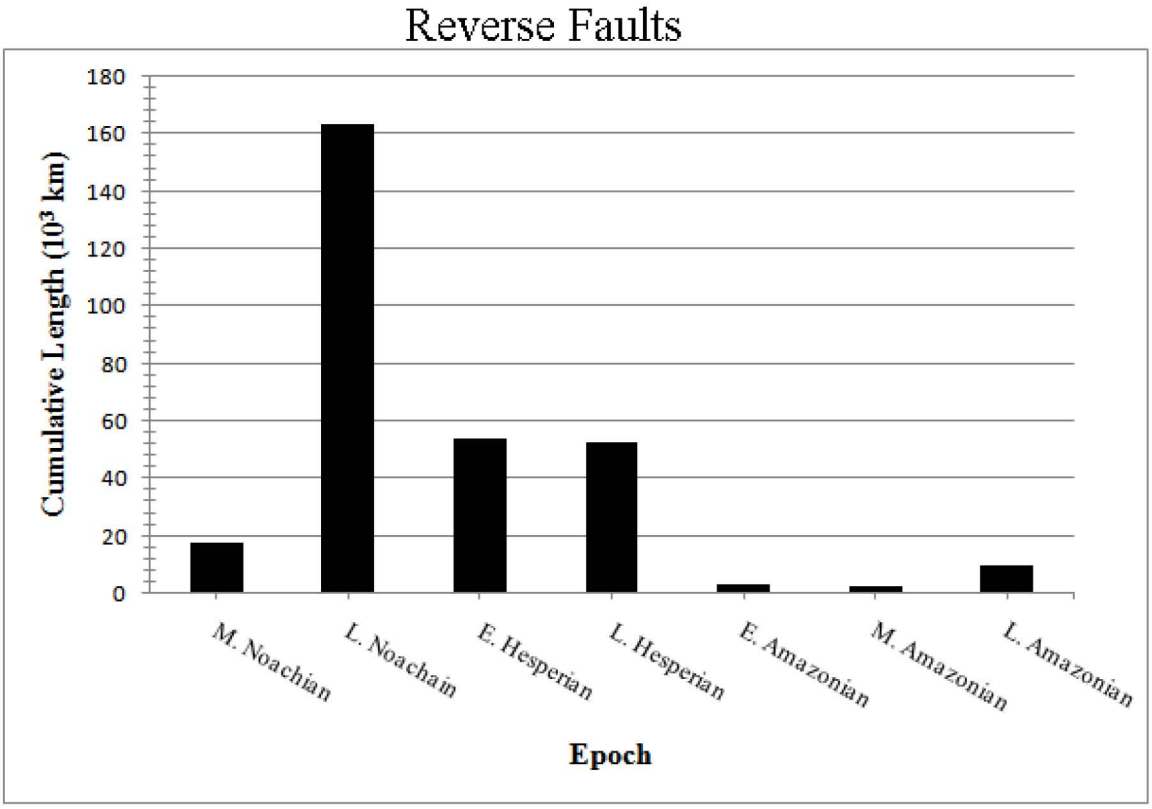

Figure 16: Histogram of the cumulative length of the surface faults as a function of their assigned age. Note that this age is based on the age of the deformed units containing the faults.

Bibliography

Anderson, R. C., J. M. Dohm, A. F. C. Haldemann, E. Pounders, and M. P. Golombek, Tectonic evolution of Mars, in *37th Annual Lunar and Planetary Science Conference*, vol. 37, p. 1883, 2006.

Anderson, R. C., J. M. Dohm, A. F. C. Haldermann, E. Pounders, M. Golombek, and A. Castano, Centers of tectonic activity in the eastern hemisphere of Mars, *Icarus*, *195*(2), 537–546, 2008, Anderson, R. C. Dohm, J. M. Haldermann, A. F. C. Pounders, E. Golombek, M. Castano, A.

Banerdt, W. B., and M. P. Golombek, The evolution of Tharsis: Implications of gravity, topography, and tectonics, in *Lunar and Planetary Institute Conference Abstracts*, vol. 21, p. 42, 1990.

Banerdt, W. B., and M. P. Golombek, Tectonics of the Tharsis region of Mars: Insights from MGS topography and gravity, in *Lunar and Planetary Institute Conference Abstracts*, vol. 31, p. 2038, 2000.

Banerdt, W. B., M. P. Golombek, and K. L. Tanaka, Stress and tectonics on Mars, in *Mars*, pp. 249–297, 1992, n/a 1, 1992.

Carr, M. H., Tectonism and volcanism of Tharsis region of Mars, *Journal of Geophysical Research*, *79*(26), 3943–3949, 1974.

Carr, M. H., *The surface of Mars*, Yale University Press, New Haven, 1981.

Chicarro, A. F., P. H. Schultz, and P. Masson, Global and regional ridge patterns on Mars, *Icarus*, *63*, 153–174, 1985, DOI: 10.1016/0019-1035(85)90025-9.

Dimitrova, L. L., W. E. Holt, A. J. Haines, and R. A. Schultz, Toward understanding the history and mechanisms of martian faulting: The contribution of gravitational potential energy, *Geophysical Research Letters*, *33*, 08202, 2006, DOI: 10.1029/2005GL025307.

England, P., and D. McKenzie, A thin vsicous sheet model for continental deformation, *Geophysical Journal of the Royal Astronomical Society*, *70*(2), 295–321, 1982.

Flesch, L. M., A. J. Haines, and W. E. Holt, Dynamics of the India-Eurasia collision zone, *Journal of Geophysical Research*, *106*, 16435–16460, 2001, DOI: 10.1029/2001JB000208.

Flesch, L. M., W. E. Holt, A. J. Haines, L. Wen, and B. Shen-Tu, The dynamics of Western North America: stress magnitudes and the relative role of gravitational potential energy, plate interaction at the boundary and basal tractions, *Geophysical Journal International*, *169*, 866–896, 2007, DOI: 10.1111/j.1365-246X.2007.03274.x.

Ghosh, A., W. E. Holt, L. Wen, A. J. Haines, and L. M. Flesch, Joint modeling of lithosphere and mantle dynamics elucidating lithosphere-mantle coupling, *Geophysical Research Letters*, *35*, 16309, 2008, DOI: 10.1029/2008GL034365.

Golombek, M. P., J. B. Plescia, and B. J. Franklin, Faulting and folding in the formation of planetary wrinkle ridges, *Proceedings of Lunar and Planetary Science*, *21*, 679–693, 1991.

Greeley, R., and J. E. Guest, Geologic map of the western equatorial region of Mars, 1987.

Hartmann, W. K., and G. Neukum, Cratering chronology and the evolution of Mars, *Space Science Reviews*, *96*(1-4), 165–194, 2001.

Hauck, I., S. A., S. C. Solomon, and R. J. Phillips, Potential sources of Hesperian contractional tectonics on Mars, in *Lunar and Planetary Institute Conference Abstracts*, vol. 34, p. 1667, 2003.

Holt, W. E., and A. J. Haines, The kinematics of northern South Island, New Zealand,

determined from geologic strain rates, *Journal of Geophysical Research-Solid Earth*, *100*(B9), 17991–18010, 1995.

Knapmeyer, M., J. Oberst, E. Hauber, M. Whlisch, C. Deuchler, and R. Wagner, Working models for spatial distribution and level of Mars' seismicity, *Journal of Geophysical Research (Planets)*, *111*, 11006, 2006, DOI: 10.1029/2006JE002708.

Kostrov, V. V., Seismic moment and energy of earthquares, and seismic flow of rock, *Izv.., Earth Physics*, *1*, 23–40, 1974.

Mangold, N., P. Allemand, P. G. Thomas, and G. Vidal, Chronology of compressional deformation on Mars: evidence for a single and global origin, *Planetary and Space Science*, *48*, 1201–1211, 2000.

Neumann, G. A., M. T. Zuber, M. A. Wieczorek, P. J. McGovern, F. G. Lemoine, and D. E. Smith, Crustal structure of Mars from gravity and topography, *Journal of Geophysical Research (Planets)*, *109*, 08002, 2004, DOI: 10.1029/2004JE002262.

Okubo, C. H., and R. A. Schultz, Variability in Early Amazonian Tharsis stress state based on wrinkle ridges and strike-slip faulting, *Journal of Structural Geology*, *28*, 2169–2181, 2006, DOI: 10.1016/j.jsg.2005.11.008.

Phillips, R. J., et al., Ancient geodynamics and global-scale hydrology on Mars, *Science*, *291*, 2587–2591, 2001, DOI: 10.1126/science.1058701.

Plescia, J. B., and R. S. Saunders, Tectonic history of the Tharsis region, Mars, *Journal of Geophysical Research*, *87*(NB12), 9775–9791, 1982.

Schubert, G., S. C. Solomon, D. L. Turcotte, M. J. Drake, and N. H. Sleep, Origin and thermal evolution of Mars, in *Mars*, pp. 147–183, 1992, n/a 1, 1992.

Schultz, R. A., Strike-slip faulting of ridged plains near Valles Marineris, Mars, *Nature*, *341*, 424–426, 1989, DOI: 10.1038/341424a0.

Schultz, R. A., Seismotectonics of the amenthes rupes thrust fault population, Mars, *Geophysical Research Letters*, *30*, 36–1, 2003, DOI: 10.1029/2002GL016475.

Scott, D. H., and K. L. Tanaka, Geologic map of the western equatorial region of Mars, 1986.

Searls, M. L., and R. J. Phillips, Tectonics of utopia basin, Mars: Results from finite element loading models, in *Lunar and Planetary Institute Conference Abstracts*, vol. 38, p. 1965, 2007.

Sleep, N. H., and R. J. Phillips, Gravity and lithospheric stress on the terrestrial planets with reference to the Tharsis region of Mars, *Journal of Geophysical Research*, *90*, 4469–4489, 1985, DOI: 10.1029/JB090iB06p04469.

Tanaka, K. L., and D. H. Scott, Geologic map of the polar regionss of Mars, 1987.

Tanaka, K. L., M. P. Golombek, and W. B. Banerdt, Reconciliation of stress and structural histories of the Tharsis region of Mars, *Journal of Geophysical Research-Planets*, *96*(E1), 15617–15633, 1991.

Tanaka, K. L., D. H. Scott, and R. Greeley, Global stratigraphy, in *Mars*, pp. 345–382, 1992, n/a 1, 1992.

Tanaka, K. L., J. A. Skinner, T. M. Hare, T. Joyal, and A. Wenker, Resurfacing history of the northern plains of Mars based on geologic mapping of Mars global surveyor data, *Journal of Geophysical Research-Planets*, *108*(E4), 2003.

Watters, T. R., Origin of periodically spaced wrinkle ridges on the Tharsis plateau of Mars, *Journal of Geophysical Research*, *96*, 15599, 1991, DOI: 10.1029/91JE01402.

Watters, T. R., Compressional tectonism on Mars, *Journal of Geophysical Research-Planets*, *98*(E9), 17049–17060, 1993.

Wise, D. U., M. P. Golombek, and G. E. McGill, Tharsis province of Mars - geologic sequence, geometry, and a deformation mechanism, *Icarus*, *38*, 456–472, 1979, A&AA ID. AAA025.097.039 DOI: 10.1016/0019-1035(79)90200-8.

Zuber, M. T., et al., Internal structure and early thermal evolution of Mars from Mars Global Surveyor topography and gravity, *Science*, *287*, 1788–1793, 2000, DOI: 10.1126/science.287.5459.1788.

Chapter 4

Evidence for Material Removal and/or Subsidence of the Martian Lithosphere from a Global Datset of Surface Faults and Dynamic Lithospheric Stress Models

Evidence for Material Removal and/or Subsidence of the Martian Lithosphere from a Global Datset of Surface Faults and Dynamic Lithospheric Stress Models

Lada L. Dimitrova, William E. Holt, and Richard A. Schultz

(to be submitted to *Journal of Geophysical Reseach – Planets*)

Abstract

Recent mapping of the surface of Mars has lead to the creation of expanded global data sets of normal and reverse surface faults. The normal faults are located predominantly in the Tharsis region and may not be the best indicator for global processes elsewhere. The reverse fault are much more uniformly distributed and provide better constraints; in particular, reverse faults in high topography areas are ill-fitted by a global solution of depth-integrated deviatoric stress associated with horizontal gradients in gravity potential energy per unit area (GPE).

The lithospheric stress models assume that (1) present-day topography is the paleotopography, (2) present-day crustal thickness is the paleo-crustal thickness, (3) uniform crustal and mantle densities. However, many of the tectonically generated structures formed early in the planet's history and consequently possibly formed under different conditions than we see today. Using an inverse method, I show that stresses associated with small perturbations to both GPE and membrane sources, when added to the GPE solution associated with present day topography and crustal structure, provide an improved fit to many of the faults. The inverse models show that small lateral variations $(1-6\%)$ in crust and mantle density in conjunction with small vertical displacement, $O(100m)$, provide sufficient additional GPE and membrane stress to fit the majority of the fault data. The density differences are only a few percent and are within the noise of the fit of the crustal model to the gravity field. These inverse models are consistent with lithosphere modification by erosion from running water since the time of faulting. The final depth integrated deviatoric stress magnitudes are Earth-like, and consequently the ratio of brittle-frictional layer thickness

to ductile layer thickness on Mars at the time of faulting may have been similar to what is found on Earth today within moderately actively deforming orogens.

4.1 Introduction

Geologic features reflect the dynamic forces shaping the surfaces, crust, lithosphere and deep interior of a planet. Identifying these features and how they are arranged relative to one another can allow the global history of a planet to be reconstructed. For Mars, through careful mapping from the Viking image data, geologic units and their relative age have long been studied (*Tanaka*, 1986; *Tanaka et al.*, 1992; *Scott and Tanaka*, 1986; *Tanaka and Scott*, 1987; *Greeley and Guest*, 1987; *Tanaka et al.*, 1992; *Banerdt et al.*, 1992) and continue to be of interest (*Tanaka et al.*, 2007, 2008). The resulting relative geologic history for Mars reflects the main themes of the Martian evolution and the relative importance of different processes through time (*Head et al.*, 2001).

Tectonic features on Mars are abundant. Brittle-frictional deformation is indicated by a variety of structural features – tensional (simple and complex grabens, rifts, tension cracks, troughs)(*Wise et al.*, 1979; *Frey*, 1979), compressional (wrinkle ridges, lobate scarps)(*Watters and Maxwell*, 1986; *Chicarro et al.*, 1985), and to a much smaller extent strike-slip (*Schultz*, 1989; *Mangold et al.*, 2000; *Tanaka et al.*, 2003; *Okubo and Schultz*, 2006). Theoretical models of deformation mechanisms can be compared to the surficial expression of the tectonic features observed today and interpreted in terms of major tectonic events, thus allowing us insights into the internal structure and processes on Mars.

The Tharsis province, due to its large scale and complex deformation has long been the focus of studies. Early models seemed to require more than one mechanism – a combination of lithospheric uplift, isostasy and flexure – to explain the region's evolution (*Banerdt et al.*, 1992, and references therein). More recently, *Banerdt and Golombek* (2000) proposed that the seeming need of multiple mechanisms was due to the quality of the data available prior to MGS. The model of *Banerdt and Golombek* (2000) is dominated by the flexural response due to a load centered on Tharsis. Consequently, the resulting stress field has radial compressive stresses throughout Tharsis. *Banerdt and Golombek* (2000) show

only the extensional component of the strains, which is consistent with normal faulting on pre-existing faults radial to Tharsis and away from the load, for example, Memnonia, Sirenum, Thaumasia, southern Claritas, and Tempe Fossae. However, the faulting extending from northern Claritas Fossae north to Tantalus and Alba Fossae is not well explained by a flexure-dominated model, which predicts zero extension in these areas. Therefore, as pointed out by *Banerdt and Golombek* (2000), these faults may have formed under different conditions (topography and gravity) than we see today. Recent mappings (*Anderson et al.*, 2001, 2006; *Knapmeyer et al.*, 2006; *Anderson et al.*, 2008) have resulted in even more extensional features in this area than in the *Scott and Tanaka* (1986) data. However, it has been argued, e.g. *Phillips et al.* (2001), *Head et al.* (2001), and *Golombek and Phillips* (2009) that the faulting is explained by membrane and flexure alone.

An alternative model (*Dimitrova et al.*, 2006), based on stresses associated with gravitational potential energy (GPE) differences, has been shown to fit ($\sim 70\%$) faults in Tharsis, as mapped by *Anderson et al.* (2001), with the majority of the misfit restricted to the region north and northeast of Alba Patera. The GPE differences are double integrals of the density with depth derived from the topography of *Zuber et al.* (2000) and the crustal thickness model of *Neumann et al.* (2004). Benchmarking by *Ghosh et al.* (2008) shows that the thinshell method used can recover the depth integrated deviatoric stresses within the lithosphere of Earth, even in the presence of significant dynamic topography. The excellent fit of the GPE stress model of *Dimitrova et al.* (2006) to the normal fault data from *Anderson et al.* (2001) implies that possibly the normal faults in and around Tharsis formed early in the Martian history when elastic thicknesses, as well as membrane and flexural stresses, were small, and viscous rather than elastic processes dominated. Alternatively, the combined stress from other sources (e.g. flexure, global contraction, etc.), which may have dominated the GPE stresses, must have a stress field style – orientation and relative magnitude of principal axes of the deviatoric stress field – that is similar to the stresses associated with GPE differences.

The studies of *Banerdt and Golombek* (2000) and *Dimitrova et al.* (2006) were biased towards the normal faults in the Tharsis province, in part due to the available datasets. Continued mapping has lead to the creation of expanded fault data sets (*Anderson et al.*,

2001, 2006; *Knapmeyer et al.*, 2006; *Anderson et al.*, 2008). In these data, the majority of the normal faults mapped to date are clustered in the western hemisphere around Tharsis, and hence, may provide a poor constraint on processes elsewhere. On the other hand, the reverse faults are much more uniformly distributed. Consequently, a reevaluation of these stress models outside of Tharsis is needed.

Watters (2003) argue that the normal faulting associated with the dichotomy boundary in the eastern hemisphere, may be in response to bending stresses, but the formation of the thrust faulting in the lowlands requires additonal stresses from erosion or global contraction. *Searls and Phillips* (2007) studied normal and reverse faulting in Utopia and show that stresses resulting from the deflection of the lithosphere under the weight of the material infilling the basin and also from self-deformation of the fill material itself are insufficient to explain the fault patterns. *Andrews-Hanna and Zuber* (2007) show that the flexure dominated model cannot fit recently mapped strike-slip faults on the flanks of Tharsis.

In Chapter 3, we reevaluated the fit of the GPE model to the global fault dataset of *Knapmeyer et al.* (2006). Almost all normal faults are located in Tharsis, and consequently, as in *Dimitrova et al.* (2006), the fit of the GPE model to them is very high. The GPE associated stresses tend to be deviatorically extensional in areas of high topography, and deviatorically compressional in areas of low topography. Consequently, the GPE stress model fits the reverse faults in the northern hemisphere very well, but misfits those in the southern hemisphere with the exception of the reverse faults in Hellas. In Chapter 3, we also evaluated if global contraction can be used to explain the misfitted southern hemisphere faults, and find that although a small stress, and associated radius curvature ($\sim 0.08-0.16km$) and temperature change ($5-10^{\circ}K$), can explain the reverse faulting alone, the timing and the formation of the normal faulting then becomes a problem, suggesting that global contraction may not be a signifficant contributing factor for the formation of the reverse faults on Mars.

The GPE model assumes (1) that present-day topography is the paleotopography, (2) that present-day crustal thickness is the paleo-crustal thickness, and (3) uniform crustal and mantle densities. In this paper we consider if small perturbations in GPE or membrane stresses, when added to the depth integrated deviatoric stresses associated with present

day GPE differences, might explain the misfit to the faults. Perturbations in the GPE and membrane-related stresses, which optimize the fit to the fault data, can be due to either modifications of the lithosphere since the time of faulting and/or deviations from the assumptions of laterally constant densities. Physical processes that modify the lithosphere such as dynamic topography present at the time of Tharsis formation and/or faulting, volcanic construction, giant impacts, erosion, etc., lead to both a membrane displacement and a GPE change. We estimate the minimum necessary modification of the lithosphere and lateral variation in lithospheric densities for several scenarios for the timing of the normal and reverse faulting.

4.2 Methodology

We perform inversions for stresses due to GPE variations and membrane displacements, which when added to the GPE stress model of *Dimitrova et al.* (2006), minimize the surface integral of a misfit function that quantifies the fit of the stress tensor field to the fault data. We use the strain associated with the faults as discussed in Chapter 3 (Fig 3, 4,5, 6, 3.4 on pages 48, 49,50, 51, 3.4).

First, we use the forward thin-sheet model (*Flesch et al.*, 2001, also Chapter 3) to calculate the Green's function responses to forcing terms of spherical harmonics degree and order 17. We take the thin sheet approach, which minimizes a functional J in order to solve the depth-integrated 3-D force balance equations. This functional can be written in spherical coordinates as

$$J = \int\int \left\{ \left[\begin{pmatrix} \overline{\tau}_{\phi\phi} \\ \overline{\tau}_{\theta\theta} \\ \overline{\tau}_{\phi\theta} \end{pmatrix} - \begin{pmatrix} \Phi_{\phi\phi}^{obs} \\ \Phi_{\theta\theta}^{obs} \\ \Phi_{\phi\theta}^{obs} \end{pmatrix} \right]^T V^{-1} \left[\begin{pmatrix} \overline{\tau}_{\phi\phi} \\ \overline{\tau}_{\theta\theta} \\ \overline{\tau}_{\phi\theta} \end{pmatrix} - \begin{pmatrix} \Phi_{\phi\phi}^{obs} \\ \Phi_{\theta\theta}^{obs} \\ \Phi_{\phi\theta}^{obs} \end{pmatrix} \right] \right\} \cos\theta d\phi d\theta \tag{1}$$

where θ, ϕ are longitude and co-latitude respectively, $\overline{\tau}_{ij}$ are the depth integrated deviatoric

stresses that balance the effective body force distribution, V^{-1} is given by

$$V^{-1} = \begin{pmatrix} \frac{1}{1-\nu} & \frac{\nu}{1-\nu} & 0 \\ \frac{\nu}{1-\nu} & \frac{1}{1-\nu} & 0 \\ 0 & 0 & 2 \end{pmatrix}, \tag{2}$$

where ν is Poisson's ratio. To construct the basis functions, we set the potentials, Φ, to be components of spherical harmonics

$$\Phi^{obs}_{\theta\theta} = \Phi^{obs}_{\phi\phi} = \begin{cases} P_{lm}(\cos\theta)\cos m\phi \\ P_{lm}(\cos\theta)\sin m\phi \end{cases}, \quad \Phi^{obs}_{\phi\theta} = 0. \tag{3}$$

The potentials, Φ, in 1 represent horizontal integrals of the effective body forces, which for GPE are

$$\Phi^{obs}_{\theta\theta} = \Phi^{obs}_{\phi\phi} = -\frac{1}{3}\overline{\sigma}_{zz}, \Phi^{obs}_{\theta\phi} = 0, \tag{4}$$

and for membrane response are

$$\Phi^{obs}_{\theta\theta} = \Phi^{obs}_{\phi\phi} = -\frac{2\mu}{r}u_r, \Phi^{obs}_{\theta\phi} = 0, \tag{5}$$

where μ is the shear modulus or shear viscosity.

We minimize the J functional for each component of spherical harmonics up to degree and order 17 to define the global deviatoric stress field solution responses. These stress fields are the GPE basis functions. For each degree and order, the membrane basis function is the sum of the corresponding GPE basis function and an additional stress, $\tilde{\tau}_{ij}$, given by

$$\tilde{\tau}_{\theta\theta} = \tilde{\tau}_{\phi\phi} = -\frac{2\mu}{r}u_r, \tilde{\tau}_{\theta\phi} = 0. \tag{6}$$

The GPE and membrane Green's functions are not completely uncorrelated: a positive vertical uplift leads to a positive GPE signal with a similar, but not identical stress field response.

We invert for the coefficients (A_{lm} and B_{lm} for the $P_{lm}(\cos\theta)\cos m\phi$ and $P_{lm}(\cos\theta)\sin m\phi$

terms respectively) for these Green's functions responses such that the resultant stress field, when added to the GPE stress field, minimizes the surface integral of a misfit measure. We modify the misfit measure M_{full} of *Dimitrova et al.* (2006) as follows

$$M_{inv} = T * M_{full} = \frac{1}{2}\left(T - \frac{\varepsilon \cdot \tau}{E}\right), \tag{7}$$

where the metrics E and T and the inner product are defined in terms of the fault strain ε_{ij} and the model stress τ_{ij} as:

$$E = \sqrt{\varepsilon_{ij}\varepsilon_{ij}}, T = \sqrt{\tau_{ij}\tau_{ij}}, \varepsilon \cdot \tau = \varepsilon_{ij} \cdot \tau_{ij} \tag{8}$$

Like M_{full}, M_{inv} is minimized when the tensor solution of stress from the model stress is consistent with the formation of faults with the same strike and style as the fault data; thus, it accounts for fault strike and fault style, defined by the relative magnitudes of the principal axis of the stress tensor. Likewise, M_{inv} is insensitive to the strain magnitudes derived from faulting due to the normalization of the $\varepsilon \cdot \tau$ term by E; however, it is not insensitive to the magnitude of the model stress, i.e., one way M_{inv} can be minimized is by having zero model stress. We use M_{inv} rather than M_{full} for numerical stability. The inversion for the coefficients A_{lm} and B_{lm} that minimize 7 is performed using a conjugate gradient method (*Press et al.*, 1992, powell subroutine)

We sum the spherical harmonics weighted by these coefficients to calculate the corresponding membrane displacements, δu_r, or GPE changes, δGPE. The perturbations to the vertically integrated vertical stress (δGPE) is given by

$$\delta GPE(\phi, \theta) = -3 \sum_l \sum_m P_{lm}(\cos\theta) \left[A_{lm} \cos m\phi + B_{lm} \sin m\phi\right], \tag{9}$$

and the vertical displacement is given by

$$\delta u_r(\phi, \theta) = -\frac{r}{2\mu} \sum_l \sum_m P_{lm}(\cos\theta) \left[A_{lm} \cos m\phi + B_{lm} \sin m\phi\right]. \tag{10}$$

Recall that the base GPE solution is derived from present-day topography and crustal

thickness, assuming laterally constant densities for the crust and mantle. Perturbations in the GPE and membrane related stresses, which optimize the fit to the fault data, can be due to either modifications of the lithosphere since the time of faulting and/or deviations from the assumptions of laterally constant densities. Physical processes that modify the lithosphere such as dynamic topography present at the time of Tharsis formation and/or faulting, volcanic construction, giant impacts, erosion, etc., lead to both a membrane displacement and a GPE change. For the solved for membrane displacement, δu_r, the associated GPE change is given by

$$GPE_{\delta u_r} = \rho_{crust} * g * h_{crust} * \delta u_r + \rho_{mantle} * g * \left(L_0 + h_{topography} - h_{crust}\right) * \delta u_r, \qquad (11)$$

where $\rho_{crust} = 2900 kg.m^{-3}$ and $\rho_{mantle} = 3500 kg.m^{-3}$ are the crust and mantle densities, $g = 3.7 m.s^{-2}$ is Mars gravity, h_{crust} is the crustal thickness, $h_{topopgraphy}$ is the surface topography, and $L_0 \simeq 92.84 km$ is the reference level (maximum depth of integration) from the GPE model.

Errors in the crustal thickness model, e.g., from the assumptions of uniform lateral crust and mantle densities, lead only to a GPE change. The GPE signal from the inversion that is not accounted for by the GPE change associated with the membrane displacement, $\delta\delta GPE = \delta GPE - GPE_{\delta u_r}$, reflects possible errors in the crustal model due to assumptions of laterally uniform mantle and crustal densities and small variations in mohography that may not be uniquely reflected in the gravity data. Thus, we will interpret the $\delta\delta GPE$ signal as end-member cases for lateral variations in crustal density alone ($\delta\rho_{crust}$), mantle density alone ($\delta\rho_{mantle}$), and both crustal and mantle density with the constraint from the moment of inertia that the crust-mantle density difference should be $600 kg.m^{-3}$ ($\delta\rho$).

For the end-member case for crust density variations alone we solve

$$\delta\delta GPE = \delta\rho_{crust} * g * h_{crust} * \left(L_0 + h_{topography} - \frac{1}{2} h_{crust}\right) \text{ for } \delta\rho_{crust}. \qquad (12)$$

for the end-member case for mantle density variations alone we solve

$$\delta\delta GPE = \frac{1}{2}\delta\rho_{mantle} * g * \left(L_0 + h_{topography} - h_{crust}\right)^2 \text{ for } \delta\rho_{mantle}. \quad (13)$$

Finally, for the end-member case for mantle density variations with crustal-mantle difference at $600 kg.m^{-3}$ we solve

$$\delta\delta GPE = \delta\rho * g * h_{crust} * \left(L_0 + h_{topography} - \frac{1}{2}h_{crust}\right) + \frac{1}{2}\delta\rho * g * \left(L_0 + h_{topography} - h_{crust}\right)^2 \quad (14)$$

for $\delta\rho$, the perturbations to both the crust and mantle density.

4.3 Results

We performed inversions, minimizing the surface integral of the misfit M_{inv}, for additional stresses due to GPE variations and/or membrane displacements. We examine separately the fit to the normal and reverse faults. Due to the complementary nature of the areas containing each type of fault, we also consider a combined dataset where we include areas with either normal or reverse faulting but not both, i.e. we exclude the 3% of areas with both normal and reverse faulting. For each of these strain fields, we performed inversions minimizing the surface integral of the misfit for additional stresses due to GPE variations only or membrane displacements only or both GPE and membrane, based on Greens basis function responses to forcing terms of spherical harmonics degree and order 17. The resulting surface integral of the residual misfit for each degree and order (up to 9) per number of coefficients solved for, is shown in Figure 1.

The fit to the normal faults is better than the fit to the reverse faults. This is due to the fact that the background GPE model fits the majority of the normal faults, while the reverse faults in the southern highlands are misfitted. In all cases, there is a sharp improvement of the fit to the data up to degree 5; at degree 9 almost all the faults are fitted well. The number of coefficients solved for a given degree l is $2 * (l-1) * (l+3)$.

We will consider two scenarios for the evolution of deformation on Mars: (1) that the

normal and reverse faulting either happened simultaneously or interchangeably, and hence we will invert to fit both normal and reverse faults, and (2) that the normal and reverse faulting are a result of two distinct deformation events, and since the normal faults are well fitted by the GPE base model, we will invert to fit the reverse faults only.

4.3.1 Inversion for both normal and reverse faults

We show the perturbation to the stress tensor field (the optimal sum of all basis stress field solutions up to degree and order 5, obtained in the inversions, and hereby referred to as the NR stress solution)(Figure 2), the combined GPE and NR stress tensor field (Figure 3), and the misfit of the combined GPE and NR stress to the normal and reverse faults (Figure 4). The combined solution (Figure 3) continues to fit the normal faults in Tharsis and the reverse faults in the northern hemipshere (see Figure 4 and compare with Fig 3.4, 3.4). The normal faults along the dichotomy boundary are not well fitted. *Watters* (2003) argue that features associated with the dichotomy boundary in the region formed as a result of a combination of bending stresses related to the modification of the dichotomy boundary. Although the normal faults associated with the region north of Alba Patera are better fitted in the combined GPE and NR solution, some misfit remains (Fig. 4). However, *Mege* (1999); *Mege et al.* (2003) argued these structures have been created by dike intrusions.

Overall, the combined GPE and NR model provides an improved fit to many of the faults. For the normal faults, besides the the improvement north/north-east of Alba Patera, additional improvement is seen in the north/northeast portion of Arabia Terra and minor improvement is seen in the vicinity of Elysium Mons. For the reverse faults, significant improvement is seen for the classical wrinkle ridges in Solis and Lunae Planae, while some improvement is seen in Sirenum and Cimmeria Terrae and in the highlands surrounding Hellas Planitia.

The solved for GPE variation, δGPE, and the membrane displacement, δu_r, show correlated changes (Fig 5, 6), requiring additional GPE and/or upward vertical displacement west of Tharsis and at Margaritifer Terra and Meridiani Planum in the western hemisphere and Hellas and Utopia Planitia in the eastern hemisphere, i.e., a decrease in GPE and verti-

cal displacement since the time of faulting. The results for Tharsis may reflect deviations from the average crustal density as proposed by *Neumann et al.* (2004), which will significantly affect the base GPE model. The variations in density of the crustal layer can result through variations in the composition of the ascending and extruded material as proposed by *Woerner et al.* (2009). If the extensional features north and north-east of Alba Patera are dike intrusions, rather than faults, the additional GPE and/or upward vertical displacement in the region may be unnecessary.

Physical processes that modify the lithosphere such as dynamic topography present at the time of Tharsis formation and/or faulting, volcanic construction, giant impacts, erosion, etc., lead to both a membrane displacement and a GPE change. For the solved for membrane displacement, δu_r, the associated GPE, $GPE_{\delta u_r}$, is given in Figure 7. Note that $GPE_{\delta u_r}$ is an order of magnitude smaller than the solved for δGPE. Therefore, the difference, $\delta\delta GPE = \delta GPE - GPE_{\delta u_r}$, is not much different than the solved for GPE perturbation (Fig 8). This difference can be interpreted as possible lateral deviations in crust and/or mantle density from the uniform values assumed. If all the signal is attributed to lateral mantle density deviations only, we have variations of $\pm 170 kg \cdot m^{-3}$(Figure 9). If all the signal is attributed to lateral crust density deviations only, we have variation of $\pm 72 kg \cdot m^{-3}$(Figure 10). This range is smaller than the mantle density range since the crust is located at a larger distance away from the GPE reference level (in this case, the base of the lithosphere). The smallest variations of $\pm 37 kg \cdot m^{-3}$ (Figure 11) are achieved if we attribute $\delta\delta GPE$ to lateral density variations in both the crust and mantle such that the density contrast remains $600 kg \cdot m^{-3}$ consistent with values derived from the moment of inertia. In all cases, these density differences are only $1-5\%$ and will not affect the gravity field significantly.

It is important to note that the vertical displacements are small– $\pm 140 m$ (Figure 6). They are much smaller than the vertical displacements in the flexure and membrane models (Chapter 2, Appendix). This is due to the fact that the base solution, in this case a GPE stress model, calibrates the magnitude of the stresses needed to fit the data.

4.3.2 Inversion for reverse faults only

We show the perturbation to the stress tensor field (the optimal sum of all basis stress field solutions up to degree and order 5, obtained in the inversions, and hereby refereed to as the R stress solution)(Figure 12) , the combined GPE and R stress (Figure 13), and the misfit of the combined GPE and R stress to the reverse faults (Figure 14). The combined GPE and R stress solution continues to fit the normal faults in the center of Tharsis, but misfits the faults in the periphery of Tharsis (Fig 15). Therefore, fitting only the reverse faults has resulted in a degraded fit to the normal faults. There is little to no significant difference in the fit to the reverse faults between the GPE and NR model and the GPE and R stress model from section 4.3.1 (compare Fig 4 and 14).

Since the GPE associated stress model fits almost all the normal fault data in Tharsis, then the stress field at the time of normal fault formation was either the GPE stress field alone (see Chapters 2,3) or a stress field similar in style and orientation to the GPE stress field. However, such a stress field pattern is not consistent with models of upward or downward flexure, global contraction, or planetary despinning (*Banerdt et al.*, 1992, and references therein). Therefore, so far the GPE associated stress field remains the one model stress field that fits the normal fault data, and as such places an important constraint on the timing of faulting and lithospheric modification. If the normal faults formed before the reverse faults, then the majority of the processes (erosion, excavation, etc) which lead to the lithosphere modification occurred after the reverse fault formation. More importantly, this scenario requires an additional change to the stress regime following the formation of the normal faults, but before the formation of the reverse faults. Such a stress field change is opposite in stress style to the change after the reverse faulting, i.e., similar to the one shown in Fig. 12. Alternatively, if the normal faults formed after the reverse faults, then the majority of the lithosphere modification (opposite in sign to the scenario above) occurred after the reverse faults formed, but before the normal faults formed.

The solved for GPE variation, δGPE, and membrane displacement, δu_r, show correlated changes (Fig 16, 17) requiring additional GPE and/or upward vertical displacement west of Tharsis and at Margaritifer Terra and Meridiani Planum in the western hemisphere

and Hellas and Utopia Planitia in the eastern hemisphere, i.e., a decrease in GPE and vertical displacement since the time of faulting. These areas also correlate with the results from the combined GPE and NR model; however, the magnitude of the associated GPE deviation and vertical displacement is a factor of 2 or 3 larger for the case obtained from the inversion to the reverse faults alone. Furthermore, the areas of additional GPE and displacement around Utopia is a factor of 2 to 3 more diffuse.

For the combined GPE and R stress the solved for membrane displacement, δu_r, and the associated GPE, $GPE_{\delta u_r}$, are given in Figures 16, 17. Note that again the $GPE_{\delta u_r}$ is an order of magnitude smaller than the solved for δGPE. Therefore, the difference, $\delta\delta GPE = \delta GPE - GPE_{\delta u_r}$, is small (Figure 19). Interpretting this difference as possible lateral deviations in crust and/or mantle density from the uniform values assumed gives $\pm 212 kg \cdot m^{-3}$ for the mantle density alone (Figure 20), $\pm 82 kg \cdot m^{-3}$ for the crust density alone (Figure 21), and $\pm 54 kg \cdot m^{-3}$ for both the crust and mantle (Figure 22). In all cases, these density differences are only $1-6\%$ and will not affect the gravity field significantly. The vertical displacements are $\pm 240 m$.

4.4 Conclusions

Small lateral variations $(1-6\%)$ in crust and mantle density in conjuncion with small vertical displacement ($O(100m)$) provide sufficient additional GPE and membrane stress to fit the majority of the data. At the time of faulting, the inversions predict additional GPE and positive (upward) displacement (in comparison to today) in areas such as Margaritifer Terra, Meridiani Planum, Utopia and Hellas Plantiae. These areas are associated with large craters and/or networks of outflow channels. To first order, the models are consistent with modification of the lithosphere by erosion, impact excavation (or post impact cooling and associated subsidence), or other material transport processes since the time of faulting. In particular, the material removed is of the same order of magnitude as the estimate of *Hynek and Phillips* (2001) for liquid water erosion in Meridiani Planum and Margaritifer Terra since the time of faulting.

The inversion models cannot distinguish whether the normal and reverse faulting oc-

curred separately or intermittently. However, if they occurred separately two scenarios exist: (1) The normal faults formed first, followed by lithospheric modification that resulted in reverse faulting in the southern hemisphere. The stress style associated with this lithosphere modification would have looked like the one shown in Fig. 12. Following the southern hemisphere reverse faulting, a second lithosphere modification must have occurred in opposite sense, resulting in the present day structure and stress field. or (2) The reverse faults formed first, followed by the majority of the lithosphere modification that resulted in the normal faulting in the Tharsis province. The stress style associated with this lithosphere modification would have looked opposite to the one shown in Fig. 12. After the formation of the normal faults, little to no further stress style change is expected, and this can happen if there is no further lithosphere modification, or through significant increase in the strength of the lithosphere.

The final depth integrated deviatoric stress magnitudes we calculate are Earth-like ($1-4*\times10^{12}N/m$)(*Ghosh et al.*, 2008) and at least an order of magnitude smaller than the stresses associated with flexure-dominated models (see also Chapter 2). These magnitudes are calibrated by the base stress solution – in this case the GPE associated stresses. Like on earth, such stress magnitudes can lead to considerable permanent strain through accumulation of fault displacement over time. For the case of Mars, the total strain is small. This small strain would not have lead to a significant relaxation of topography, and therefore would not have lead to significant change in stress magnitudes. If the inverted stress magnitudes are correct, then the ratio of brittle-frictional layer thickness to ductile layer thickness on Mars at the time of faulting may have been similar to what is found on Earth today within moderately actively deforming orogens. On the other hand, the likely large present-day elastic thickness on Mars, precludes the possibility of active faulting today.

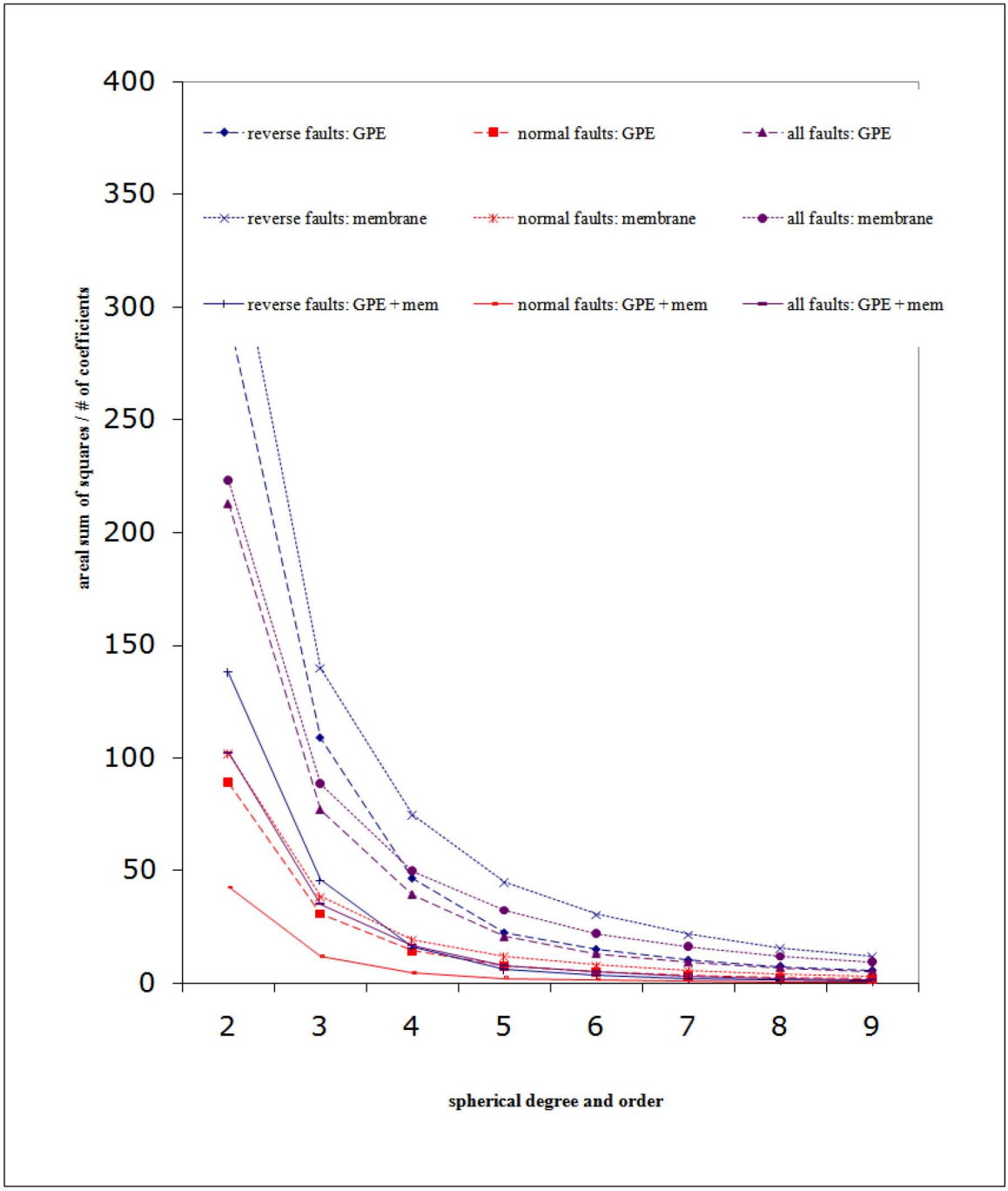

Figure 1: Surface integral of the residual misfit by spherical degree and order cut-off, inversion, and type of fault for each inversion. Red lines indicate inversions to the normal fault data only; blue lines indicate inversions to the reverse fault data only; and purple lines indicate inversions to both the normal and reverse data. Solid lines indicate inversions for perturbations in both GPE and membrane stresses; dashed lines indicates inversions for perturbations to GPE alone; and dotted lines indicates inversions for perturbations to membrane stresses alone

Figure 2: The inverted NR depth integrated deviatoric stress field (see text). Red arrows signify deviatoric extension, while black arrows signify deviatoric compression

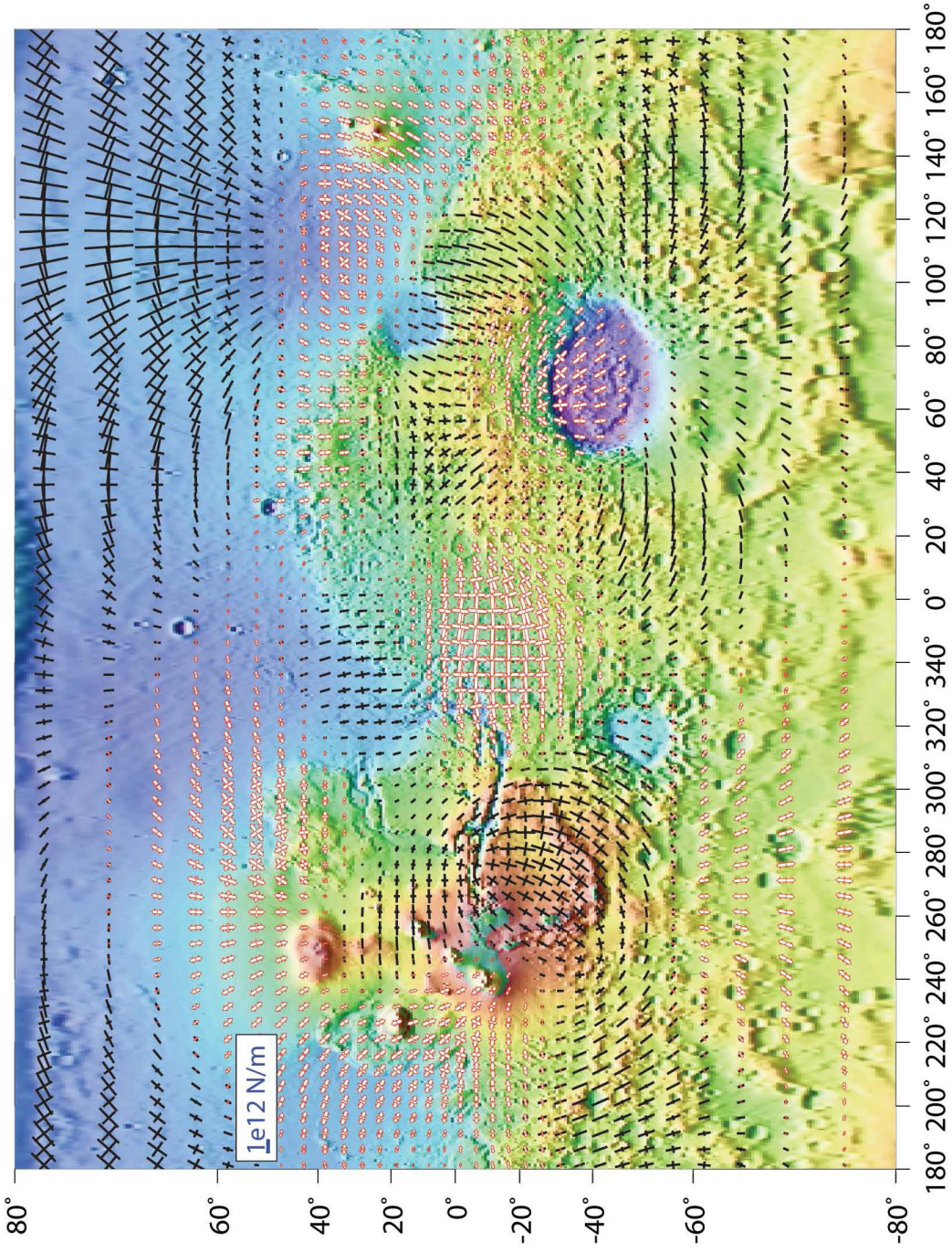
80°
60°
40°
20°
0°
-20°
-40°
-60°
-80°
180° 200° 220° 240° 260° 280° 300° 320° 340° 0° 20° 40° 60° 80° 100° 120° 140° 160° 180°
1e12 N/m

Figure 3: The combined GPE and NR depth integrated deviatoric stress field. Red arrows signify deviatoric extension, while black arrows signify deviatoric compression

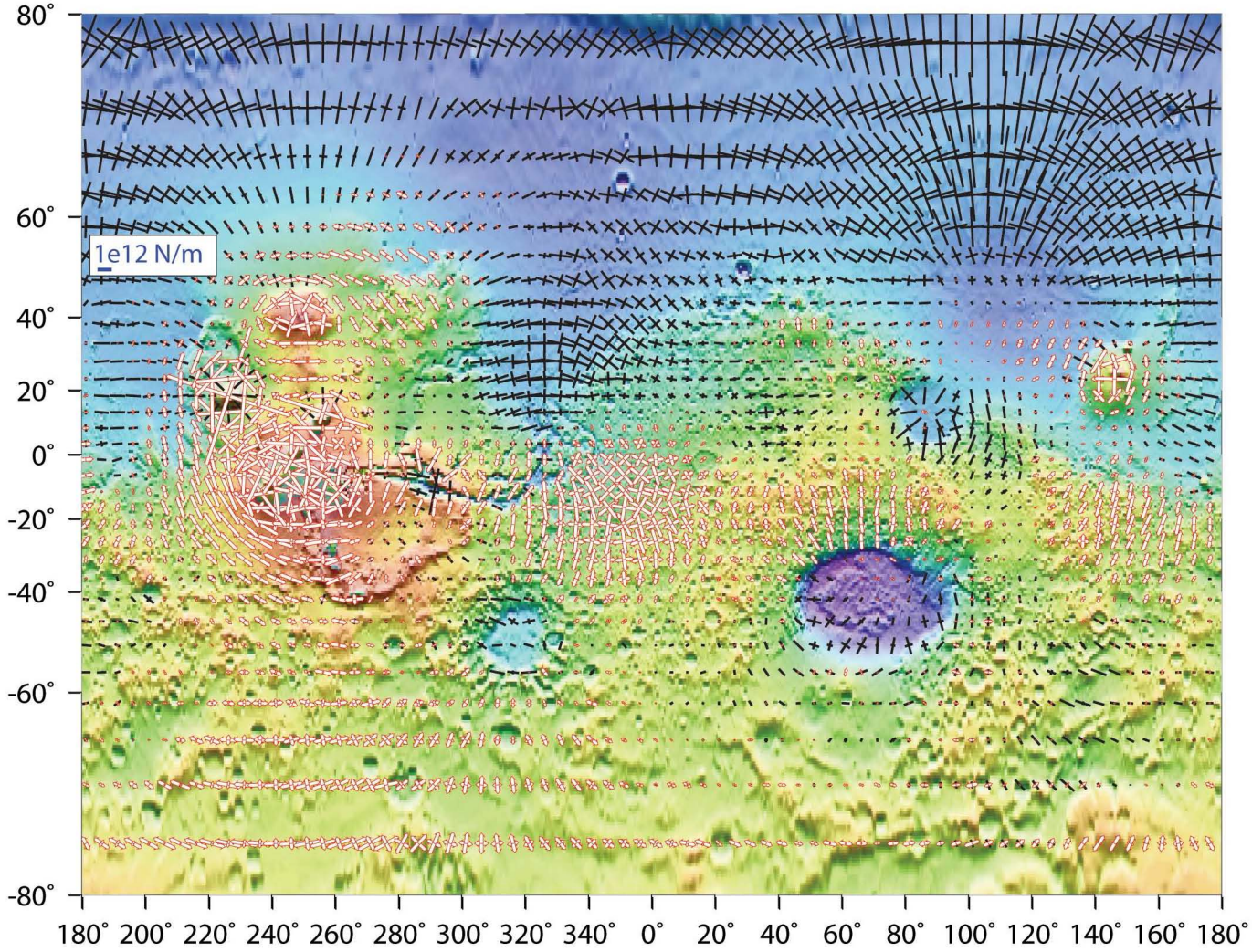
80°
60°
40°
20°
0°
-20°
-40°
-60°
-80°
1e12 N/m
180° 200° 220° 240° 260° 280° 300° 320° 340° 0° 20° 40° 60° 80° 100° 120° 140° 160° 180°

Figure 4: The misfit M_{full} as defined in 2 between the normal and reverse faults of *Knapmeyer et al.* [2006] and the stress field in 3. Red indicates a very good fit, while green and blues indicate a misfit.

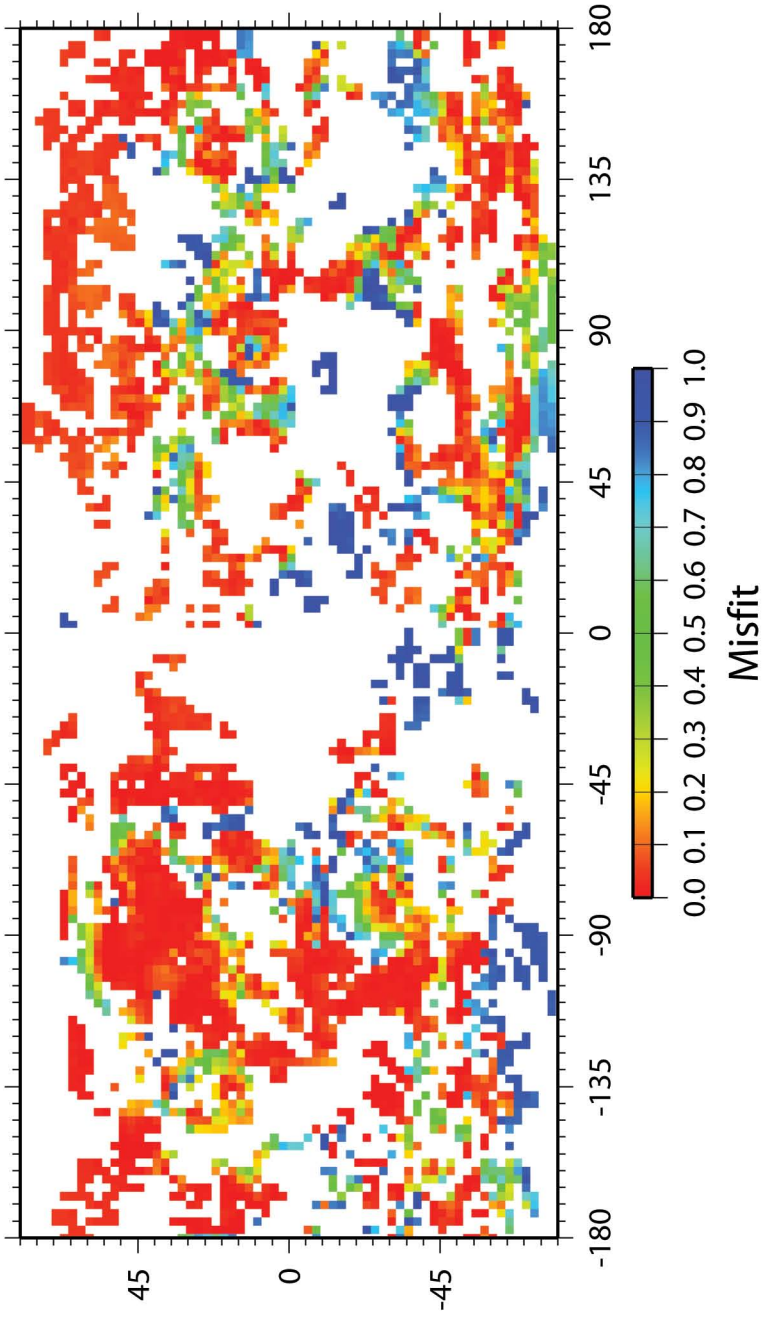
45
0
-45
-180
-135
-90
-45
0
45
90
135
180
0.0 0.1 0.2 0.3 0.4 0.5 0.6 0.7 0.8 0.9 1.0
Misfit

Figure 5: The GPE variation, δGPE from the inversion to both the normal and reverse faults.

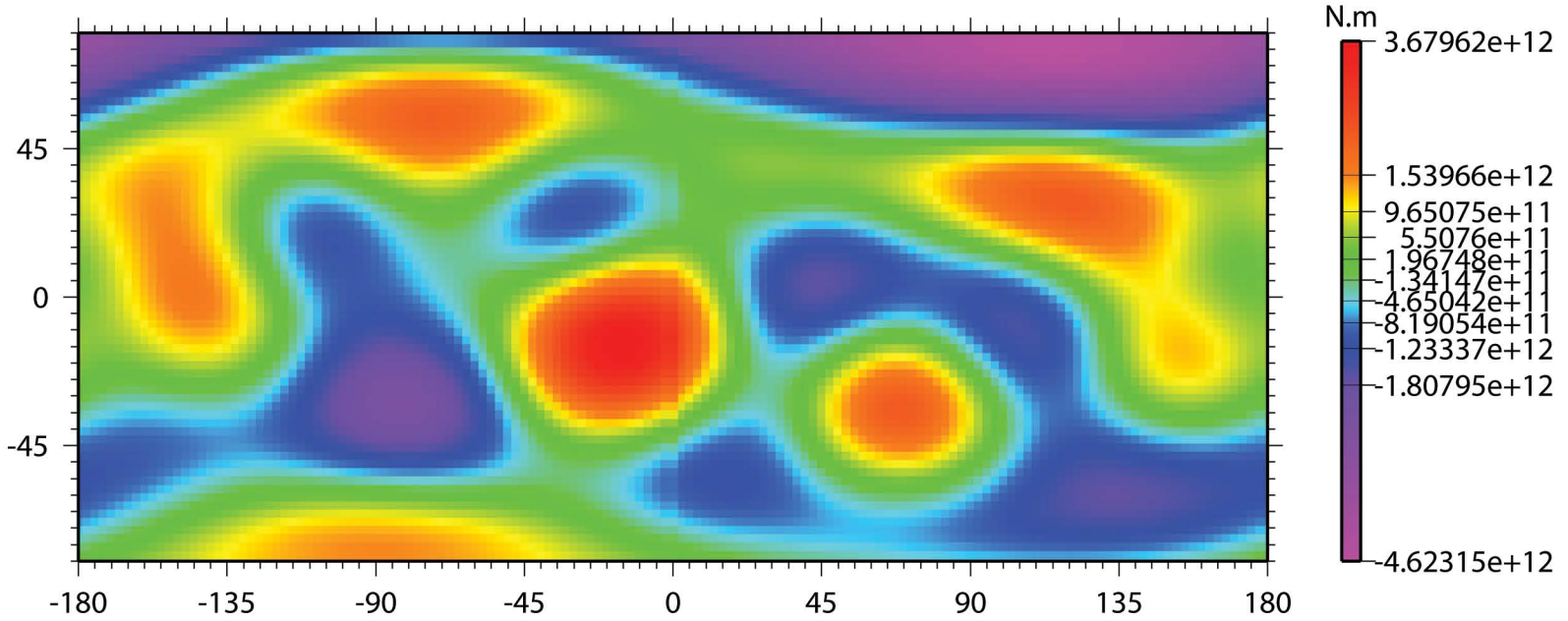
N.m
3.67962e+12
1.53966e+12
9.65075e+11
5.5076e+11
1.96748e+11
-1.34147e+11
-4.65042e+11
-8.19054e+11
-1.23337e+12
-1.80795e+12
-4.62315e+12
45
0
-45
-180
-135
-90
-45
0
45
90
135
180

Figure 6: The vertical displacement, u_r from the inversion to both the normal and reverse faults.

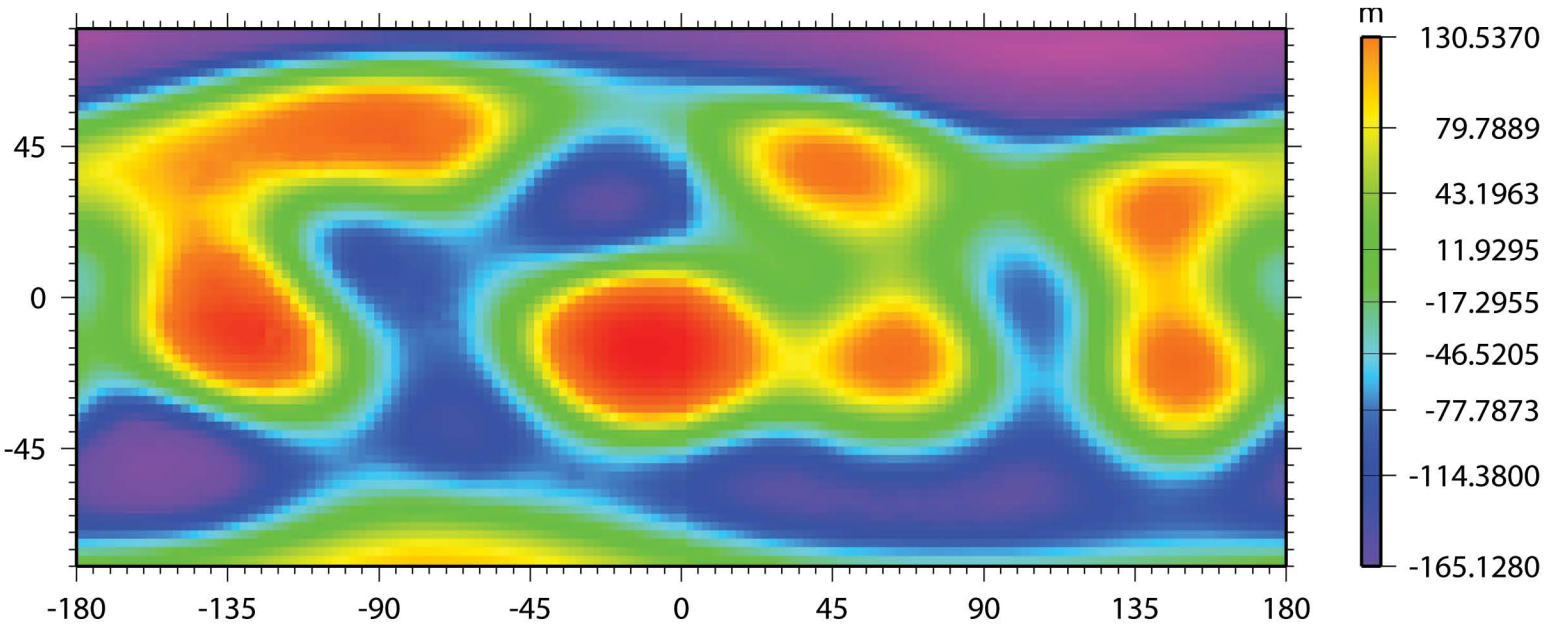
m
130.5370
79.7889
43.1963
11.9295
-17.2955
-46.5205
-77.7873
-114.3800
-165.1280
45
0
-45
-180
-135
-90
-45
0
45
90
135
180

Figure 7: The GPE change, GPE_{u_r}, associated with the vertical displacement from Figure 6

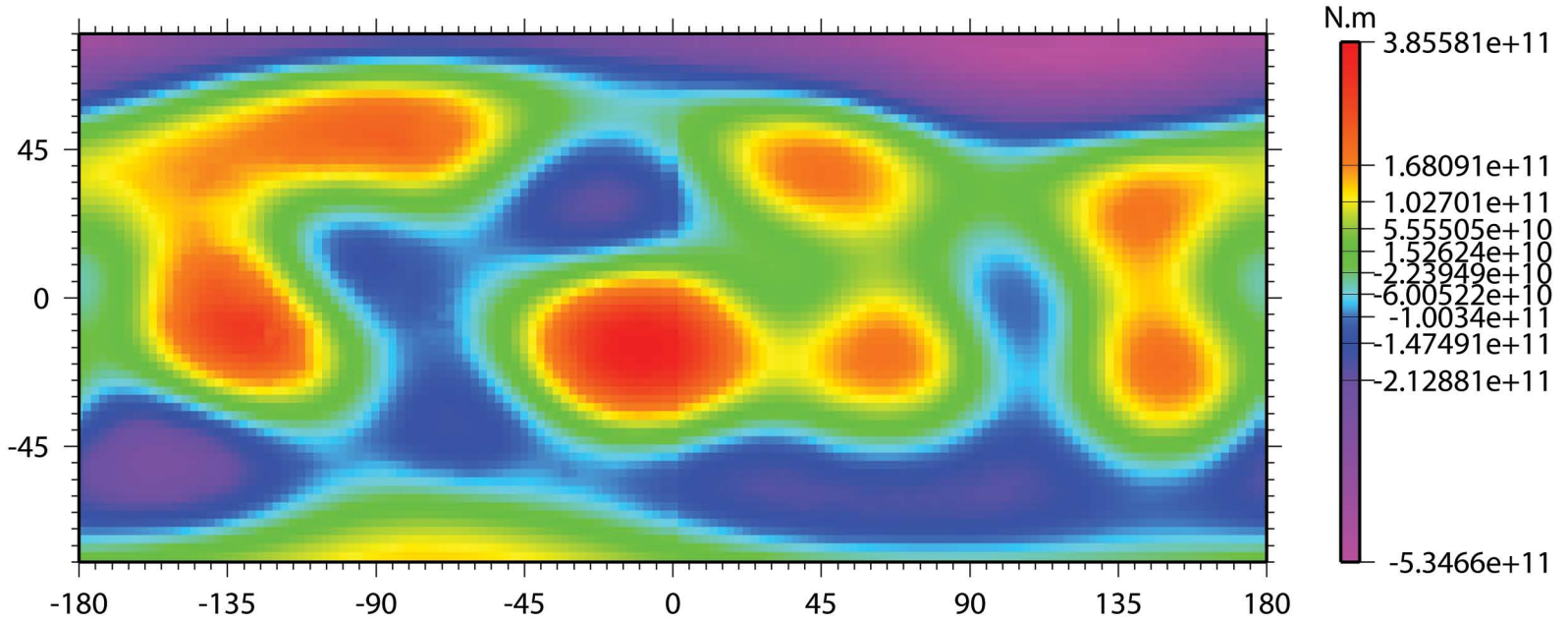
N.m
3.85581e+11
1.68091e+11
1.02701e+11
5.55505e+10
1.52624e+10
-2.23949e+10
-6.00522e+10
-1.0034e+11
-1.47491e+11
-2.12881e+11
-5.3466e+11
45
0
-45
-180
-135
-90
-45
0
45
90
135
180

Figure 8: The GPE change, $\delta\delta GPE$, associated with lateral density variations.

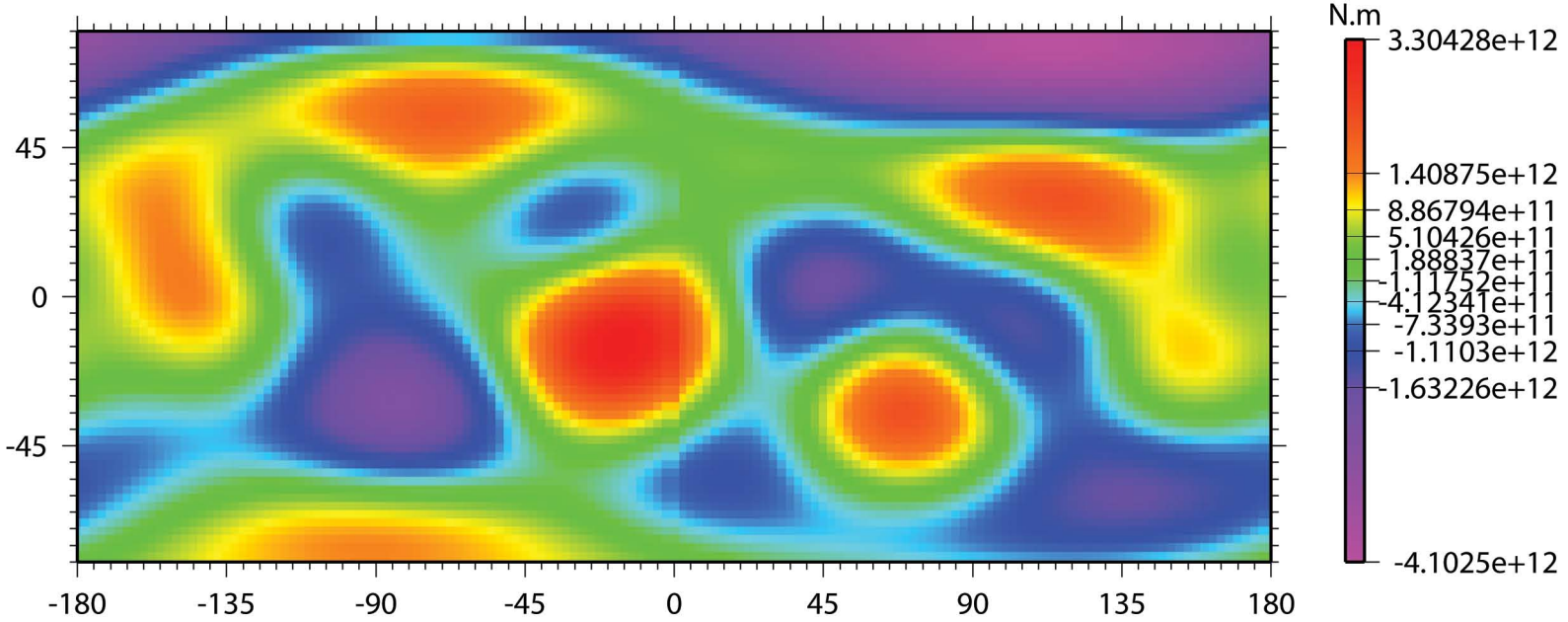
N.m
3.30428e+12
1.40875e+12
8.86794e+11
5.10426e+11
1.88837e+11
-1.11752e+11
-4.12341e+11
-7.3393e+11
-1.1103e+12
-1.63226e+12
-4.1025e+12
45
0
-45
-180
-135
-90
-45
0
45
90
135
180

Figure 9: The lateral density variation in mantle density associated with the residual GPE signal, $\delta\delta GPE$.

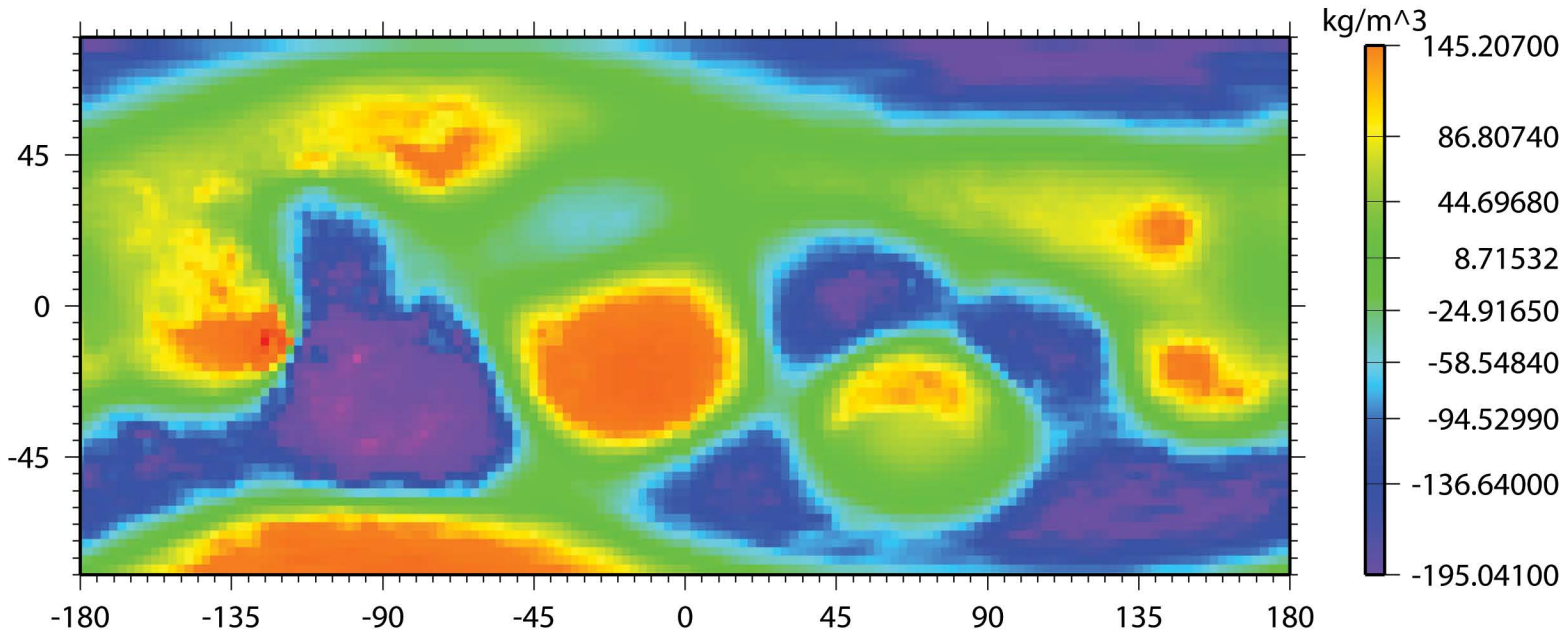
kg/m^3
145.20700
86.80740
44.69680
8.71532
-24.91650
-58.54840
-94.52990
-136.64000
-195.04100
45
0
-45
-180
-135
-90
-45
0
45
90
135
180

Figure 10: The lateral density variation in crust density associated with the residual GPE signal, $\delta\delta GPE$.

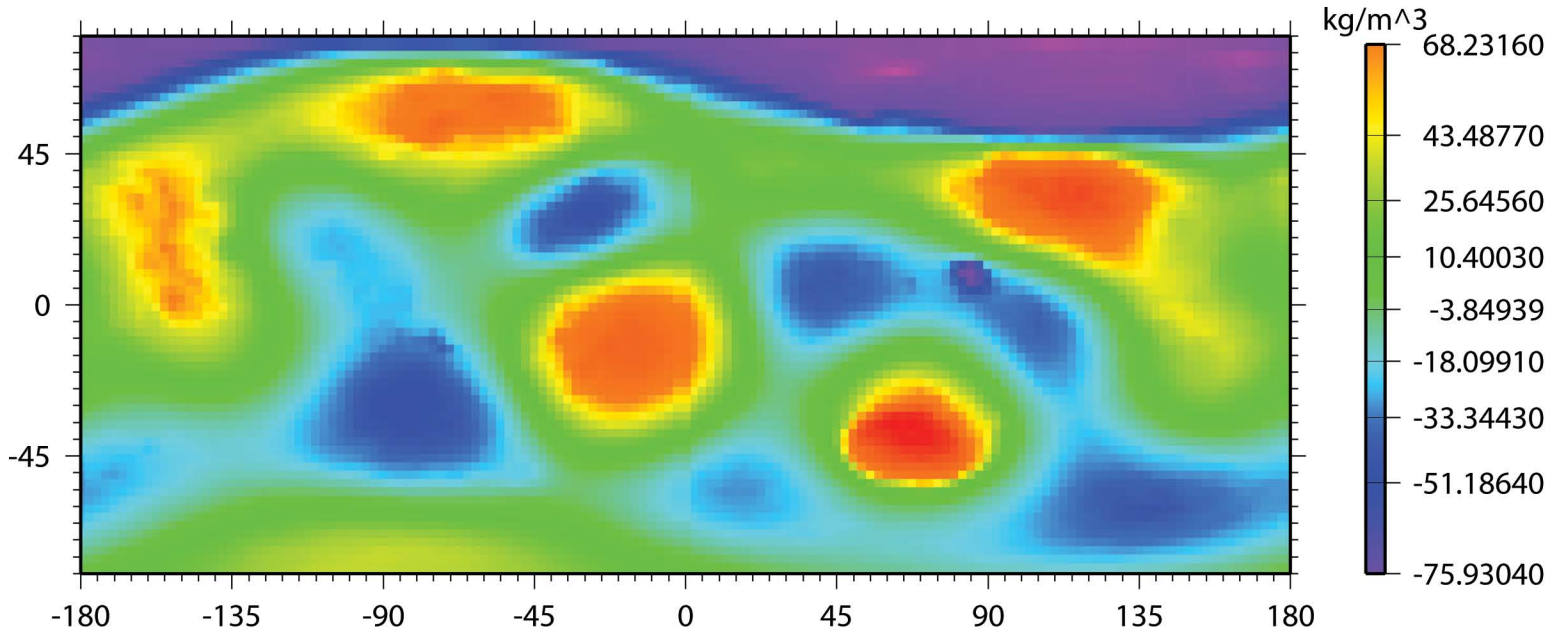
kg/m^3
68.23160
43.48770
25.64560
10.40030
-3.84939
-18.09910
-33.34430
-51.18640
-75.93040
45
0
-45
-180
-135
-90
-45
0
45
90
135
180

Figure 11: The lateral density variation in crust and mantle density associated with the residual GPE signal, $\delta\delta GPE$.

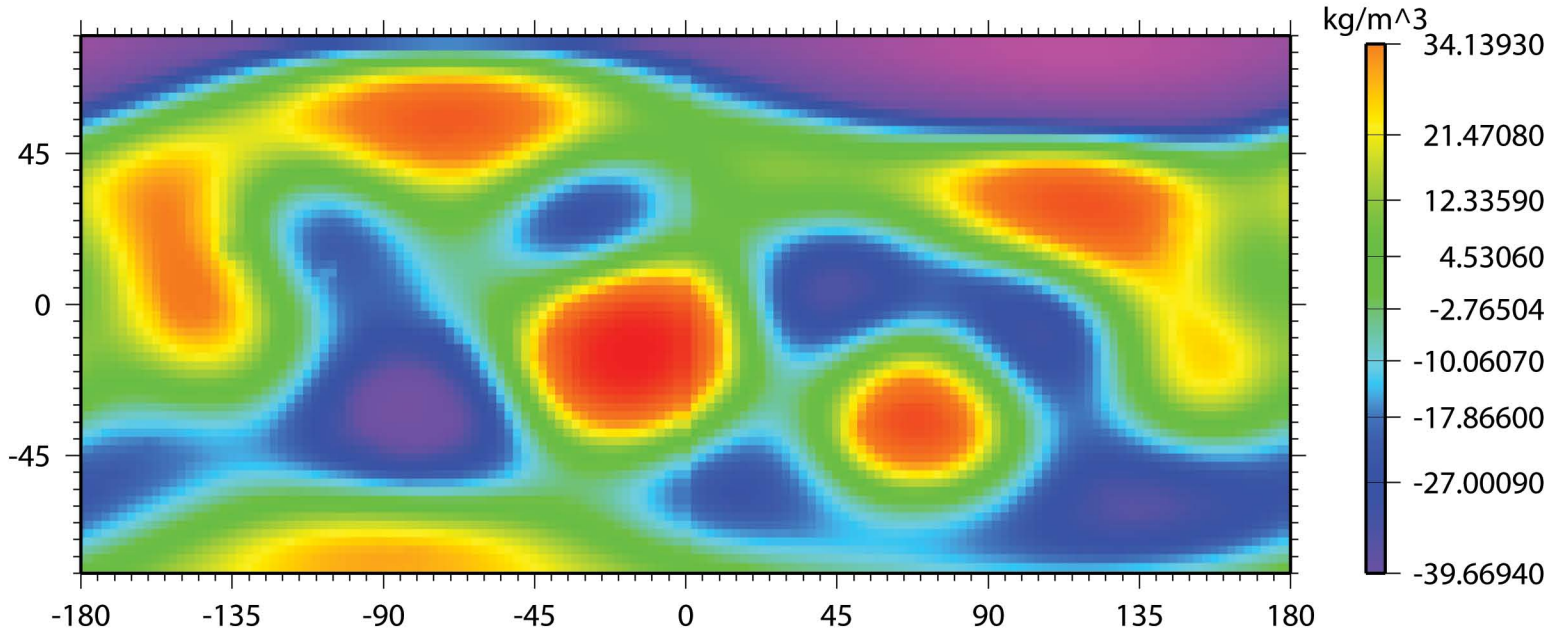
kg/m^3
34.13930
21.47080
12.33590
4.53060
-2.76504
-10.06070
-17.86600
-27.00090
-39.66940
45
0
-45
-180
-135
-90
-45
0
45
90
135
180

Figure 12: The inverted R depth integrated deviatoric stress field (see text). Red arrows signify deviatoric extension, while black arrows signify deviatoric compression.

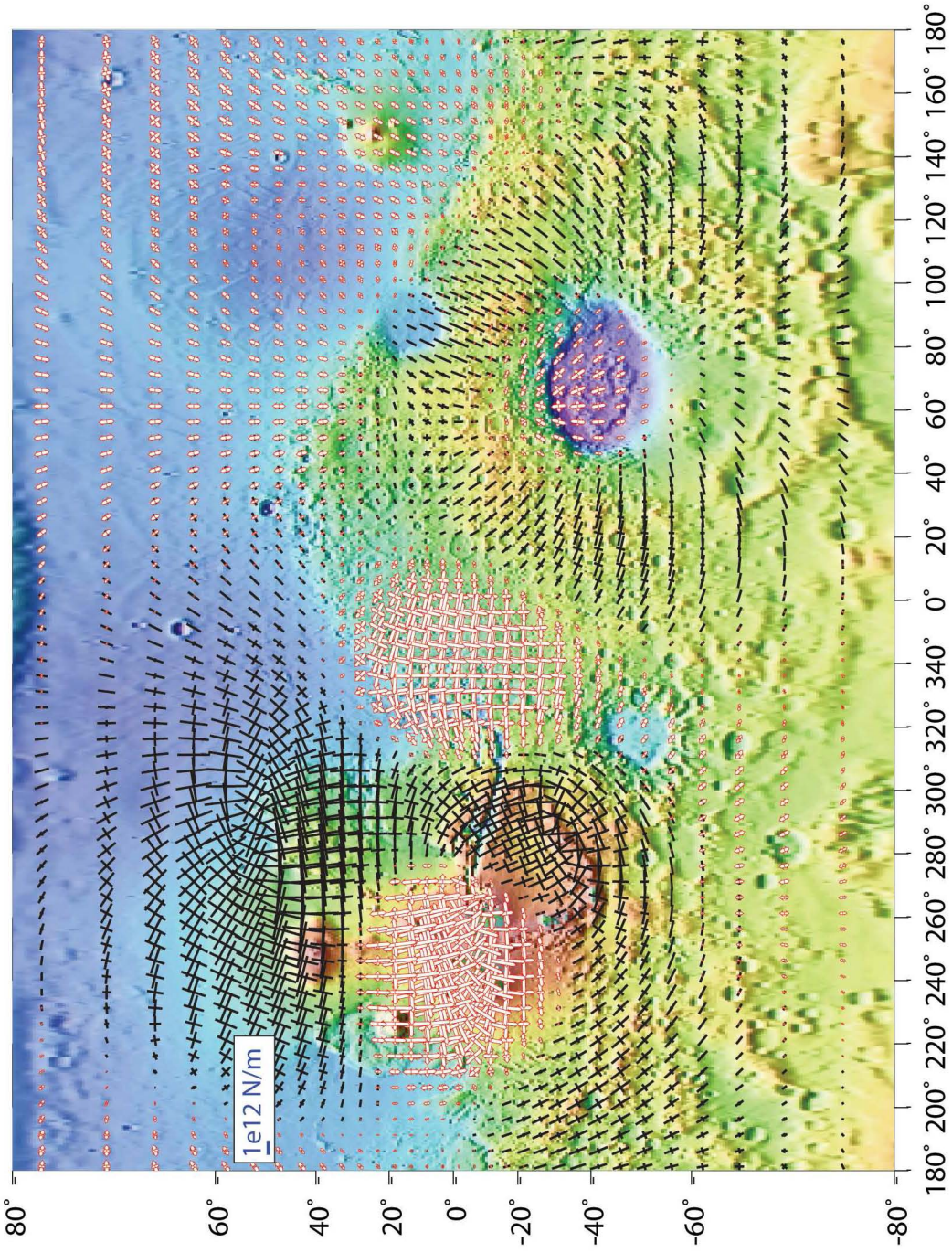
80°
60°
40°
20°
0°
-20°
-40°
-60°
-80°
180° 200° 220° 240° 260° 280° 300° 320° 340° 0° 20° 40° 60° 80° 100° 120° 140° 160° 180°
1e12 N/m

Figure 13: The combined GPE and R depth integrated deviatoric stress field. Red arrows signify deviatoric extension, while black arrows signify deviatoric compression.

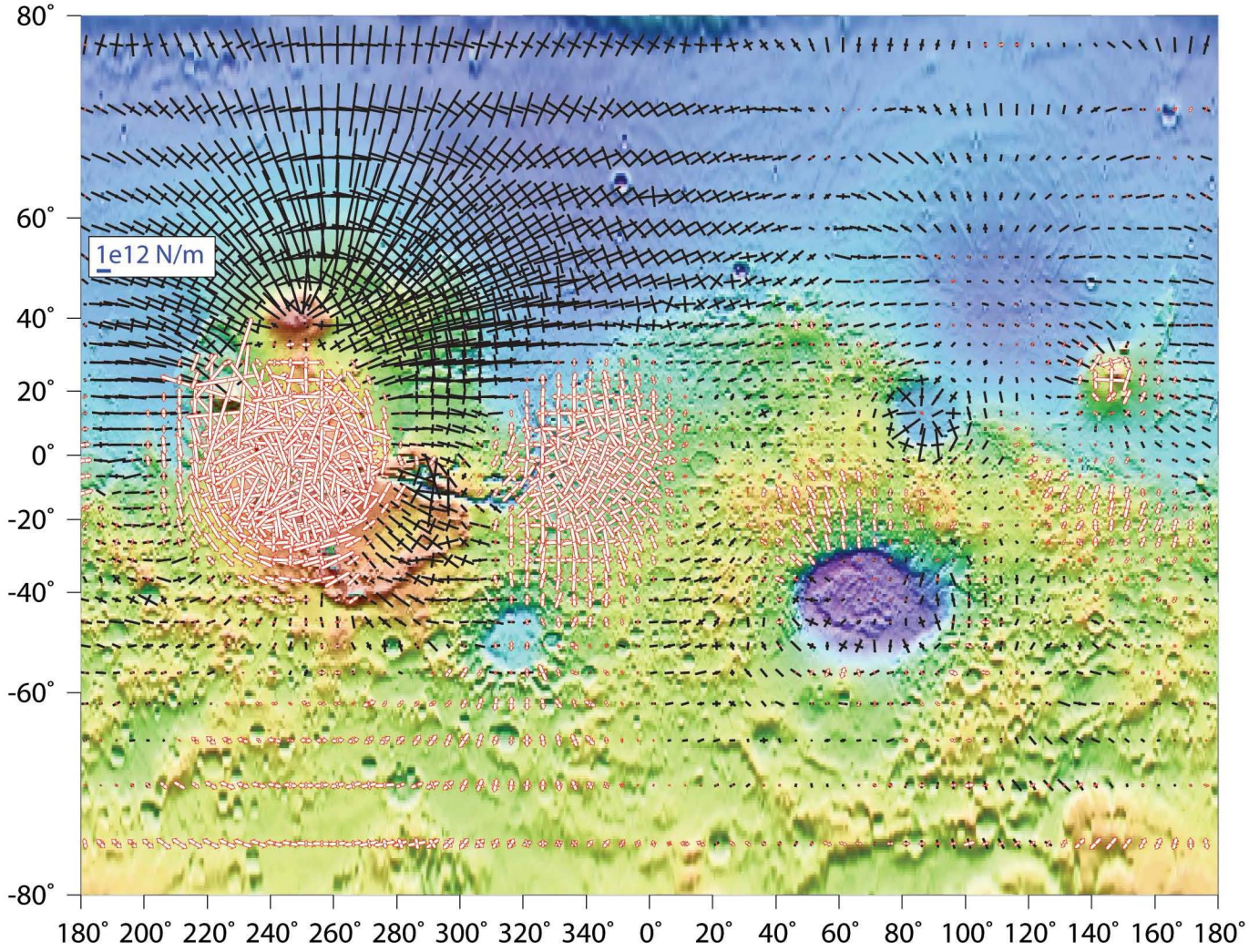
80°
60°
40°
20°
0°
-20°
-40°
-60°
-80°
1e12 N/m
180° 200° 220° 240° 260° 280° 300° 320° 340° 0° 20° 40° 60° 80° 100° 120° 140° 160° 180°

Figure 14: The misfit M_{full} as defined in 2 between the reverse faults of *Knapmeyer et al.* [2006] and the stress field in 13. Red indicates a very good fit, while green and blues indicate a misfit.

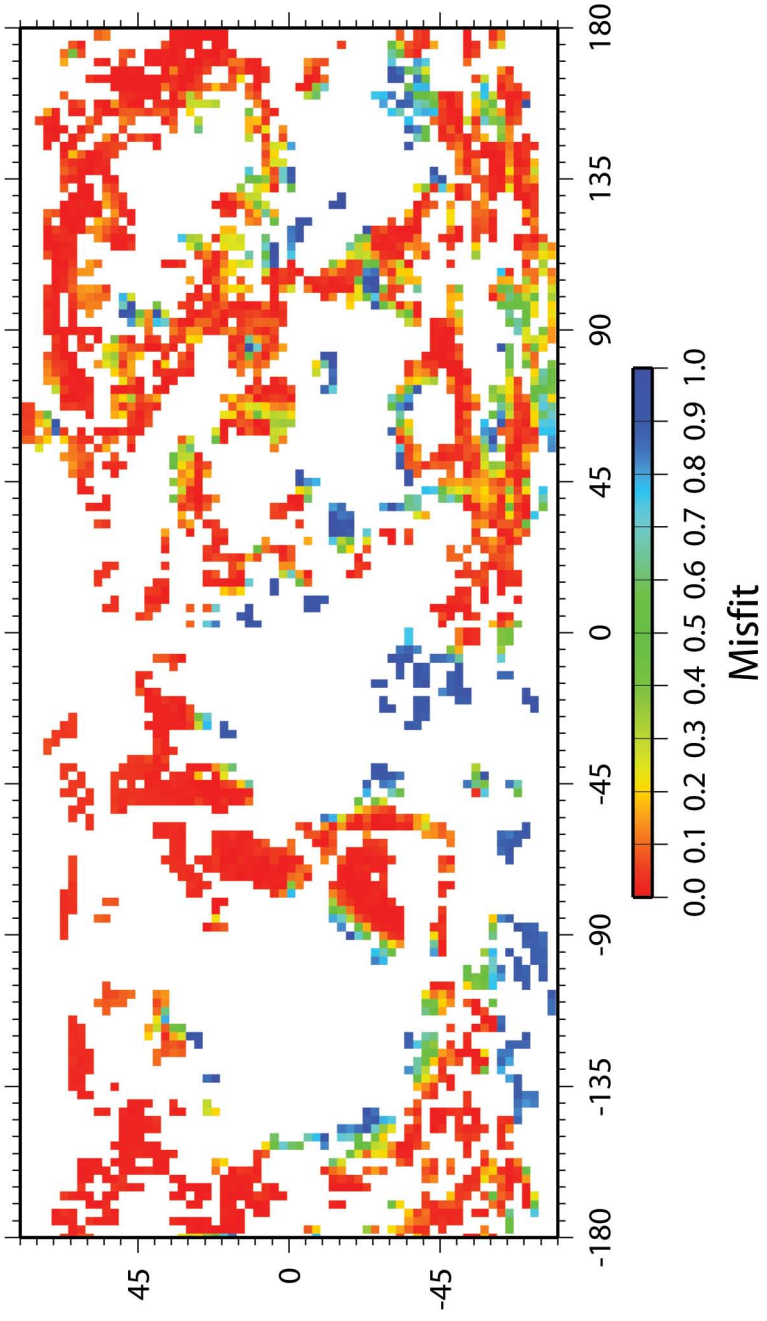
45
0
-45
-180
-135
-90
-45
0
45
90
135
180
0.0 0.1 0.2 0.3 0.4 0.5 0.6 0.7 0.8 0.9 1.0
Misfit

Figure 15: The misfit M_{full} as defined in 2 between the normal faults of *Knapmeyer et al.* [2006] and the stress field in 13. Red indicates a very good fit, while green and blues indicate a misfit.

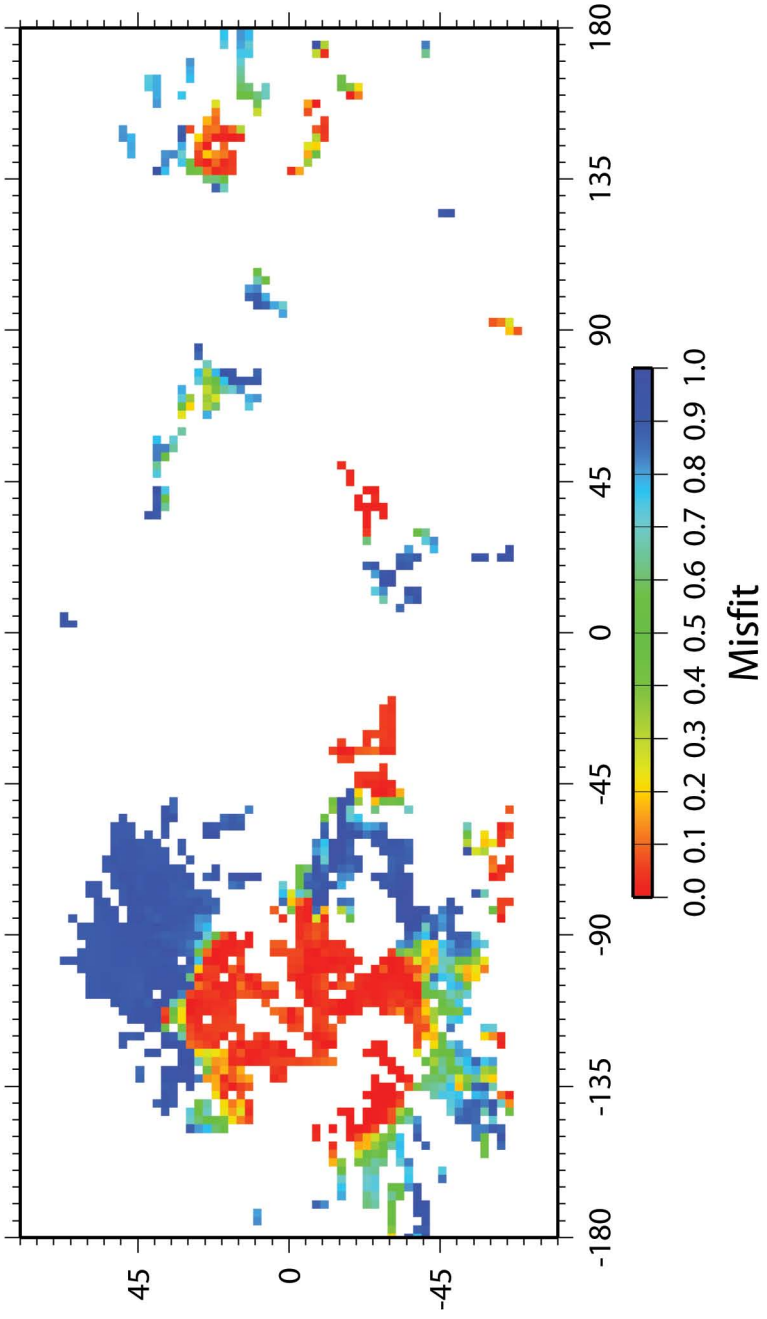
45
0
-45
-180
-135
-90
-45
0
45
90
135
180
0.0 0.1 0.2 0.3 0.4 0.5 0.6 0.7 0.8 0.9 1.0
Misfit

Figure 16: The GPE variation, δGPE from the inversion to the reverse faults only.

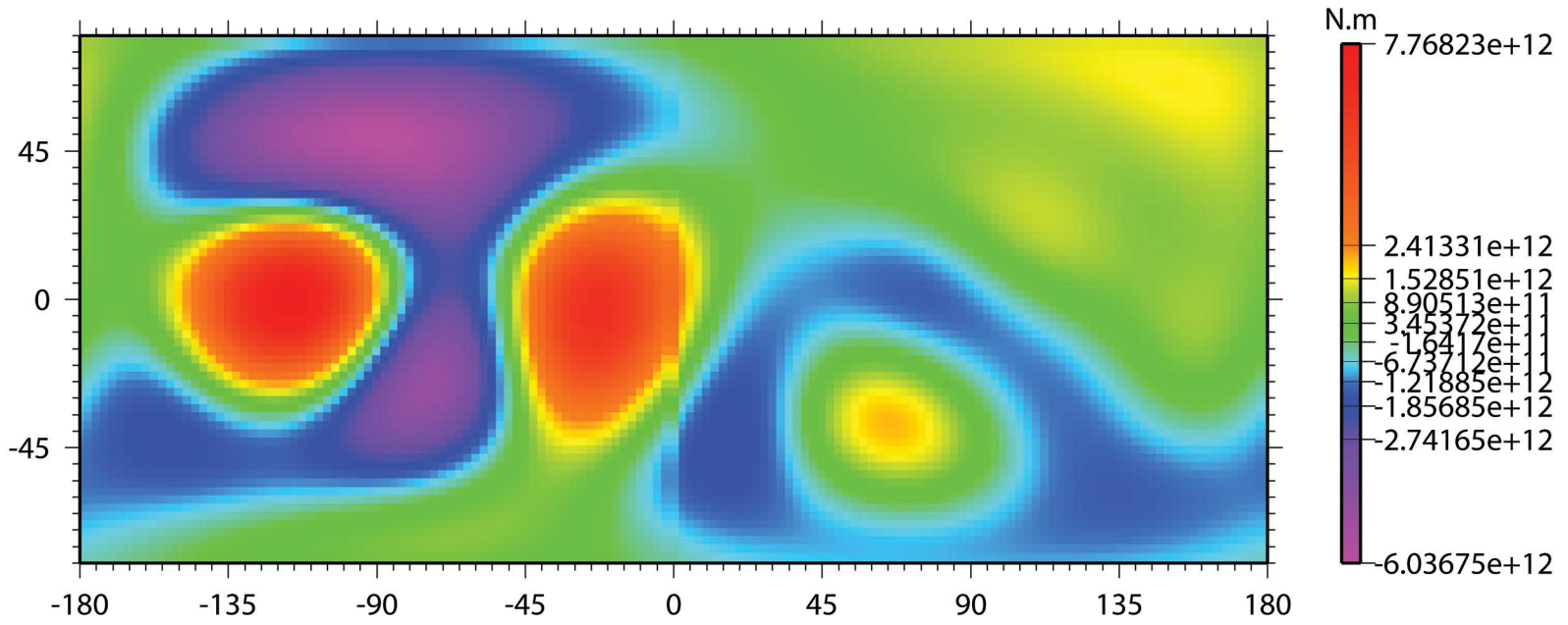
N.m
7.76823e+12
2.41331e+12
1.52851e+12
8.90513e+11
3.45372e+11
-1.6417e+11
-6.73712e+11
-1.21885e+12
-1.85685e+12
-2.74165e+12
-6.03675e+12
45
0
-45
-180
-135
-90
-45
0
45
90
135
180

Figure 17: The vertical displacement, u_r from the inversion to both the reverse faults only.

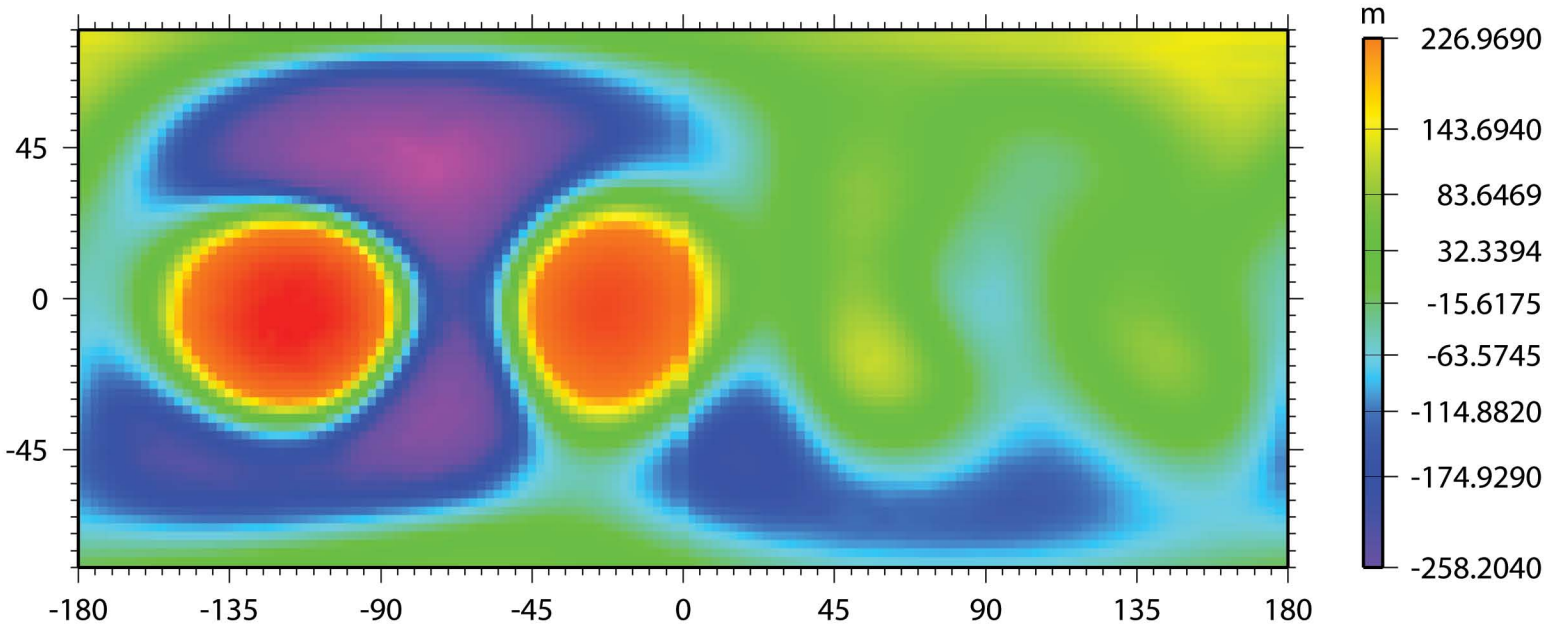
m
226.9690
143.6940
83.6469
32.3394
-15.6175
-63.5745
-114.8820
-174.9290
-258.2040
45
0
-45
-180
-135
-90
-45
0
45
90
135
180

Figure 18: The GPE change, GPE_{u_r}, associated with the vertical displacement from Figure 17

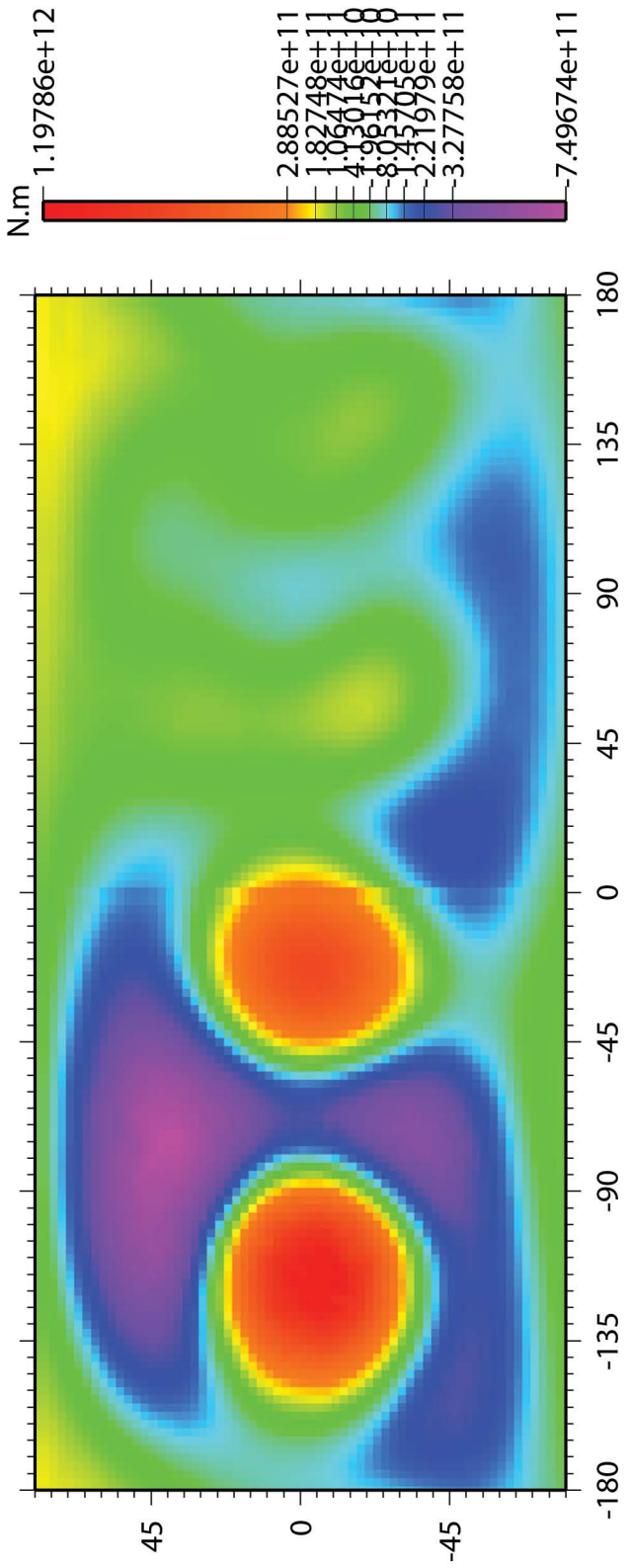
N.m
1.19786e+12
2.88527e+11
1.82748e+11
1.06474e+11
4.13016e+10
-8.03321e+10
-1.45705e+11
-2.21979e+11
-3.27758e+11
-7.49674e+11
180
135
90
45
0
-45
-90
-135
-180
45
0
-45

Figure 19: The GPE change, $\delta\delta GPE$, associated with lateral density variations.

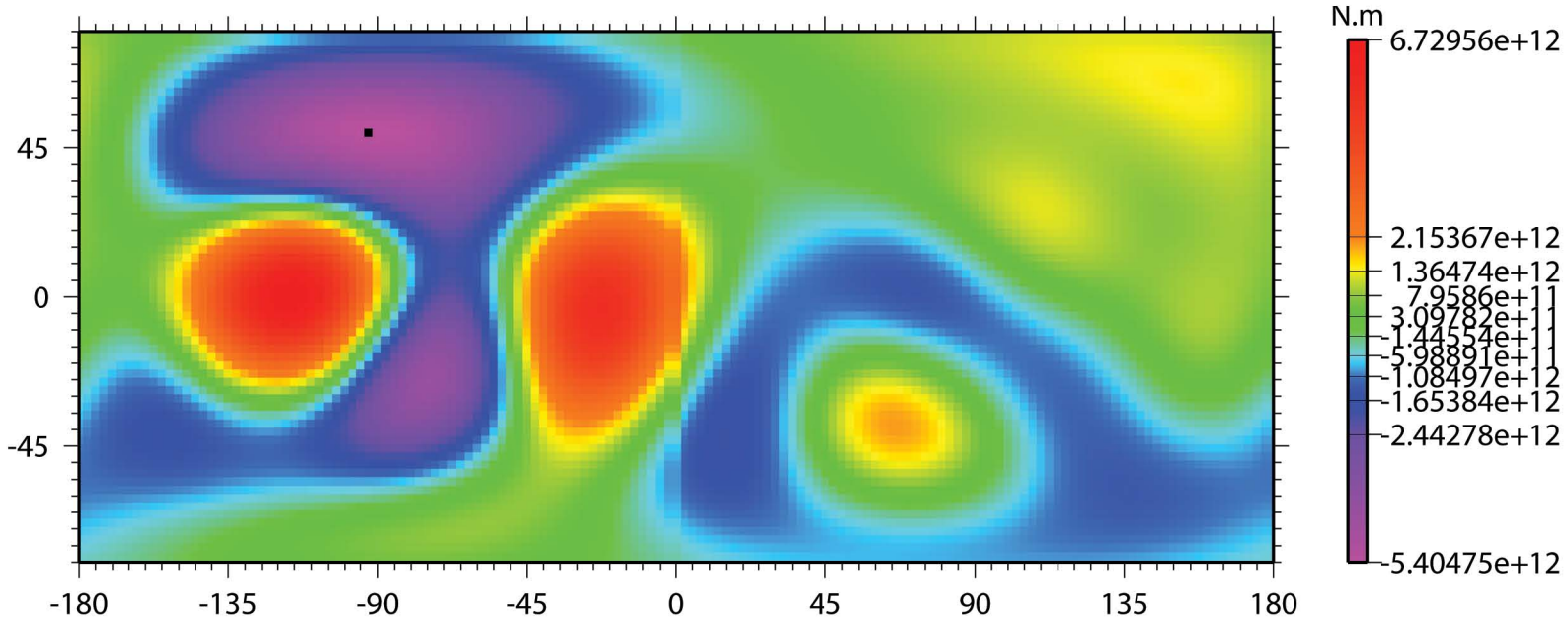
N.m
6.72956e+12
2.15367e+12
1.36474e+12
7.9586e+11
3.09782e+11
-1.44554e+11
-5.98891e+11
-1.08497e+12
-1.65384e+12
-2.44278e+12
-5.40475e+12
45
0
-45
-180
-135
-90
-45
0
45
90
135
180

Figure 20: The lateral density variation in mantle density associated with the residual GPE signal, $\delta\delta GPE$.

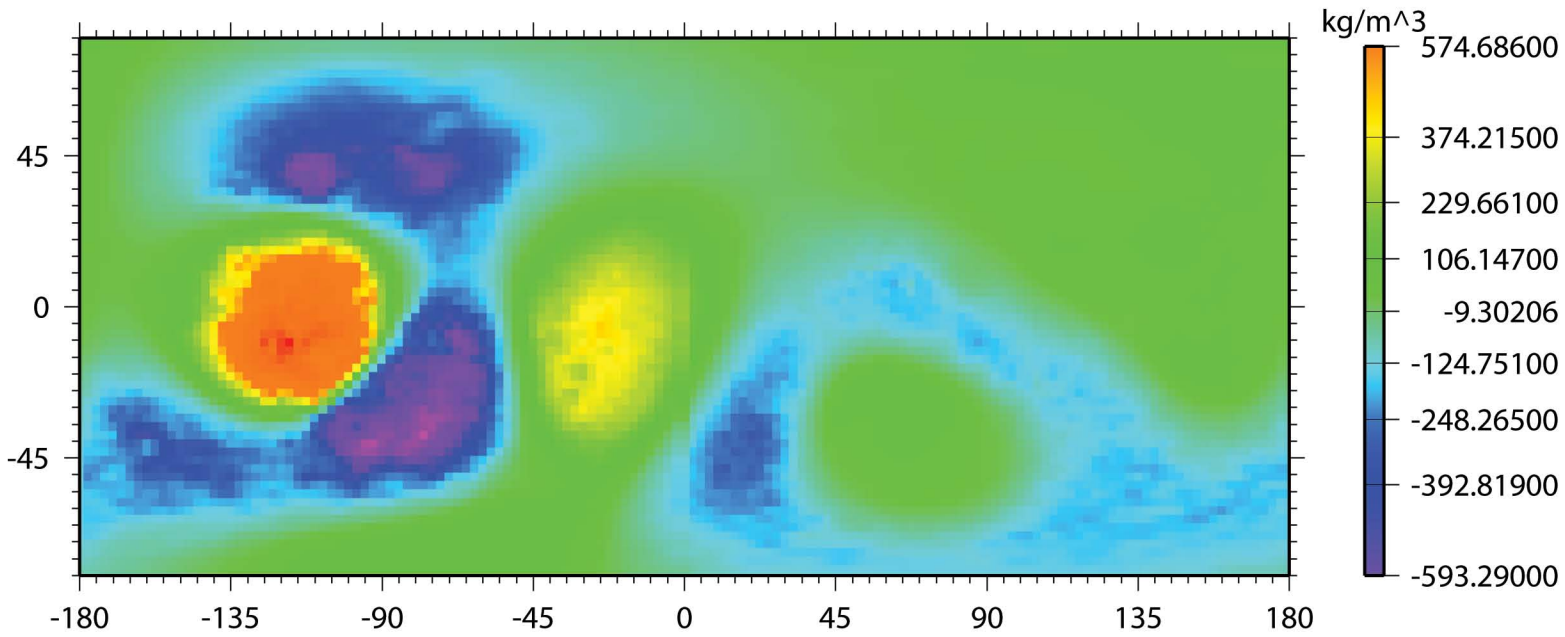
kg/m^3
574.68600
374.21500
229.66100
106.14700
-9.30206
-124.75100
-248.26500
-392.81900
-593.29000
45
0
-45
-180
-135
-90
-45
0
45
90
135
180

Figure 21: The lateral density variation in crust density associated with the residual GPE signal, $\delta\delta GPE$.

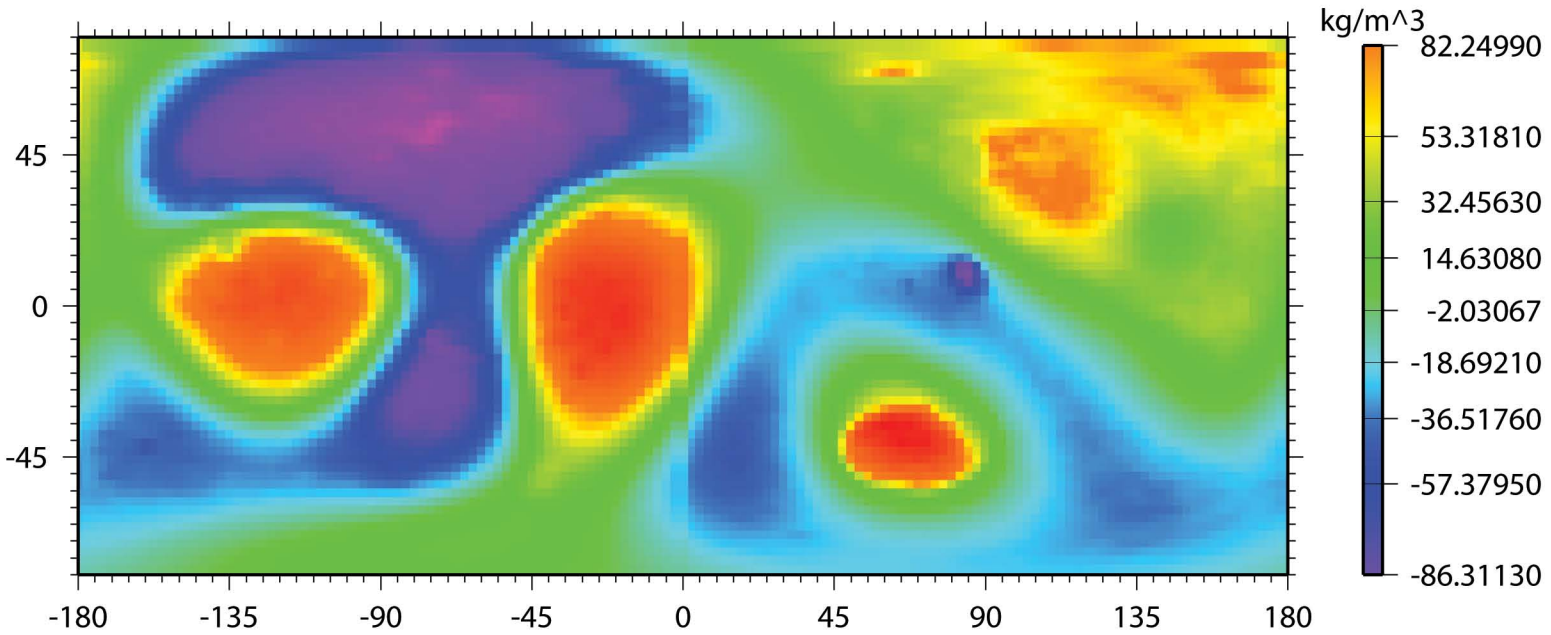
kg/m^3
82.24990
53.31810
32.45630
14.63080
-2.03067
-18.69210
-36.51760
-57.37950
-86.31130
45
0
-45
-180
-135
-90
-45
0
45
90
135
180

Figure 22: The lateral density variation in crust and mantle density associated with the residual GPE signal, $\delta\delta GPE$.

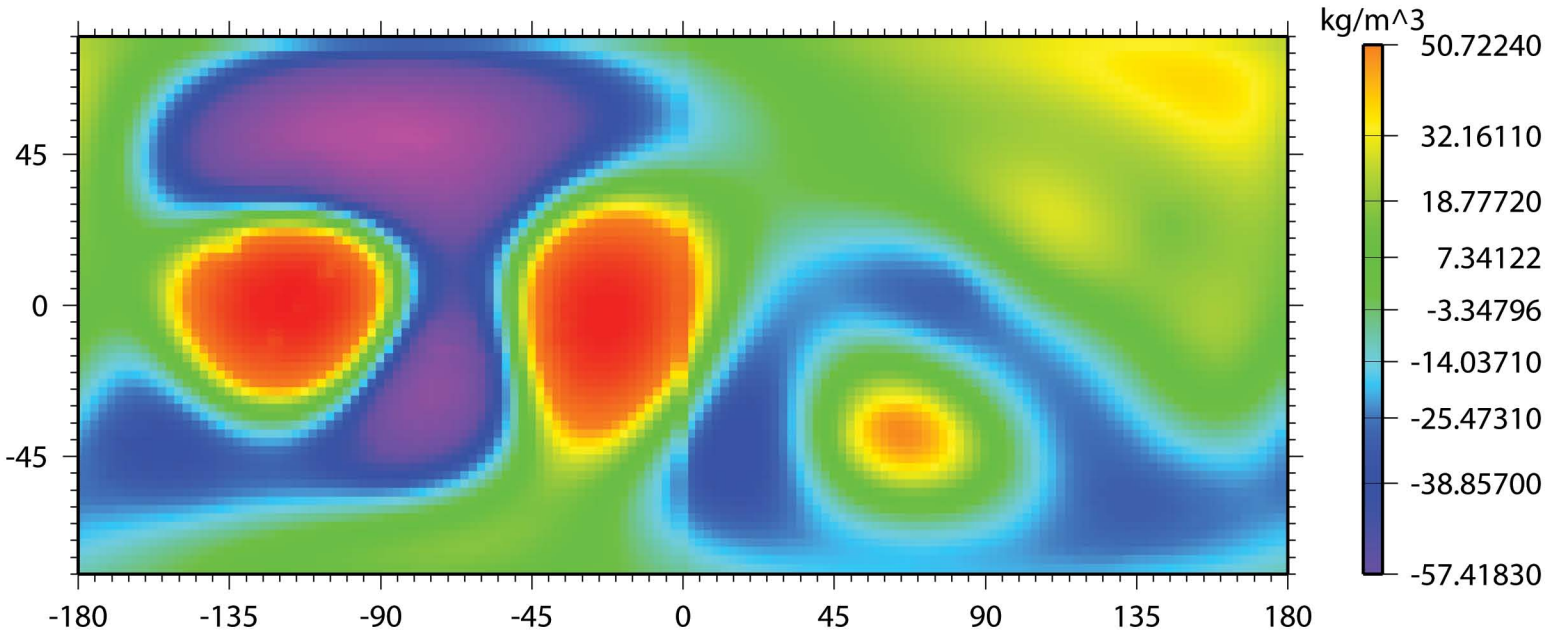
kg/m^3
50.72240
32.16110
18.77720
7.34122
-3.34796
-14.03710
-25.47310
-38.85700
-57.41830
45
0
-45
-180
-135
-90
-45
0
45
90
135
180

Bibliography

Anderson, R. C., J. M. Dohm, M. P. Golombek, A. F. C. Haldemann, B. J. Franklin, K. L. Tanaka, J. Lias, and B. Peer, Primary centers and secondary concentrations of tectonic activity through time in the western hemisphere of Mars, *Journal of Geophysical Research*, *106*, 20563–20586, 2001, DOI: 10.1029/2000JE001278.

Anderson, R. C., J. M. Dohm, A. F. C. Haldemann, E. Pounders, and M. P. Golombek, Tectonic evolution of Mars, in *37th Annual Lunar and Planetary Science Conference*, vol. 37, p. 1883, 2006.

Anderson, R. C., J. M. Dohm, A. F. C. Haldermann, E. Pounders, M. Golombek, and A. Castano, Centers of tectonic activity in the eastern hemisphere of Mars, *Icarus*, *195*(2), 537–546, 2008, Anderson, R. C. Dohm, J. M. Haldermann, A. F. C. Pounders, E. Golombek, M. Castano, A.

Andrews-Hanna, J. C., and M. T. Zuber, Strike-slip faulting and the tectonic evolution of Mars, in *Lunar and Planetary Institute Conference Abstracts*, vol. 38, p. 1897, 2007.

Banerdt, W. B., and M. P. Golombek, Tectonics of the Tharsis region of Mars: Insights from MGS topography and gravity, in *Lunar and Planetary Institute Conference Abstracts*, vol. 31, p. 2038, 2000.

Banerdt, W. B., M. P. Golombek, and K. L. Tanaka, Stress and tectonics on Mars, in *Mars*, pp. 249–297, 1992, n/a 1, 1992.

Chicarro, A. F., P. H. Schultz, and P. Masson, Global and regional ridge patterns on Mars, *Icarus*, *63*, 153–174, 1985, DOI: 10.1016/0019-1035(85)90025-9.

Dimitrova, L. L., W. E. Holt, A. J. Haines, and R. A. Schultz, Toward understanding the history and mechanisms of martian faulting: The contribution of gravitational potential energy, *Geophysical Research Letters*, *33*, 08202, 2006, DOI: 10.1029/2005GL025307.

Flesch, L. M., A. J. Haines, and W. E. Holt, Dynamics of the India-Eurasia collision zone, *Journal of Geophysical Research*, *106*, 16435–16460, 2001, DOI: 10.1029/2001JB000208.

Frey, H., Martian canyons and African rifts - structural comparisons and implications, *Icarus*, *37*, 142–155, 1979, A&AA ID. AAA025.097.008 DOI: 10.1016/0019-1035(79)90122-2.

Ghosh, A., W. E. Holt, L. Wen, A. J. Haines, and L. M. Flesch, Joint modeling of lithosphere and mantle dynamics elucidating lithosphere-mantle coupling, *Geophysical Research Letters*, *35*, 16309, 2008, DOI: 10.1029/2008GL034365.

Golombek, M. P., and R. J. Phillips, Mars, in press, 2009.

Greeley, R., and J. E. Guest, Geologic map of the western equatorial region of Mars, 1987.

Head, J. W., et al., Geological processes and evolution, *Space Science Reviews*, *96*, 263–292, 2001.

Hynek, B. M., and R. J. Phillips, Evidence for extensive denudation of the martian highlands, *Geology*, *29*, 407, 2001, DOI: 10.1130/0091-7613(2001)029.

Knapmeyer, M., J. Oberst, E. Hauber, M. Whlisch, C. Deuchler, and R. Wagner, Working models for spatial distribution and level of Mars' seismicity, *Journal of Geophysical Research (Planets)*, *111*, 11006, 2006, DOI: 10.1029/2006JE002708.

Mangold, N., P. Allemand, P. G. Thomas, and G. Vidal, Chronology of compressional deformation on Mars: evidence for a single and global origin, *Planetary and Space Science*, *48*, 1201–1211, 2000.

Mege, D., Graben morphology, dike emplacement, and tension fracturing in the Tharsis igneous province of Mars, in *The Fifth International Conference on Mars*, p. 6182, 1999.

Mege, D., A. C. Cook, E. Garel, Y. Lagabrielle, and M.-H. Cormier, Volcanic rifting at martian grabens, *Journal of Geophysical Research (Planets)*, *108*, 5044, 2003, DOI: 10.1029/2002JE001852.

Neumann, G. A., M. T. Zuber, M. A. Wieczorek, P. J. McGovern, F. G. Lemoine, and D. E. Smith, Crustal structure of Mars from gravity and topography, *Journal of Geophysical Research (Planets)*, *109*, 08002, 2004, DOI: 10.1029/2004JE002262.

Okubo, C. H., and R. A. Schultz, Variability in Early Amazonian Tharsis stress state based on wrinkle ridges and strike-slip faulting, *Journal of Structural Geology*, *28*, 2169–2181, 2006, DOI: 10.1016/j.jsg.2005.11.008.

Phillips, R. J., et al., Ancient geodynamics and global-scale hydrology on Mars, *Science*, *291*, 2587–2591, 2001, DOI: 10.1126/science.1058701.

Press, W. H., S. A. Teukolsky, W. T. Vetterling, and B. P. Flannery, *Numerical recipes in C. The art of scientific computing*, Cambridge: University Press, —c1992, 2nd ed., 1992, n/a 1, 1992.

Schultz, R. A., Strike-slip faulting of ridged plains near Valles Marineris, Mars, *Nature*, *341*, 424–426, 1989, DOI: 10.1038/341424a0.

Scott, D. H., and K. L. Tanaka, Geologic map of the western equatorial region of Mars, 1986.

Searls, M. L., and R. J. Phillips, Tectonics of Utopia basin, Mars: Results from finite element loading models, in *Lunar and Planetary Institute Conference Abstracts*, vol. 38, p. 1965, 2007.

Tanaka, K. L., The stratigraphy of Mars, *Journal of Geophysical Research*, *91*, 1986.

Tanaka, K. L., and D. H. Scott, Geologic map of the polar regions of Mars, 1987.

Tanaka, K. L., D. H. Scott, and R. Greeley, Global stratigraphy, in *Mars*, pp. 345–382, 1992, n/a 1, 1992.

Tanaka, K. L., J. A. Skinner, T. M. Hare, T. Joyal, and A. Wenker, Resurfacing history of the northern plains of Mars based on geologic mapping of Mars global surveyor data, *Journal of Geophysical Research-Planets*, *108*(E4), 2003.

Tanaka, K. L., J. M. Dohm, T. M. Hare, R. P. Irwin, E. J. Kolb, and J. A. Skinner, Mars geologic mapping: The next generation, *LPI Contributions*, *1353*, 3143, 2007.

Tanaka, K. L., J. A. P. Rodriguez, J. A. Skinner, M. C. Bourke, C. M. Fortezzo, K. E. Herkenhoff, E. J. Kolb, and C. H. Okubo, North polar region of Mars: Advances in stratigraphy, structure, and erosional modification, *Icarus*, *196*, 318–358, 2008, DOI: 10.1016/j.icarus.2008.01.021.

Watters, T. R., Thrust faults along the dichotomy boundary in the eastern hemisphere of Mars, *Journal of Geophysical Research (Planets)*, *108*, 5054, 2003, DOI: 10.1029/2002JE001934.

Watters, T. R., and T. A. Maxwell, Orientation, relative age, and extent of the Tharsis plateau ridge system, *Journal of Geophysical Research*, *91*, 8113–8125, 1986, DOI: 10.1029/JB091iB08p08113.

Wise, D. U., M. P. Golombek, and G. E. McGill, Tharsis province of Mars - geologic sequence, geometry, and a deformation mechanism, *Icarus*, *38*, 456–472, 1979, A&AA ID. AAA025.097.039 DOI: 10.1016/0019-1035(79)90200-8.

Woerner, W. R., E. K. Coraor, F. M. McCubbin, H. Nekvasil1, and D. H. Lindsley, The effect of pressure on residual liquid compositions from crystalization of a Humphrey-like magma: Implications for crustal stratigraphy in martian volcanic provinces., in *Lunar and Planetary Institute Conference Abstracts*, vol. 40, p. 2203, 2009.

Zuber, M. T., et al., Internal structure and early thermal evolution of Mars from Mars Global Surveyor topography and gravity, *Science*, *287*, 1788–1793, 2000, DOI: 10.1126/science.287.5459.1788.

Chapter 5

Dynamical Modelling for Generally Shaped, Layered Lithospheric Geometries Using Continuous Field Variables

Dynamical Modelling for Generally Shaped, Layered Lithospheric Geometries Using Continuous Field Variables

L.L. Dimitrova, A. J. Haines, L. M. Flesch, W. E. Holt, M. Haines, S. S.B. Haq

(to be submitted as part of collaborative paper to *Geophysical Journal International*)

5.1 Mathematical Development

Finite difference techniques optimize a functional of the form

$$\int_V W(u_i, \nabla_j u_i) dV - \int_{\partial V} \underline{u} \cdot \underline{T} dS \tag{1}$$

for static or pseudo-static problems to obtain the Euler-Lagrange equations

$$\nabla_j \left(\frac{\partial W}{\partial (\nabla_j u_i)} \right) - \frac{\partial W}{\partial u_i} = 0. \tag{2}$$

A choice of W such that

$$\frac{\partial W}{\partial (\nabla_j u_i)} = \sigma_{ij} \tag{3}$$

is the stress tensor and

$$-\frac{\partial W}{\partial u_i} = f_i \tag{4}$$

are the body forces, where $\underline{u}$ is velocity (fluid case) or displacement (elastic case), gives the force balance equations.

We modify the standard Euler-Lagrange variational approach for constructing the governing equations as follows to improve the stability and accuracy of numerical calculations. The key innovation is that, for the geophysical flow and elastic deformation problems of interest, the calculations are performed by separating all spatial dependencies into terms that can be related to coordinates on a reference surface and variations perpendicular to that surface. This results in considerable computational efficiency, as the problems are reduced to finite element calculations only in terms of the coordinates on the reference surface.

The second key ingredient, in common with the methodology developed for general

wave scattering problems *Haines and de Hoop* (1996); *Haines et al.* (2004), is that the computations are performed using only physical field quantities that are continuous across discontinuities in the medium, i.e., velocities/displacements and tractions. The advantage in this case is computational accuracy for laterally varying layers, including pinch outs. To formulate the problem in this way requires modification of the standard Euler-Lagrange variational approach for constructing the governing equations.

We introduce the key elements of solving the force balance equations using COMSOL Multiphysics. First, we will outline the geometry including the transformed vertical coordinates, the forms of tangential derivative and surface normals. We then explain the variational approach, including the forms of the functional minimized and the boundary constraints. Last, we discuss how medium properties are incorporated, to show that the the methodology can handle rheologies that are linear and non linear, spatially varying, and isotropic or anisotropic, followed by detailed expressions for the isotropic case.

5.1.1 Geometry

We address the aspect ratio problem of conventional finite difference methods by separating the problem into a horizontal component on a reference surface and a vertical component. In other words, we want to convert all non vertical surface integrals to integrals on the reference surface, and all volume integrals to integrals on the reference surface and integrals over the vertical coordinate. For reasons discussed below, the reference surface needs to be a line or a circle for 2-D problems, and a plane or a sphere for 3-D problems. Generally shaped reference surfaces cannot be used because of a need for forms of the spatial derivatives with respect to the reference-surface coordinates to be tangential to the reference surface at all points in the medium. However, sphere/circle reference surfaces (and plane/lines if using the flat-planet approximation) are perfectly adequate for real-planet problems where the deviation of the actual surface normal from the radial direction is small. We will denote the circle or sphere radius by r_0, where the line and plane case are derived in the limit of $r_0 \to \infty$.

We begin by introducing a modified depth χ below the reference surface:

$$\chi = \frac{1}{N r_0^{N-1}} \left(r_0^N - r^N \right) = \frac{r_0}{N} \left[1 - \left(\frac{r}{r_0} \right)^N \right], \tag{5}$$

where r is the radius at the point in question, measured from the origin of the reference surface, and $N = 2$ or 3 is the dimension.

Consider a general layered geometry, with layer boundaries chosen where discontinuities can exist in physical quantities (e.g. viscosity) and where quantities, for which we solve, are discontinuous (e.g. displacements across fault surfaces). Note that vertical boundaries project on the reference surface as curves and will be treated separately. The shape of each boundary can be denoted by $\chi_k(\phi, \theta)$ for $k = 1, 2, \ldots$, where ϕ is the longitude and θ is the latitude. We introduce a general depth coordinate ξ, which has a constant value at the layer boundaries. Inside the k^{th} layer we define, using linear interpolation,

$$\chi(\xi, \phi, \theta) = (k - \xi) \chi_{k-1}(\phi, \theta) + (\xi + 1 - k) \chi_k(\phi, \theta) \tag{6}$$

Note that $\chi(k, \phi, \theta) = \chi_k(\phi, \theta)$, and that within each layer, say the k^{th} layer,

$$\frac{\partial \chi}{\partial \xi} = \chi_k(\phi, \theta) - \chi_{k-1}(\phi, \theta), \tag{7}$$

which is constant, and equals the layer thickness in terms of the modified depth χ within each layer.

Next we convert all spatial derivatives to either tangential derivatives on the reference surface or derivatives with respect to the layer based depth coordinate ξ. We note that the tangential derivative with respect to the reference surface is given by

$$\nabla_0^{\perp} = \frac{r}{r_0} \left(\nabla - \hat{x} \frac{\partial}{\partial r} \right), \tag{8}$$

where $\hat{x}$ is the unit radial vector. Using eq. 5 in eq. 8 we obtain

$$\nabla = \frac{r_0}{r} \left\{ \nabla_0^{\perp} - \underline{\hat{x}} \left[1 - N \frac{\chi}{r_0} \right] \frac{\partial}{\partial \chi} \right\}, \tag{9}$$

In the above expression, the $\nabla_0^\perp$ is the tangential derivative of functions defined solely on the reference surface, where $\chi = 0$ and $r = r_0$. The $\frac{r_0}{r}$ factor in front of $\nabla_0^\perp$ modifies $\nabla_0^\perp$ to give the contribution to ∇ from derivatives with respect to the tangential coordinates at other values of χ or r. What we want is the contribution to ∇ from derivatives with respect to the tangential derivatives for fixed values of ξ, not χ. The expressions that follow are valid only when the reference surface is a sphere, a circle, a plane or a line. We will use ˜ to denote variables in expressions where ξ and not χ is held fixed, i.e. the curvilinear coordinates (χ, ϕ, θ) are transformed to coordinates $\left(\xi, \tilde{\phi}, \tilde{\theta}\right)$, where $\chi = \chi\left(\tilde{\phi}, \tilde{\theta}\right), \phi = \tilde{\phi}, \theta = \tilde{\theta}$, the velocity/displacement $\underline{u}$ becomes $\underline{\tilde{u}}$, etc.

Equation 9 can then be rewritten as

$$\nabla = \frac{r_0}{r}\nabla_0^\perp + (\nabla\chi)\frac{\partial}{\partial\chi}. \tag{10}$$

A similar expression for ∇ is obtained in terms of $\tilde{\nabla}^\perp$ and ξ

$$\nabla = \frac{r_0}{r}\tilde{\nabla}^\perp + (\nabla\xi)\frac{\partial}{\partial\xi}, \tag{11}$$

where $\tilde{\nabla}^\perp$ is the tangential derivative with respect to the reference surface with ξ fixed and relates to the tangential derivative with respect to the reference surface,$\nabla_0^\perp$ by

$$\frac{\partial\chi}{\partial\xi}\nabla_0^\perp = \frac{\partial\chi}{\partial\xi}\tilde{\nabla}^\perp - \left(\tilde{\nabla}^\perp\chi\right)\frac{\partial}{\partial\xi}. \tag{12}$$

The gradient, $\nabla\xi$, and the derivative,$\frac{\partial}{\partial\xi}$, of ξ are expressed in terms of the known expressions for $\nabla\chi$, $\tilde{\nabla}^\perp\chi$, and $\frac{\partial\chi}{\partial\xi}$ as follows

$$\frac{\partial\chi}{\partial\xi}(\nabla\xi) = -\frac{r_0}{r}\tilde{\nabla}^\perp\chi - \hat{x}\frac{r_0}{r}\left(1 - N\frac{\chi}{r_0}\right), \text{ and} \tag{13}$$

$$\frac{\partial}{\partial\xi} = \frac{\partial\chi}{\partial\xi}\frac{\partial}{\partial\chi}. \tag{14}$$

Finally, a scaled normal to layer boundaries (and all surface defined by $\xi = const$) is

given by

$$\underline{\tilde{n}} = -\tilde{\nabla}^{\perp}\chi - \underline{\hat{x}}\left[1 - N\frac{\chi}{r_0}\right]. \tag{15}$$

Rewriting eq. 13 and eq. 11 in terms of $\underline{\tilde{n}}$ results in

$$\frac{\partial\chi}{\partial\xi}(\nabla\xi) = \frac{r_0}{r}\underline{\tilde{n}}, \text{ and} \tag{16}$$

$$\frac{\partial\chi}{\partial\xi}\nabla = \frac{r_0}{r}\left\{\frac{\partial\chi}{\partial\xi}\tilde{\nabla}^{\perp} + \underline{\tilde{n}}\frac{\partial}{\partial\xi}\right\} \tag{17}$$

Lastly, we will note that within each layer, functions are defined as polynomials, and consequently, the lower the order of polynomials the more accurate the computation. To that effect, $\underline{\tilde{n}}$ is a linear function of ξ within each layer, since χ is a linear function of ξ within each layer.

5.1.2 Modified Euler-Lagrange Equations

The functional optimized is

$$\begin{aligned}\int_V W\left(u_i, \nabla_j u_i\right) dV \quad &- \int_{\partial V_T} \underline{u}\cdot\underline{T}\, dS \\ &- \int_{\partial V_u} \underline{\tau}\cdot(\underline{u} - \underline{U})\, dS,\end{aligned} \tag{18}$$

where ∂V_T and ∂V_u are the portions of the boundary ∂V of the volume V, with the traction boundary condition, $\underline{T}$, applied on ∂V_T, and the velocity/displacement boundary condition $\underline{U}$ applied velocity/displacement on ∂V_u. $\underline{\tau}$ is the Lagrange multiplier introduced so that optimizing with respect to τ determines that the corresponding velocity/displacement boundary condition is satisfied on ∂V_u.

To use COMSOL Multiphysics, the integrals involved in this functional have to be converted into combinations of integrals on the reference surface and integrals with respect to the layer based depth coordinate ξ. Therefore, we subdivide V into the volumes V_k in L layers $k = 1, \ldots, L$, and some geometries will have vertical boundaries to the V_k volumes.

Then eq. 18 becomes

$$\sum_{k=1}^{L}\left\{\int_{V_k} W dV - \int_{\partial V_T^k} \underline{u}\cdot\underline{T} dS - \int_{\partial V_u^k} \underline{\tau}\cdot(\underline{u}-\underline{U})\, dS\right\} \tag{19}$$
$$- \int_{\substack{\xi=0\\ \underline{x}\in\partial V_T}} \underline{u}\cdot\underline{T} dS - \int_{\substack{\xi=0\\ \underline{x}\in\partial V_u}} \underline{\tau}\cdot(\underline{u}-\underline{U})\, dS$$
$$- \sum_{k=1}^{L-1}\left\{\int_{\xi=k} \underline{v}^k\cdot\left(\underline{T}^{k+1}-\underline{T}^k\right) dS\right.$$
$$\left. - \int_{\xi=k} \underline{\tau}^k\cdot\left(\underline{u}^{k+1}-\underline{u}^k\right) dS\right\}$$
$$- \int_{\substack{\xi=L\\ \underline{x}\in\partial V_T}} \underline{u}\cdot\underline{T} dS - \int_{\substack{\xi=L\\ \underline{x}\in\partial V_u}} \underline{\tau}\cdot(\underline{u}-\underline{U})\, dS.$$

Here ∂V_T^k and ∂V_u^k denote the portions of the vertical boundaries (if any) of the k^{th} layer where traction and velocity/displacement boundary conditions are applied; $\left\{\begin{smallmatrix}\xi=0\\ \underline{x}\in\partial V_T\end{smallmatrix}\right\}$, $\left\{\begin{smallmatrix}\xi=0\\ \underline{x}\in\partial V_u\end{smallmatrix}\right\}$, and $\left\{\begin{smallmatrix}\xi=L\\ \underline{x}\in\partial V_T\end{smallmatrix}\right\}$, $\left\{\begin{smallmatrix}\xi=L\\ \underline{x}\in\partial V_u\end{smallmatrix}\right\}$, are the corresponding portions of the top ($\xi=0$) and bottom ($\xi=L$) boundaries of the model, $\underline{T}^k$ and $\underline{T}^{k+1}$are the tractions, and $\underline{u}^k$ and $\underline{u}^{k+1}$are the velocities/displacements on the k^{th} and $(k+1)^{th}$ layer on either side of the layer boundary $k=\xi$. For the intermediate layer boundaries ($\xi=1,\ldots,L-1$) we have introduced Lagrange constraints to ensure continuity of tractions and velocity/displacement with the associated Lagrange multipliers denoted by $\underline{v}^k$ and $\underline{\tau}^k$. Increments in volume dV are given by

$$dV = \frac{\partial\chi}{\partial\xi} d\xi dS_0. \tag{20}$$

Increments in surface area dS is given by

$$\underline{n} dS = \pm\frac{r_0}{r}\tilde{\underline{n}} dS_0 \tag{21}$$

for surfaces on which $\xi = const$, where dS_0 is the increment in area of the projection onto

the reference surface of dS, and

$$\underline{n}dS = \pm\frac{r_0}{r}\underline{n}^0 dl_0 \frac{\partial \chi}{\partial \xi} d\xi \tag{22}$$

for vertical boundaries, where dl_0 is the increment in arc-length of the projection onto the reference surface of dS, and $\underline{n}^0$ is the normal to that projection curve in the reference surface.

We next note that the functions integrated in the surface integrals of eq. 19 are all of the form of velocity/displacement multiplied by a traction/traction-like term, i.e., the surface integral terms are generally of the form

$$\begin{aligned}
\int \underline{u} \cdot \underline{T} dS &= \int u_i T_i dS \\
&= \int u_i \sigma_{ij} n_j dS \\
&= \begin{cases} \pm\iint u_i \sigma_{ij} \frac{r_0}{r} \tilde{n}_j dS_0 \text{ for boundaries } \xi\text{=}const \\ \pm\iint u_i \sigma_{ij} \frac{r_0}{r} n_j^0 dl_0 \frac{\partial \chi}{\partial \xi} d\xi \text{ for vertical boundaries} \end{cases} \\
&= \begin{cases} \pm\iint \tilde{u}_i \tilde{\sigma}_{in} dS_0 \text{ for boundaries } \xi\text{=}const \\ \pm\iint \tilde{u}_i \sigma_{in}^0 dl_0 \frac{\partial \chi}{\partial \xi} d\xi \text{ for vertical boundaries} \end{cases},
\end{aligned} \tag{23}$$

where we have introduced the modified velocity/displacement

$$\underline{\tilde{u}} = \frac{r_0}{r}\underline{u}, \tag{24}$$

and modified tractions

$$\tilde{\sigma}_{in} = \sigma_{ij}\tilde{n}_j \text{ for boundaries } \xi\text{=}const \tag{25}$$

$$\sigma_{in}^0 = \sigma_{ij} n_j^0 \text{ for vertical boundaries.} \tag{26}$$

The gradient of velocity/displacement $\underline{u}$ can be expressed using eq. 17 and 24 as

$$\frac{\partial \chi}{\partial \xi} \nabla_j u_i = \frac{\partial \chi}{\partial \xi} \tilde{\nabla}_j^{\perp} \tilde{u}_i + \tilde{n}_j \frac{\partial \tilde{u}_i}{\partial \xi} + \frac{\partial \chi}{\partial \xi} \hat{x}_j \frac{\tilde{u}_i}{r_0}. \tag{27}$$

The quantities $\tilde{u}_i$, $\tilde{\nabla}_j^{\perp} \tilde{u}_i$, and $\tilde{\sigma}_{in}$ are continuous across non-vertical interfaces, while $\frac{\partial \tilde{u}_i}{\partial \xi}$ is not. Therefore, we convert to using $\tilde{u}_i$, $\tilde{\nabla}_j^{\perp} \tilde{u}_i$, and $\tilde{\sigma}_{in}$ as the basic variables in the variational approach. We first note that

$$\tilde{\sigma}_{in} = \frac{\partial W}{\partial \left(\frac{\partial \tilde{u}_i}{\partial \xi} \right)} \frac{\partial \chi}{\partial \xi}, \tag{28}$$

and define a new functional

$$\tilde{W} \left(\tilde{u}_i, \tilde{\nabla}_j^{\perp} \tilde{u}_i, \tilde{\sigma}_{in} \right) = \tilde{\sigma}_{in} \frac{\partial \tilde{u}_i}{\partial \xi} - W \frac{\partial \chi}{\partial \xi}. \tag{29}$$

Derivatives of $\tilde{W}$ are given by:

$$\frac{\partial \tilde{W}}{\partial \tilde{\sigma}_{in}} = \frac{\partial \tilde{u}_i}{\partial \xi}, \tag{30}$$

$$\frac{\partial \tilde{W}}{\partial \tilde{u}_i} = \frac{\partial \chi}{\partial \xi} \left(\frac{r}{r_0} f_i - \frac{1}{r_0} \sigma_{ij} \hat{x}_j \right), \tag{31}$$

and

$$\frac{\partial \tilde{W}}{\partial (\tilde{\nabla}_j^{\perp} \tilde{u}_i)} = -\frac{\partial \chi}{\partial \xi} \sigma_{il} (\delta_{jl} - \hat{x}_j \hat{x}_l), \tag{32}$$

where $(\delta_{jl} - \hat{x}_j \hat{x}_l)$ is the horizontal projection operator. We thus define $\tilde{f}_i = \frac{r}{r_0} f_i$. Note that then $\underline{u} \cdot \underline{f} = \underline{\tilde{u}} \cdot \underline{\tilde{f}}$.

We replace $W\frac{\partial\chi}{\partial\xi}$ with $\left[\tilde{\sigma}_{in}\frac{\partial\hat{u}_i}{\partial\xi}-\tilde{W}\right]$ in eq. 19 to obtain

$$\sum_{k=1}^{L}\int_{k-1}^{k}\left\{\int_{S_0}\left[\tilde{\sigma}_{in}\frac{\partial\hat{u}_i}{\partial\xi}-\tilde{W}\right]dS_0-\left[\int_{\partial S_{0T}^k}\underline{\tilde{u}}\cdot\underline{T}^0dl_0-\int_{\partial S_{0u}^k}\underline{\tau}^0\cdot\left(\underline{\tilde{u}}-\underline{\tilde{U}}\right)dl_0\right]\frac{\partial\chi}{\partial\xi}\right\}d\xi \quad (33)$$
$$+\int_{\substack{\xi=0\\ \underline{x}\in\partial V_T}}\underline{\tilde{u}}\cdot\underline{\tilde{T}}^{\xi}dS_0+\int_{\substack{\xi=0\\ \underline{x}\in\partial V_u}}\underline{\tilde{\tau}}^{\xi}\cdot\left(\underline{\tilde{u}}-\underline{\tilde{U}}\right)dS_0$$
$$-\sum_{k=1}^{L-1}\left\{\int_{\xi=k}\underline{\tilde{v}}^k\cdot\left(\tilde{\sigma}_{in}^{k+1}-\tilde{\sigma}_{in}^k\right)dS_0+\int_{\xi=k}\underline{\tilde{\tau}}^{\xi k}\cdot\left(\underline{\tilde{u}}^{k+1}-\underline{\tilde{u}}^k\right)dS_0\right\}$$
$$-\int_{\substack{\xi=L\\ \underline{x}\in\partial V_T}}\underline{\tilde{u}}\cdot\underline{\tilde{T}}^{\xi}dS_0-\int_{\substack{\xi=L\\ \underline{x}\in\partial V_u}}\underline{\tilde{\tau}}^{\xi}\cdot\left(\underline{\tilde{u}}-\underline{\tilde{U}}\right)dS_0,$$

where $T_i^0=\sigma_{ij}n_j^0$ and $\tilde{T}_i^{\xi}=\sigma_{ij}\tilde{n}_j$.

On optimizing eq. 33 with respect to $\tilde{\sigma}_{in}$ we get back eq. 30

$$\frac{\partial\tilde{u}_i}{\partial\xi}=\frac{\partial\tilde{W}}{\partial\tilde{\sigma}_{in}}, \quad (34)$$

and optimizing eq. 33 with respect to $\tilde{u}_i$ and integrating by parts with respect to the horizontal coordinates as well as ξ, the Euler-Lagrange equation is then

$$-\frac{\partial\tilde{\sigma}_{in}}{\partial\xi}=\frac{\partial\tilde{W}}{\partial\tilde{u}_i}-\tilde{\nabla}_j^{\perp}\left(\frac{\partial\tilde{W}}{\partial(\tilde{\nabla}_j^{\perp}\tilde{u}_i)}\right). \quad (35)$$

Additionally we get $T_i^0=\sigma_{ij}n_j^0=\underline{\tau}_i^0,\tilde{T}_i^{\xi}=\tilde{\sigma}_{in}=\underline{\tilde{\tau}}_i^{\xi}$, and $\tilde{\sigma}_{in}^{k+1}=\tilde{\sigma}_{in}^k$.

Together eqs. 34 and 35 define the dependence of $\tilde{u}_i$ and $\tilde{\sigma}_{in}$ on the depth coordinate ξ. All that remains to be done is to obtain expressions for σ_{ij} and $\frac{\partial\tilde{W}}{\partial\tilde{\sigma}_{in}}$, which will require the additional of the stress-strain relationship and will account for the material properties.

5.1.3 Material Properties

To obtain expressions for σ_{ij} and $\frac{\partial \tilde{W}}{\partial \tilde{\sigma}_{in}}$, we need the stress-strain relation, which depends on the material properties. We begin by showing the relations for an anisotropic rheology, which have a compact form, and then give the expression for an isotropic rheology.

Anisotropic Rheology

Consider an anisotropic rheology with W of the form

$$W(u_i, \nabla_j u_i) = \frac{1}{2} F(D^2) - u_i f_i, \tag{36}$$

where

$$D^2 = \nu_{ijpq} (\nabla_j u_i)(\nabla_p u_q) \text{ and } \nu_{ijpq} = \nu_{qpji}. \tag{37}$$

For such a rheology, eq. 3 gives

$$\sigma_{ij} = \frac{\partial W}{\partial (\nabla_j u_i)} = F'(D^2) \nu_{ijpq} (\nabla_p u_q), \tag{38}$$

where $F'(D^2)$ is the derivative of $F(D^2)$ with respect to D^2. Examples include power-law rheologies

$$F(D^2) = b \frac{2n}{(n+1)} D^{1+\frac{1}{n}}, F'(D^2) = b D^{\frac{1}{n}-1}, \tag{39}$$

where the case $n = 1$ corresponds to a standard linear anisotropic relationship between σ_{ij} and $\nabla_j u_i$.

Recall that from eq. 25 and 27

$$\frac{\partial \chi}{\partial \xi} \nabla_j u_i = \frac{\partial \chi}{\partial \xi} \left[\tilde{\nabla}_j^{\perp} \tilde{u}_i + \frac{1}{r_0} \hat{x}_j \tilde{u}_i \right] + \tilde{n}_j \frac{\partial \tilde{u}_i}{\partial \xi}, \text{ and} \tag{40}$$

$$\tilde{\sigma}_{in} = \sigma_{ij} \tilde{n}_j \tag{41}$$

We want to convert the relationship between σ_{ij} and $\nabla_j u_i$ into a relationship between σ_{ij}

and a combination of $\tilde{u}_i$, $\tilde{\nabla}_j^{\perp}\tilde{u}_i$ and $\tilde{\sigma}_{in}$. We define

$$d_{pq} = \tilde{\nabla}_p^{\perp}\tilde{u}_q + \frac{1}{r_0}\hat{x}_p\tilde{u}_q, \tag{42}$$

$$\tilde{\nu}_{inpq} = \nu_{ijpq}\tilde{n}_j, \tag{43}$$

$$\tilde{\nu}_{ijnq} = \nu_{ijpq}\tilde{n}_p, \tag{44}$$

$$\tilde{\nu}_{innq} = \nu_{ijpq}\tilde{n}_j\tilde{n}_p, \tag{45}$$

and $\tilde{\eta}_{iq}$ will denote the second-rank tensor inverse of $\tilde{\nu}_{innq}$. From

$$\frac{\partial\chi}{\partial\xi}\sigma_{ij} = \frac{\partial\chi}{\partial\xi}F'(D^2)\nu_{ijpq}d_{pq} + F'(D^2)\tilde{\nu}_{ijnq}\frac{\partial\tilde{u}_q}{\partial\xi} \tag{46}$$

it follows that

$$\frac{\partial\chi}{\partial\xi}\tilde{\sigma}_{in} = \frac{\partial\chi}{\partial\xi}F'(D^2)\tilde{\nu}_{inpq}d_{pq} + F'(D^2)\tilde{\nu}_{innq}\frac{\partial\tilde{u}_q}{\partial\xi}, \tag{47}$$

and hence,

$$\frac{\partial\tilde{u}_i}{\partial\xi} = \frac{\partial\chi}{\partial\xi}\left\{\frac{1}{F'(D^2)}\tilde{\eta}_{ik}\tilde{\sigma}_{kn} - \tilde{\eta}_{ik}\tilde{\nu}_{knrs}d_{rs}\right\}. \tag{48}$$

The right-hand side of this last equation (48) is one of the desired expressions, that for $\frac{\partial\tilde{W}}{\partial\tilde{\sigma}_{in}}$. To obtain the expression for σ_{ij} we substitute for $\frac{\partial\tilde{u}_q}{\partial\xi}$ into the first of the above equations (46):

$$\sigma_{ij} = F'(D^2)\left[\nu_{ijrs} - \tilde{\nu}_{ijnq}\tilde{\eta}_{qk}\tilde{\nu}_{knrs}\right]d_{rs} + \tilde{\nu}_{ijnq}\tilde{\eta}_{qk}\tilde{\sigma}_{kn} \tag{49}$$

Isotropic Rheology

For a linear rheology $F(D^2) = D^2$. Then $F'(D^2) = 1$ and equation 38 becomes

$$\sigma_{ij} = \nu_{ijpq}\nabla_p u_q \tag{50}$$

In terms of the Lamé parameters λ and μ the constitutive relation in the isotropic case is given by

$$\sigma_{ij} = \lambda\varepsilon_{kk}\delta_{ij} + 2\mu\varepsilon_{ij}, \tag{51}$$

where $\varepsilon_{ij} = \frac{1}{2}\left(\frac{\partial u_i}{\partial x_j} + \frac{\partial u_j}{\partial x_i}\right)$ is the strain, δ_{ij} is the Kronecker delta function, and summation notation is implied, i.e., ε_{kk} is the dilatation. Rewriting in terms of $\nabla_p u_q$ gives

$$\sigma_{ij} = \left[\lambda\delta_{ij}\delta_{pq} + \mu\left(\delta_{ip}\delta_{jq} + \delta_{iq}\delta_{jp}\right)\right]\nabla_p u_q. \tag{52}$$

Then

$$\nu_{ijpq} = \lambda\delta_{ij}\delta_{pq} + \mu\left(\delta_{ip}\delta_{jq} + \delta_{iq}\delta_{jp}\right), \tag{53}$$

and equations 43-45 become

$$\begin{aligned}
\tilde{\nu}_{inpq} &= \nu_{ijpq}\tilde{n}_j = \lambda\tilde{n}_i\delta_{pq} + \mu\left(\delta_{ip}\tilde{n}_q + \delta_{iq}\tilde{n}_p\right) && (54)\\
\tilde{\nu}_{ijnq} &= \nu_{ijpq}\tilde{n}_p = \lambda\delta_{ij}\tilde{n}_q + \mu\left(\delta_{jq}\tilde{n}_i + \delta_{iq}\tilde{n}_j\right) && (55)\\
\tilde{\nu}_{innq} &= \nu_{ijpq}\tilde{n}_j\tilde{n}_p = \lambda\tilde{n}_i\tilde{n}_q + \mu\left(\tilde{n}_i\tilde{n}_q + \delta_{iq}|\tilde{n}|^2\right) && (56)\\
&= (\lambda+2\mu)\,\tilde{n}_i\tilde{n}_q + \mu|\tilde{n}|^2\left(\delta_{iq} - \frac{\tilde{n}_i\tilde{n}_q}{|\tilde{n}|^2}\right).
\end{aligned}$$

The second rank tensor inverse of $\tilde{\nu}_{innq}$ is

$$\tilde{\eta}_{iq} = \frac{1}{(\lambda+2\mu)\,|\tilde{n}|^4}\tilde{n}_i\tilde{n}_q + \frac{1}{\mu|\tilde{n}|^2}\left(\delta_{iq} - \frac{\tilde{n}_i\tilde{n}_q}{|\tilde{n}|^2}\right). \tag{57}$$

The last term that needs to be evaluated for equation 48 is

$$\begin{aligned}
\tilde{\eta}_{ik}\tilde{\nu}_{knrs} = &\quad \tfrac{\lambda}{(\lambda+2\mu)|\tilde{n}|^2}\tilde{n}_i\delta_{rs} + \tfrac{2\mu}{(\lambda+2\mu)|\tilde{n}|^4}\tilde{n}_i\tilde{n}_r\tilde{n}_s && (58)\\
+ &\quad \tfrac{1}{|\tilde{n}|^2}\left[\left(\delta_{ir} - \tfrac{\tilde{n}_i\tilde{n}_r}{|\tilde{n}|^2}\right)\tilde{n}_s + \left(\delta_{is} - \tfrac{\tilde{n}_i\tilde{n}_s}{|\tilde{n}|^2}\right)\tilde{n}_r\right]
\end{aligned}$$

Finally, for equation 49 we need to evaluate

$$\begin{aligned}
\nu_{ijrs} - \tilde{\nu}_{ijnq}\tilde{\eta}_{qk}\tilde{\nu}_{knrs} = &\quad \tfrac{2\lambda\mu}{\lambda+2\mu}\left(\delta_{ij} - \tfrac{\tilde{n}_i\tilde{n}_j}{|\tilde{n}|^2}\right)\left(\delta_{rs} - \tfrac{\tilde{n}_r\tilde{n}_s}{|\tilde{n}|^2}\right) && (59)\\
+ &\quad \mu\left[\left(\delta_{ir} - \tfrac{\tilde{n}_i\tilde{n}_r}{|\tilde{n}|^2}\right)\left(\delta_{js} - \tfrac{\tilde{n}_j\tilde{n}_s}{|\tilde{n}|^2}\right)\right.\\
+ &\quad \left.\left(\delta_{is} - \tfrac{\tilde{n}_i\tilde{n}_s}{|\tilde{n}|^2}\right)\left(\delta_{jr} - \tfrac{\tilde{n}_j\tilde{n}_r}{|\tilde{n}|^2}\right)\right].
\end{aligned}$$

5.2 2-D Example for a Two Layer Lithosphere on a Circle

We consider a simple 2-D example on a circle consisting of a crust with density of $2900 kg.m^{-3}$ and mantle with density of $3500 kg.m^{-3}$ and shear modulus or viscosity ratio of crust to mantle of 0.5. We define a mountain with sinusoidal shape with adjusted maximum height (-χ) of 0.005 on a unit circle (see Fig 1). These numbers correspond roughly to the height and wavelength of Tharsis on Mars. The crustal thickness is calculated as the one needed to achieve Airy isostasy, which results in a pinch out in the mantle layer underneath the peak. In addition, since the pressure differences at the base of the lithosphere are zero, we expect no flexural stresses. We insert a zero thickness layer between the crust and the mantle, which we use to allow for slip between the two layers.

We show the radial (Ur) and tangential (Up) adjusted displacements (Figure 2), radial (Tr) and tangential (Tp) adjusted tractions (Figure 3), and the three components of adjusted stress (Figure 4) for three cases with increasing amount of slip between the layers.

In all three cases, the radial displacement is large and negative (pointing downwards) at the peak and gradually transitions to smaller and positive in the periphery. The tangential displacement is symmetric around the peak. This is consistent with the expected behavior of a mountain relaxation and slight overall crustal thickening. If no slip is allowed between the two layers, the displacements are continuous. As we increase the amount of slip between the layers, a larger portion of the displacement is accommodated by the slip, leading to decreased displacement in the mantle. At slip of $5e-1$, $\sim 40\%$ of the horizontal displacements in the upper layer are accounted for in the slip layer, leaving $\sim 60\%$ for the lower layer. At slip of $5e0$, $\sim 80\%$ of the horizontal displacements in the upper layer are accounted for in the slip layer, leaving $\sim 20\%$ for the lower layer.

The tractions are continuous, and do not change much for the different slip cases, because they are dominated by the pressure, which also dominated the mean normal stress component $(Srr+Spp)/2$.

Layers that pinch out represent a singularity for the system of differential equations we solve. However, singularities in this method are well contained both spatially and in magnitude (see the $(Spp-Srr)/2$ component of stress for the no slip case in Fig. 4).

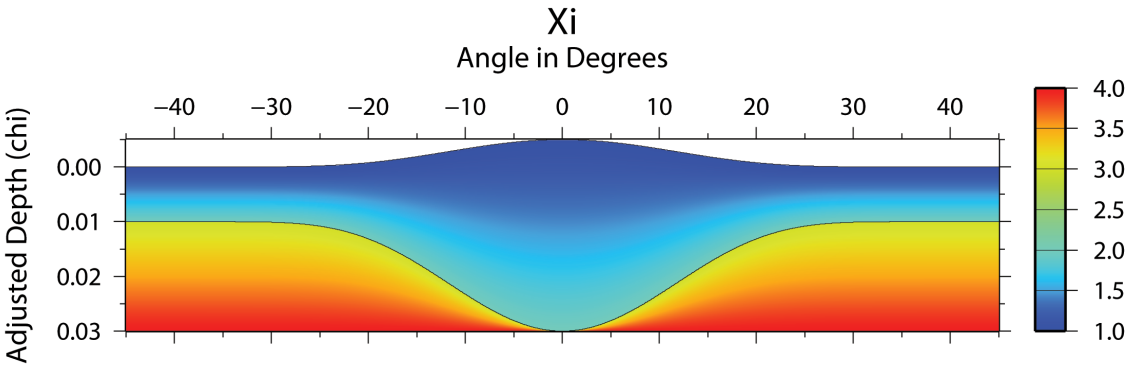

Figure 1: Geometry of a 2-D example on a circle in terms of adjusted depth χ consisting of 3 layers – crust, mantle and an infinitesimally thin layer used to allow for slip between the other two layers. The layer boundaries ξ take values from 1 to 4.

Figure 2: The radial and tangential components of displacement for three values of slip between the layers: 0, $5e-1$, $5e0$.

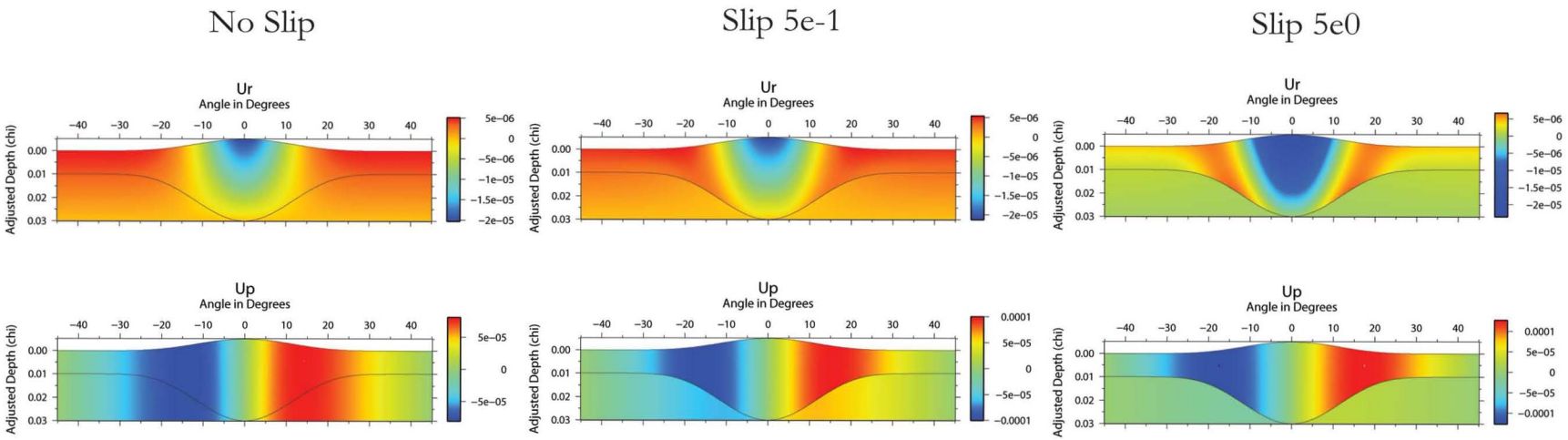
No Slip
Slip 5e-1
Slip 5e0
Ur
Up
Angle in Degrees
Adjusted Depth (chi)

Figure 3: The radial and tangential components of adjusted tractions for three values of slip between the layers: 0, $5e-1$, $5e0$.

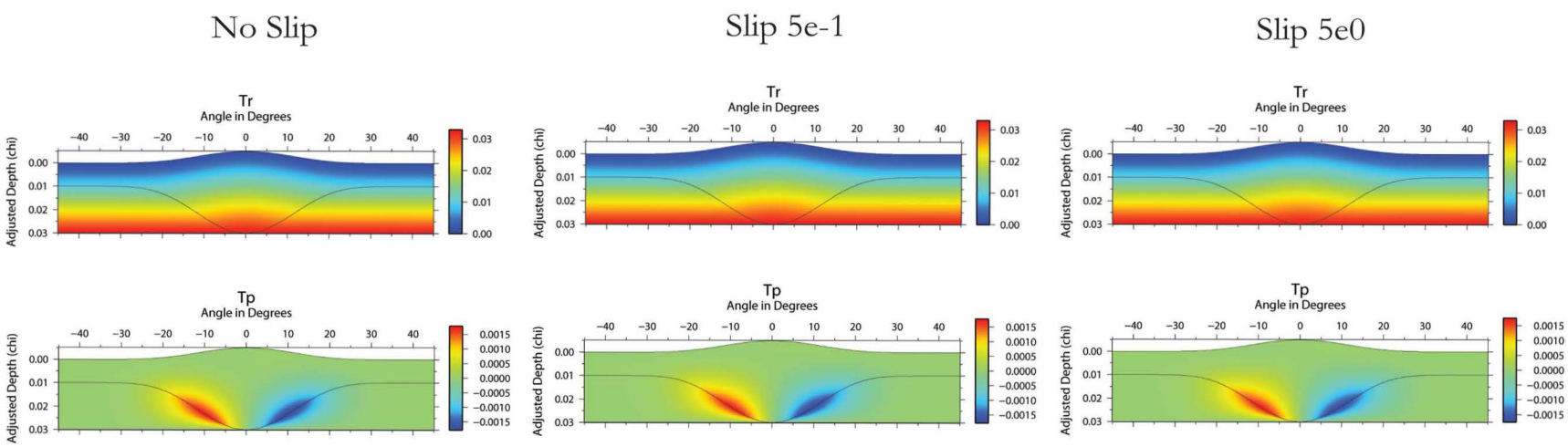
No Slip
Slip 5e-1
Slip 5e0
Tr
Angle in Degrees
Adjusted Depth (chi)
Tp
Angle in Degrees
Adjusted Depth (chi)

Figure 4: The radial and tangential components of three components of adjusted stress for three values of slip between the layers: 0, $5e-1$, $5e0$. Note the well contained (in space and magnitude) singularity due to the pinched out mantle layer.

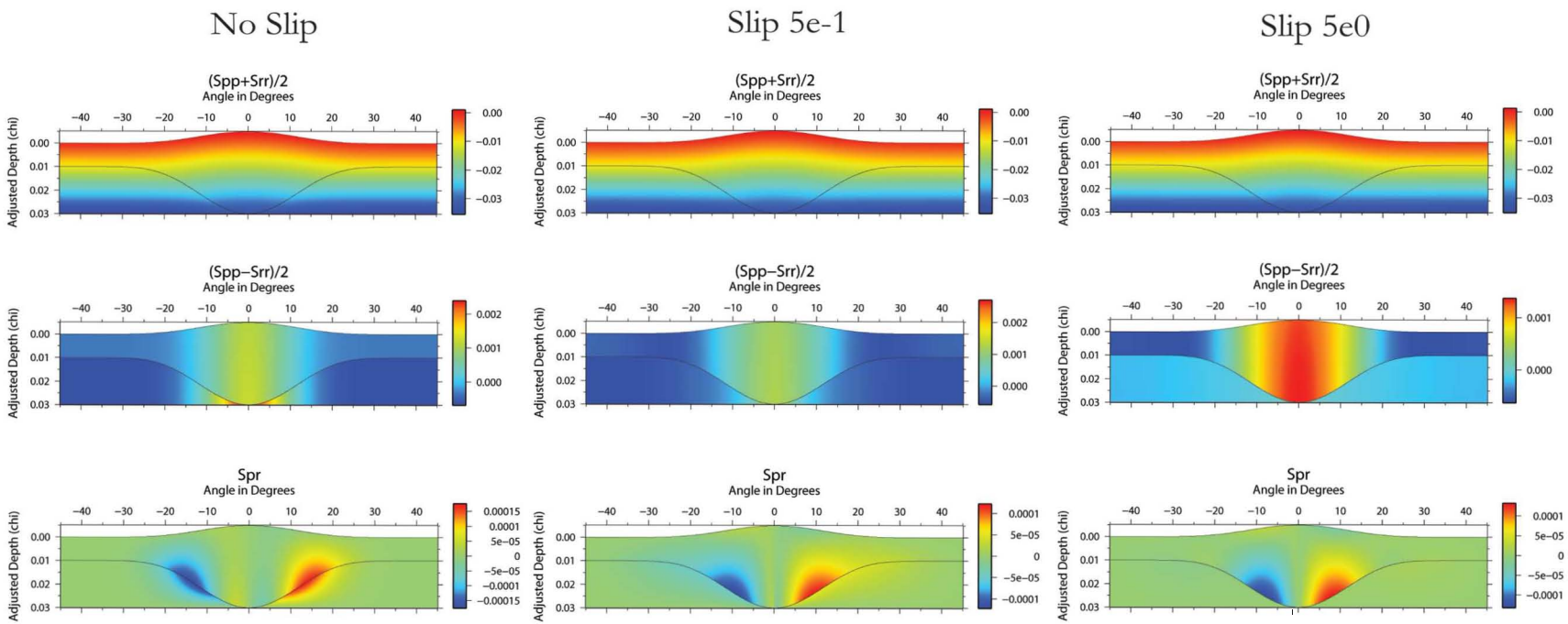
No Slip
Slip 5e-1
Slip 5e0
(Spp+Srr)/2
(Spp−Srr)/2
Spr
Angle in Degrees
Adjusted Depth (chi)

Bibliography

Haines, A. J., and M. V. de Hoop, An invariant imbedding analysis of general wave scattering problems, *Journal of Mathematical Physics*, *37*, 3854–3881, 1996, DOI: 10.1063/1.531606.

Haines, A. J., T. Hulme, and J. Yu, General elastic wave scattering problems using an impedance operator approach - i. mathematical development, *Geophysical Journal International*, *159*, 643–657, 2004, DOI: 10.1111/j.1365-246X.2004.02405.x.

Chapter 6

Conclusions

Conclusions

In this work, I use MGS MOLA and Radio Science data products (topography and gravity) to systematically test new geodynamic models and evaluate lithosphere dynamics on Mars as a function of time, while satisfying geologic surface observations (surface features) that have been and are being catalogued and studied from Viking, MOLA, MOC, and THEMIS IR images. Normal faults and wrinkle ridges are not synchronous according to the inferred stratigraphic ages.

I investigate (1) the role of internal loads (internal body force effects), (2) loading from the surface and base of lithosphere, and the effects of this loading on membrane and flexural strains and stresses, and (3) the role of global contraction, all viewed in the context of how the surface elastic layer has changed as the planet has evolved.

Previous stress solutions for Mars match the long wavelength signal of present day topography and gravity but fail to match many of the surface faults, including northern Claritas Fossae north to Tantalus and Alba Fossae. Here, I have shown that a deviatoric stress field associated with horizontal gradients of gravitational potential energy (GPE) provides an excellent fit to most of the normal faults in Tharsis as well as many wrinkle ridges circumferential to Tharsis. This result suggests that many of the faults were created at times when elastic thicknesses and membrane and flexural stresses were small, a combination of brittle and ductile deformation was likely to be widespread, and GPE stresses dominated.

Global stress models need to be scored by global tectonic data. Currently two datasets of surface breaking normal and reverse faults exist – *Anderson* [2001], *Anderson et al.* [2008] and *Knapmeyer et al.* [2006]. I compare the two datasets using a misfit function designed to compare fault styles and strikes only. The two datasets are similar, with very few exceptions. Firstly, while both *Anderson et al.* [2001] and *Knapmeyer et al.* [2006] mapped faults whose strikes vary into two or more segments, only the *Knapmeyer* [2006] dataset retains the information about the segmentation. Therefore, the absolute magnitude of the strain will vary depending on which dataset is used. The spatial coverage by the two datasets differs only in the periphery of Tharsis.

I also consider end-member flexure-dominated models. I examine the flexure-dominated

model of *Banerdt and Golombek* [2000] and a membrane model, associated with dynamic topography, and show that they fail to fit coevally the current fault data. These models demonstrate just a few of the possible scenarios for the non-unique problem of the loading history of Tharsis. Yet, neither model fits the normal faults in and around Tharsis as well as the GPE model. Since the faults reflect the thermal state of the planet at the time of their formation, I argue that many of the faults were created at times when elastic thicknesses and membrane and flexural stresses were small and topography was supported by buoyancy forces.

It has long been known that the cooling of a planet gives rise to global deviatorically compressive thermal stresses. These thermal stresses have been considered as a possible explanation for reverse faulting on Mercury and Mars. I have evaluated the contribution of global contraction as recorded by the global fault data set in the presence of a lithospheric stress field associated with horizontal GPE gradients.

Fitting only the reverse faults, while disregarding other tectonic features, can be achieved trivially with global contraction stresses. The associated strains, radius decrease, and required temperature changes, are very small and are consistent with forward thermodynamical models of global contraction. However, global contraction cannot fit both normal and reverse faults. Consequently, the normal faults may have formed before the southern hemisphere reverse faulting. Alternatively, either the global contraction stresses dissipated after the formation of the southern reverse faults, but before the formation of the radial grabens in the Tharsis province, or an additional source of stress is needed, and this stress must be large and deviatorically extensional in the center of Tharsis and deviatorically compressional in the periphery. Both scenarios are problematic, suggesting that global contraction may not be a significant contributing factor for the formation of the reverse faults on Mars.

The lithospheric stress models assume that (1) present-day topography is the paleotopography, (2) present-day crustal thickness is the paleo-crustal thickness, (3) uniform crustal and mantle densities. However, many of the tectonically generated structures formed early in the planet's history and consequently possibly formed under different conditions than we see today. I show that stresses associated with small perturbations to both GPE and membrane sources, improve the fit to many of the faults. The inverse models show

that small lateral variations $(1-6\%)$ in crust and mantle density in conjunction with small vertical displacement, $O(100m)$, provide sufficient additional GPE and membrane stress to fit the majority of the fault data. The density differences are only a few percent and are within the noise of the fit of the crustal model to the gravity field. The results from the inverse models are consistent with lithosphere modification by erosion from running water.

Thinsheet and flexure models solve the force-balance equations using simplified assumptions of zero vertical gradients in horizontal or vertical velocities. In discontinuous media, derivatives of displacement/velocity perpendicular to interfaces are not continuous and are not adequately represented in discretization schemes that are not aligned with the interfaces. Also, problems are often encountered where material properties are discontinuous as well as where layers pinch out, requiring infinitesimally small elements for fully accurate results.

I present a new approach, which has neither of these deficiencies. The key innovation is that, for the geophysical flow and elastic deformation problems of interest, the calculations are performed by separating all spatial dependencies into terms that can be related to coordinates on a reference surface and variations perpendicular to that surface. This results in considerable computational efficiency, as the problems are reduced to finite element calculations only in terms of the coordinates on the reference surface. The second key ingredient is that the computations are performed using only physical field quantities that are continuous across discontinuities in the medium, i.e., velocities/displacements and tractions. The advantage in this case is computational accuracy for laterally varying layers, including layer pinch-outs.

Bibliography

Bibliography

Anderson, E. M. (1951), *The dynamics of faulting and dike formation with application to Britain*, 2 ed., 206 pp., Oliver and Boyd, Edinburgh.

Anderson, R. C., J. M. Dohm, M. P. Golombek, A. F. C. Haldemann, B. J. Franklin, K. L. Tanaka, J. Lias, and B. Peer, Primary centers and secondary concentrations of tectonic activity through time in the western hemisphere of Mars, *Journal of Geophysical Research*, *106*, 20563–20586, 2001, DOI: 10.1029/2000JE001278.

Anderson, R. C., J. M. Dohm, A. F. C. Haldemann, E. Pounders, and M. P. Golombek, Tectonic evolution of Mars, in *37th Annual Lunar and Planetary Science Conference*, vol. 37, p. 1883, 2006.

Anderson, R. C., J. M. Dohm, A. F. C. Haldermann, E. Pounders, M. Golombek, and A. Castano, Centers of tectonic activity in the eastern hemisphere of Mars, *Icarus*, *195*(2), 537–546, 2008, Anderson, R. C. Dohm, J. M. Haldermann, A. F. C. Pounders, E. Golombek, M. Castano, A.

Andrews-Hanna, J. C., and M. T. Zuber, Strike-slip faulting and the tectonic evolution of Mars, in *Lunar and Planetary Institute Conference Abstracts*, vol. 38, p. 1897, 2007.

Artita, K. S., and R. A. Schultz, Significance of deformation band-like strike-slip faults on Mars, in *36th Annual Lunar and Planetary Science Conference*, vol. 36, p. 2225, 2005.

Banerdt, W. B., Support of long-wavelength loads on Venus and implications for internal structure, 1986, DOI: 10.1029/JB091iB01p00403.

Banerdt, W. B., and M. P. Golombek, The evolution of Tharsis: Implications of gravity, topography, and tectonics, in *Lunar and Planetary Institute Conference Abstracts*, vol. 21, p. 42, 1990.

Banerdt, W. B., and M. P. Golombek, Tectonics of the Tharsis region of Mars: Insights from MGS topography and gravity, in *Lunar and Planetary Institute Conference Abstracts*, vol. 31, p. 2038, 2000.

Banerdt, W. B., M. P. Golombek, and K. L. Tanaka, Stress and tectonics on Mars, in *Mars*, pp. 249–297, 1992, n/a 1, 1992.

Carr, M. H., Tectonism and volcanism of Tharsis region of Mars, *Journal of Geophysical Research*, *79*(26), 3943–3949, 1974.

Carr, M. H., *The surface of Mars*, Yale University Press, New Haven, 1981.

Chicarro, A. F., P. H. Schultz, and P. Masson, Global and regional ridge patterns on Mars, *Icarus*, *63*, 153–174, 1985, DOI: 10.1016/0019-1035(85)90025-9.

Connerney, J. E. P., et al., Magnetic lineations in the ancient crust of Mars, *Science*, *284*, 794, 1999, DOI: 10.1126/science.284.5415.794.

Dimitrova, L. L., W. E. Holt, A. J. Haines, and R. A. Schultz, Toward understanding the history and mechanisms of martian faulting: The contribution of gravitational potential energy, *Geophysical Research Letters*, *33*, 08202, 2006, DOI: 10.1029/2005GL025307.

England, P., and D. McKenzie, A thin vsicous sheet model for continental deformation, *Geophysical Journal of the Royal Astronomical Society*, *70*(2), 295–321, 1982.

Fleitout, L., The sources of lithospheric tectonic stresses, *Philosophical Transactions of the Royal Society of London Series a-Mathematical Physical and Engineering Sciences*, *337*(1645), 73–81, 1991.

Flesch, L. M., A. J. Haines, and W. E. Holt, Dynamics of the India-Eurasia collision zone, *Journal of Geophysical Research*, *106*, 16435–16460, 2001, DOI: 10.1029/2001JB000208.

Flesch, L. M., W. E. Holt, A. J. Haines, L. Wen, and B. Shen-Tu, The dynamics of western North America: stress magnitudes and the relative role of gravitational potential energy, plate interaction at the boundary and basal tractions, *Geophysical Journal International*, *169*, 866–896, 2007, DOI: 10.1111/j.1365-246X.2007.03274.x.

Frey, H., Martian canyons and African rifts - structural comparisons and implications, *Icarus*, *37*, 142–155, 1979, A&AA ID. AAA025.097.008 DOI: 10.1016/0019-1035(79)90122-2.

Ghosh, A., W. E. Holt, L. Wen, A. J. Haines, and L. M. Flesch, Joint modeling of lithosphere and mantle dynamics elucidating lithosphere-mantle coupling, *Geophysical Research Letters*, *35*, 16309, 2008, DOI: 10.1029/2008GL034365.

Golombek, M. P., J. B. Plescia, and B. J. Franklin, Faulting and folding in the formation of planetary wrinkle ridges, *Proceedings of Lunar and Planetary Science*, *21*, 679–693, 1991.

Golombek, M. P., and R. J. Phillips, Mars, in press, 2009.

Greeley, R., and J. E. Guest, Geologic map of the western equatorial region of Mars, 1987.

Haines, A. J., and M. V. de Hoop, An invariant imbedding analysis of general wave scattering problems, *Journal of Mathematical Physics*, *37*, 3854–3881, 1996, DOI: 10.1063/1.531606.

Haines, A. J., T. Hulme, and J. Yu, General elastic wave scattering problems using an impedance operator approach - i. mathematical development, *Geophysical Journal International*, *159*, 643–657, 2004, DOI: 10.1111/j.1365-246X.2004.02405.x.

Frey, H., Martian canyons and african rifts - structural comparisons and implications, *Icarus*, *37*, 142–155, 1979, A&AA ID. AAA025.097.008 DOI: 10.1016/0019-1035(79)90122-2.

Harder, H., Mantle convection and the dynamic geoid of Mars, *Geophysical Research Letters*, *27*, 301, 2000, DOI: 10.1029/1999GL008418.

Harder, H., and U. R. Christensen, A one-plume model of martian mantle convection, *Nature*, *380*, 507–509, 1996, DOI: 10.1038/380507a0.

Hartmann, W. K., and G. Neukum, Cratering chronology and the evolution of Mars, *Space Science Reviews*, *96*(1-4), 165–194, 2001.

Hauck, I., S. A., S. C. Solomon, and R. J. Phillips, Potential sources of Hesperian contractional tectonics on Mars, in *Lunar and Planetary Institute Conference Abstracts*, vol. 34, p. 1667, 2003.

Head, J. W., et al., Geological processes and evolution, *Space Science Reviews*, *96*, 263–292, 2001.

Head, J. W., M. A. Kreslavsky, and S. Pratt, Northern lowlands of Mars: Evidence for widespread volcanic flooding and tectonic deformation in the Hesperian period, *Journal of Geophysical Research (Planets)*, *107*, 5003, 2002, DOI: 10.1029/2000JE001445.

Holt, W. E., and A. J. Haines, The kinematics of northern South Island, New Zealand, determined from geologic strain rates, *Journal of Geophysical Research-Solid Earth*, *100*(B9), 17991–18010, 1995.

Hynek, B. M., and R. J. Phillips, Evidence for extensive denudation of the martian highlands, *Geology*, *29*, 407, 2001, DOI: 10.1130/0091-7613(2001)029.

http://pds.nasa.gov, NASA planetary data system

Jones, C. H., J. R. Unruh, and L. J. Sonder, The role of gravitational potential energy in active deformation in the southwestern united states, *Nature*, *381*(6577), 37–41, 1996.

Kiefer, W. S., B. G. Bills, and R. S. Nerem, An inversion of gravity and topography for mantle and crustal structure on Mars, *Journal of Geophysical Research*, *101*, 9239–9252, 1996, DOI: 10.1029/95JE03699.

Knapmeyer, M., J. Oberst, E. Hauber, M. Whlisch, C. Deuchler, and R. Wagner, Working models for spatial distribution and level of Mars' seismicity, *Journal of Geophysical Research (Planets)*, *111*, 11006, 2006, DOI: 10.1029/2006JE002708.

Kostrov, B. (1974), Seismic moment and energy of earthquakes, and seismic flow of rock, *Izv. Acad. Sci. USSR Phys. Solid Earth*, *1*, 23–40.

Lemoine, F. G., D. E. Smith, D. D. Rowlands, M. T. Zuber, G. A. Neumann, D. S. Chinn, and D. E. Pavlis, An improved solution of the gravity field of Mars (gmm-2b) from Mars Global Surveyor, *Journal of Geophysical Research*, *106*, 23359–23376, 2001, DOI: 10.1029/2000JE001426.

Lowry, A. R., and S. Zhong, Surface versus internal loading of the Tharsis rise, Mars, *Journal of Geophysical Research (Planets)*, *108*, 5099, 2003, DOI: 10.1029/2003JE002111.

Mangold, N., P. Allemand, P. G. Thomas, and G. Vidal, Chronology of compressional deformation on Mars: evidence for a single and global origin, *Planetary and Space Science*, *48*, 1201–1211, 2000.

McGovern, P., et al. (2001), Surface versus internal loading of the Tharsis rise, Mars, *J. Geophys. Res.*, *107*, 23,769, DOI: 10.1029/2000JE001314.

Mege, D., Graben morphology, dike emplacement, and tension fracturing in the Tharsis igneous province of Mars, in *The Fifth International Conference on Mars*, p. 6182, 1999.

Mege, D., A. C. Cook, E. Garel, Y. Lagabrielle, and M.-H. Cormier, Volcanic rifting at martian grabens, *Journal of Geophysical Research (Planets)*, *108*, 5044, 2003, DOI: 10.1029/2002JE001852.

Molnar, P., and H. Lyon-Caen, Some simple physical aspects of the support, structure, and evolution of mountain belts, *Processes in Continental Lithospheric Deformation, Geol. Soc. Amer. Spec. Pap*, *218*, 6203–6227, 1998.

Montesi, L. G. J., and M. T. Zuber (2003), Clues to the lithospheric structure of Mars from wrinkle ridge sets and localization instability, *J. Geophys. Res.*, *108*, 5048, DOI: 10.1029/2002JE001974.

Neuffer, D. P., and R. A. Schultz, Mechanisms of slope failure in Valles Marineris, Mars,

Quarterly Journal of Engineering Geology and Hydrogeology, *39*, 227–240, 2006, Neuffer, D. P. Schultz, R. A. Part 3.

Neumann, G. A., M. T. Zuber, M. A. Wieczorek, P. J. McGovern, F. G. Lemoine, and D. E. Smith, Crustal structure of Mars from gravity and topography, *Journal of Geophysical Research (Planets)*, *109*, 08002, 2004, DOI: 10.1029/2004JE002262.

Nimmo, F., and K. Tanaka, Early crustal evolution of Mars, *Annual Review of Earth and Planetary Sciences*, *33*, 133–161, 2005, DOI: 10.1146/annurev.earth.33.092203.122637.

Okubo, C. H., and R. A. Schultz, Variability in Early Amazonian Tharsis stress state based on wrinkle ridges and strike-slip faulting, *Journal of Structural Geology*, *28*, 2169–2181, 2006, DOI: 10.1016/j.jsg.2005.11.008.

Phillips, R. J., et al., Ancient geodynamics and global-scale hydrology on Mars, *Science*, *291*, 2587–2591, 2001, DOI: 10.1126/science.1058701.

Plescia, J. B., and R. S. Saunders, Tectonic history of the Tharsis region, Mars, *Journal of Geophysical Research*, *87*(NB12), 9775–9791, 1982.

Press, W. H., S. A. Teukolsky, W. T. Vetterling, and B. P. Flannery, *Numerical recipes in C. The art of scientific computing*, Cambridge: University Press, —c1992, 2nd ed., 1992, n/a 1, 1992.

Roberts, J. H., and S. Zhong, Plume-induced topography and geoid anomalies and their implications for the Tharsis rise on Mars, *Journal of Geophysical Research (Planets)*, *109*, 03009, 2004, DOI: 10.1029/2003JE002226.

Schubert, G., S. C. Solomon, D. L. Turcotte, M. J. Drake, and N. H. Sleep, Origin and thermal evolution of Mars, in *Mars*, pp. 147–183, 1992, n/a 1, 1992.

Schultz, R. A., Strike-slip faulting of ridged plains near Valles Marineris, Mars, *Nature*, *341*, 424–426, 1989, DOI: 10.1038/341424a0.

Schultz, R. A., Localization of bedding plane slip and backthrust faults above blind thrust faults: Keys to wrinkle ridge structure, *Journal of Geophysical Research*, *105*, 12035–12052, 2000b, DOI: 10.1029/1999JE001212.

Schultz, R., Fault-population statistics at the Valles Marineris extensional province, Mars: implications for segment linkage, crustal strains, and its geodynamical development, *Tectonophysics*, *316*, 169–193, 2000a, DOI: 10.1016/S0040-1951(99)00228-0.

Schultz, R. A., Seismotectonics of the Amenthes Rupes thrust fault population, Mars, *Geophysical Research Letters*, *30*, 36–1, 2003, DOI: 10.1029/2002GL016475.

Scott, D. H., and K. L. Tanaka, Geologic map of the western equatorial region of Mars, 1986.

Searls, M. L., and R. J. Phillips, Tectonics of utopia basin, Mars: Results from finite element loading models, in *Lunar and Planetary Institute Conference Abstracts*, vol. 38, p. 1965, 2007.

Sleep, N. H., Martian plate tectonics, *Journal of Geophysical Research*, *99*, 5639, 1994, DOI: 10.1029/94JE00216.

Sleep, N. H., and R. J. Phillips, Gravity and lithospheric stress on the terrestrial planets with reference to the Tharsis region of Mars, *Journal of Geophysical Research*, *90*, 4469–4489, 1985, DOI: 10.1029/JB090iB06p04469.

Tanaka, K. L., The stratigraphy of Mars, *Journal of Geophysical Research*, *91*, 1986.

Tanaka, K. L., and M. P. Golombek, Martian tension fractures and the formation of grabens and collapse features at Valles Marineris, in *Lunar and Planetary Science Conference*, vol. 19, pp. 383–396, 1989.

Tanaka, K. L., and D. H. Scott, Geologic map of the polar regions of Mars, 1987.

Tanaka, K. L., M. P. Golombek, and W. B. Banerdt, Reconciliation of stress and structural histories of the Tharsis region of Mars, *Journal of Geophysical Research-Planets*, *96*(E1), 15617–15633, 1991.

Tanaka, K. L., D. H. Scott, and R. Greeley, Global stratigraphy, in *Mars*, pp. 345–382, 1992, n/a 1, 1992.

Tanaka, K. L., J. A. Skinner, T. M. Hare, T. Joyal, and A. Wenker, Resurfacing history of the northern plains of Mars based on geologic mapping of Mars Global Surveyor data, *Journal of Geophysical Research-Planets*, *108*(E4), 2003.

Tanaka, K. L., J. M. Dohm, T. M. Hare, R. P. Irwin, E. J. Kolb, and J. A. Skinner, Mars geologic mapping: The next generation, *LPI Contributions*, *1353*, 3143, 2007.

Tanaka, K. L., J. A. P. Rodriguez, J. A. Skinner, M. C. Bourke, C. M. Fortezzo, K. E. Herkenhoff, E. J. Kolb, and C. H. Okubo, North polar region of Mars: Advances in stratigraphy, structure, and erosional modification, *Icarus*, *196*, 318–358, 2008, DOI: 10.1016/j.icarus.2008.01.021.

Turcotte, D. L., R. J. Willemann, W. F. Haxby, and J. Norberry, Role of membrane stresses in the support of planetary topography, *Journal of Geophysical Research*, *86*, 3951–3959, 1981, DOI: 10.1029/JB086iB05p03951.

Tyler, G. L., G. Balmino, D. P. Hinson, W. L. Sjogren, D. E. Smith, R. A. Simpson, S. W. Asmar, P. Priest, and J. D. Twicken, Radio science observations with Mars global surveyor: Orbit insertion through one Mars year in mapping orbit, *Journal of Geophysical Research*, *106*, 23327–23348, 2001, DOI: 10.1029/2000JE001348.

Valencia, D., R. J. O'Connell, and D. D. Sasselov, Inevitability of plate tectonics on super-earths, *Astrophysical Journal*, *670*, L45–L48, 2007, DOI: 10.1086/524012; eprintid: arXiv:0710.0699.

Watters, T. R., Origin of periodically spaced wrinkle ridges on the Tharsis plateau of Mars, *Journal of Geophysical Research*, *96*, 15599, 1991, DOI: 10.1029/91JE01402.

Watters, T. R. (1993), The mechanical and thermal structure of Mercury's early lithosphere, *J. Geophys. Res.*, *98*(9), 17,049–17,060.

Watters, T. R., Thrust faults along the dichotomy boundary in the eastern hemisphere of Mars, *Journal of Geophysical Research (Planets)*, *108*, 5054, 2003, DOI: 10.1029/2002JE001934.

Watters, T. R., and T. A. Maxwell, Orientation, relative age, and extent of the Tharsis plateau ridge system, *Journal of Geophysical Research*, *91*, 8113–8125, 1986, DOI: 10.1029/JB091iB08p08113.

Willemann, R. J., and D. L. Turcotte, The role of lithospheric stress in the support of the Tharsis rise, *Journal of Geophysical Research*, *87*(NB12), 9793–9801, 1982.

Wise, D. U., M. P. Golombek, and G. E. McGill, Tharsis province of Mars - geologic sequence, geometry, and a deformation mechanism, *Icarus*, *38*, 456–472, 1979, A&AA ID. AAA025.097.039 DOI: 10.1016/0019-1035(79)90200-8.

Woerner, W. R., E. K. Coraor, F. M. McCubbin, H. Nekvasil1, and D. H. Lindsley, The effect of pressure on residual liquid compositions from crystalization of a Humphrey-like magma: Implications for crustal stratigraphy in martian volcanic provinces., in *Lunar and Planetary Institute Conference Abstracts*, vol. 40, p. 2203, 2009.

Withers, P., and G. A. Neumann (2001), Enigmatic northern plains of Mars: A network of ridges in this region opens a new tectonic window onto this planet, *Nature*, *410*, 651–651, DOI: 10.1038/35070640.

Zhong, S., Effects of lithosphere on the long-wavelength gravity anomalies and their implications for the formation of the Tharsis rise on Mars, *Journal of Geophysical Research (Planets)*, *107*, 5054, 2002, DOI: 10.1029/2001JE001589.

Zhong, S., and M. T. Zuber, Degree-1 mantle convection and the crustal dichotomy on Mars, *Earth and Planetary Science Letters*, *189*, 75–84, 2001, DOI: 10.1016/S0012-821X(01)00345-4.

Zuber, M. T., et al., Internal structure and early thermal evolution of Mars from Mars Global Surveyor topography and gravity, *Science*, *287*, 1788–1793, 2000, DOI: 10.1126/science.287.5459.1788.

Appendix

Appendix 1. Auxiliary Material for Chapter 2

Appendix 1.1. Auxiliary Material

Figure S1: *Zuber et al.* (2000) topography.

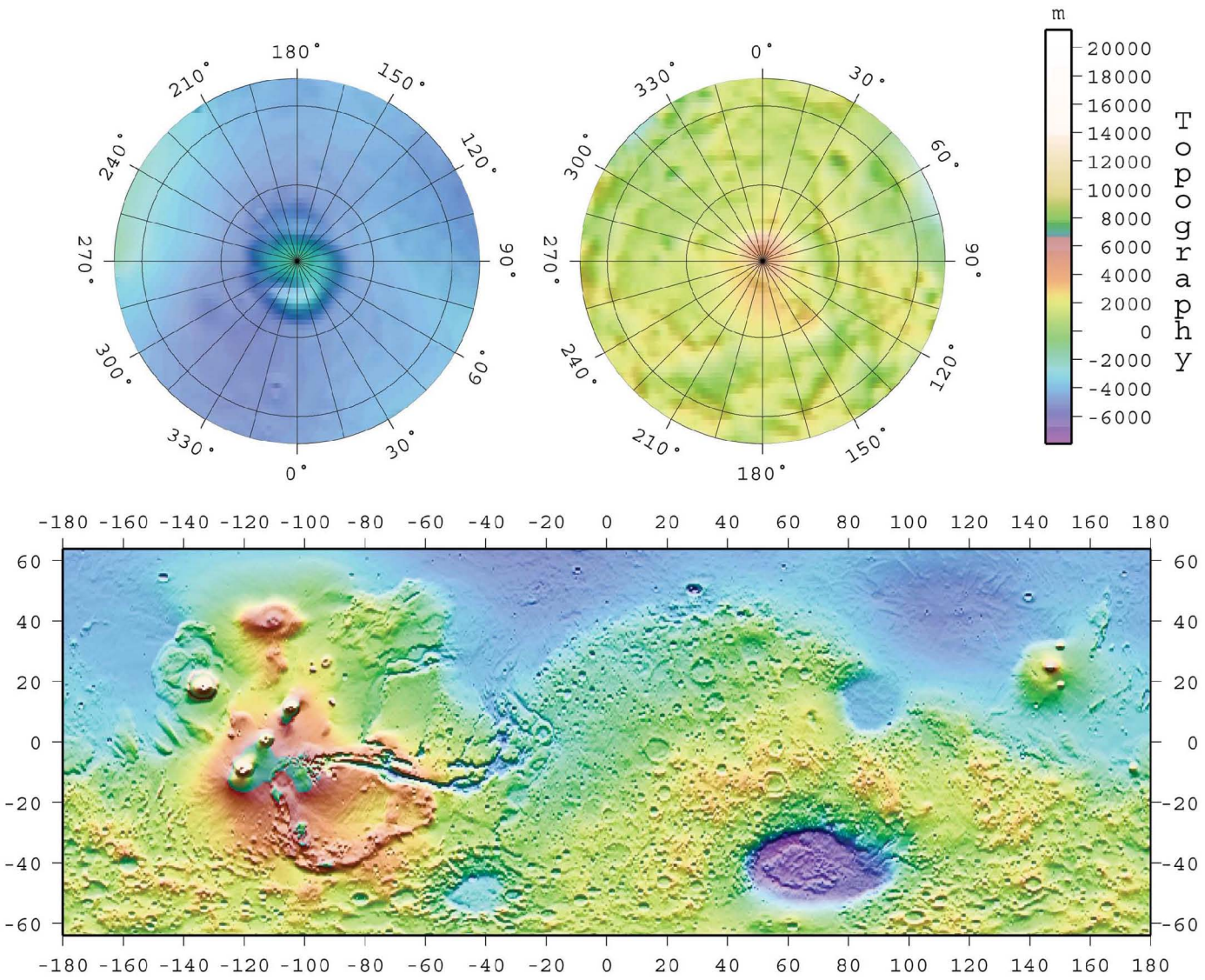
m
20000
18000
16000
14000
12000
10000
8000
6000
4000
2000
0
-2000
-4000
-6000
Topography
180°
210°
150°
240°
120°
270°
90°
300°
60°
330°
30°
0°
-180 -160 -140 -120 -100 -80 -60 -40 -20 0 20 40 60 80 100 120 140 160 180
60
40
20
0
-20
-40
-60

Figure S2: *Neumann et al.* (2004) crustal thickness.

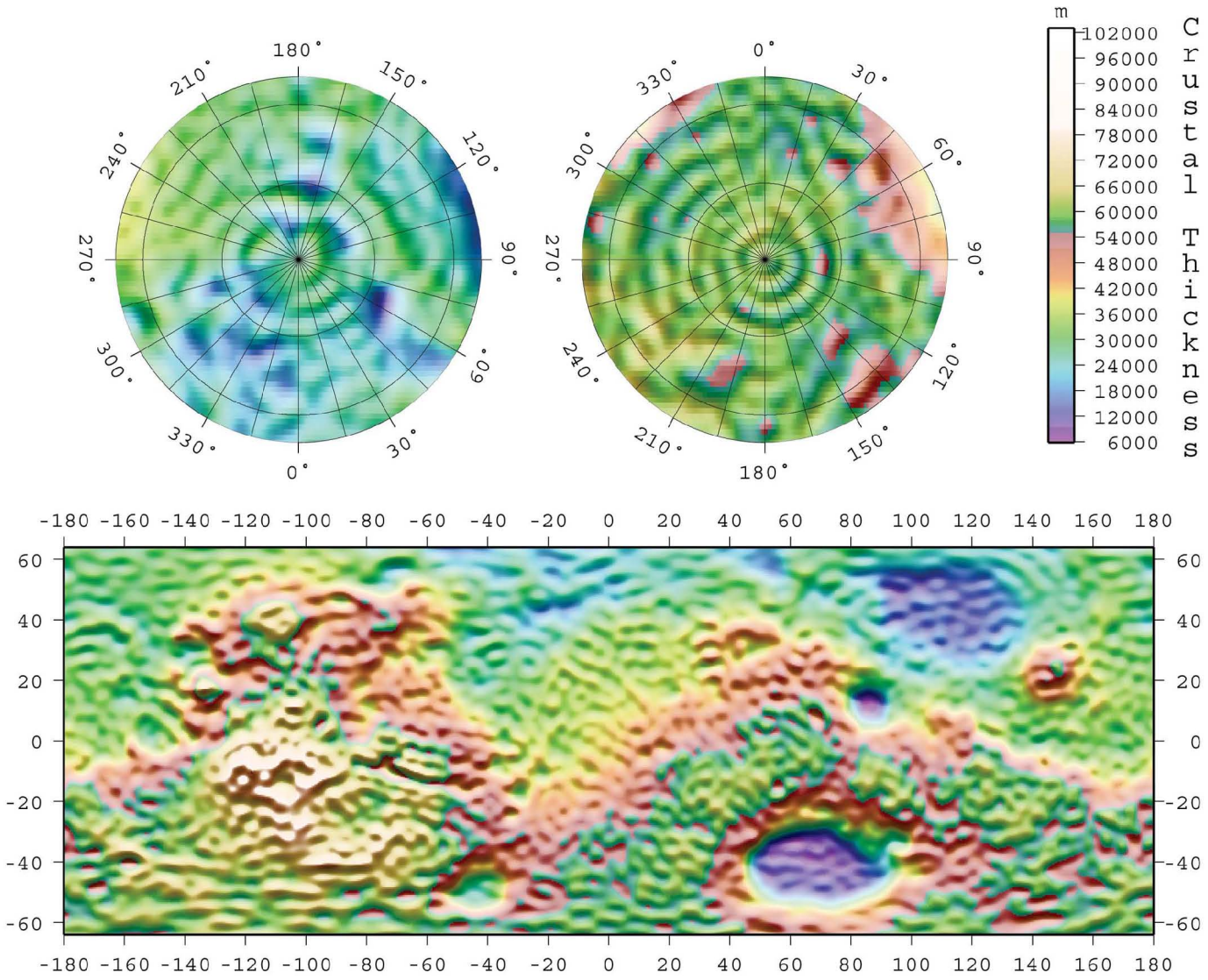
m
102000
96000
90000
84000
78000
72000
66000
60000
54000
48000
42000
36000
30000
24000
18000
12000
6000
Crustal Thickness
180°
210°
150°
240°
120°
270°
90°
300°
60°
330°
30°
0°
-180 -160 -140 -120 -100 -80 -60 -40 -20 0 20 40 60 80 100 120 140 160 180
60
40
20
0
-20
-40
-60

Figure S3: Global map of GPE and vertically integrated (L=92.8km) deviatoric lithospheric stresses associated with GPE variations calculated from MOLA topography and inferred crustal thickness (*Neumann et al.*, 2004), and assuming Poisson's ratio of 0.5. Red arrows represent deviatoric extension, while black arrows represent deviatoric compression.

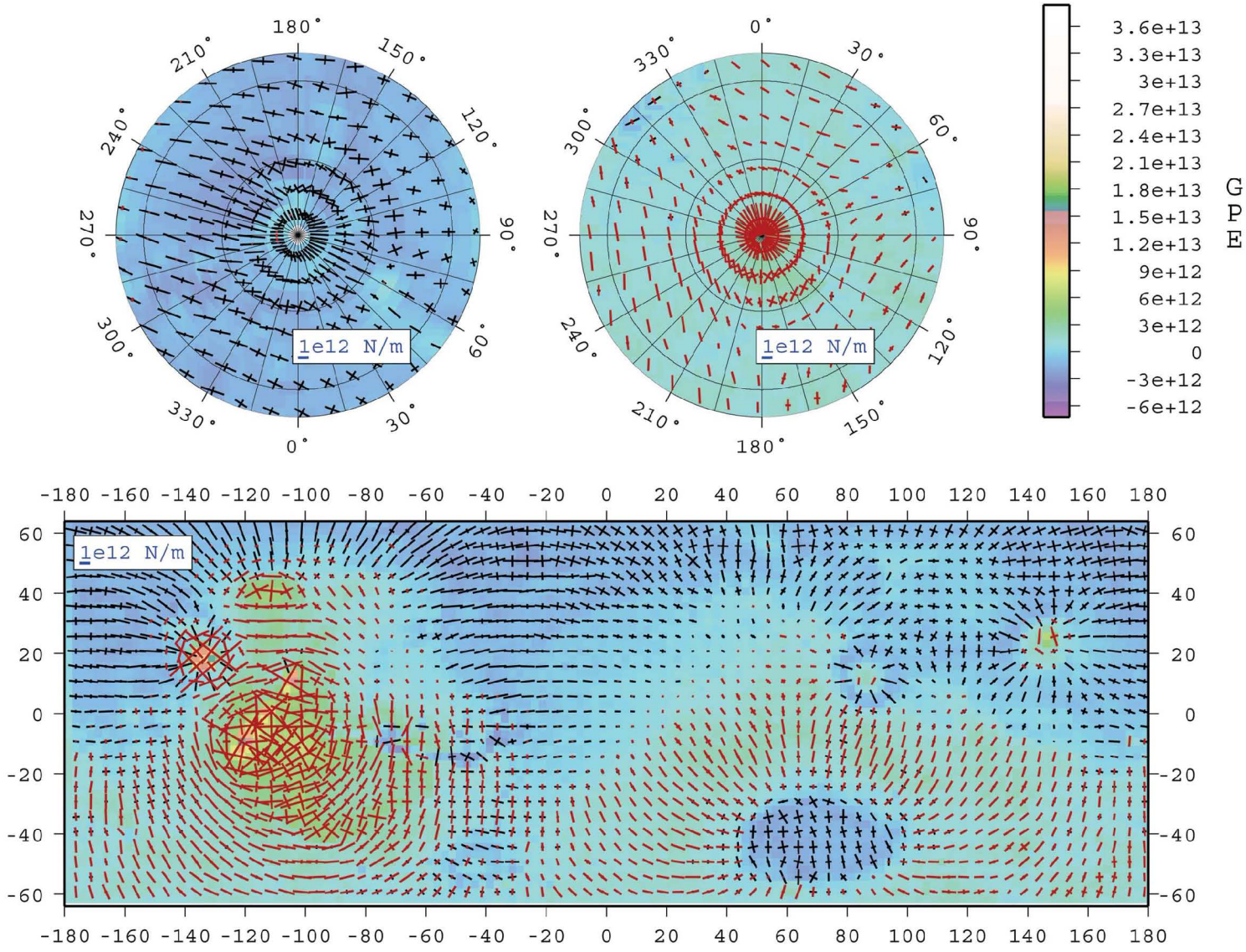
180°
210°
150°
240°
120°
270°
90°
300°
60°
330°
30°
0°
1e12 N/m
0°
330°
30°
300°
60°
270°
90°
240°
120°
210°
150°
180°
1e12 N/m
3.6e+13
3.3e+13
3e+13
2.7e+13
2.4e+13
2.1e+13
1.8e+13
1.5e+13
1.2e+13
9e+12
6e+12
3e+12
0
-3e+12
-6e+12
GPE
-180 -160 -140 -120 -100 -80 -60 -40 -20 0 20 40 60 80 100 120 140 160 180
60
40
20
0
-20
-40
-60
1e12 N/m

Figure S4: Global map of GPE and vertically integrated (L=185.6km) deviatoric lithospheric stresses associated with GPE variations calculated from MOLA topography and inferred crustal thickness (*Neumann et al.*, 2004), and assuming Poisson's ratio of 0.5. Red arrows represent deviatoric extension, while black arrows represent deviatoric compression.

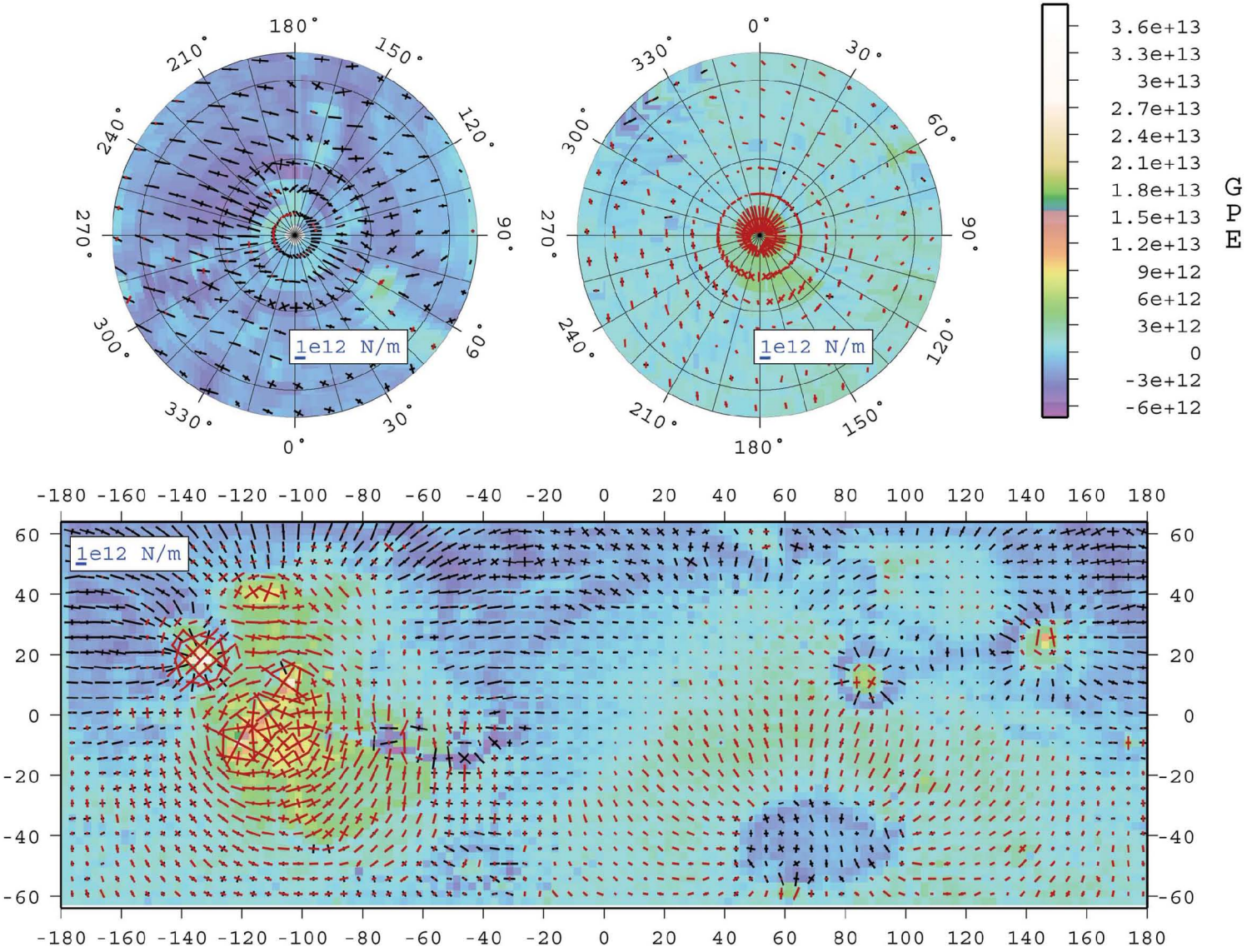
180°
210°
150°
240°
120°
270°
90°
300°
60°
330°
30°
0°
1e12 N/m
0°
330°
30°
300°
60°
270°
90°
240°
120°
210°
150°
180°
1e12 N/m
3.6e+13
3.3e+13
3e+13
2.7e+13
2.4e+13
2.1e+13
1.8e+13
1.5e+13
1.2e+13
9e+12
6e+12
3e+12
0
-3e+12
-6e+12
GPE
-180 -160 -140 -120 -100 -80 -60 -40 -20 0 20 40 60 80 100 120 140 160 180
60
40
20
0
-20
-40
-60
1e12 N/m

Figure S5: Predicted fault style, as defined in equation (1) from the deviatoric stress field in Figure S3.

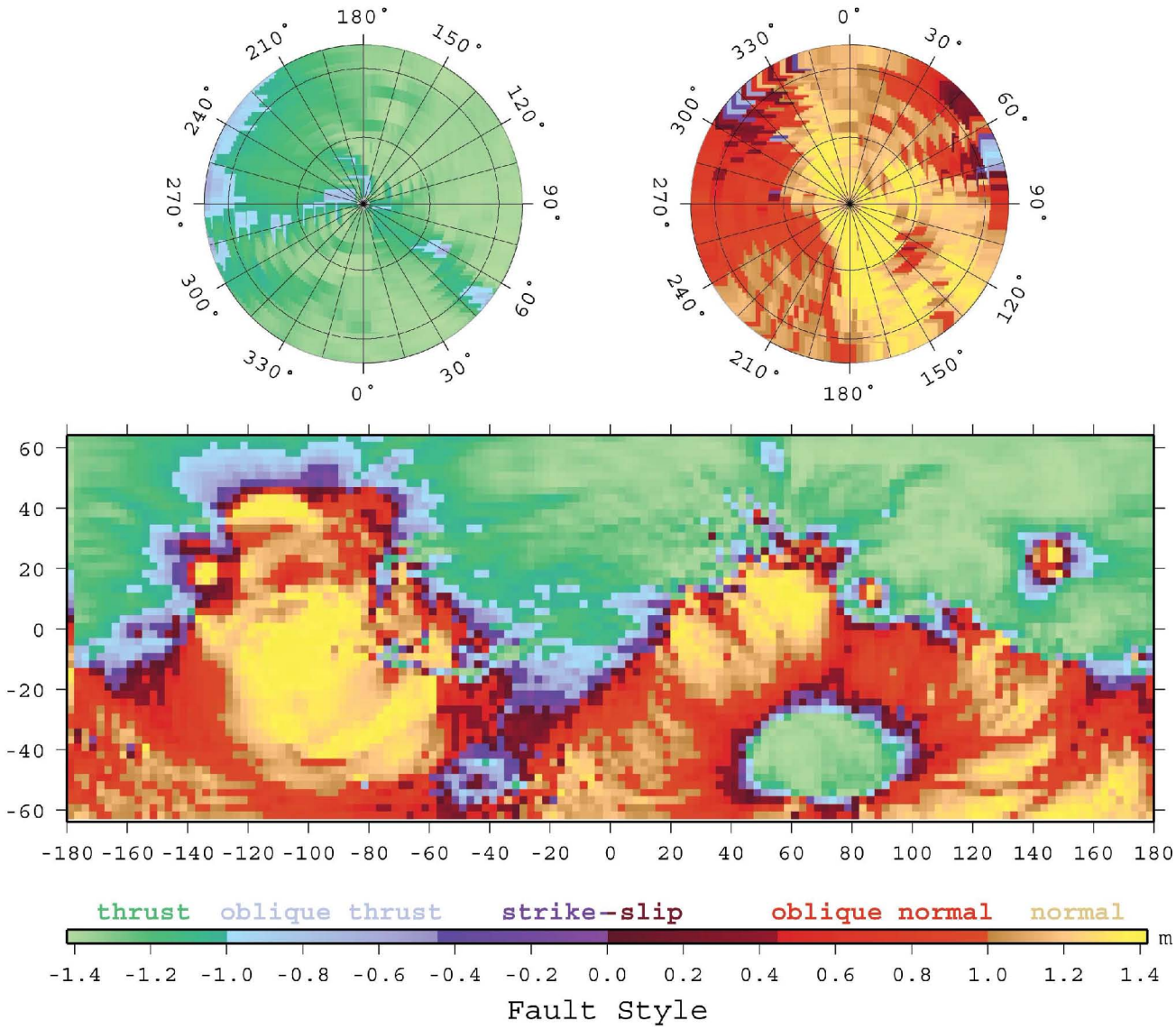
180°
210°
150°
240°
120°
270°
90°
300°
60°
330°
30°
0°
0°
330°
30°
300°
60°
270°
90°
240°
120°
210°
150°
180°
60
40
20
0
-20
-40
-60
-180 -160 -140 -120 -100 -80 -60 -40 -20 0 20 40 60 80 100 120 140 160 180
thrust
oblique thrust
strike-slip
oblique normal
normal
m
-1.4 -1.2 -1.0 -0.8 -0.6 -0.4 -0.2 0.0 0.2 0.4 0.6 0.8 1.0 1.2 1.4
Fault Style

Figure S6: Predicted fault style, as defined in text from the deviatoric stress field in Figure S4.

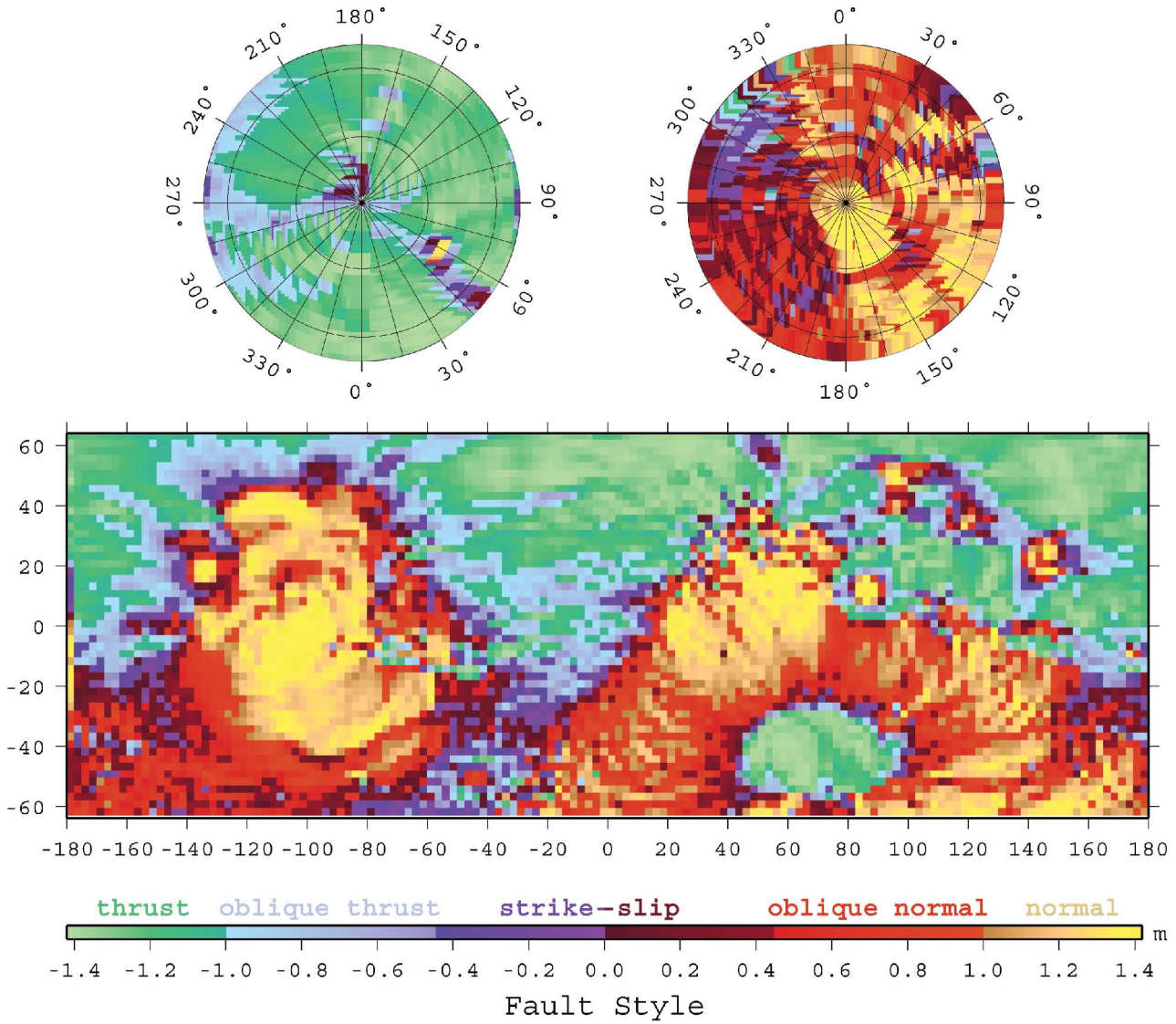
180°
210°
150°
240°
120°
270°
90°
300°
60°
330°
30°
0°
0°
330°
30°
300°
60°
270°
90°
240°
120°
210°
150°
180°
60
40
20
0
-20
-40
-60
-180 -160 -140 -120 -100 -80 -60 -40 -20 0 20 40 60 80 100 120 140 160 180
thrust
oblique thrust
strike-slip
oblique normal
normal
m
-1.4 -1.2 -1.0 -0.8 -0.6 -0.4 -0.2 0.0 0.2 0.4 0.6 0.8 1.0 1.2 1.4
Fault Style

Figure S7: Wrinkle ridge structures with transects roughly perpendicular to the ridges in (a) Solis Planum, (b) northern Lunae Planum, and (c) Hesperia Planum (*Montesi and Zuber*, 2003) overlain by the GPE deviatoric stress field from Figure S3.

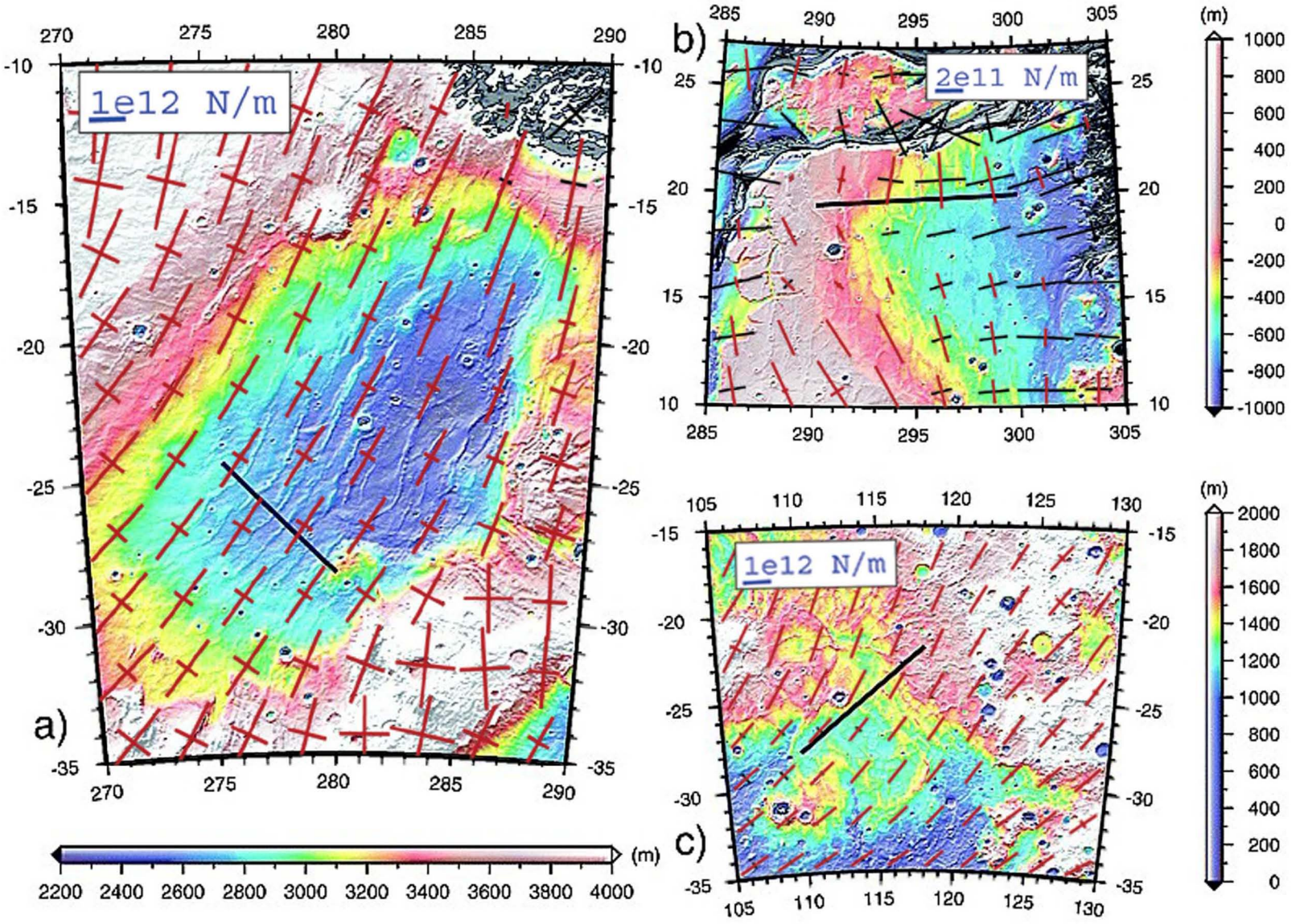
a)
1e12 N/m
b)
2e11 N/m
c)
1e12 N/m
(m)
2200 2400 2600 2800 3000 3200 3400 3600 3800 4000
(m)
1000 800 600 400 200 0 -200 -400 -600 -800 -1000
(m)
2000 1800 1600 1400 1200 1000 800 600 400 200 0

Figure S8: Wrinkle ridge structures with transects roughly perpendicular to the ridges in (a) the northern Flank of Alba Patera, (b) southeast Arcadia Planitia, and (c) Chryse Planitia (*Montesi and Zuber*, 2003) overlain by the GPE deviatoric stress field from Figure S3.

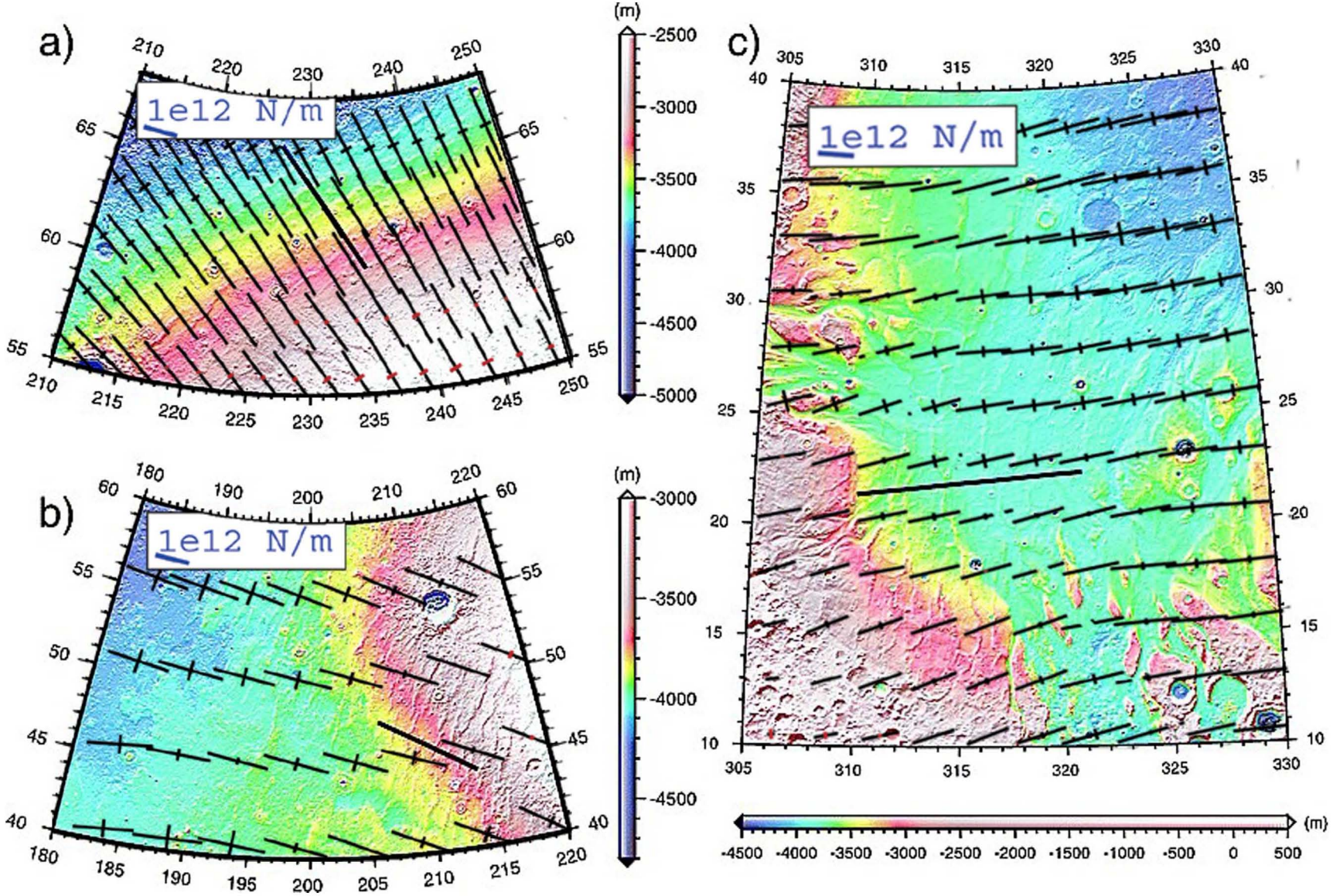
a)
1e12 N/m
b)
1e12 N/m
c)
1e12 N/m
(m)
-4500 -4000 -3500 -3000 -2500 -2000 -1500 -1000 -500 0 500

Bibliography

Montesi, L. G. J., and M. T. Zuber (2003), Clues to the lithospheric structure of Mars from wrinkle ridge sets and localization instability, *J. Geophys. Res.*, *108*, 5048, doi: 10.1029/2002JE001974.

Neumann, G., M. Zuber, M. Wieczorek, P. McGovern, F. Lemoine, and D. Smith (2004), The crustal structure of Mars from gravity and topography, *J. Geophys. Res.*, *108*, E08002, doi:10.1029/2004JE002262.

Zuber, M. T., et al. (2000), Internal structure and early thermal evolution of Mars from Mars Global Surveyor topography and gravity, *Science*, *287*(5459), 1788–1793.

Appendix 1.2. Comparison of Two Normal Fault Datasets for Tharsis, Mars

Overall studies of the tectonic and geologic history of Mars as well as small scale detailed tectonic and geologic features have been produced from Mariner and Viking images; however, there are very few attempts to produce datasets on a global stratigraphic framework. Some of the earlier maps show grabens present mostly in the western hemisphere and wrinkle ridges spread through both hemispheres (*Banerdt et al.*, 1992, and references therein)(Figure S9A).

Anderson et al. (2001) examined Viking images of the western hemisphere and compiled a database of 24 452 tectonic features in the western hemisphere of Mars (Figure S9B). Of those, 19,896 were identified as extensional features distributed radially and 4,556 compressional features distributed concentrically around Tharsis. For simplicity, curvilinear features were broken into multiple linear segments at points where the trend seemed to diverge and information on fault segmentation, spacing and linkage was not recognized in the data set. Mapped features were assigned the age of the youngest stratigraphic unit they crossed and the faults were assigned to one of five time stages. Recently the study was extended to cover the eastern hemisphere as well (*Anderson et al.*, 2006, 2008) (Figure S9C). The extensional features are predominantly in the western hemisphere and are associated with Tharsis and Elysium, while the compressional features are found in both hemispheres and can be associated with large impact crates and Syria Planum.

An alternative dataset was produced by *Knapmeyer et al.* (2006) (Figure S9D). Based on MOLA maps artificially illuminated from two orthogonal viewing directions, they mapped faults 4km or longer. They focused on normal and thrust faults only and dated each fault based on the unit containing the fault. Such ages represent an upper limit only since the fault could have formed any time after the formation of the geologic unit. Absolute ages were reassigned afterwards based on frequency of craters with diameter or larger and updated polynomial crater chronology model of *Hartmann and Neukum* (2001).

A natural question arises: are there differences between the two datasets? Both studies focus on normal and reverse faulting, since only a few strike-slip faults have been identified

(*Schultz*, 1989; *Mangold et al.*, 2000; *Tanaka et al.*, 2003; *Okubo and Schultz*, 2006). Both studies dated each fault based on the unit containing the fault and absolute ages were reassigned afterwards, based on crater chronology models of *Hartmann and Neukum* (2001). Therefore, differences, if they exist, will be in the completeness of each fault data set and the interpretation of the style of faulting.

For geodynamics studies such as the one presented in Chapter 2, the proper comparison of a model stress field is with the paleo-strain. The strain that can be inferred from observed faults is just one component of the paleo-strain field. Yet, for Mars these fault data sets are the only current evidence available for the paleo-strain. The strain that can be inferred from these faults is only a lower bound to this paleo-strain. Additional sources of strain, which could be either large or small compared to the fault strain, include residual elastic strain, accommodated in non brittle-frictional deformation, as well as strain taken up by faults that either never broke the surface or were subsequently buried. Therefore, using fault data to constrain anything more than orientation and relative magnitude of paleo-strain would be over-interpreting the observations.

For each dataset, we calculate the *Kostrov* (1974) tensor summation estimate of the total strain tensor, ε_{ij}, for a given volume, V, for each fault

$$\varepsilon_{ij} = \frac{1}{2\mu V} \sum M_0 m_{ij}(\theta, \lambda, \delta), \tag{A1}$$

where μ is the shear modulus, M_0 is the moment of slip on the fault and m_{ij} is the unit moment tensor, which is a function of the fault strike, θ, rake, λ, and dip, δ . The moment of slip is defined as:

$$M_0 = \mu L D u, \tag{A2}$$

where L is the fault length, D is the depth of faulting, and u is the magnitude of slip. Substituting into equation (A1) above we have the average strain tensor associated with the fault-related deformation within the volume l:

$$\varepsilon_{ij}^{l} = \frac{1}{2} \sum_{k=1}^{n} \frac{L_k u_k}{A} m_{ij}^{k}(\theta, \lambda, \delta), \tag{A3}$$

where A is the area containing n fault segments, each having length L_k (*Holt and Haines*, 1995; *Schultz*, 2003). Note that the assumed thickness and shear modulus do not enter into the final estimate of the strain tensor for the area, since it is implicitly assumed in this formula that $m_{ij}(\theta,\lambda,\delta)$ and u do not vary with depth within the faulted or elastic layer.

Although fault displacements, u, scale primarily with length, mechanical length depends on fault segmentation, spacing, and linkage, which are often not recognized in global datasets. In particular, while both *Anderson et al.* (2001) and *Knapmeyer et al.* (2006) mapped faults whose strikes vary into two or more segments, only the *Knapmeyer et al.* (2006) dataset retains the information about the segmentation. Therefore, the absolute magnitude of the strain will vary depending on which dataset is used.

To compare the two datasets, we assume uniform slip on each fault segment. The resulting ε_{ij} reflects the simplest and least-biased approach to incorporating fault-related strain to compare with the stress model. Furthermore, we define the objective function that measures the fit between the fault datasets such that it is insensitive to scalar multiples of either fault data strain tensor, and thus it is insensitive to the actual value of u. This objective function is given by

$$C_{full} = (\varepsilon \cdot \tau) \,/\, (ET), \quad M_{full} = 0.5\,(1 - C_{full}), \tag{A4}$$

where the metrics E and T and the inner product $\varepsilon \cdot \tau$ are defined as

$$E = \sqrt{\varepsilon_{ij}\varepsilon_{ij}}, \quad T = \sqrt{\tau_{ij}\tau_{ij}}, \quad \varepsilon \cdot \tau = \varepsilon_{ij}\tau_{ij}. \tag{A5}$$

Here ε_{ij} and τ_{ij} are the 3-D strain from the (*Kostrov*, 1974) summation of the two fault datasets.

This objective function is minimized when the two fault data sets have, in each grid area, faults in the same style and orientation as each other. The misfit function has values from 0 to 1, with 0 misfit indicating a perfect fit. For example the misfit function will have a value of 0 in a grid area if both datasets have normal fault(s) with the same strike, 0.5 if one of them predicts strike slip fault(s) with the same orientation instead, and 1 if one of

them predicts a reverse fault with the same orientation instead.

The misfit, M_{full}, between the strain fields associated with the *Anderson et al.* (2001) and *Knapmeyer et al.* (2006) datasets, assuming unit slip and that faulting extended through the entire lithosphere is shown in Fig S10. Note that in general there is excellent agreement between the two datasets. The few areas in yellow reflect variation of fault strike between the datasets. The coverage by the two datasets differs only in the periphery of Tharsis as signified by the gray (*Anderson et al.* (2001) data but no *Knapmeyer et al.* (2006) data) and black (*Knapmeyer et al.* (2006) data but no *Anderson et al.* (2001) data).

Figure S9: A) Normal (in black) and reverse (in blue) faults in the western hemisphere of Mars after *Banerdt et al.* (1992). B) Normal (in color) and reverse (in blue) faults in the western hemisphere of Mars after *Anderson et al.* (2001). C) Normal (in color) and reverse (in blue) faults in the western hemisphere of Mars after *Anderson et al.* (2001). D) Normal (in red) and reverse (in green) faults in the western hemisphere of Mars after *Knapmeyer et al.* (2006). Panels A),B),C) are centered approximately on the 90W meridian while panel D is centered on the 0 one. Note the increased number of faults in the 2001 data set (panel B) compared to the 1992 data set (panel A), as well as the differences in the fault distributions in the eastern hemisphere between the two most recent fault maps (panels C and D).

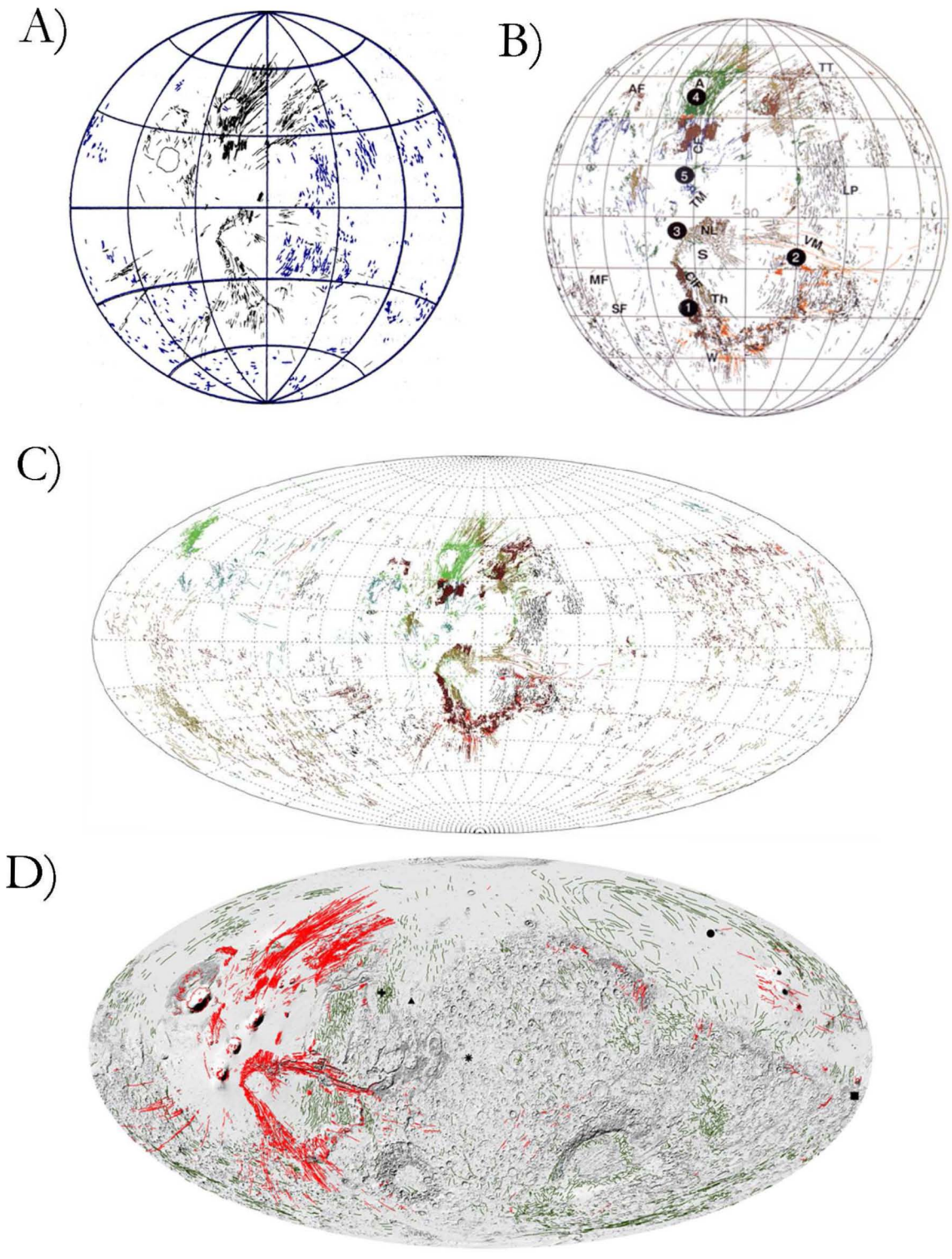
A)
B)
AF
A
4
TT
CF
5
TM
LP
3
NL
S
VM
2
MF
OF
Th
SF
1
W
C)
D)

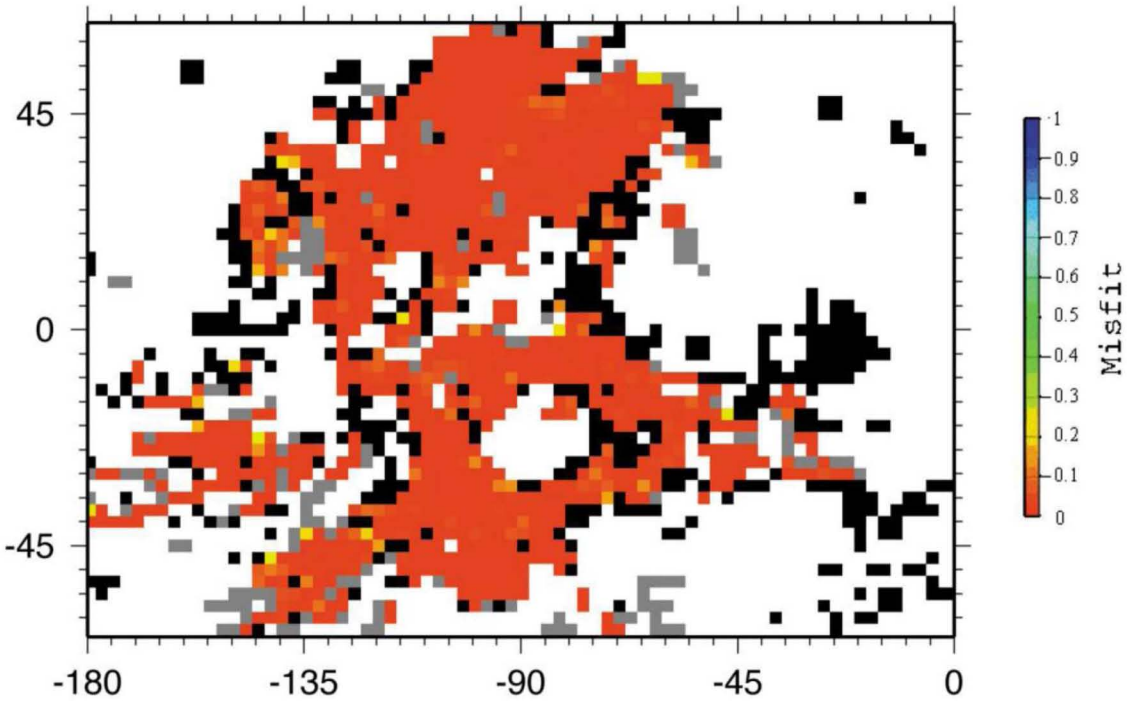

Figure S10: Misfit between the strain fields derived from *Anderson et al.* (2001) and *Knapmeyer et al.* (2006) datasets for the normal faults in the western hemisphere. Red indicates good fit, while yellow through green to blue indicates a misfit. Gray signifies areas where data exists in the *Anderson et al.* (2001) data set but not in the *Knapmeyer et al.* (2006) dataset, while black signifies areas where data exists in the *Knapmeyer et al.* (2006) dataset but not in the *Anderson et al.* (2001) dataset.

Appendix 1.3. Flexure-Dominated Stress Models for Tharsis, Mars

The Tharsis province, due to its large scale and complex deformation, was the focus of the majority of the early studies. These early models seemed to require more than one mechanism - a combination of lithospheric uplift, isostasy, and flexure - to explain the region's evolution (*Banerdt et al.*, 1992, and references therein). Downward displacement, due to a surface load, produces radial compression within Tharsis and concentric extension in the periphery. Upward displacement, caused by a load at the base of the lithosphere, produces stresses of the same orientation but opposite sign, i.e., radial extension within Tharsis and concentric compression in the periphery. Isostatic stresses, defined as those stresses which result when buoyancy forces were balanced such that there was no deflection (and thus no contribution to the stress field from flexure), exhibit a pattern similar to that due to upward displacement.

Neither one of these mechanisms could coevally produce the radial grabens in Tharsis to their fullest extent and presented a major problem in the creating of a self-consistent history of the evolution of the lithosphere connecting the observed tectonic features with the stress models.

More recently, *Banerdt and Golombek* (2000) proposed that the seeming need of multiple mechanisms was due to the quality of data available prior to MGS. They calculated the deflection of the lithosphere due to the Tharsis load alone while satisfying the long wavelength signal of present day topography and gravity. The resulting stress field has radial compressive stresses throughout Tharsis. *Banerdt and Golombek* (2000) show only the extensional component of the strains, which is consistent with normal faulting on pre-existing faults radial to Tharsis and away from the load, for example, Memnonia, Sirenum, Thaumasia, southern Claritas, and Tempe Fossae. However, the faulting extending from northern Claritas Fossae north to Tantalus and Alba Fossae is not well explained by the membrane model, which predicts zero extension in these areas (Fig. S11).

Golombek and Phillips (2009) show the extensional component as well as the radial compressional component of the strains from the *Banerdt and Golombek* (2000) model (Fig S11). For each panel, the colour of pixels 3.5 x 3.5 was extracted and assigned a

value based on the scale provided with the panel (scripts provided by Mark Haines). These values represent the magnitudes of the principal strains, which we use to calculate the expected fault styles associated with this model following *Anderson* (1951). Since the Martian surface is a free surface and the vertical stress is a principal stress, we can define a normalized parameter

$$A_0 = (\tau_1 + \tau_2)/\sqrt{\tau_1^2 + \tau_2^2} \tag{A6}$$

to discriminate among the three major geologic fault styles associated with the styles of the deviatoric stress field from the dynamic solution. Here τ_1 and τ_2 are the principal horizontal deviatoric stresses, and the vertical deviatoric stress is $-(\tau_1 + \tau_2)$. The results are plotted in Figure S12 together with the normal and reverse faults from *Knapmeyer et al.* (2006). We note that while the magnitude of the circumferential principal strain was extracted wherever it is extensional, we have no information as to the magnitude of the compressional circumferential principal strain in Figure S11, i.e., in central Tharsis. This means that in these regions, our measure will predict more extensional regime than the actual model would, i.e., the model could be predicting pure thrust, whereas our mesure will be predicting oblique-thrust. Note that besides the normal faults in central Tharsis, this model fits only the reverse faults in Lunae and Solis planea and misfits the remaining circumferential wrinkle ridges. It is important to note that the strains shown are applied on the original deformed layer; the strains experienced by the load are not shown. However, it is unclear which faults are on the load and which are on the underlying crust, and for those faults that are not on the load, how far they extend underneath the load.

We calculate a model of membrane stresses due to dynamic topography (calculated using the deviation from average pressure at the reference level $L = 92.84$), as opposed to volcanic surface loads, inferred from the topography and crustal thickness models (*Zuber et al.*, 2000; *Neumann et al.*, 2004). Firstly, we calculate the pressure at the reference level. Then, for each grid area we calculate the vertical displacement by which the column of lithosphere needs to be shifted up or down to achieve the average pressure. Once the vertical displacement is known (see Fig. S13A), the associated membrane stress is calculated (see Chapter 4 for details). Note that the flexural contributions are ignored; however, flexure

and membrane act in the same direction. In addition, flexural stresses integrate to zero vertically, and thus only membrane stresses contribute to the depth-integrated stress.

To first order, membrane deviatoric stresses associated with dynamic topography show similar results to the GPE ones, but with circumferential deviatoric compression on the flanks of Tharsis and deviatoric extension occurring over the areas with low topography and thin crust (Figure S13). The stress field is consistent with two diffuse centers of extensional features - a small one in the Tharsis region and a much larger one antipodal to Tharsis. Comparing the models of stresses associated with horizontal GPE gradients with the model of membrane stress associated with dynamic topography, we can see that the fit has worsened (only %46 of the faults have $M_{full} \leq 0.1$).

Note that this model predicts fault styles opposite those expected from the model of *Banerdt and Golombek* (2000) due to the different source of membrane stress. The driving force for their models is a downward force on a uniform elastic layer due to the load of Tharsis. The driving force for our membrane model is the vertical force required to push the topography up or down from a reference state with uniform pressure at the reference depth. This driving force can be attributed to a combination of radial push from mantle convection and flexural resistance to that push.

The two models discussed above represent the two end-member hypotheses for the origins of Tharsis topographic and aeroid signal. The first hypothesis proposes that Tharsis rise represents volcanically constructed surface load (*Willemann and Turcotte*, 1982; *Solomon and Head*, 1982; *Banerdt and Golombek*, 2000; *Phillips et al.*, 2001), while the second attributes Tharsis topography and aeroid as a dynamic response to internal loading from a buoyancy due to basalt depletion or a single-plume mantle convection (*Kiefer et al.*, 1996; *Harder and Christensen*, 1996; *Harder*, 2000).

We have examined two end-member flexure dominated models and compared them with the normal and reverse faults in the western hemisphere of Mars. The range of the associated vertical displacements is similar ($\sim 13km$). Assuming shear modulus of $4-8\times10^{10}Pa$, the surface flexure stresses of *Banerdt and Golombek* (2000) are on average an order of magnitude larger than the GPE associated stresses. These flexural strains would dominate the surface strains and stress field, if present at the time of faulting. Shal-

low faults may respond to the stresses within a shallow layer of the lithosphere and hence surface stresses may be an appropriate comparison. However, displacement/length/width relationships for the faults indicate that the majority of the faults are sufficiently long to be breaking the majority of the lithosphere (*Knapmeyer et al.*, 2006). In this case, the appropriate comparison is with the depth-integrated stresses. However, the depth integral of any flexural stresses is zero (*Turcotte and Schubert*, 2002) leaving only the membrane component. Since the flexural stresses dominate the surface stresses shown by *Banerdt and Golombek* (2000), it is unclear what the magnitude of the vertically integrated membrane and isostatic stresses will be in their model. However, the style of the membrane response is similar to the style of the surface flexural response, which is known and fails to fit many of the normal and reverse faults in the western hemisphere of Mars (Figure S12). Our dynamic topography model shows that membrane stresses do not have to dominate the GPE stresses, especially outside of Tharsis: the stresses vary from being much larger than the GPE associated stresses (e.g., Arsia and Olympus Mons, Valles Marineris) to being roughly the same order of magnitude (periphery of Tharsis).

The flexure-dominated model of *Banerdt and Golombek* (2000), the isostatic model in *Banerdt et al.* (1992), and our membrane model, associated with dynamic topography, demonstrate just a few of the possible scenarios for the non-unique problem of the loading history of Tharsis. Yet, none of these models fit the normal faults in and around Tharsis as well as the GPE model. Since the faults reflect the thermal state of the planet at the time of their formation, these results argue that many of the faults were created at times when elastic thicknesses and membrane and flexural stresses were small, a combination of brittle and ductile deformation was likely to be widespread, and GPE stresses dominated.

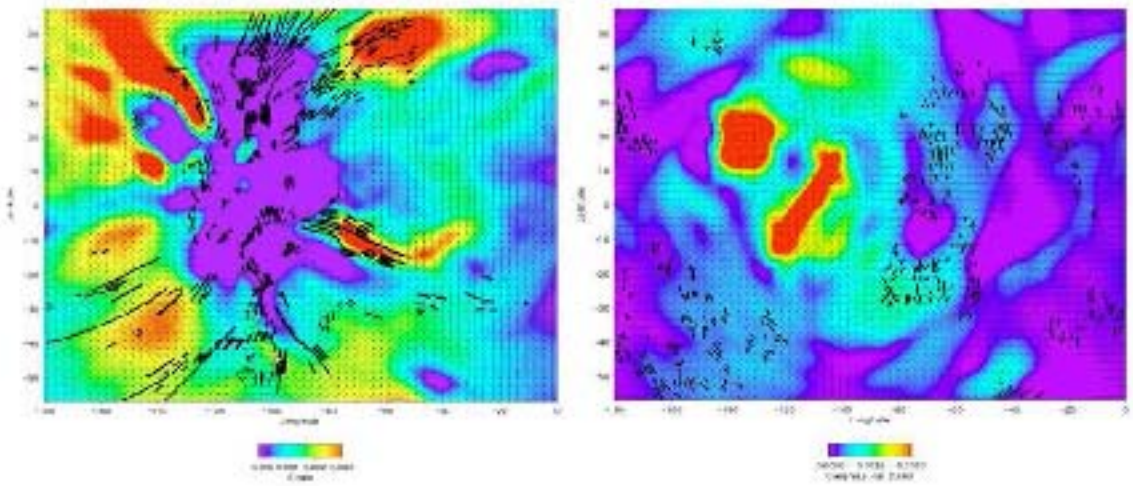

Figure S11: Magnitude(in colour) and direction(black arrow) of A) the circumferential deviatorically extentionsal horizontal strain and B) the radial deviatorically compressional horizontal strain of the flexure model of *Banerdt and Golombek* (2000) (from *Golombek and Phillips* (2009))

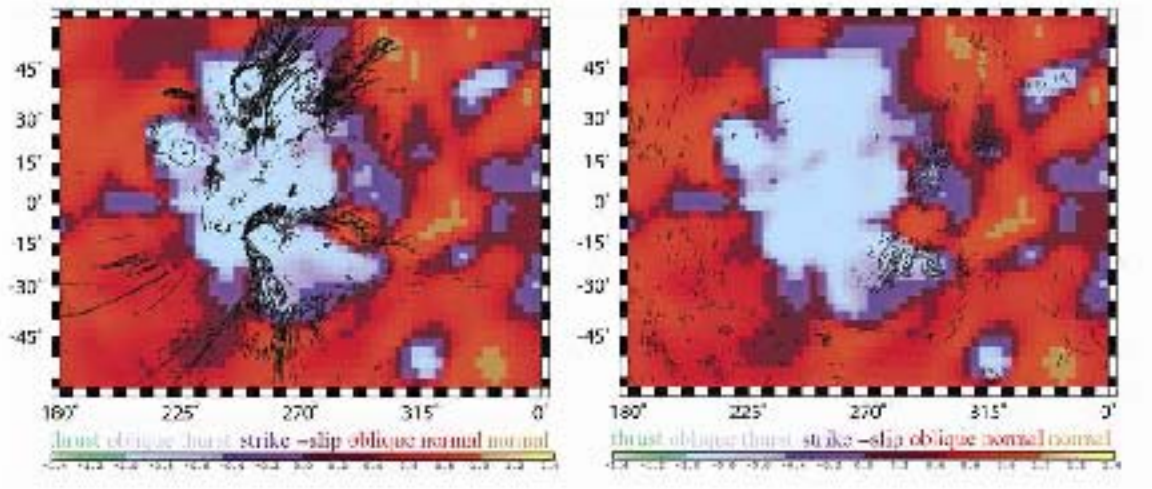

Figure S12: Predicted fault style from the deviatoric strain in Fig S11. Overlain are A) the normal and B) reverse faults from *Knapmeyer et al.* (2006).

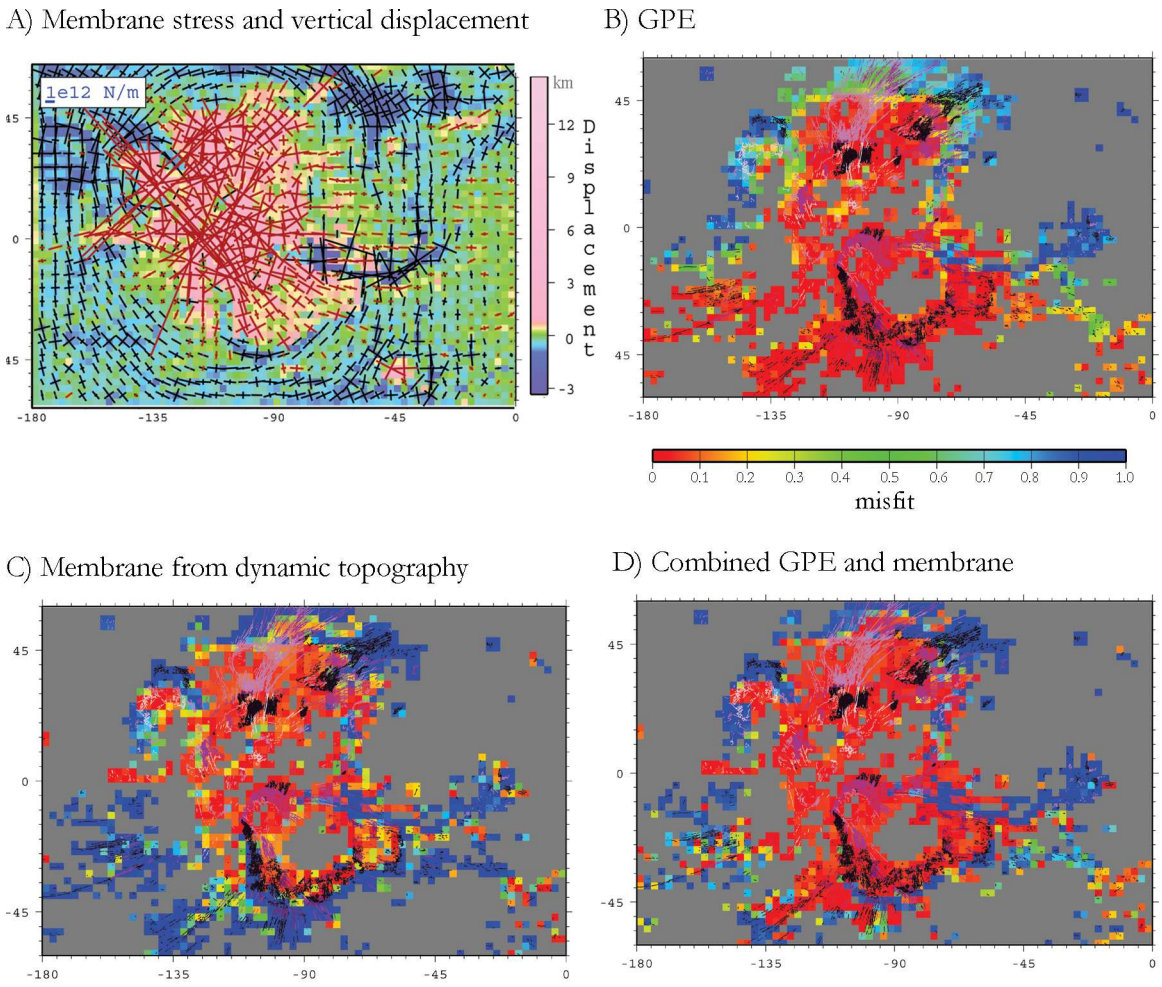

Figure S13: A) Misfit, defined by objective function, between the normal faults of *Anderson et al.* (2001) and the B) GPE, C) membrane (from dynamic topography, opposite in sign to surface loading), and D) combined CPE and membrane stress fields from Figure 1. The GPE stresses fit the fault styles and orientations well, while the fit for membrane only and the combined GPE and membrane stresses is worse.

Bibliography

Anderson, E., *The Dynamics of Faulting and Dike Formation with Application*, 2nd ed., Oliver and Boyd, White Plains, NY, 1951.

Anderson, R. C., J. M. Dohm, M. P. Golombek, A. F. C. Haldemann, B. J. Franklin, K. L. Tanaka, J. Lias, and B. Peer, Primary centers and secondary concentrations of tectonic activity through time in the western hemisphere of Mars, *Journal of Geophysical Research*, *106*, 20563–20586, 2001, DOI: 10.1029/2000JE001278.

Anderson, R. C., J. M. Dohm, A. F. C. Haldemann, E. Pounders, and M. P. Golombek, Tectonic evolution of Mars, in *37th Annual Lunar and Planetary Science Conference*, vol. 37, p. 1883, 2006.

Anderson, R. C., J. M. Dohm, A. F. C. Haldermann, E. Pounders, M. Golombek, and A. Castano, Centers of tectonic activity in the eastern hemisphere of Mars, *Icarus*, *195*(2), 537–546, 2008, Anderson, R. C. Dohm, J. M. Haldermann, A. F. C. Pounders, E. Golombek, M. Castano, A.

Banerdt, W. B., and M. P. Golombek, Tectonics of the Tharsis region of Mars: Insights from MGS topography and gravity, in *Lunar and Planetary Institute Conference Abstracts*, vol. 31, p. 2038, 2000.

Banerdt, W. B., M. P. Golombek, and K. L. Tanaka, Stress and tectonics on Mars, in *Mars*, pp. 249–297, 1992, n/a 1, 1992.

Golombek, M. P., and R. J. Phillips, Mars, in press, 2009.

Harder, H., Mantle convection and the dynamic geoid of Mars, *Geophysical Research Letters*, *27*, 301, 2000, DOI: 10.1029/1999GL008418.

Harder, H., and U. R. Christensen, A one-plume model of martian mantle convection, *Nature*, *380*, 507–509, 1996, DOI: 10.1038/380507a0.

Hartmann, W. K., and G. Neukum, Cratering chronology and the evolution of Mars, *Space Science Reviews*, *96*(1-4), 165–194, 2001.

Holt, W. E., and A. J. Haines, The kinematics of northern South Island, New Zealand, determined from geologic strain rates, *Journal of Geophysical Research-Solid Earth*, *100*(B9), 17991–18010, 1995.

Kiefer, W. S., B. G. Bills, and R. S. Nerem, An inversion of gravity and topography for mantle and crustal structure on Mars, *Journal of Geophysical Research*, *101*, 9239–9252, 1996, DOI: 10.1029/95JE03699.

Knapmeyer, M., J. Oberst, E. Hauber, M. Wahlisch, C. Deuchler, and R. Wagner, Working models for spatial distribution and level of Mars' seismicity, *Journal of Geophysical Research-Planets*, *111*(E11), 2006, Knapmeyer, M. Oberst, J. Hauber, E. Waehlisch, M. Deuchler, C. Wagner, R.

Kostrov, V. V., Seismic moment and energy of earthquares, and seismic flow of rock, *Izv., Earth Physics*, *1*, 23–40, 1974.

Mangold, N., P. Allemand, P. G. Thomas, and G. Vidal, Chronology of compressional deformation on Mars: evidence for a single and global origin, *Planetary and Space Science*, *48*, 1201–1211, 2000.

Neumann, G., M. Zuber, M. Wieczorek, P. McGovern, F. Lemoine, and D. Smith (2004), The crustal structure of Mars from gravity and topography, *J. Geophys. Res.*, *108*, E08002, DOI:10.1029/2004JE002262.

Okubo, C. H., and R. A. Schultz, Variability in Early Amazonian Tharsis stress state based

on wrinkle ridges and strike-slip faulting, *Journal of Structural Geology*, *28*, 2169–2181, 2006, DOI: 10.1016/j.jsg.2005.11.008.

Phillips, R. J., et al., Ancient geodynamics and global-scale hydrology on Mars, *Science*, *291*, 2587–2591, 2001, DOI: 10.1126/science.1058701.

Schultz, R. A., Strike-slip faulting of ridged plains near Valles Marineris, Mars, *Nature*, *341*, 424–426, 1989, DOI: 10.1038/341424a0.

Schultz, R. A., Seismotectonics of the amenthes rupes thrust fault population, Mars, *Geophysical Research Letters*, *30*, 36–1, 2003, DOI: 10.1029/2002GL016475.

Solomon, S. C., and J. W. Head, Evolution of the Tharsis province of Mars - the importance of heterogeneous lithospheric thickness and volcanic construction, *Journal of Geophysical Research*, *87*, 9755–9774, 1982, A&AA ID. AAA032.097.068 DOI: 10.1029/JB087iB12p09755.

Tanaka, K. L., J. A. Skinner, T. M. Hare, T. Joyal, and A. Wenker, Resurfacing history of the northern plains of Mars based on geologic mapping of Mars global surveyor data, *Journal of Geophysical Research-Planets*, *108*(E4), 2003.

Turcotte, D. L., and G. Schubert, *Geodynamics - 2nd Edition*, Geometriae Dedicata, 2002, April 1, 2002 ISBN: 9780521661867 DOI: 10.2277/0521661862.

Willemann, R. J., and D. L. Turcotte, The role of lithospheric stress in the support of the Tharsis rise, *Journal of Geophysical Research*, *87*(NB12), 9793–9801, 1982.

Zuber, M. T., et al. (2000), Internal structure and early thermal evolution of Mars from Mars Global Surveyor topography and gravity, *Science*, *287*(5459), 1788–1793.

Appendix 2. Auxiliary Material for Chapter 3

Appendix 2.1. Spherical Treatment of the Thin Sheet Methodology

The 3-D Stoke's equation is given by

$$\nabla \cdot \sigma + \rho \mathbf{g} = 0, \tag{B1}$$

where **g** is a vector in the negative radial direction. In spherical coordinates, the deviatoric stress tensor (equation 3) is:

$$\sigma_{ij} = \tau_{ij} + \delta_{ij}(\sigma_{rr} - \tau_{rr}), \tag{B2}$$

Expanding equation (B1) in spherical coordinates gives:

$$\frac{1}{\cos\theta}\frac{\partial}{\partial\phi}\left(r^2\sigma_{\phi\phi}\right) + \frac{1}{\cos^2\theta}\frac{\partial}{\partial\theta}\left(r^2\sigma_{\phi\theta}\cos^2\theta\right) + \frac{\partial}{\partial r}\left(r^3\sigma_{\phi r}\right) = 0 \tag{B3}$$

$$\begin{aligned}\frac{1}{\cos\theta}\frac{\partial}{\partial\phi}\left(r^2\sigma_{\phi\theta}\right) \quad + \quad & \frac{1}{2}\frac{\partial}{\partial\theta}\left(r^2\left[\sigma_{\theta\theta}+\sigma_{\phi\phi}\right]\right) \\ & + \frac{1}{2\cos^2\theta}\frac{\partial}{\partial\theta}\left(r^2\cos^2\theta\left[\sigma_{\theta\theta}-\sigma_{\phi\phi}\right]\right) + \frac{\partial}{\partial r}\left(r^3\sigma_{\theta r}\right) = 0\end{aligned} \tag{B4}$$

$$\frac{1}{r\cos\theta}\frac{\partial\sigma_{\phi r}}{\partial\phi} + \frac{1}{r\cos\theta}\frac{\partial}{\partial\theta}\left(\cos\theta\sigma_{\theta r}\right) + \frac{1}{r}\left(2\sigma_{rr} - \sigma_{\phi\phi} - \sigma_{\theta\theta}\right) + \frac{\partial\sigma_{rr}}{\partial r} - \rho g = 0 \tag{B5}$$

Vertically integrating equations (B3),(B4) gives:

$$\begin{aligned}\frac{1}{\cos\theta}\frac{\partial}{\partial\phi}\left(\int_{r_L}^{r_0} r^2\sigma_{\phi\phi}dr\right) \quad + \quad & \frac{1}{\cos^2\theta}\frac{\partial}{\partial\theta}\left(\int_{r_L}^{r_0} r^2\sigma_{\phi\theta}dr\cos^2\theta\right) \\ & + r_0^3\sigma_{\phi r}(r_0) - r_L^3\sigma_{\phi r}(r_L) = 0\end{aligned} \tag{B6}$$

and

$$\frac{1}{\cos\theta}\frac{\partial}{\partial\phi}\left(\int_{r_L}^{r_0} r^2\sigma_{\phi\theta}\right) + \frac{1}{2}\frac{\partial}{\partial\theta}\left(\int_{r_L}^{r_0} r^2\left[\sigma_{\theta\theta}+\sigma_{\phi\phi}\right]\right) + \frac{1}{2\cos^2\theta}\frac{\partial}{\partial\theta}\left(\int_{r_L}^{r_0} r^2\cos^2\theta\left[\sigma_{\theta\theta}-\sigma_{\phi\phi}\right]\right) + r_0^3\sigma_{\theta r}(r_0) - r_L^3\sigma_{\theta r}(r_L) = 0 \tag{B7}$$

where r_0 is the radius from the center of the planet to the surface and r_L is the radius from the center to the reference level. Substitute $\sigma_{rr}-\frac{1}{3}\sigma_{kk}$ for τ_{rr} in equations (B6),(B7) and note that $\sigma_{\phi r}(r_0)=0$ and $\sigma_{\theta r}(r_0)=0$ to obtain:

$$\frac{1}{\cos\theta}\frac{\partial}{\partial\phi}\left(\int_{r_L}^{r_0} r^2\tau_{\phi\phi}dr\right) - \frac{1}{\cos\theta}\frac{\partial}{\partial\phi}\left(\int_{r_L}^{r_0} r^2\tau_{rr}dr\right) + \frac{1}{\cos^2\theta}\frac{\partial}{\partial\theta}\left(\cos^2\theta\int_{r_L}^{r_0} r^2\tau_{\phi\theta}dr\right) + \frac{1}{\cos\theta}\frac{\partial}{\partial\phi}\left(\int_{r_L}^{r_0} r^2\sigma_{rr}dr\right) - r_L^3\tau_{\phi r}(r_L) = 0 \tag{B8}$$

and

$$\frac{1}{\cos\theta}\frac{\partial}{\partial\phi}\left(\int_{r_L}^{r_0} r^2\tau_{\phi\theta}dr\right) + \frac{1}{2}\frac{\partial}{\partial\theta}\left(\int_{r_L}^{r_0} r^2\tau_{\theta\theta}dr + \int_{r_L}^{r_0} r^2\tau_{\phi\phi}dr\right) - \frac{\partial}{\partial\theta}\left(\int_{r_L}^{r_0} r^2\tau_{rr}dr\right) + \frac{1}{2\cos^2\theta}\frac{\partial}{\partial\theta}\left(\cos^2\theta\left[\int_{r_L}^{r_0} r^2\tau_{\theta\theta}dr - \int_{r_L}^{r_0} r^2\tau_{\phi\phi}dr\right]\right) + \frac{\partial}{\partial\theta}\left(\int_{r_L}^{r_0} r^2\sigma_{rr}dr\right) - r_L^3\tau_{\theta r}(r_L) = 0, \tag{B9}$$

which are equivalent to equations (4).

For a thin sheet, the gradients of $\sigma_{\phi r}$ and $\sigma_{\theta r}$ are negligibly small, and $\frac{1}{r}(2\sigma_{rr}-\sigma_{\phi\phi}-\sigma_{\theta\theta})$ is small compared to ρg. Hence, equation (B5) can be approximated as

$$\frac{\partial\sigma_{rr}}{\partial r} - \rho g = 0 \tag{B10}$$

which implies

$$\sigma_{rr} = -\int_r^{r_0} \rho g dr \tag{B11}$$

so that the equation (5) in spherical coordinates is equivalent to

$$\begin{aligned}\int_{r_L}^{r_0} r^2\sigma_{rr}dr &= -\int_{r_L}^{r_0} r^2\left[\int_r^{r_0}\rho g dr'\right]dr = -\int_{r_L}^{r_0}\rho g\left[\int_{r_L}^{r'} r^2 dr\right]dr' \\ &= -\int_{r_L}^{r_0}\frac{1}{3}\rho g\left(r'^3 - r_L^3\right)dr'\end{aligned} \tag{B12}$$

The I functional in equation (6) is given by

$$\begin{aligned}I &= \int\int\frac{1}{\mu}\left[\bar{\tau}_{\phi\phi}^2 + 2\bar{\tau}_{\phi\theta}^2 + \bar{\tau}_{\theta\theta}^2 + (\bar{\tau}_{\phi\phi}+\bar{\tau}_{\theta\theta})^2\right]\cos\theta d\phi d\theta \\ &+ \int\int\left\{2\lambda_\phi\left[\frac{1}{\cos\theta}\frac{\partial\bar{\tau}_{\phi\phi}}{\partial\phi} + \frac{1}{\cos\theta}\frac{\partial}{\partial\phi}(\bar{\tau}_{\phi\phi}+\bar{\tau}_{\theta\theta}) + \frac{1}{\cos^2\theta}\frac{\partial}{\partial\theta}(\cos^2\theta\bar{\tau}_{\phi\theta}) + \frac{1}{\cos\theta}\frac{\partial}{\partial\phi}\bar{\sigma}_{rr}\right]\right. \\ &+ 2\lambda_\theta\left[\frac{1}{\cos\theta}\frac{\partial}{\partial\phi}\bar{\tau}_{\phi\theta} + \frac{3}{2}\frac{\partial}{\partial\theta}(\bar{\tau}_{\theta\theta}+\bar{\tau}_{\phi\phi}) + \frac{1}{2\cos^2\theta}\frac{\partial}{\partial\theta}(\cos^2\theta[\bar{\tau}_{\theta\theta}-\bar{\tau}_{\phi\phi}])\right. \\ &+ \left.\left.\frac{\partial\bar{\sigma}_{rr}}{\partial\theta}\right]\right\}\cos\theta d\phi d\theta\end{aligned} \tag{B13}$$

where $\bar{\tau}_{ij}$ are the vertically integrated deviatoric stresses, $\bar{\sigma}_{rr}$ is the vertically integrated vertical stress, or GPE, $\lambda_\phi, \lambda_\theta$ are the Lagrange multipliers.

The J functional in equation (8) can be written in spherical coordinates as

$$J = \int\int\left\{\left[\begin{pmatrix}\bar{\tau}_{\phi\phi}\\ \bar{\tau}_{\theta\theta}\\ \bar{\tau}_{\phi\theta}\end{pmatrix} - \begin{pmatrix}\Phi_{\phi\phi}^{obs}\\ \Phi_{\theta\theta}^{obs}\\ \Phi_{\phi\theta}^{obs}\end{pmatrix}\right]^T V^{-1}\left[\begin{pmatrix}\bar{\tau}_{\phi\phi}\\ \bar{\tau}_{\theta\theta}\\ \bar{\tau}_{\phi\theta}\end{pmatrix} - \begin{pmatrix}\Phi_{\phi\phi}^{obs}\\ \Phi_{\theta\theta}^{obs}\\ \Phi_{\phi\theta}^{obs}\end{pmatrix}\right]\right\}\cos\theta d\phi d\theta \tag{B14}$$

where

$$\bar{\tau}_{\phi\phi} = \mu\left(\frac{1}{\cos\theta}\frac{\partial\lambda_\phi}{\partial\phi} - \lambda_\theta\tan\theta\right), \tag{B15}$$

$$\bar{\tau}_{\theta\theta} = \mu\frac{\partial\lambda_\theta}{\partial\theta}, \tag{B16}$$

$$\bar{\tau}_{\phi\theta} = \frac{\mu}{2}\left(\frac{\partial\lambda_\phi}{\partial\theta} + \frac{1}{\cos\theta}\frac{\partial\lambda_\theta}{\partial\phi} + \lambda_\phi\tan\theta\right), \tag{B17}$$

$$V^{-1} = \begin{pmatrix} \frac{1}{1-\nu} & \frac{\nu}{1-\nu} & 0 \\ \frac{\nu}{1-\nu} & \frac{1}{1-\nu} & 0 \\ 0 & 0 & 2 \end{pmatrix}, \tag{B18}$$

and

$$\begin{pmatrix} \Phi^{obs}_{\phi\phi} \\ \Phi^{obs}_{\theta\theta} \\ \Phi^{obs}_{\phi\theta} \end{pmatrix} = \begin{pmatrix} -\overline{\sigma}_{rr}/3 \\ -\overline{\sigma}_{rr}/3 \\ 0 \end{pmatrix} \tag{B19}$$

Appendix 3. Auxiliary Material for Chapter 5

Appendix 3.1. Expanded Geometry Expressions

For the 3-D case of a reference sphere of radius r_0, the tangential derivative with χ fixed is

$$\begin{aligned} \nabla_0^{\perp} &= (-\sin\phi, \cos\phi, 0)\frac{1}{r_0\cos\theta}\frac{\partial}{\partial\phi} \\ &\quad + (-\sin\theta\cos\phi, -\sin\theta\sin\phi, \cos\theta)\frac{1}{r_0}\frac{\partial}{\partial\theta}, \end{aligned} \tag{C1}$$

and is equivalent to eq. 8 for the unit radial vector $\hat{x} = (\cos\theta\cos\phi, \cos\theta\sin\phi, \sin\theta)$. The tangential derivative with ξ fixed is:

$$\begin{aligned} \tilde{\nabla}^{\perp} &= \left(-\sin\tilde{\phi}, \cos\tilde{\phi}, 0\right)\frac{1}{r_0\cos\tilde{\theta}}\frac{\partial}{\partial\tilde{\phi}} \\ &\quad + \left(-\sin\tilde{\theta}\cos\tilde{\phi}, -\sin\tilde{\theta}\sin\tilde{\phi}, \cos\tilde{\theta}\right)\frac{1}{r_0}\frac{\partial}{\partial\tilde{\theta}}. \end{aligned} \tag{C2}$$

Eqns. 10, 11 are obtained as follows. First we note that from eq. 9 for ϕ we have $\nabla\phi = \frac{r_0}{r}\left\{\nabla_0^{\perp}\phi - \underline{\hat{x}}\left[1 - N\frac{\chi}{r_0}\right]\frac{\partial\phi}{\partial\chi}\right\} = \frac{r_0}{r}\nabla_0^{\perp}\phi$, and similarly we have $\nabla\theta = \frac{r_0}{r}\nabla_0^{\perp}\theta$, $\nabla\tilde{\phi} = \frac{r_0}{r}\nabla_0^{\perp}\tilde{\phi}$,

and $\nabla\tilde{\theta} = \frac{r_0}{r}\nabla_0^{\perp}\tilde{\theta}$. Then

$$\begin{aligned}
\nabla &= (\nabla\phi)\frac{\partial}{\partial\phi} + (\nabla\theta)\frac{\partial}{\partial\theta} + (\nabla\chi)\frac{\partial}{\partial\chi} \\
&= \left(\frac{r_0}{r}\nabla_0^{\perp}\phi\right)\frac{\partial}{\partial\phi} + \left(\frac{r_0}{r}\nabla_0^{\perp}\theta\right)\frac{\partial}{\partial\theta} + (\nabla\chi)\frac{\partial}{\partial\chi} \\
&= \frac{r_0}{r}\nabla_0^{\perp} + (\nabla\chi)\frac{\partial}{\partial\chi}, \text{ and}
\end{aligned} \tag{C3}$$

$$\begin{aligned}
\nabla &= \left(\nabla\tilde{\phi}\right)\frac{\partial}{\partial\tilde{\phi}} + \left(\nabla\tilde{\theta}\right)\frac{\partial}{\partial\tilde{\theta}} + (\nabla\xi)\frac{\partial}{\partial\xi} \\
&= \left(\frac{r_0}{r}\tilde{\nabla}^{\perp}\tilde{\phi}\right)\frac{\partial}{\partial\tilde{\phi}} + \left(\frac{r_0}{r}\tilde{\nabla}^{\perp}\tilde{\theta}\right)\frac{\partial}{\partial\tilde{\theta}} + (\nabla\xi)\frac{\partial}{\partial\xi} \\
&= \frac{r_0}{r}\tilde{\nabla}^{\perp} + (\nabla\xi)\frac{\partial}{\partial\xi}.
\end{aligned} \tag{C4}$$

Likewise, for the 3-D case of a reference plane (a flat-planet case with $r_0 \to \infty$), $\chi = z$ and the tangential derivative with χ fixed is

$$\nabla_0^{\perp} = \left(\frac{\partial}{\partial x}, \frac{\partial}{\partial y}, 0\right), \tag{C5}$$

and is equivalent to eq. 8 for the unit radial vector $\hat{x} = (0,0,1)$. The tangential derivative with ξ fixed is:

$$\tilde{\nabla}^{\perp} = \left(\frac{\partial}{\partial\tilde{x}}, \frac{\partial}{\partial\tilde{y}}, 0\right). \tag{C6}$$

Eqns. 10, 11 are obtained as follows

$$\begin{aligned}
\nabla &= (\nabla x)\frac{\partial}{\partial x} + (\nabla y)\frac{\partial}{\partial y} + (\nabla\chi)\frac{\partial}{\partial\chi} \\
&= \left(\nabla_0^{\perp}x\right)\frac{\partial}{\partial x} + \left(\nabla_0^{\perp}y\right)\frac{\partial}{\partial y} + (\nabla\chi)\frac{\partial}{\partial\chi} \\
&= \nabla_0^{\perp} + (\nabla\chi)\frac{\partial}{\partial\chi}, \text{ and}
\end{aligned} \tag{C7}$$

$$\begin{aligned}\nabla &= (\nabla\tilde{x})\frac{\partial}{\partial\tilde{x}} + (\nabla\tilde{y})\frac{\partial}{\partial\tilde{y}} + (\nabla\xi)\frac{\partial}{\partial\xi} \\ &= \left(\tilde{\nabla}^{\perp}\tilde{x}\right)\frac{\partial}{\partial\tilde{x}} + \left(\tilde{\nabla}^{\perp}\tilde{y}\right)\frac{\partial}{\partial\tilde{y}} + (\nabla\xi)\frac{\partial}{\partial\xi} \\ &= \tilde{\nabla}^{\perp} + (\nabla\xi)\frac{\partial}{\partial\xi}.\end{aligned} \tag{C8}$$

Likewise, for the 2-D case of a reference circle of radius r_0. the tangential derivative with χ fixed is

$$\nabla_0^{\perp} = (-\sin\phi, \cos\phi)\frac{1}{r_0}\frac{\partial}{\partial\phi}, \tag{C9}$$

and is equivalent to eq. 8 for the unit radial vector $\hat{x} = (\cos\phi, \sin\phi)$. The tangential derivative with ξ fixed is:

$$\tilde{\nabla}^{\perp} = \left(-\sin\tilde{\phi}, \cos\tilde{\phi}\right)\frac{1}{r_0}\frac{\partial}{\partial\tilde{\phi}}. \tag{C10}$$

Eqns. 10, 11 are obtained as follows

$$\begin{aligned}\nabla &= (\nabla\phi)\frac{\partial}{\partial\phi} + (\nabla\chi)\frac{\partial}{\partial\chi} \\ &= \left(\frac{r_0}{r}\nabla_0^{\perp}\phi\right)\frac{\partial}{\partial\phi} + (\nabla\chi)\frac{\partial}{\partial\chi} \\ &= \frac{r_0}{r}\nabla_0^{\perp} + (\nabla\chi)\frac{\partial}{\partial\chi}, \text{ and}\end{aligned} \tag{C11}$$

$$\begin{aligned}\nabla &= \left(\nabla\tilde{\phi}\right)\frac{\partial}{\partial\tilde{\phi}} + (\nabla\xi)\frac{\partial}{\partial\xi} \\ &= \left(\frac{r_0}{r}\tilde{\nabla}^{\perp}\tilde{\phi}\right)\frac{\partial}{\partial\tilde{\phi}} + (\nabla\xi)\frac{\partial}{\partial\xi} \\ &= \frac{r_0}{r}\tilde{\nabla}^{\perp} + (\nabla\xi)\frac{\partial}{\partial\xi}.\end{aligned} \tag{C12}$$

Likewise, for the 2-D case of a reference line (a flat-planet case with $r_0 \to \infty$), $\chi = z$ and the tangential derivative with χ fixed is

$$\nabla_0^{\perp} = \left(\frac{\partial}{\partial x}, 0\right), \tag{C13}$$

and is equivalent to eq. 8 for the unit radial vector $\hat{x} = (0, 1)$. The tangential derivative with

ξ fixed is:

$$\tilde{\nabla}^{\perp} = \left(\frac{\partial}{\partial \tilde{x}}, 0\right). \tag{C14}$$

Eqns. 10, 11 are obtained as follows

$$\begin{aligned} \nabla &= (\nabla x)\frac{\partial}{\partial x} + (\nabla \chi)\frac{\partial}{\partial \chi} \\ &= \left(\nabla_0^{\perp} x\right)\frac{\partial}{\partial x} + (\nabla \chi)\frac{\partial}{\partial \chi} \\ &= \nabla_0^{\perp} + (\nabla \chi)\frac{\partial}{\partial \chi}, \text{ and} \end{aligned} \tag{C15}$$

$$\begin{aligned} \nabla &= (\nabla \tilde{x})\frac{\partial}{\partial \tilde{x}} + (\nabla \xi)\frac{\partial}{\partial \xi} \\ &= \left(\tilde{\nabla}^{\perp} \tilde{x}\right)\frac{\partial}{\partial \tilde{x}} + (\nabla \xi)\frac{\partial}{\partial \xi} \\ &= \tilde{\nabla}^{\perp} + (\nabla \xi)\frac{\partial}{\partial \xi}. \end{aligned} \tag{C16}$$

Appendix 3.2. Expanded Expressions for the Modified Variational Approach

For the 3-D case of a reference sphere of radius r_0, integrals on the reference sphere are of the form

$$\int dS_0 = r_0^2 \iint \cos\theta d\phi d\theta = r_0^2 \iint \cos\tilde{\theta} d\tilde{\phi} d\tilde{\theta}, \tag{C17}$$

and volume integrals are of the form

$$\begin{aligned} \int dV = \int \left[\int d\chi\right] dS_0 &= r_0^2 \iiint d\chi \cos\theta d\phi d\theta \\ &= r_0^2 \iiint \frac{\partial \chi}{\partial \xi} d\xi \cos\tilde{\theta} d\tilde{\phi} d\tilde{\theta}. \end{aligned} \tag{C18}$$

Likewise, for the 3-D case of a reference plane (a flat-planet case with $r_0 \to \infty$), $\chi = z$

and integrals on the reference plane are of the form

$$\int dS_0 = \iint dxdy = \iint d\tilde{x}d\tilde{y}, \tag{C19}$$

and volume integrals are of the form

$$\begin{aligned} \int dV = \int \left[\int d\chi \right] dS_0 &= \iiint d\chi dxdy \\ &= \iiint \frac{\partial \chi}{\partial \xi} d\xi d\tilde{x}d\tilde{y}. \end{aligned} \tag{C20}$$

Likewise, for the 2-D case of a reference circle of radius r_0. integrals on the reference circle are of the form

$$\int dS_0 = r_0 \int d\phi = r_0 \int d\tilde{\phi}, \tag{C21}$$

and volume integrals are of the form

$$\begin{aligned} \int dV = \int \left[\int d\chi \right] dS_0 &= r_0 \iint d\chi d\phi \\ &= r_0^2 \iint \frac{\partial \chi}{\partial \xi} d\xi d\tilde{\phi}. \end{aligned} \tag{C22}$$

Likewise, for the 2-D case of a reference line (a flat-planet case with $r_0 \to \infty$), $\chi = z$ and integrals on the reference line are of the form

$$\int dS_0 = \int dx = \int d\tilde{x}, \tag{C23}$$

and volume integrals are of the form

$$\begin{aligned} \int dV = \int \left[\int d\chi \right] dS_0 &= \iint d\chi dx \\ &= \iint \frac{\partial \chi}{\partial \xi} d\xi d\tilde{x}. \end{aligned} \tag{C24}$$

The gradient of velocity/displacement $\underline{u}$ (eq. 27) can be expressed using eq. 17 and 24

as

$$\begin{aligned}
\frac{\partial\chi}{\partial\xi}\nabla_j u_i &= \frac{r_0}{r}\left\{\frac{\partial\chi}{\partial\xi}\tilde{\nabla}_j^{\perp}u_i+\underline{\tilde{n}}_j\frac{\partial u_i}{\partial\xi}\right\} \\
&= \frac{r_0}{r}\left\{\frac{\partial\chi}{\partial\xi}\tilde{\nabla}_j^{\perp}\left(\frac{r}{r_0}\tilde{u}_i\right)+\underline{\tilde{n}}_j\frac{\partial}{\partial\xi}\left(\frac{r}{r_0}\tilde{u}_i\right)\right\} \\
&= \frac{r_0}{r}\left\{\frac{\partial\chi}{\partial\xi}\frac{r}{r_0}\tilde{\nabla}_j^{\perp}\tilde{u}_i+\frac{\partial\chi}{\partial\xi}\frac{\tilde{u}_i}{r_0}\tilde{\nabla}_j^{\perp}r\right. \\
&\quad \left.+\underline{\tilde{n}}_j\frac{r}{r_0}\frac{\partial}{\partial\xi}\tilde{u}_i+\underline{\tilde{n}}_j\frac{\tilde{u}_i}{r_0}\frac{\partial}{\partial\xi}r\right\} \\
&= \frac{\partial\chi}{\partial\xi}\tilde{\nabla}_j^{\perp}\tilde{u}_i+\underline{\tilde{n}}_j\frac{\partial\tilde{u}_i}{\partial\xi} \\
&\quad +\frac{\tilde{u}_i}{r_0}\frac{r_0}{r}\left\{\frac{\partial\chi}{\partial\xi}\tilde{\nabla}_j^{\perp}r+\underline{\tilde{n}}_j\frac{\partial r}{\partial\xi}\right\} \\
&= \frac{\partial\chi}{\partial\xi}\tilde{\nabla}_j^{\perp}\tilde{u}_i+\underline{\tilde{n}}_j\frac{\partial\tilde{u}_i}{\partial\xi}+\frac{\tilde{u}_i}{r_0}\frac{\partial\chi}{\partial\xi}\nabla_j r \\
&= \frac{\partial\chi}{\partial\xi}\tilde{\nabla}_j^{\perp}\tilde{u}_i+\underline{\tilde{n}}_j\frac{\partial\tilde{u}_i}{\partial\xi}+\frac{\tilde{u}_i}{r_0}\frac{\partial\chi}{\partial\xi}\hat{x}_j
\end{aligned} \tag{C25}$$

Eq. 28 can be obtained by first differentiating $W\left(u_i,\nabla_j u_i\right)$ with respect to $\frac{\tilde{u}_i}{\xi}$ using the chain rule

$$\frac{\partial W}{\partial\left(\frac{\tilde{u}_i}{\xi}\right)}=\frac{\partial u_i}{\partial\left(\frac{\tilde{u}_i}{\xi}\right)}\frac{\partial W}{\partial u_i}+\frac{\partial\nabla_j u_i}{\partial\left(\frac{\tilde{u}_i}{\xi}\right)}\frac{\partial W}{\partial\nabla_j u_i}. \tag{C26}$$

Since u_i is not dependent on $\frac{\tilde{u}_i}{\xi}$ (see eq. 24), the first term is 0. Multiply the remaining terms by $\frac{\partial\chi}{\partial\xi}$ to obtain

$$\frac{\partial\chi}{\partial\xi}\frac{\partial W}{\partial\left(\frac{\tilde{u}_i}{\xi}\right)}=\frac{\partial\chi}{\partial\xi}\frac{\partial\left(\nabla_j u_i\right)}{\partial\left(\frac{\tilde{u}_i}{\xi}\right)}\frac{\partial W}{\partial\nabla_j u_i}, \tag{C27}$$

Note that from eq. 27 we have that $\frac{\partial\chi}{\partial\xi}\nabla_j u_i$ depends on $\frac{\tilde{u}_i}{\xi}$ only through $\underline{\tilde{n}}_j$. Therefore,

$$\frac{\partial\chi}{\partial\xi}\frac{\partial W}{\partial\left(\frac{\tilde{u}_i}{\xi}\right)}=\underline{\tilde{n}}_j\sigma_{ij}=\tilde{\sigma}_{in}, \tag{C28}$$

where we have also used the definitions of σ_{ij} and $\tilde{\sigma}_{in}$ from eq. 3 and 25.

In order to obtain eq. 30, we differentiate eq. 29 as follows

$$\begin{aligned}\frac{\partial \tilde{W}}{\partial \tilde{\sigma}_{in}} &= \frac{\partial}{\partial \tilde{\sigma}_{in}}\left\{\tilde{\sigma}_{kn}\frac{\partial \tilde{u}_k}{\partial \xi} - W\frac{\partial \chi}{\partial \xi}\right\} \\ &= \delta_{ik}\frac{\partial u_i}{\partial \xi} + \tilde{\sigma}_{kn}\frac{\partial\left(\frac{\partial u_k}{\partial \xi}\right)}{\partial \tilde{\sigma}_{kn}} - \frac{\partial\left(\nabla_j u_k\right)}{\partial \tilde{\sigma}_{in}}\frac{\partial W}{\partial\left(\nabla_j u_k\right)}\frac{\partial \chi}{\partial \xi}\end{aligned} \tag{C29}$$

Differentiating eq. 27 with respect to $\tilde{\sigma}_{kn}$, and noting that $\tilde{u}$ and $\tilde{\nabla}_j^{\perp} u_k$ are not dependent on $\tilde{\sigma}_{kn}$ gives us

$$\frac{\partial\left(\nabla_j u_k\right)}{\partial \tilde{\sigma}_{in}}\frac{\partial \chi}{\partial \xi} = \tilde{n}_j\frac{\partial\left(\frac{\partial u_k}{\partial \xi}\right)}{\partial \tilde{\sigma}_{in}} \tag{C30}$$

Substituting eq. 3 and C30 into the third term of eq. C29 we get

$$\frac{\partial \tilde{W}}{\partial \tilde{\sigma}_{in}} = \delta_{ik}\frac{\partial u_i}{\partial \xi} + \tilde{\sigma}_{kn}\frac{\partial\left(\frac{\partial u_k}{\partial \xi}\right)}{\partial \tilde{\sigma}_{kn}} - \tilde{n}_j\frac{\partial\left(\frac{\partial u_k}{\partial \xi}\right)}{\partial \tilde{\sigma}_{in}}\sigma_{ij} \tag{C31}$$

Since $\tilde{\sigma}_{in} = \tilde{n}_j\sigma_{ij}$ (eq. 25) the second and third term above cancel and we are left with eq. 30

$$\frac{\partial \tilde{W}}{\partial \tilde{\sigma}_{in}} = \delta_{ik}\frac{\partial u_i}{\partial \xi} = \frac{\partial u_k}{\partial \xi}. \tag{C32}$$

In order to obtain eq. 31, we differentiate eq. 29 as follows

$$\begin{aligned}\frac{\partial \tilde{W}}{\partial \tilde{u}_i} &= \frac{\partial}{\partial \tilde{u}_i}\left\{\tilde{\sigma}_{kn}\frac{\partial \tilde{u}_k}{\partial \xi} - W\frac{\partial \chi}{\partial \xi}\right\} \\ &\quad \text{apply product rule with } \tilde{\nabla}_j^{\perp} u_i \text{ and } \tilde{\sigma}_{in} \text{held fixed for all } i, j \\ &= \tilde{\sigma}_{kn}\frac{\partial\left(\frac{\partial \tilde{u}_k}{\partial \xi}\right)}{\partial \tilde{u}_i} - \frac{\partial W}{\partial \tilde{u}_i}\frac{\partial \chi}{\partial \xi \tilde{u}_i} \\ &\quad \text{apply the chain rule for } W \text{ considered as a function} \\ &\quad \text{of } \left(\tilde{u}_p, \tilde{\nabla}_q^{\perp}\tilde{u}_p, \frac{\partial \tilde{u}_p}{\partial \xi}\right) \\ &= \tilde{\sigma}_{kn}\frac{\partial\left(\frac{\partial \tilde{u}_k}{\partial \xi}\right)}{\partial \tilde{u}_i} - \left\{\frac{\partial \tilde{u}_p}{\partial \tilde{u}_i}\frac{\partial W}{\partial \tilde{i}_p} + \frac{\partial\left(\tilde{\nabla}_q^{\perp}\tilde{u}_p\right)}{\partial \tilde{u}_i}\frac{\partial W}{\partial\left(\tilde{\nabla}_q^{\perp}\tilde{u}_p\right)}\right. \\ &\quad \left. + \frac{\partial\left(\frac{\partial \tilde{u}_p}{\partial \xi}\right)}{\partial \tilde{u}_i}\frac{\partial W}{\partial\left(\frac{\partial \tilde{u}_p}{\partial \xi}\right)}\right\}\frac{\partial \chi}{\partial \xi}\end{aligned} \tag{C33}$$

noting that the third term is 0

$$= \tilde{\sigma}_{kn}\frac{\partial\left(\frac{\partial\tilde{u}_k}{\partial\xi}\right)}{\partial\tilde{u}_i} - \left\{\delta_{ip}\frac{\partial W}{\partial\tilde{u}_p} + \frac{\partial\left(\frac{\partial\tilde{u}_p}{\partial\xi}\right)}{\partial\tilde{u}_i}\frac{\partial W}{\partial\left(\frac{\partial\tilde{u}_p}{\partial\xi}\right)}\right\}\frac{\partial\chi}{\partial\xi}$$

$$= \tilde{\sigma}_{kn}\frac{\partial\left(\frac{\partial\tilde{u}_k}{\partial\xi}\right)}{\partial\tilde{u}_i} - \frac{\partial W}{\partial\tilde{u}_i}\frac{\partial\chi}{\partial\xi} - \frac{\partial\left(\frac{\partial\tilde{u}_p}{\partial\xi}\right)}{\partial\tilde{u}_i}\frac{\partial W}{\partial\left(\frac{\partial\tilde{u}_p}{\partial\xi}\right)}\frac{\partial\chi}{\partial\xi}$$

apply the chain rule for W considered as a function of $(u_s, \nabla_t u_s)$ and note that u_i depends only on $\tilde{u}_i$(eq. 24)

$$= \tilde{\sigma}_{kn}\frac{\partial\left(\frac{\partial\tilde{u}_k}{\partial\xi}\right)}{\partial\tilde{u}_i} - \frac{\partial u_s}{\partial\tilde{u}_i}\frac{\partial W}{\partial u_s}\frac{\partial\chi}{\partial\xi}$$
$$- \left\{\frac{\partial(\nabla_t u_s)}{\partial\tilde{u}_i} + \frac{\partial\left(\frac{\partial\tilde{u}_p}{\partial\xi}\right)}{\partial\tilde{u}_i}\frac{\partial(\nabla_t u_s)}{\partial\left(\frac{\partial\tilde{u}_p}{\partial\xi}\right)}\right\}\frac{\partial W}{\partial(\nabla_t u_s)}\frac{\partial\chi}{\partial\xi}$$

$$= \tilde{\sigma}_{kn}\frac{\partial\left(\frac{\partial\tilde{u}_k}{\partial\xi}\right)}{\partial\tilde{u}_i} - \frac{\partial u_s}{\partial\tilde{u}_i}\frac{\partial W}{\partial u_s}\frac{\partial\chi}{\partial\xi}$$
$$- \frac{\partial(\nabla_t u_s)}{\partial\tilde{u}_i}\frac{\partial W}{\partial(\nabla_t u_s)}\frac{\partial\chi}{\partial\xi} - \frac{\partial\left(\frac{\partial\tilde{u}_p}{\partial\xi}\right)}{\partial\tilde{u}_i}\frac{\partial W}{\partial\left(\frac{\partial\tilde{u}_p}{\partial\xi}\right)}\frac{\partial\chi}{\partial\xi}$$

substituting eq. 28 in the fourth term

$$= \tilde{\sigma}_{kn}\frac{\partial\left(\frac{\partial\tilde{u}_k}{\partial\xi}\right)}{\partial\tilde{u}_i} - \frac{\partial u_s}{\partial\tilde{u}_i}\frac{\partial W}{\partial u_s}\frac{\partial\chi}{\partial\xi} - \frac{\partial(\nabla_t u_s)}{\partial\tilde{u}_i}\frac{\partial W}{\partial(\nabla_t u_s)}\frac{\partial\chi}{\partial\xi} - \frac{\partial\left(\frac{\partial\tilde{u}_p}{\partial\xi}\right)}{\partial\tilde{u}_i}\tilde{\sigma}_{pn}$$

$$= -\frac{\partial u_s}{\partial\tilde{u}_i}\frac{\partial W}{\partial u_s}\frac{\partial\chi}{\partial\xi} - \frac{\partial(\nabla_t u_s)}{\partial\tilde{u}_i}\frac{\partial W}{\partial(\nabla_t u_s)}\frac{\partial\chi}{\partial\xi}$$

using eq. 27 in the first term and eq. 4 in the second term

$$= \left(\frac{r}{r_0}f_i - \frac{1}{r_o}\sigma_{ij}\hat{x}_j\right)\frac{\partial\chi}{\partial\xi}$$

Similarly eq. 32 is obtained

$$\begin{aligned}
\frac{\partial \tilde{W}}{\partial\left(\tilde{\nabla}_j^{\perp} u_i\right)} &= \frac{\partial}{\partial \tilde{u}_i}\left\{\tilde{\sigma}_{kn}\frac{\partial \tilde{u}_k}{\partial \xi} - W\frac{\partial \chi}{\partial \xi}\right\} \qquad \text{(C34)}\\
&\quad \text{applying the chain rule twice}\\
&= \tilde{\sigma}_{kn}\frac{\partial\left(\frac{\partial \tilde{u}_k}{\partial \xi}\right)}{\partial\left(\tilde{\nabla}_j^{\perp} u_i\right)} - \left[\frac{\partial\left(\frac{\partial \tilde{u}_k}{\partial \xi}\right)}{\partial\left(\tilde{\nabla}_j^{\perp} u_i\right)}\frac{\partial\left(\nabla_p u_q\right)}{\partial\left(\frac{\partial \tilde{u}_k}{\partial \xi}\right)}\right.\\
&\quad \left. + \frac{\partial\left(\nabla_p u_q\right)}{\partial\left(\tilde{\nabla}_j \tilde{u}_i\right)}\right]\frac{\partial W}{\partial\left(\nabla_p u_q\right)}\frac{\partial \chi}{\partial \xi}\\
&\quad \text{the first two terms cancel}\\
&= -\frac{\partial\left(\nabla_p u_q\right)}{\partial\left(\tilde{\nabla}_j \tilde{u}_i\right)}\frac{\partial W}{\partial\left(\nabla_p u_q\right)}\frac{\partial \chi}{\partial \xi}\\
&\quad \text{using } \tilde{\nabla}_j^{\perp} u_i = \left(\delta_{jl} - \hat{x}_j \hat{x}_l\right)\tilde{\nabla}_l^{\perp} u_i \text{ and eq. 3}\\
&= \left(\delta_{jl} - \hat{x}_j \hat{x}_l\right)\sigma_{il}\frac{\partial \chi}{\partial \xi}
\end{aligned}$$

To optimizing eq. 33 with respect to $\tilde{\sigma}_{in}$ we first let $\tilde{\sigma}_{in} \to \tilde{\sigma}_{in} + \varepsilon\psi_i$, where ψ_i is an arbitrary function. We require that first order terms in ε sum to zero for all functions of ψ_i

$$\begin{aligned}
0 &= \sum_{k=1}^{L}\int_{k-1}^{k}\left\{\int_{S_0}\left[\varepsilon\psi_i\frac{\partial \tilde{u}_i}{\partial \xi} - \varepsilon\psi_i\frac{\partial \tilde{W}}{\partial \tilde{\sigma}_{in}}\right]dS_0\right\}d\xi \qquad \text{(C35)}\\
&= \varepsilon\sum_{k=1}^{L}\int_{k-1}^{k}\left\{\int_{S_0}\psi_i\left[\frac{\partial \tilde{u}_i}{\partial \xi} - \frac{\partial \tilde{W}}{\partial \tilde{\sigma}_{in}}\right]dS_0\right\}d\xi,
\end{aligned}$$

i.e. $0 = \frac{\partial \tilde{u}_i}{\partial \xi} - \frac{\partial \tilde{W}}{\partial \tilde{\sigma}_{in}}$

Similarly, to optimize optimizing eq. 33 with respect to $\tilde{u}_i$ we first let $\tilde{u}_i \to \tilde{u}_i + \varepsilon\psi_i$, where ψ_i is an arbitrary function. We require that first order terms in ε sum to zero for all

functions of ψ_i

$$
\begin{aligned}
0 \;=\; & \sum_{k=1}^{L} \int_{k-1}^{k} \left\{ \int_{S_0} \left[\varepsilon \tilde{\sigma}_{in} \frac{\partial \psi_i}{\partial \xi} - \varepsilon \psi_i \frac{\partial \tilde{W}}{\partial \tilde{u}_i} \right. \right. \\
& \left. - \varepsilon \tilde{\nabla}_j^{\perp} \psi_i \frac{\partial \tilde{W}}{\partial \left(\tilde{\nabla}_j^{\perp} \tilde{u}_i \right)} \right] dS_0 \\
& - \left[\int_{\partial S_{oT}^k} \varepsilon \psi_i T_i^0 dl_0 + \int_{\partial S_{0u}^k} \varepsilon \tau_i^0 \psi_i dl_0 \right] \frac{\partial \chi}{\partial \xi} \Bigg\} d\xi \\
& + \int_{\substack{\xi=0 \\ \underline{x} \in \partial V_T}} \varepsilon \psi_i \tilde{T}_i^{\xi} dS_0 + \int_{\substack{\xi=0 \\ \underline{x} \in \partial V_u}} \varepsilon \tilde{\tau}_i^{\xi} \psi_i dS_0 \\
& - \int_{\substack{\xi=L \\ \underline{x} \in \partial V_T}} \varepsilon \psi_i \tilde{T}_i^{\xi} dS_0 - \int_{\substack{\xi=L \\ \underline{x} \in \partial V_u}} \varepsilon \tilde{\tau}_i^{\xi} \psi_i dS_0 \\
= \; & \varepsilon \sum_{k=1}^{L} \int_{k-1}^{k} \left\{ \int_{S_0} \psi_i \left[- \frac{\partial \tilde{\sigma}_{in}}{\partial \xi} - \frac{\partial \tilde{W}}{\partial \tilde{u}_i} \right. \right. \\
& \left. + \tilde{\nabla}_j^{\perp} \left(\frac{\partial \tilde{W}}{\partial \left(\tilde{\nabla}_j^{\perp} \tilde{u}_i \right)} \right) \right] dS_0 \\
& - \left[\int_{\partial S_{0T}^k} \psi_i \left\{ T_i^0 \frac{\partial \chi}{\partial \xi} + n_j^0 \frac{\partial \tilde{W}}{\partial \left(\tilde{\nabla}_j^{\perp} \tilde{u}_i \right)} \right\} dl_0 \right. \\
& \left. \left. + \int_{\partial S_{0u}^k} \psi_i \left\{ T_i^0 \frac{\partial \chi}{\partial \xi} + n_j^0 \frac{\partial \tilde{W}}{\partial \left(\tilde{\nabla}_j^{\perp} \tilde{u}_i \right)} \right\} dl_0 \right] \right\} d\xi \\
& + \int_{\substack{\xi=0 \\ \underline{x} \in \partial V_T}} \psi_i \left\{ \tilde{T}_i^{\xi} - \tilde{\sigma}_{in} \right\} dS_0 + \int_{\substack{\xi=0 \\ \underline{x} \in \partial V_u}} \psi_i \left\{ \tilde{\tau}_i^{\xi} - \tilde{\sigma}_{in} \right\} dS_0 \\
& - \sum_{k=1}^{L-1} \int_{\xi=k} \psi_i \left(\tilde{\sigma}_{in}^{k+1} - \tilde{\sigma}_{in}^{k} \right) dS_0 \\
& - \int_{\substack{\xi=L \\ \underline{x} \in \partial V_T}} \psi_i \left\{ \tilde{T}_i^{\xi} - \tilde{\sigma}_{in} \right\} dS_0 - \int_{\substack{\xi=L \\ \underline{x} \in \partial V_u}} \psi_i \left\{ \tilde{\tau}_i^{\xi} - \tilde{\sigma}_{in} \right\} dS_0
\end{aligned}
\tag{C36}
$$